# Anthropogenic effects on the concentration of hydroxyl radicals in the troposphere

A thesis presented in partial fulfilment of the requirements for the degree of

Doctor of Philosophy
in
Chemistry

at Massey University, Albany, New Zealand

Jade Pope
Submitted 30th August 2025

# Contents

**Abstract** .......... **v**
**Acknowledgements** .......... **vi**
**List of Abbreviations** .......... **viii**
**List of Figures** .......... **x**
**List of Tables** .......... **xv**
**1.0 Introduction** .......... **1**

1.1 Chapter Overview .......... 3
1.2 Structure of the Atmosphere .......... 4
1.3 Climate Drivers: What Molecules Do We Blame? .......... 7

1.3.1 $CO_2$, $CH_4$, and $N_2O$ .......... 9
1.3.2 Short-Lived Climate Forcers and Other GHGs .......... 12
1.3.3 Other Climate Forcers .......... 14

1.4 What Are We Doing About It? .......... 15

1.4.1 Mitigation .......... 17
1.4.2 $CO_2$ Removal (CDR) .......... 18
1.4.3 Solar Radiation Management .......... 19

1.5 Reducing $CH_4$ Concentration .......... 21
1.6 The Hydroxyl Radical .......... 24
1.7 Titanium Dioxide as a Photocatalyst .......... 27
1.8 Research Statement .......... 30
1.9 References .......... 32

**2.0 Establishing a MI-FTIR Correction Function** .......... **37**

2.1 Introduction .......... 37
2.2 Computational Procedure .......... 40

2.2.1 Reference Library Molecules .......... 44

2.3 Experimental Procedure .......... 46

2.3.1 Experimental Details .......... 46
2.3.2 Matrix-Isolation Spectroscopy .......... 47

2.4 Establishing the Functions .......... 50

2.4.1 Peak Assignments .......... 50
2.4.2 Correction Function .......... 52
2.4.3 Scaling Factor .......... 59
2.4.4 Comparison of Functions .......... 63

2.5 Conclusion .......... 67
2.6 References .......... 68

**3.0 Radical Formation and Detection** .......... **70**

3.1 Introduction .......... 70
3.2 Establishing the Tesla-Coil Method of Radical Formation .......... 71
3.3 Direct Detection of Formed Radicals Using the Tesla-Coil Method .......... 75

3.3.1 Literature Studies .......... 76
3.3.2 Results .......... 78

3.4 Radical Reaction Experiments .......... 83

3.4.1 ·OH + Propyne .......... 85
3.4.2 ·OH + Isoprene .......... 87

3.4.3 ·OH + β-pinene ........ 90
3.4.4 Common Peaks Across Spectra ........ 93
3.4.5 Radical Reaction Conclusions ........ 98

3.5 Conclusion ........ 99
3.6 References ........ 100

**4.0 Photochemistry and $TiO_2$ Experiments ........ 102**

4.1 Introduction ........ 102
4.2 Depositing $TiO_2$ ........ 103
4.3 Fluorescent Probe Studies ........ 105

4.3.1 Introduction ........ 105
4.3.2 Experimental Details and Results ........ 108

4.4 Experimental Infrastructure ........ 117

4.4.1 RGA Infrastructure and Experimental Conditions ........ 117
4.4.2 Fluorescence Cell ........ 119
4.4.3 Sensitivity Test for RGA 300 ........ 121

4.5 Residual Gas Analyser Experiments ........ 123

4.5.1 Using RGA Software to Collect and Visualise Data ........ 123
4.5.2 Using the RGA with MCS to Collect and Visualise Data ........ 126

4.6 Conclusion ........ 132
4.7 References ........ 134

**5.0 Atmospheric Modelling ........ 136**

5.1 Introduction ........ 136
5.2 Literature Studies ........ 139
5.3 Model Details ........ 140

5.3.1 SMARTS and Photolysis Rates ........ 147

5.4 Results ........ 150

5.4.1 Targeting $CH_4$ Removal Rates ........ 154

5.5 Conclusion ........ 162
5.6 References ........ 164

**6.0 Conclusion and Future Work ........ 167**

# Abstract

This thesis investigated the use of a $TiO_2$ catalyst to increase atmospheric ·OH concentrations in order to reduce atmospheric $CH_4$ concentrations, an important greenhouse gas that contributes to climate change effects. Firstly, a reference library of important atmospheric molecules was created using the Matrix-Isolation technique coupled with Fourier-Transform Infrared Spectroscopy (MI-FTIR). The spectra collected for these molecules were assigned using a combination of literature data and data calculated by Gaussian-16 software. This reference library was then used to create correction functions that could be applied to spectra collected of other molecules. Detection of ·OH was then attempted using the MI-FTIR technique, combined with Tesla-coil discharge applied to gas-phase water mixtures to form the radicals. This technique was ultimately deemed unsuitable due to difficulties in detection. A spectrofluorophotometer was then used as the excitation source, in combination with a built in-house cell that housed a $TiO_2$-coated slide in the presence of water and hydrocarbons, detected by a residual gas analyser (RGA). The results of these experiments were also inconclusive due to detection difficulties. The photocatalytic activity of $TiO_2$ slides under aqueous conditions was tested and confirmed using probe molecules of coumarin and terephthalic acid to detect for ·OH oxidation products using emission fluorescence spectroscopy, from which a quantum yield for ·OH formation under aqueous conditions was established. Finally, a rough atmospheric model was established to give insight to the effect of changing atmospheric concentrations of molecules on other concentrations. A perturbation rate for a specific particle density of $TiO_2$ was added to this model to establish the effect on the concentrations, and it was found that ·OH, HOO·, and $H_2O_2$ concentrations remained relatively stable, whereas $CH_4$ and $O_3$ experienced significant decreases. Overall, $TiO_2$ was predicted to be an appropriate atmospheric catalyst for removal of methane, but further research is required for implementation.

# Acknowledgements

Firstly, I would like to thank my supervisors, Associate Professor John Harrison and Dr Marie-Anne Thelen for their assistance, guidance, expertise, and ability to redirect any of my attempts to overcomplicate matters. Their limitless patience and willingness to explain concepts and talk through ideas has been invaluable throughout this process, alongside the pastoral care provided throughout the numerous challenges faced. I'd also like to thank Associate Professor Winston Sweatman for stepping into the role of supervisor in the final stages of this thesis, an action I greatly appreciate – thank you for your support, enthusiasm, and eagerness to help.

I'd also like to thank the Chemistry Department at Massey University, Albany, both past and present, for their assistance. Professor Al Nielson, Associate Professor Jon Kitchen, and Dr Debbie Jordan have all provided me with expertise or alternative perspectives on my research at times, alongside Grace Zhang, who was a delight to work with and be around for the short time I had her. I'd also like to thank Dr Marilou Raduban for her assistance and kindness. Additionally, the star team of technicians who held down the fort during my time as a technician cannot be left with praises unsung, and are not limited to Erin Moffet, Margaret Peace, Jarod Young, and Odette Howarth – I am deeply grateful for your support.

I am grateful to the New Zealand Institute of Advanced Studies and specifically Distinguished Professor Peter Schwerdtfeger for use of their supercomputer, which was invaluable to the theoretical section of my research, as well as Mike Yap for his help with using the supercomputer. I would also like to extend a special thanks to Massey University solely for granting me a scholarship to undertake my studies.

Without the help of my family and friends, this project would have taken significantly longer than it already did. Thanks to my family, Tania, Dave, and Jordan Pope; to my fellow postgraduate students, Gaby Sansom, Alex Burton, Holly Scott, and Antony Burrows, who suffered alongside me; and my friends, whether current or past, who at some point have all provided a shoulder to cry on or an excuse to be distracted from my work, being Maddie Couprie, Gina Treleaven, Jenny Hanley, Sean Tholen, Adam Stock, and Dani Montallana.

An enormous, world rounding, indescribable heaping of thanks to Erin Moffet, as a colleague, a manager, and a friend, for providing life advice and research advice, being great to work with and for, and also feeding me an army's worth of baked goods. Without you this thesis would not exist; I am forever grateful.

Finally, I owe a huge sum of thanks to Dr Alex O'Neil for assistance over the entire process, from the first year of undergraduate up to the submission of this thesis. Thank you for supporting me throughout the years, providing phrasing help, chemistry advice, a materials chemist's perspective on a physical chemistry project, as well as moral and emotional support. You have been integral to this work.

# List of Abbreviations

B3LYP – Becke 3-parameter Lee-Yang-Parr

BECCS – Bioenergy carbon capture and storage

CB – Conduction band

cc-pVDZ, DZ – Correlation-consistent polarised valence double zeta

cc-pVTZ, TZ - Correlation-consistent polarised valence triple zeta

cc-pVQZ, QZ - Correlation-consistent polarised valence quadruple zeta

CCS – Carbon capture and storage

CCCBDB – Computational Chemistry Comparison and Benchmark Database

CEM – Channel electron multiplier

CDR – Carbon dioxide removal

CFC – Chlorofluorocarbon

COP26 – Conference of the parties 26

cw-CRD – Continous wave cavity ring down

DAC – Direct air capture

DU – Dobson unit

EPR – Electron paramagnetic resonance

ERF – Effective radiative forcing

FPT – Freeze-pump-thaw

FTIR – Fourier-Transform Infra-Red

FWHM – Full width at half maximum

GHG – greenhouse gas

GSAT – Global surface air temperature

GMSL – Global mean sea level

GMST – Global mean surface temperature

GWP – Global warming potential

HCFC – Hydrochlorofluorocarbon

HF – Hatree Fock

HFC – Hydrofluorocarbon

IPCC – International Panel on Climate Change

IR – Infra-Red

LIF – Laser induced fluorescence

MCS – Multichannel scalar

MI – Matrix isolation

MP2 – Second order Møller-Plesset

MPI – Ministry for Primary Industries

NH – Northern Hemisphere

NIST – National Institute of Standards and Technology

NMVOC – Non-methane volatile organic compound

PgC – Pentagrams of carbon

$PM_x$ – Particulate matter (X size diameter)

RASSS – Rapid-Annealing-Self-Solution-Shearing

RF – Radiative forcing

RGA – Residual gas analyser

RMSE – Root mean square error

SAI – Stratospheric aerosol injection

SF – Scaling factor

SH – Southern Hemisphere

SLCF – Short lived climate forcer

SMARTS – Simple Model of the Atmospheric Radiative Transfer of Sunshine

SOA – Secondary organic aerosol

SRM – Solar radiation management

SS – Steady-state

SZA – Solar zenith angle

TCD – Tesla-coil discharge

TPA – Terephthalic acid

UHV – Ultra high vacuum

UV – Ultra Violet

VB – Valence band

VOC – Volatile organic compound

2TPA – 2-Hydroxyterephthalic acid

7HC – 7-Hydroxycoumarin

5HC – 5-Hydroxycoumarin

3HC – 3-Hydroxycoumarin

# List of Figures

Figure 1.1 Layers of the atmosphere. The troposphere, the closest layer to the Earth's surface, contains most of the greenhouse gases of interest, as well as weather and chemical reactions. The stratosphere contains the ozone layer and plane flights. The mesosphere contains meteors, and the thermosphere and exosphere contain satellites. ....................................4

Figure 1.2 Summary of atmospheric processes that affect incoming and outgoing radiation. Incoming solar radiation of 100% represents 342 W m$^{-2}$. Only about half of incoming radiation makes it to the Earth's surface. Reproduced with permission from Berger et al. (1992).[89] .5

Figure 1.3 Incoming radiation in microns versus percentage transmitted by the atmosphere. Absorption bands are labelled by corresponding molecule. The window of atmospheric importance is highlighted. This is the region where energy can be radiated away from Earth, so any molecule that absorbs in that region will have a large warming impact. The solar window is where all energy comes in from the Sun, with a lot of absorption in that region from water vapour. Image adapted from open access source Mikolajcyzk et al. (2017).[16] .....................6

Figure 1.4 Annual anthropogenic emissions (in tonnes) of $N_2O$, $CH_4$, and $CO_2$, the three main GHGs involved in global warming. $N_2O$ and $CH_4$ are plotted in units of tonnes of $CO_2$ equivalents, which weights emissions against the GWP of each molecule. The rate of increase in all three skyrockets in the mid 20th century, but has been increasing since 1850. Data reproduced from Our World in Data under a Creative Commons license.[20-22] ...................11

Figure 1.5 Summary of how increasing $CH_4$ concentrations will affect the atmosphere. Notably, [·OH] would be reduced from an increase in reactions with $CH_4$ which would extend $CH_4$'s atmospheric lifetime. An increase in $CH_4$ also would mean a greater amount migrating to the stratosphere, where the impact of water vapour (produced as an oxidation product) would have a greater impact in blocking radiation than the water vapour produced in the troposphere by the same reaction. Data summarised from Reisinger (2018).[54] ...............23

Figure 1.6 Major reactions affecting $HO_X$ in the troposphere. Interconversion between ·OH and HOO· is rapid and mediated by reactions with $O_3$ and NO·. Reproduced with permission from Logan et al. (1981).[65] ..........................................................................................25

Figure 1.7 Representation of the photocatalysis process, where a semiconductor (represented by the large circle) absorbs a photon of wavelength greater than or equal to its bandgap, creating an electron-hole pair which can react with other molecules (R). .......................................27

Figure 1.8 Simplified diagram of a $TiO_2$ surface with and without an oxygen vacancy. Blue circles are oxygen, red are titanium. Surface vacancies can act as charge traps or can react themselves with molecules like oxygen to form adsorbed OH or other products..............28

Figure 2.1 Image of the matrix-isolation setup, specifically the vacuum chamber housing, with an inset diagram of how the sample and carrier gas are distributed on the $CaF_2$ window. .............37

Figure 2.2 Harmonic and anharmonic potentials for bond stretching. Reproduced with permission from Allinger (2010).[31] ..................................................................................................42

Figure 2.3 Schematic diagram of gas-handling layout for MI setup. The argon and sample lines are separate to avoid sample in the argon line and therefore in the 'baseline' spectrum. Both lines are connected to the vacuum housing such that the gas stream will contact the ~ 20 K $CaF_2$ window to form the matrix. ....................................................................................47

Figure 2.4 Background spectrum of benzene matrix-isolation experiment. This spectrum is automatically subtracted from the collected data to remove any atmospheric background peaks. Peaks from water and $CO_2$ are often still seen in sample spectra but at a much lesser intensity due to the automatic subtraction. .....................................................................................47

Figure 2.5 Argon baseline for benzene matrix-isolation experiment. Even though an atmospheric baseline is automatically subtracted from the sample spectrum, small changes in the atmospheric background cause the presence of peaks from $CO_2$ and $H_2O$. The presence of these peaks can make it difficult to see sample peaks in these areas. There are also clearly peaks in the argon spectrum that are not from the atmospheric background; these peaks are noted in the sample spectrum and will not be assigned as they were present before the introduction of the sample. ......... 48

Figure 2.6 Annotated section from ~ 3100 - 3000 $cm^{-1}$ of the benzene matrix-isolation spectrum. These are a few of the peaks that are seen when the sample is introduced to the system. These peaks are then assigned using a combination of literature and computational data. ........ 49

Figure 2.7 Graphs of assigned experimental wavenumber versus calculated wavenumber for benzene. Calculations are done with either B3LYP or MP2 levels of theory, and a cc-pVQZ basis set. Assigned frequencies are given in Table 2.2. ......... 52

Figure 2.8 Plot of experimental frequency versus corresponding computed value for molecules in the reference library, by level of theory. It is assumed that the relationship between the two values is given by the linear regression trendline. ......... 54

Figure 2.9 Plot of experimental frequency versus corresponding computed value for molecules in the reference library, by level of theory calculated at the cc-pVDZ level. It is assumed that the relationship between the two values is given by the linear regression trendline. .............. 56

Figure 2.10 Plot of experimental frequency versus corresponding computed value for molecules in the reference library, by level of theory calculated at the cc-pVTZ level. It is assumed that the relationship between the two values is given by the linear regression trendline. .............. 56

Figure 2.11 Plot of experimental frequency versus corresponding computed value for molecules in the reference library, by level of theory calculated at the cc-pVQZ level. It is assumed that the relationship between the two values is given by the linear regression trendline. .............. 57

Figure 2.12 Plot of experimental frequency versus corresponding computed value in the high frequency range for molecules in the reference libray, by level of theory calculated at the cc-pVTZ level. ......... 58

Figure 2.13 RMSE between the corrected computed wavenumbers and the corresponding assigned experimental wavenumbers for acetone. The corrections applied are the correction and scaling factors calculated in this work, and the literature factors given by Sinha et al. (2004).[28] The assignments are split into B3LYP and MP2 levels of theory and are calculated using the cc-pVQZ basis set. ......... 65

Figure 2.14 RMSE between the corrected computed wavenumbers and the corresponding assigned experimental wavenumbers for 2-propanol. The corrections applied are the correction and scaling factors calculated in this work, and the literature factors given by Sinha et al. (2004).[28] The wavenumbers are calculated using the cc-pVQZ basis set. .......................... 65

Figure 3.1 Gas-handling layout used for the acetone Tesla-coil test experiment. The Tesla-coil discharges to the sample through a borosilicate glass tube, which is connected to the vacuum chamber by initially a metal tee, and then subsequently a PTFE union with rubber o-rings to prevent radical scavenging. This is a modified layout of the one used in section 2.4. ... 72

Figure 3.2 Peaks assigned to CO from a spectrum of acetone subject to Tesla-coil discharge. ................ 74

Figure 3.3 Typical peaks seen for water and its multimers in water/oxygen/argon mixture experiments. The section of the spectra shown is from W6 but is typical to the “baseline” established for mixtures before being subjected to Tesla-coil discharge. ......... 80

Figure 3.4 Behaviour of the CO attributed peaks during annealing. This section comes from the spectra of W8, with the red being deposited at 8 K and the blue having been annealing slowly up to 35 K. The 2138 $cm^{-1}$ peak completely disappears at 35 K, and a shoulder peak appears at 2151 $cm^{-1}$. ......... 82

Figure 3.5 Final gas-handling layout for matrix-isolation radical reaction experiments. There are three lines; the water and argon line connect before being subjected to Tesla-coil discharge, after which the sample line connects by way of a PTFE union tee (to avoid radical scavenging). Each line can be valved off and rough pumped individually. ..........................83

Figure 3.6 Behaviour of CO attributed peaks during annealing process. These spectra are taken from the isoprene experiment. Blue: Mixture deposited at 8 K subject to Tesla-coil discharge. Red: Annealed to 35 K. Green: Cooled to 8 K. ..........................................................................93

Figure 3.7 CO attributed peaks for the propyne blank experiment (blue) and propyne TC-discharge experiment (red). For the TC-discharge experiment, the 2149 $cm^{-1}$ and 2138 $cm^{-1}$ peaks are of similar intensity, but for the blank experiment, the 2138 $cm^{-1}$ peak is more intense, second only to the 2136 $cm^{-1}$ peak. ....................................................................94

Figure 3.8 CO attributed peaks for the propyne TC-discharge experiment. Similar peak shape and behaviour is experienced as noted in Givan et al. (1996).[25] ..............................................96

Figure 3.9 2120 – 2160 $cm^{-1}$ section of spectra of 100:1:1 Ar:$H_2O$:CO mixtures. Spectra are recorded at 5 K but are deposited at different temperatures: A. 5 K, B. 10 K, C. 15 K, and D. 20 K. Reproduced from Givan et al. (1996).[25] .............................................................................96

Figure 4.1 Initial $TiO_2$ coating test with one layer (top) and two layers (bottom) deposited. Adding extra layers dissolved the preceding layers..............................................................................103

Figure 4.2 Slides in order of film retention after being submerged in distilled water. 1: RASSS-deposited slide. 2 & 3: 1 mg/mL suspension spun at 700 rpm. 4: 1 mg/mL suspension spun at 1000 rpm. 5 & 6: 0.5g/mL suspension spun at 1000 rpm. 7: 0.5g/mL suspension spun at 1000 rpm, then 2000 rpm. Slides 5 & 6 are glass, all other slides are quartz. All slides are cleaned with piranha solution and then stored in milli-Q water before depositing. ......................104

Figure 4.3 Top: Reaction of terephthalic acid (TPA) with ·OH to form the fluorescent product, 2-hydroxyterephthalic acid (2TPA). Bottom: Reaction of coumarin with OH· to form the only fluorescent product, 7-hydroxycoumarin (7HC). Source: Ishibashi, 2000.[5] ......................105

Figure 4.4 Top: Emission plot for the 1 mM coumarin solution containing a $TiO_2$-coated slide undergoing continuous UV irradiation ($\lambda_{ex}$ = 332 nm). Data were recorded every 10 minutes but for simplicity scans taken every 30 minutes are shown. Slit widths were 5 nm, and a 360 nm filter was used. The intensity is normalised to the highest intensity for each scan. There is a clear increase in intensity at 460 nm with irradiance time. Bottom: Monitoring emission intensity at 460 nm. There is an increase in intensity with irradiation time.....................110

Figure 4.5 Top: Emission plot for the 0.5 mM terephthalic acid solution containing a $TiO_2$-coated slide undergoing continuous UV irradiation ($\lambda_{ex}$ = 315 nm). Slit widths were 5 nm, and a 340 nm filter was used. The data were normalised to the peak present at 315 nm which corresponds to the excitation light. There is a clear increase in intensity at 425 nm with irradiance time. Bottom: Monitoring emission intensity at 425 nm. There is an increase in emission intensity with irradiation time. ........................................................................111

Figure 4.6 Emission plot for the 1 mM coumarin solution containing a $TiO_2$-coated slide undergoing continuous UV irradiation ($\lambda_{ex}$ = 332 nm). Slit widths were 10 nm, and a 360 nm filter was used. The intensity is normalised to the highest intensity for each scan. There is a clear increase in intensity at 460 nm with irradiance time, as well as little significant change seen when the solution was left to stir in the dark for 150 minutes, indicating reactions only occur when an excitation source is present. ............................................................112

Figure 4.7 "Blank" run of the 1 mM coumarin probe solution, run without a $TiO_2$ slide. There is no significant increase observed in the 460 nm region, proving the increase observed in probe tests is due to a reaction involving the $TiO_2$. Slit width 10 nm, $\lambda_{ex}$ = 332 nm....................113

Figure 4.8 Plot of emission intensity vs concentration, monitored at 460 nm, for different concentrations of 7-hydroxycoumarin. $\lambda_{ex}$ = 332 nm, slit widths of 5 nm. The slope of the line is the rate of production of 7-hydroxycoumarin. ..................................................................................114

Figure 4.9 Plot of emission intensity vs concentration, monitored at 425 nm, for different concentrations of 2-hydroxyterephthalic acid. $\lambda_{ex} = 332$ nm, slit widths of 5 nm. The slope of the line is the rate of production of 2-hydroxyterephthalic acid. .......... 114

Figure 4.10 Plot of concentration of 7-hydroxycoumarin produced from photooxidation of coumarin vs illumination time. .......... 116

Figure 4.11 Plot of concentration of 2-terephthalic acid produced from photooxidation of terephthalic acid vs illumination time. .......... 116

Figure 4.12 Diagram of vacuum chamber setup (top-down view). The translational stage can bring the gas line closer to the vacuum chamber entrance, which has an adjustable size entry hole. .......... 117

Figure 4.13: Schematic representation of the fluorescence cell and associated gas-handling for RGA experiments. The cell is connected to both a gas source and rough pump which can be valved off individually, and to the vacuum chamber. .......... 119

Figure 4.14 Slide holder inside the fluorescence cell. The holder can be rotated so that angle of incidence can be changed. .......... 120

Figure 4.15 Simplified layout of gas-handling for the fluorescence cell. Leak valves allow for precise flow control. .......... 120

Figure 4.16 Experimental setup for $H_2O_2$ sensitivity testing. .......... 121

Figure 4.17 Mass spectrum whilst flowing $H_2O_2$ into the vacuum chamber. The large peak at 34 m/z indicates the detector is sensitive to $H_2O_2$, especially since the peak is insignificant in background data. This spectrum comes specifically from run 5. .......... 122

Figure 4.18 Plot of pressure-vs-time for a mixture of ethylene/argon/$H_2O$, monitoring chosen m/z peaks. This experiment was run using the CEM to give appreciable signal. The graph shows the repeating frequency experienced in all experiments when using the CEM which makes detecting small changes in pressure very difficult and resulted in changing methods for collecting and visualising data. .......... 125

Figure 4.19 Plot of average counts for a mixture of ethylene/argon/$H_2O$, irradiated with $\lambda_{ex} = 360$ nm in the presence of a $TiO_2$ slide (experiment M10). Scan 0 is the empty cell, 1 the cell containing the gas mixture, 2 after 60 minutes of irradiation, 3 after 120 minutes of irradiation, and 4 after 180 minutes of irradiation. .......... 128

Figure 4.20 Plot of average counts for a mixture of ethylene/argon/$H_2O$ in the presence of a $TiO_2$ slide. The experiment, M8, is run as a blank so no excitation light is added. Scan 0 is the empty cell, 1 the cell containing the gas mixture, 2 after 60 minutes of irradiation, 3 after 120 minutes of irradiation, and 4 after 180 minutes of irradiation. .......... 129

Figure 4.21 Plot of average counts vs irradiation time for a mixture of ethylene, argon, and $H_2O$ (experiment M11). The mixture is held in the fluorescence cell in the presence of a $TiO_2$ slide irradiated by $\lambda_{ex} = 360$ nm. The masses tracked are $CO_2$ (44), a final oxidation product, and ethylene (28), to track reactant consumption. There is a general decrease in counts for mass 28, and little significant change for mass 44 over time. .......... 130

Figure 4.22 Plot of average counts vs irradiation time for a mixture of ethylene, argon, and $H_2O$ (experiment M9). The mixture is held in the fluorescence cell with no $TiO_2$ slide, irradiated by $\lambda_{ex} = 360$ nm, to act as a blank. The masses tracked are $CO_2$ (44), a final oxidation product, and ethylene (28), to track reactant consumption. There is a general decrease in counts for mass 28, and little significant change for mass 44 over time. .......... 130

Figure 4.23 Plot of average counts vs irradiation time for experiments M9 and M11, monitoring mass 44. The gas mixture of $H_2O$/ethylene/argon is held in the fluorescence cell with a $TiO_2$ slide irradiated by $\lambda_{ex} = 360$ nm (with no slide in the case of the blank). There is little significant change in counts for the experiment, with larger variation seen in the blank. .......... 131

Figure 5.1 Representations of differing dimensions of models: a) zero-dimensional or box model, b) 1-D or column model, c) 2-D model, and d) 3-D model. Reproduced from Seinfeld et al. (2016).[1] ........................................................................................................................137

Figure 5.2 Graph of concentration vs time for $NO_2\cdot$ in the V14 simulation. $NO_2\cdot$ is considered to have reached steady-state as it remains at a constant value over a large time period as shown in the graph, as well as equal and unchanging production and loss values..........................145

# List of Tables

Table 1.1 Summary of major indicators of global warming and the magnitude/direction of their change. Information summarised from Gulev et al. (2021).[1] NH = Northern Hemisphere, SH = Southern Hemisphere. .......... 2

Table 1.2 Table of lifetimes, ERF, and GWP for significant forcers. The only net negative (cooling) forcers are aerosols and the intrinsic albedo (ratio of reflected light from the surface) of the Earth, both of which can be affected by anthropogenic activities. Attention is drawn to the ERF for $CO_2$ and to the GWP of $CH_4$. Data adapted from IPCC AR6 and AR5 Reports.[1, 17] .......... 8

Table 1.3 Sources, lifetime, pre-industrial (1750) concentrations and 2019 concentrations of important GHGs. The huge increase in $CH_4$ is starkly laid out here. The fossil-fuel industry is a source for all but $N_2O$. Data adapted from IPCC AR6 report (2021) and Graedel et al. (1993).[6, 23, 24, 28] .......... 15

Table 2.1 Reference library molecules, structures, and highest basis set used for anharmonic calculations for B3LYP and MP2 levels of theory. .......... 45

Table 2.2 Table of assigned literature and calculated frequencies to experimental data for benzene. Calculations are anharmonic and at QZ level. Not all calculated or experimental peaks are assigned. .......... 50

Table 2.3 Table of $R^2$ and adjusted $R^2$ values for plotted graphs of calculated versus assigned experimental wavenumber (graphs in appendix A) for both levels of theory, as well as reference data where available for each molecule. Most $R^2$ values, if not 1.0000, are 0.9990 or higher. This tight spread indicates a consistency in the assignment of calculated to experimental wavenumbers. .......... 53

Table 2.4 Linear regression values, adjusted $R^2$, and RMSE for plots of experimental frequency versus corresponding computational value, split into level of basis set. .......... 55

Table 2.5 Linear regression analysis outputs for plots of experimental frequency versus corresponding computational value, split into spectral region by level of basis set. .......... 57

Table 2.6 RMSE for plots of experimental frequency versus corresponding computational value, split into spectral region by level of basis set. The overall RMSE for each basis set by level of theory is given for comparison (data from Table 2.4). .......... 58

Table 2.7 Table of calculated scaling factors for each molecule in the reference library. Here, “literature” refers to the scaling factor calculated using the literature data assigned in section 2.4.1. 59

Table 2.8 Scaling factors calculated in this work for B3LYP and MP2 levels of theory with scaling factors calculated using the CCCBDB data.[29] Note only TZ level calculations for isoprene were available in the CCCBDB; all other reference scale factors were calculated using QZ level data, in line with those calculated in this work. .......... 60

Table 2.9 Table of scaling factor calculated by basis set, using the data from all molecules in the reference library, along with reference scaling factors, calculated using data from the CCCBDB (reference 1) and Sinha et al. (2004) (reference 2).[28, 29] Here, “literature” refers to the scaling factor calculated using the literature data assigned in section 2.4.1. .......... 60

Table 2.10 Table of calculated scaling factor by spectral region and basis set level. .......... 61

Table 2.11 Table of scale factors (SF) by spectral region calculated in this work and in the work of Zapata Trujillo et al. (2023) for each B3LYP and MP2 levels of theory at cc-pVDZ and cc-pVTZ basis sets.[27] .......... 61

Table 2.12 Correction function, and scaling and literature factors used to transform raw computed frequencies for assigning experimental spectra of acetone and 2-propanol. The scaling and literature factors are multiplicative, and the correction function is applied as an equation. Literature factors are from Sinha et al.’s (2004) work.[28] .......... 63

Table 2.13 $R^2$ and adjusted $R^2$ values for the assigned experimental and corresponding cc-pVQZ computed values for acetone. ....64

Table 2.14 $R^2$ and adjusted $R^2$ values for the assigned experimental and corresponding cc-pVQZ computed values for 2-propanol. ....64

Table 2.15 RMSE error for the assigned experimental and corresponding cc-pVQZ computed values for acetone. ....64

Table 2.16 RMSE error for the assigned experimental and corresponding cc-pVQZ computed values for 2-propanol. ....65

Table 3.1 Table of assigned calculated and literature wavenumbers to experimental data for acetone, before being subjected to Tesla-coil discharge. Calculations are anharmonic, at QZ level, and are transformed using the correction factor established in Chapter 2. Literature data (Han et al., 1996) is in an argon matrix and is expected to match to experimental data.[5] ..72

Table 3.2 Table of significant peaks that appeared after acetone was subjected to Tesla-coil discharge. These peaks are associated with the formation of CO and its aggregates or complexes with water. ....73

Table 3.3 Literature studies that make or detect ·OH radicals or water complexes. Most use MI-FTIR or calculational methods for detection, and a range of techniques for radical formation. .....77

Table 3.4 Table of experiments run to test water and oxygen mixtures for use as a radical source when subjected to Tesla-coil discharge. The amount of each gas in the mixture is given. The total pressure in the mixture was ~ 1 atm. The amount of time the sample was subjected to Tesla-coil discharge is also given. ....78

Table 3.5 Peaks assigned for water and its complexes typical to mixture pre-discharge spectra. The experimental data has come from W6 but the peaks listed are typical to all water/oxygen/argon mixture experiments run. ....79

Table 3.6 Peaks assigned to $HO_x$ radicals and $O_3$, and their complexes with water for Tesla-coil discharge experiments using a mixture of water, oxygen, and argon. Each experiment gives evidence of radical formation occurring, either by the presence of $HO_x$ radicals or their precursor $H_2O_2$, or by water complexes with the radicals. ....81

Table 3.7 Table of assigned experimental peaks from the TCD spectrum. There is one vibrational frequency that could be assigned to both intermediates and propyne, and one that can be assigned to either propyne itself or an intermediate. ....86

Table 3.8 Table of assigned peaks for the isoprene TCD spectrum and behaviour during annealing (at 35 K and then cooled back to 8K). ....88

Table 3.9 Table of assigned experimental peaks from the TCD spectrum. ....91

Table 3.10 Literature vibrational frequencies and the corresponding assigned experimental values for CO, its aggregates, and its complex with water, for the radical reaction experiments conducted in section 3.2.[5] ....93

Table 3.11 List of assigned frequencies in the radical reaction spectra that relate to $HO_x$ radicals and their complexes with water, as well as the presence of CO and $CO_2$. ....97

Table 4.1 Slope, intercept, standard errors for each, and adjusted $R^2$ value for the plot of intensity vs irradiation time at 460 nm (Figure 4.4). ....109

Table 4.2 Slope, intercept, standard errors for each, and adjusted $R^2$ value for the plot of intensity vs irradiation time at 425 nm (Figure 4.5). ....109

Table 4.3 Slope, intercept, standard errors for each, and adjusted $R^2$ value for the calibration curves (Figures 4.8 and 4.9) of emission intensity vs concentration for both 7-hydroxycoumarin and 2-hydroxyterephthalic acid solutions. ....114

Table 4.4 Slope, intercept, standard errors for each, and adjusted $R^2$ value for the calculated concentration vs irradiation time plots (Figures 4.10 and 4.11) for both 7-hydroxycoumarin and 2-hydroxyterephthalic acid solutions. ........ 116

Table 4.5 List of experiments run using the RGA software to collect and visualise data. A series of experiments were run in attempts to optimise conditions. ........ 123

Table 4.6 List of experiments run using the MCS to visualise and collect data. More experiments were run but the data were lost in a hard-drive corruption event; the experiments lost consisted of a series of small changes to the mixture compositions, flow rates, or irradiation time to finetune conditions and so are not a significant loss. ........ 126

Table 4.7 Table of mass fragments for each molecule measured in RGA experiments. ........ 127

Table 5.1 Photolysis reactions and rate constants at 298K. A indicates the J value was calculated in this work, as discussed in section 5.3.1. ........ 141

Table 5.2 Unimolecular reactions and rate constants at 298K. ........ 141

Table 5.3 Bimolecular reactions and rate constants at 298 K. ........ 142

Table 5.4 Termolecular reactions and rate constants at 298 K. Rate constants and expressions listed are pseudo second order, using air density as M = 2.70 x $10^{19}$ $cm^3$ $molecule^{-1}$. ........ 143

Table 5.5 List of input concentrations for fixed variables used in simulations. ........ 144

Table 5.6 Parameters for SMARTS simulation and values chosen for each. ........ 147

Table 5.7 Literature values of $J(O^1D)$ measured, along with conditions they were measured at. Most literature is from the Northern Hemisphere and measurements are done over summer at noon, which are the conditions considered in this simulation, so results are comparable. ........ 149

Table 5.8 List of simulations conducted, with number of iterations run and calculated variables for each. Most simulations were conducted to finetune conditions, changing things like which variables were fixed, input concentrations, time steps, or adding other reactions in. ........ 150

Table 5.9 List of input, output, and literature concentrations for variables in the final "spin-up" simulation V14. $NO\cdot$, $NO_2\cdot$, and $NO_3\cdot$ had non-zero initial values so that their behaviour could be investigated as there were issues in getting the $NO_x$ concentration close to expected values. ........ 152

Table 5.10 List of input and output concentrations for variables in the final simulation V16. Input concentrations are taken from expected steady-state values to determine whether the simulation will deviate largely from them. ........ 153

Table 5.11 Variables used for determination of the quantum yield of the coumarin probe system discussed in Chapter 4. Photon flux is used at a single wavelength below the catalyst bandgap to simulate the conditions in used in Chapter 4. ........ 156

Table 5.12 Input and output values for P3 simulation which adds a term to the $\cdot OH$ production equation to account for increased formation rate due to $TiO_2$ photocatalysis. Literature values or previous steady-state values were used for input. $CH_3O\cdot$, $NO\cdot$, and $NO_2\cdot$ values were fixed. ........ 159

# 1.0 Introduction

> *"Directly observed changes in the atmosphere, ocean, cryosphere and biosphere represent unequivocal evidence of a warming world. [...] Since the late 19th century many indicators of the global climate system have changed at a rate unprecedented over at least the last two thousand years."*[1]

The Intergovernmental Panel on Climate Change's (IPCC) latest climate report AR6, released in 2021, gives a dire view of humanity's effect on the Earth and its climate system.[1] It indicates that without a doubt the planet is warming and the effects of such a warming are manifesting in bigger and more obvious ways. Evidence of warming is seen across all areas of the globe, as summarised in Table 1.1, with key indicators like Global Mean Surface Temperature (GMST) increasing, Global Mean Sea Level (GMSL) rising, $CO_2$ seasonal cycles increasing in amplitude and desyncing between hemispheres, glaciers retreating, and organisms in both terrestrial and marine biospheres changing their habitats.[1]

The world is aware of this warming and governments or international agencies like the IPCC are taking action to combat or adapt to it. Governments are backing huge research initiatives aimed at mitigating, halting, or adapting to climate change and its effects; the Ministry for Primary Industries (MPI) of Aotearoa New Zealand specifically is researching agricultural emissions, sustainable land-use, and carbon sinks.[2] However, much of our efforts are too slow or reserved to achieve the desired effect within the designated timeframe. The IPCC aim to limit warming to below 1.5 °C, but the current rate of $CO_2$ emissions combined with current climate action projects a 2.7 °C warming.[3, 4] To limit to 1.5 °C warming, immediate net-zero anthropogenic (man-made) $CO_2$ emissions are required, which alongside reduced emissions of all other greenhouse gases (GHGs) would halt human-made climate change.[5,6] Some effects can be reversed within a few years of action, like the warming caused by methane ($CH_4$) emissions; others, like sea-temperature increase and ocean acidification, will take centuries to millennia.[1,7]

Morel (1991) sums up the situation by saying that "in effect, we are now in the process of conducting a giant "experiment" with our planet, for which there is no obvious precedent in paleohistory. It is quite a pressing problem."[8]

Table 1.1 Summary of major indicators of global warming and the magnitude/direction of their change. Information summarised from Gulev et al. (2021).[1] NH = Northern Hemisphere, SH = Southern Hemisphere.

| Indicator of Change | Magnitude of Change |
|---|---|
| **Atmosphere and Surface** | |
| Stratosphere | Cooling since the 1950s; decrease in ozone concentration. |
| Troposphere | Warming since the 1950s; increase in ozone concentration. |
| Tropopause height | IPCC "virtually certain" it's risen globally between 1980 -2018. |
| Global precipitation and monsoons | Increased over land. Number of extratropical cyclones increased. |
| Global mean surface temperature (GMST) | Increased by 1.09 °C in 2011 - 2020.<br>*"Each of the last four decades has in turn been warmer than any decade that preceded it since 1850."*[1] |
| Circulation/air flow | Hadley Circulation strengthened; northern stratospheric polar vortex weakened; extratropical storm tracks likely shifted poleward. Weakening of surface wind over land. |
| Relative humidity | Decreased over land since 2000. |
| **Cryosphere** | |
| Glaciers | Retreating and at an increased rate. |
| Ice sheets | Greenland ice sheet mass loss has increased since 2000; Antarctic ice sheet has lost mass between 1992 - 2000. |
| Permafrost | Increase in temperatures in upper 30 m for the past 30 - 40 years observed. |
| Snow cover | Reduced spring snow coverage across NH since 1978. |
| Arctic sea ice | Lowest coverage since 1850, with area covered decreasing and ice becoming younger, thinner, and faster moving. |
| Antarctic sea ice | Little net change since 1979, experiencing both increases and decreases. |
| **Ocean** | |
| Temperature/global ocean heat content | Increasing in all layers; increasing surface temperature. |
| Salinity | Increasing in saline areas and decreasing in fresh/low saline areas. |
| pH | Declined globally (ocean acidification) at 0.003 - 0.026 pH per decade over the last 40 years in open ocean. |
| Global mean sea level (GMSL) | Rising; since 1901 it has risen by 0.20 m with an increasing rate of rise. |
| Deoxygenation | Has occurred in most open ocean regions. |
| **Biosphere** | |
| Marine biosphere | Ranges of marine organisms changing. |
| Terrestrial biosphere | Poleward and upslope shifts of many land species. |
| Climate zones and growing seasons | Climate zones have shifted, and the growing season has increased in length in the NH extratropics. |
| Seasonal cycles of $CO_2$ | Increase in amplitude of cycle in NH, with the seasonal variations of 2003 - 2018 being out of sync in the NH and SH; this increase is consistent with increased growing season length and more green mass during growing season. |

## 1.1 Chapter Overview

Key mitigation strategies that have either been proposed or are being researched to reduce the effect of GHGs are largely focused on $CO_2$ reduction (discussed further in section 1.4). This work investigates one mitigation strategy that has potential to act against global warming with the aim to indirectly reduce atmospheric $CH_4$ concentration by increasing its main sink, the hydroxyl radical (·OH), by utilizing a $TiO_2$ catalyst. Due to the interconnectedness of atmospheric reaction cycles and components, adding or removing large amounts of molecules could be detrimental to the atmospheric environment as a whole, especially considering a molecule as important as ·OH. Therefore, a brief introduction into the atmosphere and atmospheric chemistry is required, as one single aspect of atmospheric chemistry, like removal of $CH_4$, cannot be studied in isolation. A brief understanding of current mitigation strategies is covered to better understand the choice of selected target molecules and mitigation method, alongside a brief discussion of $CH_4$, ·OH, and $TiO_2$ chemistry.

## 1.2 Structure of the Atmosphere

The atmosphere is structured into 5 layers, seen in Figure 1.1; from Earth's surface, they are the troposphere (0 - 16 km), stratosphere (10 – 50 km), mesosphere (50 – 80 km), thermosphere (80 – 500 km), and exosphere (>500 – 700 km).[9] The troposphere is where most atmospheric reactions occur, where most of the air in the atmosphere resides, and where weather occurs, and thus it is of the most interest for this work.[9] The next layer, the stratosphere, contains the most ozone in the atmosphere, which blocks incoming radiation from the Sun of wavelength < 290 nm (ultra-violet) from reaching the Earth's surface, meaning photochemistry in the troposphere can only occur at wavelengths > 290 nm.[10]

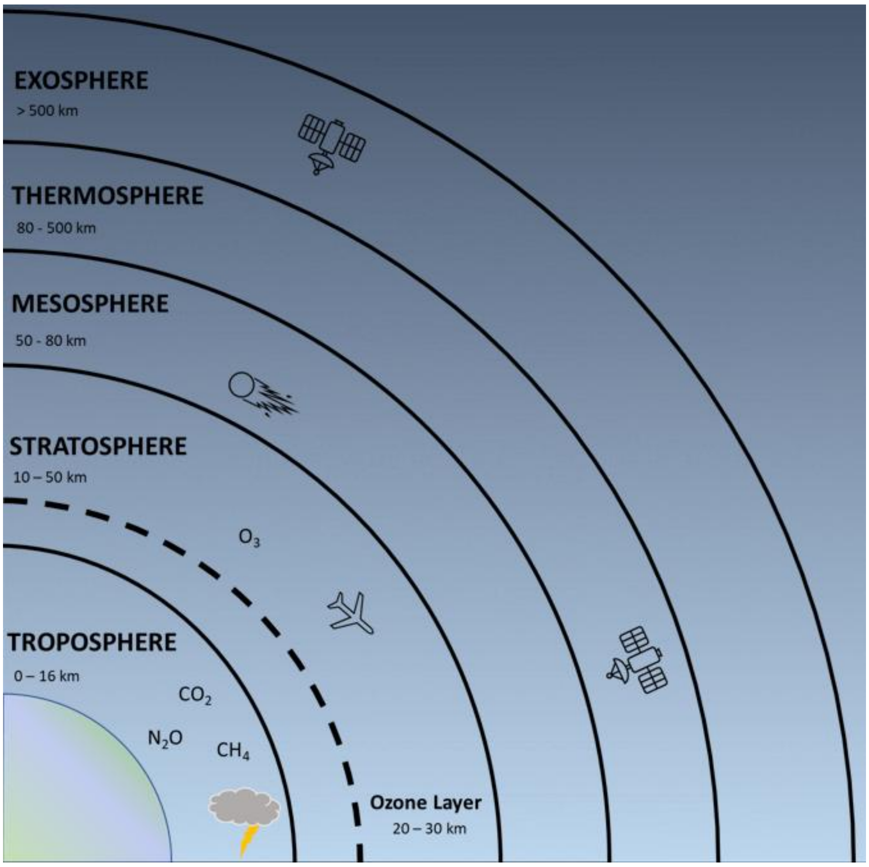

Figure 1.1 Layers of the atmosphere. The troposphere, the closest layer to the Earth's surface, contains most of the greenhouse gases of interest, as well as weather and chemical reactions. The stratosphere contains the ozone layer and plane flights. The mesosphere contains meteors, and the thermosphere and exosphere contain satellites.

This energy enters the Earth in the form of radiation from the Sun at the top of the atmosphere. The effective incoming solar radiation averaged over the Earth's surface is agreed as ~ 340 W m$^{-2}$.[11, 12] This differs from the solar constant, 1368 W m$^{-2}$, which is measured on a flat surface one astronomical unit away from the Sun, perpendicular to the incoming light.[12] In travelling to the surface of the Earth, energy is distributed through various absorption, reflection, and scattering mechanisms by gases and particulates in the atmosphere. $H_2O$, $CO_2$, and clouds are responsible for ~ 90% of this absorption.[7, 11, 13] The Earth itself then radiates energy, called "terrestrial radiation" (~ 236 W $m^{-2}$), back to space but this can also be absorbed, reflected, and scattered.[10, 11, 13, 14] A summary of the processes affecting incoming and outgoing radiation is visualised in Figure 1.2. If there was no interaction between terrestrial radiation and the atmosphere, the average temperature at Earth's surface would be -19 °C, instead of the average 15 °C.[12]

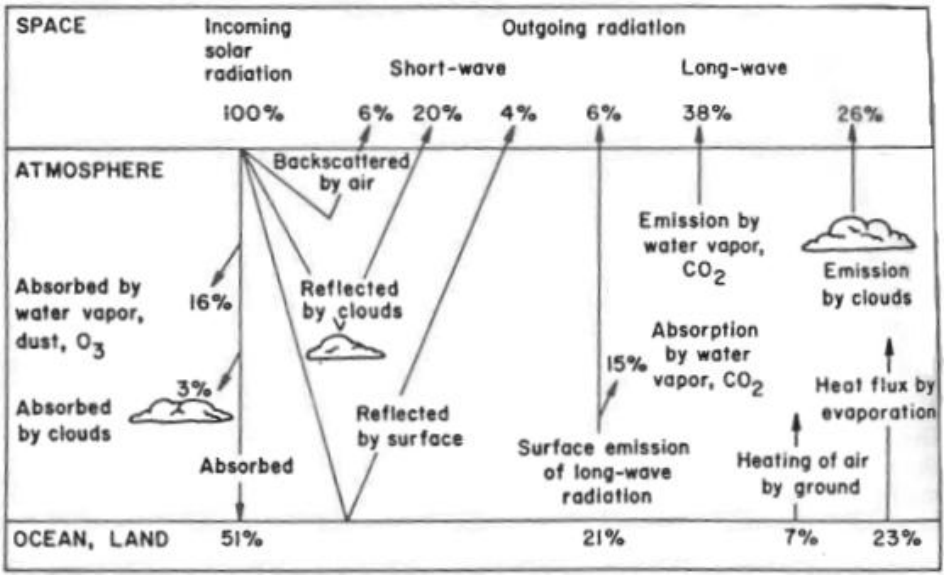

Figure 1.2 Summary of atmospheric processes that affect incoming and outgoing radiation. Incoming solar radiation of 100% represents 342 W $m^{-2}$. Only about half of incoming radiation makes it to the Earth's surface. Reproduced with permission from Berger et al. (1992).[89]

The greenhouse effect occurs when gases in the atmosphere prevent energy from leaving by absorbing it and then converting it to heat through collisions with other molecules. This effect occurs naturally to give us the aforementioned 15 ̊C average surface temperature.[6, 12] With an increase in GHG concentration there is an increase in trapped terrestrial radiation. This causes an imbalance between the incoming solar radiation and outgoing terrestrial radiation, which causes an increase in temperature, known as global warming.[6, 13] Currently, the energy imbalance is absorbed across the Earth by the ocean, land, atmosphere, and cryosphere, with the ocean taking up most of the warming (91% since 1970).[6] Most of the outgoing terrestrial radiation is in the 7 - 14 µm range, highlighted in Figure 1.3, so an increase in gases that have absorption bands within that region (like $CH_4$) have a greater warming effect than other gases that absorb in regions that are already "saturated" with absorbing molecules, like $CO_2$.[11, 12, 15]

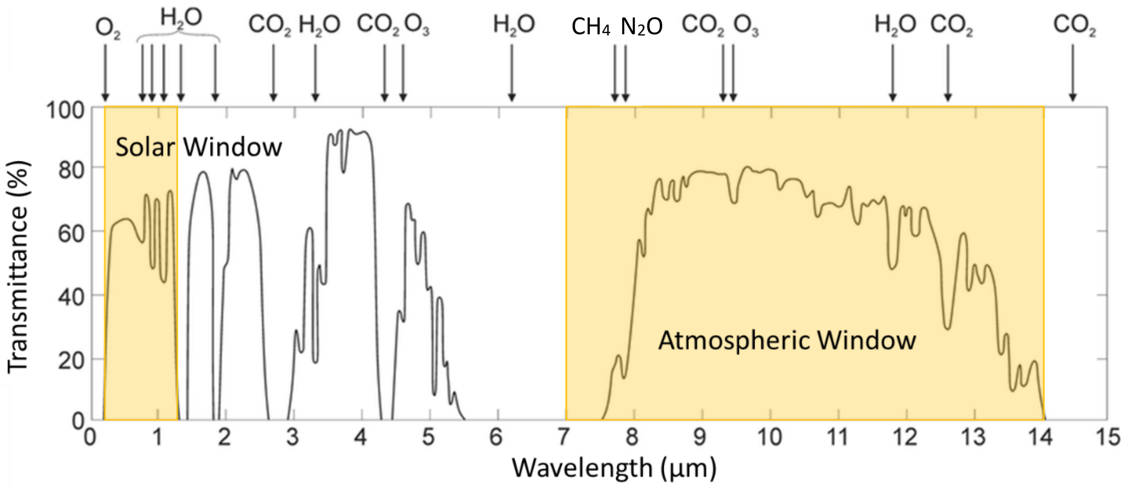

Figure 1.3 Incoming radiation in microns versus percentage transmitted by the atmosphere. Absorption bands are labelled by corresponding molecule. The window of atmospheric importance is highlighted. This is the region where energy can be radiated away from Earth, so any molecule that absorbs in that region will have a large warming impact. The solar window is where all energy comes in from the Sun, with a lot of absorption in that region from water vapour. Image adapted from open access source Mikolajcyzk et al. (2017).[16]

## 1.3 Climate Drivers: What Molecules Do We Blame?

Factors that affect the energy budget of the Earth by changing the incoming or outgoing radiation, either directly or indirectly, are called climate drivers. Climate drivers include GHGs, particles in the atmosphere, and clouds. Their effect on the energy imbalance can be measured in a few ways, the two most common being effective radiative forcing (ERF) and global warming potential (GWP). Radiative forcing (RF) is a measure of how something impacts the climate by affecting the incoming energy at the top of the atmosphere (i.e. size of energy imbalance), and is measured against pre-industrial (1750) conditions in units of W $m^{-2}$.[6] ERF is radiative forcing that has been adjusted for natural factors or factors that aren't linked to climate change.[6] Positive forcing causes warming and negative forcing causes cooling.[1, 6] In contrast, GWP indicates the RF of a volume of gas compared to the RF from the same volume of $CO_2$ over a specified timeframe.[17] Typically calculated timeframes are over 100 years ($GWP_{100}$) and 20 years ($GWP_{20}$). GWP is sensitive to the chosen timeframe since short-lived forcers will have a smaller and potentially misrepresentative GWP over a long timeframe.[17] Because $CO_2$ is the reference molecule, it has a GWP of 1 independent of timeframe chosen.[17] Since GWP puts the effect of a gas on a common scale it is the most often used metric.[17]

> *"And yet it is not generally recognised that the most portentous impact of man on the planet is the slow and unspectacular alteration of the Earth atmosphere composition [...] and the equally hidden consequences."*[8]

As Morel (1991) notes above, changes in ERF in recent years are predominantly caused by anthropogenic factors. This is mainly an increase in GHG concentrations, with a small change from natural factors since 1750.[1] The net ERF is positive and has been since 1971, hence global warming.[1, 6] Concentrations of GHGs have increased since the industrial period, with $CO_2$ being the largest contributor.[1] The main three GHGs that have contributed to the warming effect are $CO_2$, $CH_4$, and $N_2O$ as they are strong absorbers of terrestrial radiation (discussed in section 1.3.1 below).[1, 12] Other gases, like $O_3$, water vapour, and halogenated compounds, also have a warming effect but have a lesser impact due to their weak absorption bands in the atmospheric window by which terrestrial radiation leaves (see Figure 1.3 and section 1.3.2).[12] Table 1.2 summarises ERFs and GWP for relevant forcers, with the only negative (cooling) effects coming from albedo (amount of light reflected from the surface) and aerosols. $CO_2$ makes up the majority of the ERF, which is why it has the largest warming effect on the climate. $CH_4$ has the next highest ERF. However, when looking at GWP, $CH_4$ becomes a more significant forcer especially over a 20-year period. This is because ERF is dependent on concentration and $CO_2$ is highly abundant (a thousand-fold more than $CH_4$), whereas GWP is a ratio that uses the same volume of target gas and $CO_2$. Despite its potential to misrepresent the impact of some GHGs, GWP shows that a $CH_4$ molecule is more impactful than a $CO_2$ molecule despite having a lower ERF.

Table 1.2 Table of lifetimes, ERF, and GWP for significant forcers. The only net negative (cooling) forcers are aerosols and the intrinsic albedo (ratio of reflected light from the surface) of the Earth, both of which can be affected by anthropogenic activities. Attention is drawn to the ERF for $CO_2$ and to the GWP of $CH_4$. Data adapted from IPCC AR6 and AR5 Reports.[1, 17]

| **Forcer** | **Lifetime (years)[1]** | **ERF (W $m^{-2}$) for 1750 – 2019[1]** | **$GWP_{100}$[17]** | **$GWP_{20}$[17]** |
|---|---|---|---|---|
| $CO_2$ | 120 | 2.16 ± 0.26 | 1 | 1 |
| $CH_4$ | ~ 11 | 0.54 ± 0.11 | 28 | 84 |
| $N_2O$ | 109 | 0.21 ± 0.03 | 265 | 264 |
| CFCs | 1 - 100 | 0.41 ± 0.07 | 4660 | 6900 |
| $O_3$ |  | 0.47 [0.24 to 0.70] | - | - |
| Water Vapour |  | 0.05 ± 0.05 | - | - |
| Albedo | - | – 0.11 ± 0.09 | - | - |
| Aerosols | - | – 1.1 | - | - |

### 1.3.1 $CO_2$, $CH_4$, and $N_2O$

---

> *"Global mean concentrations for well-mixed GHGs ($CO_2$, $CH_4$ and $N_2O$) in 2019 correspond to increases of about 47%, 156%, and 23%, respectively, above the levels in 1750 (representative of the pre-industrial era)."* [5]

---

Since the first measurements of $CO_2$ at Mauna Loa Observatory, Hawaii (1958) and at the South Pole Observatory (1957) there has been an increasing trend in atmospheric concentration.[15] Over the 61 years of measurement there has been a 1.56 ± 0.18 ppm $yr^{-1}$ increase.[5, 15] $CO_2$ concentration has increased in the period 1750 - 2019 by 131.6 ppm, which is a 47% increase, to a level of 409.9 ± 0.4 ppm in 2019.[1] The rate of increase is variable and changes with season, but is averaged at 2.4 ppm $yr^{-1}$ for 2011 - 2019, having increased a total of 19 ppm over this period.[1] Up to 90% of emitted $CO_2$ is from fossil-fuel combustion.[5] No chemical process (except photochemical destruction above 80 km altitudes) destroys $CO_2$, so any excess is taken up by other carbon sinks.[14] The anthropogenic $CO_2$ emissions during 2011 - 2019 were taken up roughly 46% by the atmosphere, 23% by the ocean, and 31% by land via storage in plants.[5]

The relationship between the sources and sinks of $CO_2$ is complex and non-linear due to the forcers involved. The accumulation of $CO_2$ in the atmosphere is controlled by the relationship between these sinks and sources, and any effect on these can have further roll-on effects to other cycles they are involved in. Whilst the sinks of $CO_2$ may grow in response to the increasing source, they will not be able to keep up with our rate of increase, as evidenced by the current imbalance causing atmospheric accumulation of $CO_2$. The ocean sink for $CO_2$ has been growing in response to emissions, from 1.0 ± 0.3 PgC $yr^{-1}$ in the 1960s to 2.5 ± 0.6 PgC $yr^{-1}$ (where Pg = $10^{15}$ g, C = carbon) in the 2010s.[5] The roll-on effect of changes to sinks is seen in the growing ocean sink as there is potential that the increased $CO_2$ storage in the ocean (ocean acidification) is changing ocean carbonate chemistry, which can devastate marine carbonate based life forms. The land sink for $CO_2$ has also grown, mainly due to the fertilization effect, as an increase in atmospheric $CO_2$ concentration increases nitrogen deposition.[5]

Methane ($CH_4$) has been directly measured in the atmosphere since the 1970s, and has increased in atmospheric concentration from 755 ppb in 1750 to 1866.3 ppb in 2019, predominantly from human activities.[5, 17] The rate of growth of atmospheric $CH_4$ has varied and there is contention around why this variation occurred.[18] Overall, since 1850 the concentration of atmospheric $CH_4$ has more than doubled, and has experienced a 156% increase from 1750 values.[18] 90% of emitted $CH_4$ is lost to reaction with the ·OH in the troposphere, and the rest is taken up by soil.[5] The largest natural sources are wetlands and freshwater, and the largest anthropogenic emissions are from agriculture, waste, and landfills.[5] It is noted that $CH_4$ can be correlated to global population as its increase in the atmosphere is due to increase in livestock (mainly ruminant animals like cows, sheep, and goats) and rice farms, as well as increasing amounts of landfill and waste. [5, 8]

As stated, $CH_4$ is a more effective GHG than $CO_2$. This is because, despite its short lifetime of ~ 11 years, it is involved in many tropospheric reactions and is ultimately oxidized to $CO_2$.[5, 6, 14] As a result, anthropogenically emitted $CH_4$ adds $CO_2$ to the atmosphere.[6, 9] In contrast, biogenic (natural) sources have a net-zero impact on $CO_2$ as for each molecule added to the atmosphere by $CH_4$ oxidation, another is taken from the atmosphere and stored by plants.[6, 9] $CH_4$ also absorbs outgoing radiation at 7.66 μm, which is within the atmospheric window (see Figure 1.3) that most outgoing radiation is lost to space, meaning it effectively blocks more outgoing radiation than something that absorbs outside of that atmospheric window.[11, 13, 14]

$N_2O$ has increased in concentration from 270.1 ppb in 1750 to 332.1 ± 0.4 ppb in 2019.[1] $N_2O$ has a lifetime of ~ 100 years, meaning atmospheric concentrations will take a century to stabilise any changes.[1, 5] $N_2O$ is involved in the destruction of stratospheric $O_3$, acting to increase the warming effect indirectly as well as directly. The anthropogenic source of $N_2O$ is use of fertilizers as well as fossil-fuel burning.[5, 12] $N_2O$ is also released as a by-product of nitrification and de-nitrification, a bacterial oxidation process that converts ammonia to nitrite and nitrate on both land and in the ocean.[5, 12] Primary loss mechanisms for $N_2O$ are photolysis in the stratosphere and reaction with $O^1D$ atoms.[5] $N_2O$ is primarily transported to the stratosphere from its emission sources, where it then undergoes reaction.[19]

The atmospheric concentrations and anthropogenic emissions of $CO_2$, $CH_4$, and $N_2O$ are increasing and have been for some time (see Figure 1.4). These three GHGs are responsible for a large portion of warming experienced due their high concentrations and effective absorption of radiation. $CO_2$ is the main contributor, with an ERF of 2.16 ± 0.26 W $m^{-2}$, compared to the total anthropogenic ERF of ~ 2.72 W $m^{-2}$, with $CH_4$ contributing the next largest share at 0.54 ± 0.11 W $m^{-2}$ (see Table 1.2 above).[6] Any of these three gases would make a good target for climate action to reduce anthropogenically induced warming.

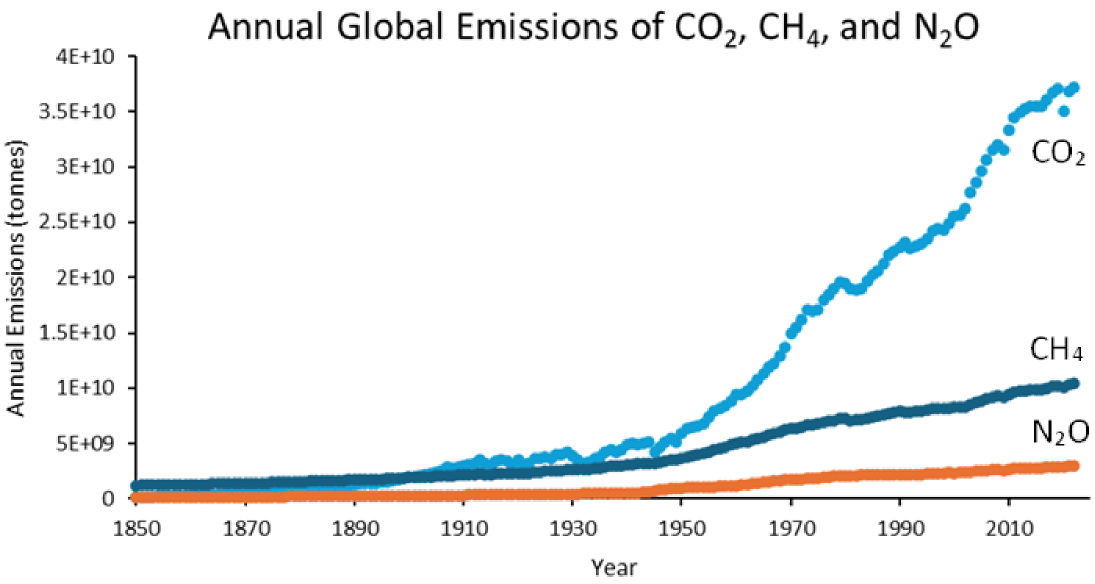

Figure 1.4 Annual anthropogenic emissions (in tonnes) of $N_2O$, $CH_4$, and $CO_2$, the three main GHGs involved in global warming. $N_2O$ and $CH_4$ are plotted in units of tonnes of $CO_2$ equivalents, which weights emissions against the GWP of each molecule. The rate of increase in all three skyrockets in the mid 20th century, but has been increasing since 1850. Data reproduced from Our World in Data under a Creative Commons license.[20-22]

### 1.3.2 Short-Lived Climate Forcers and Other GHGs

Short-lived climate forcers (SLCFs) also contribute a forcing to the Earth, though it is much smaller than that of the GHGs discussed in section 1.3.1. SLCFs have atmospheric lifetimes usually shorter than twenty years.[23] They encompass a range of compounds like $CH_4$, $O_3$, and aerosols. Some significant SLCFs and other GHGs are briefly discussed below.[23]

Chlorofluorocarbons (CFCs), found in aerosols and refrigerants, created the $O_3$ hole by breaking down and releasing chlorine in the stratosphere, which then destroys $O_3$.[1, 8] They have a lifetime greater than 100 years but were replaced by SLCFs of hydrochlorofluorocarbons (HCFCs) and hydrofluorocarbons (HFCs), which have lifetimes of days to months or years.[1, 23] These GHGs are being phased out (as of the Kigali Amendment in 2016) as although they are not as impactful as CFCS, they are still $O_3$-depleting substances and therefore have a positive ERF from destroying stratospheric $O_3$.[12]

Ozone ($O_3$) is also a direct SLCF as it blocks incoming solar radiation.[23] Its forcing effect depends on its distribution within the atmosphere.[23] $O_3$ is an air pollutant in urban areas, formed from and degraded by reactions with $NO_x$ (nitrogen oxides), but is largely found in the stratosphere (90%).[23] Its lifetime varies from a few hours in polluted areas to several months in the lower stratosphere.[23] Global mean surface $O_3$ concentration has decreased within the range of 0.69 ± 0.16 ppb to 2.28 ± 0.24 ppb, and further decrease is expected as the climate warms due to the destruction of $O_3$ by water vapour, which will increase with increased global surface air temperature (GSAT).[23]

Nitrogen oxides ($NO\cdot$ and $NO_2\cdot$, collectively referred to as $NO_X$) are indirect SLCFs that are strongly coupled to other important atmospheric reaction cycles (discussed later in section 1.6). Nitrogen compounds are released due to both chemical and industrial processes and from use of fertilizers.[8, 19] Natural emissions of $NO_x$ come from the nitrification/denitrification process in soil.[19, 23] $NO_x$ compounds have an average lifetime of about a day, meaning they vary in concentration across space and are usually higher in concentration near sources.[14, 23, 24] They are involved in reactions that convert $NO_x$ to $HNO_3$, $NO^-$, and organic nitrates.[23] Concentrations of $NO_x$ have increased, and are highest near urban and highly populated areas, mostly in the form of $NO_2\cdot$.[23] During the day, $NO\cdot$ and $NO_2\cdot$ are the dominant forms of $NO_x$ and contribute to the production of tropospheric $O_3$, and at night $NO_3\cdot$ becomes the dominant form.[24] In polluted environments, $NO_x$ concentrations control the production of secondary $\cdot OH$, an important atmospheric molecule (see section 1.6).[23, 24] $NO_x$ therefore has a positive ERF by producing $O_3$ and a negative ERF by producing $\cdot OH$, which then reduces $CH_4$ lifetime.[23]

Non-methane volatile organic compounds (NMVOCs) cover a wide range of organic molecules with different lifetimes that are present in the atmosphere.[23] As a result, concentrations are extremely variable.[23] NMVOCs are mostly biogenically emitted, but concentrations can be anthropogenically affected by actions like afforestation or deforestation as they are emitted by plant life.[23, 25] NMVOCs are involved in atmospheric reactions, often photo-oxidation reactions that form products involved in $O_3$ formation and therefore have a positive forcing, or products that form secondary organic aerosols (SOAs), which have a negative forcing.[23]

### 1.3.3 Other Climate Forcers

Other forcers like aerosols, land-use, and clouds also contribute forcing to Earth's energy budget. However, these three forcers in particular can give a negative (cooling) forcing.

Aerosols and particulate matter can come from physical sources (biogenic or anthropogenic) like sea spray or dust from irrigation, or can be formed as reaction products, called secondary organic aerosols (SOAs).[23] Aerosols provide the main negative (cooling) ERF by interacting with clouds and incoming radiation. They can act as cloud condensation nuclei, increasing the number of clouds formed and therefore the amount of radiation clouds block (indirect forcing), as well as scattering and/or absorbing incoming radiation (direct forcing).[1, 10, 12] For example, the Mt. Pinatubo eruption in 1991 caused an increase in atmospheric sulfate aerosols, which had a cooling effect of -0.5 °C over 2 years.[6, 12, 23, 26] On a global scale, the increase of anthropogenic aerosols has had a cooling effect, but has also led to water-cycle changes and reduction in global precipitation.[23]

Land-use can also provide a negative ERF as increased snow cover and leaf or green area increase the surface albedo.[1] Land-use change has had a net cooling of -0.1 °C since 1750.[1] Land used for agriculture specifically is a large source of $CH_4$ and $NH_3$, so it also indirectly provides a forcing by being a source of other GHGs.[23] Land-use also acts a source for NMVOCs and dust, which have further indirect effects as discussed.[6]

Clouds have a complex relationship with the climate, providing both a cooling and a warming effect.[8] Low clouds are dense and warm and act to reflect radiation back to space, cooling the planet.[8] High clouds are translucent and cold, and contain enough water vapour to absorb radiation from the Earth's surface, causing a heating effect which increases with altitude.[6, 8] Clouds and their number and composition are strongly affected by aerosol concentration and other reaction products, with cloud composition affecting their ability to reflect light back (cooling effect).[6] Clouds also act as surfaces on which reactions can occur; $O_3$ destruction in the stratosphere is attributed to reactions occurring on the surface of polar stratospheric clouds.[10, 27] With an increase in water vapour in the atmosphere, due to increased evaporation, there is potential for increased low cloud formation to occur; however, net modelled cloud feedback varies model to model, but the IPCC AR6 (2021) reports a positive forcing from cloud feedback as affected by other climate change aspects, like changing water vapour concentrations.[6, 12]

## 1.4 What Are We Doing About It?

From the data presented in sections 1.2 and 1.3 and summarised in Table 1.3, we can see that anthropogenic activities have increased the concentrations of GHGs in the atmosphere and led to a global warming effect estimated to have increased GSAT by 1.29 °C over 1750 - 2019.[6]

Table 1.3 Sources, lifetime, pre-industrial (1750) concentrations and 2019 concentrations of important GHGs. The huge increase in $CH_4$ is starkly laid out here. The fossil-fuel industry is a source for all but $N_2O$. Data adapted from IPCC AR6 report (2021) and Graedel et al. (1993).[6, 23, 24, 28]

| Forcer | Major Anthropogenic Source | Average Lifetime | Approx. 1750 Concentration[6] | 2019 Concentration[6] |
|---|---|---|---|---|
| $CO_2$ | Fossil-fuel combustion, deforestation | 120 Years | 283 ppm | 409.9 ppm |
| $CH_4$ | Rice fields, cattle, landfill, fossil-fuel production | 11 Years | 729 ppb | 1866.3 ppb |
| $N_2O$ | Fertilizers, deforestation, biomass burning | 130 Years | 270 ppb | 332.1 ppb |
| $NO_x$ | Fossil-fuel combustion, biomass burning | Days | - | 1 – 500 ppt[23] |
| CO | Fossil-fuel combustion, biomass burning | Months | - | 40 – 120 ppb[24] |

The Paris Agreement, an international treaty on climate change signed in 2015, aims to keep global warming below 2 °C at worst, with an ideal 1.5 °C maximum warming.[29] 1.5 °C was chosen as there is a non-linear relationship between severity of effects and degree of warming.[30] Limiting to 1.5 °C means that millions fewer people will be exposed to extreme heatwaves and droughts compared to 2 °C of warming, and also reduces the probability of increased droughts.[31] Some ecosystems can adapt to changes with only some difficulty up to 1.5 °C of warming, but once that boundary is crossed, they struggle and can face devastating effects.[31] Overall, the less warming that occurs, the lesser the impacts of warming. The global average warming projected for 2100, based on the current policies and pledges, is 2.7 °C, which is woefully inadequate.[3, 4] New pledges announced at the Glasgow Conference of the Parties (COP26) in 2021 would limit warming to 2.4 °C, and coupled with net-zero emissions 1.8 °C.[32] The biggest pledges made involved completely phasing out coal power for clean energy, committing to protection of natural habitats and a halting of deforestation, commitments to phase out fossil-fuel powered vehicles, and a commitment from six major $CH_4$ emitting countries to reduce $CH_4$ emissions (amounting to ~ 46% of $CH_4$ emissions globally).[32] These pledges and the conference itself provide insight into what could be achieved when working as one global community on a multifaceted problem from a financial, political, and scientific standpoint.

### 1.4.1 Mitigation

Mitigation strategies, like the pledges described above, aim to reduce anthropogenic emissions of GHGs. From Table 1.3 it is obvious that the fossil-fuel industry accounts for a large volume of GHG emissions – approximately 73% of global GHG emissions come from the energy sector.[33] The energy sector involves the production of energy as well as the use of energy through industry, transportation, and buildings.[34] Decarbonizing and phasing out fossil-fuels is the main and most obvious mitigation strategy that has benefits across other sectors, achieved by a move from fossil-fuels to renewable sources and nuclear power.[34, 35] In transportation, it is achieved by switching from fossil-fuels to renewable fuels and electric vehicles.[34] Additionally, increasing efficiency of energy use as a whole can also reduce emissions.[34] As of 2020, renewable energy sources account for ~ 15% of energy used in the building and industry sectors, and ~ 4% in the transport sector, accounting for ~ 28% of global energy production.[36, 37] Agriculture, forestry, and land-use is the second highest emitting sector, accounting for ~ 18.4% of emissions.[33] Effective management of land-use through afforestation and replanting of natives to restore ecosystems can reduce emissions by acting as a carbon sink.[35] Shifting to renewable power sources also reduces emissions, with ~ 15% of energy use in agriculture in 2020 being provided by renewable sources.[36]

These mitigation strategies are all present in the collective consciousness and have been known about for years. Current policies and pledges made by governments at summits like the COP mean these strategies are being deployed, but not at the rate required to halt global warming before 1.5 ℃ warming is reached. The rate of deployment or shift to lower-carbon systems can be hindered by non-scientific issues, usually due to financial costs or political issues. Therefore, other scientific strategies that approach the problem differently are being developed and tested for deployment. Geoengineering is a contentious branch of science that has been proposed to halt effects of global warming.[38] It is defined as the large-scale interference with natural systems to counter climate change effects.[35] Geoengineering refers to both $CO_2$ removal (CDR), and solar radiation management (SRM).[38]

### 1.4.2 $CO_2$ Removal (CDR)

$CO_2$ removal (or carbon capture and storage, CCS) is the removal or capture of $CO_2$ from the atmosphere and subsequent storage in liquid or solid form.[38] Conventional CDR involves the capture of $CO_2$ from smokestacks or other emission sources, which is then usually liquified and buried underground.[39] Concerns have been raised about the storage method, namely its capacity, potential for rogue emissions or leakage, and effect on the Earth from the process of injection and the holes being dug.[39] As of March 2023, Britain revealed they were intending to invest up to £20 billion over the next 20 years in CCS, despite widespread criticism, to act as an intermediary during their phase out of coal power for green energy.[40]

Biosequestration is a CCS strategy that involves replanting of trees and other plants since they act as both carbon sinks and to convert $CO_2$ to $O_2$.[39] Deforestation and other changes in land-use (like clearing patches of land for agriculture) has caused the release of stored $CO_2$ from the land. Afforestation means that carbon can be removed from the atmosphere, but the type of plant and location must be carefully considered to avoid adverse consequences to the ecosystem. These benefits and consequences must be carefully sized up and balanced if afforestation schemes are to go ahead, as proposed by many countries like Britain and Aotearoa New Zealand.[41-43]

Bioenergy carbon capture and storage (BECCS) builds off the idea of biosequestration to use plant matter as an energy source, capturing the $CO_2$ emitted from biomass burning.[44] Since trees only store additional carbon as they grow, mature forests don’t contribute a negative emission.[39] Planting fast growing trees and then using them as a source of biofuel allows trees to act as both carbon storage and an alternative fuel source.[39] BECCS can also apply to the combustion of landfill gas for energy, which would reduce landfill $CH_4$ emissions.[39]

Direct air capture (DAC) uses $CO_2$ absorbent materials to pull $CO_2$ directly from air flow across a surface.[39] Some reversible materials have been suggested for use. This technique is currently being developed across the globe, with a close-to-home version being touted in Australia by Southern Green Gas, who aim to build DAC hubs using solar-powered collectors that have modular material blocks, allowing for the removed carbon to be stored or used as a fuel which could power the hubs themselves or homes around the country.[45] DAC allows for capture from basically every emission source since it draws $CO_2$ from the atmosphere, whereas CCS captures directly from emission sources.[39] However, DAC has a high financial cost as capture plants/hubs would need to be built, as well as a high energy cost.[39]

### 1.4.3 Solar Radiation Management

Solar radiation management (SRM) involves manipulating the incoming radiation from the Sun to reduce the amount of energy reaching the Earth's surface. SRM strategies include cloud brightening and stratospheric aerosol injection (SAI), both of which build off of natural occurrences but work to amplify the cooling effects.[46]

SAI naturally occurs after volcanic eruptions, which increases the local concentration of $SO_2$. The released $SO_2$ reacts to form sulfuric acid particles, which then reflect incoming sunlight back from space. The biggest and most recent example of this effect is the 1991 Mt. Pinatubo eruption in the Philippines, which had a cooling effect of -0.5 ℃ over 2 years.[47] The aim of SAI is to find a particle that is better suited than $SO_2$ to reflect sunlight by investigating composition, size, lifetime, refractive index, and chemical reactivity with $O_3$.[47] The particle would then be injected into the atmosphere. In Moon et al.'s (2012) study, $TiO_2$ is chosen as an ideal particle as it requires a third less mass to achieve the same effect as $H_2SO_4$ aerosols.[47] SAI is often touted by its champions as a cheap and fast way of mitigating the effects of climate change; Smith and Wagner et al. (2018) calculated a 15-year sulfate SAI program at a cost of ~ USD\$2.25 billion $yr^{-1}$, a mere 1% of the required cost for decarbonizing the entire US energy sector.[48, 49]

However, there are scientific and ethical flaws associated with SAI.[47] Particles in the atmosphere experience deposition, so the aerosol would have to be replenished to continue the cooling effect, with a sudden stop of aerosol loading having a greater warming effect than if no particle was initially released.[3] The particles would also need to have limited effects on human health and other ecosystems since they are eventually going to be deposited on the surface. There are political issues involved with governing and commencing an action that has a global effect, since certain countries or states could implement SRM against the wishes of the global community.[3] Lastly, the most glaring issue is that SAI (and CCS) act as a temporary stopgap; without reducing our GHG emissions the world will continue to warm, whether or not we mask the noticeable changes. Geoengineering strategies, if used, must be employed in combination with direct emissions reductions to combat warming.

Geoengineering is steadily moving closer to being implemented. In 2020, an Australian group of researchers did a field test for marine cloud brightening to help cool the coral reef beneath the engineered cloud.[50] The Keutsch Group at Harvard University is aiming to use calcium carbonate as a SAI particle for cooling purposes in the stratosphere, but has not had test flights of their balloon platform approved as of March 2021.[51, 52] The Chair of The Royal Society of Chemistry, Professor John Shepherd, summed up the majority of the issues surrounding geoengineering in a report published in 2009, saying:

> *"The greatest challenges to the successful deployment of geoengineering may be the social, ethical, legal and political issues associated with regulation, rather than scientific and technical issues".*[53]

## 1.5 Reducing $CH_4$ Concentration

As mentioned in section 1.2.1, $CH_4$ is a more powerful GHG than $CO_2$. This is due to its absorption in the atmospheric window that the main radiation absorbers, water vapour and $CO_2$, don't cover and that most terrestrial radiation leaves by (see Figure 1.3).[11, 13, 14] As a result, the cumulative warming effect from $CH_4$ is more impactful than that of the same amount of $CO_2$ – in fact, ~ 23% of radiative forcing is attributed to the increased $CH_4$ concentrations alone since 1750.[54, 55] Since ruminant agriculture specifically is a large source, $CH_4$ emissions should be very important to Aotearoa New Zealand since our economy is largely dependent on the dairy farming industry (5% of GDP) and the "clean green" image that drives tourism.[56, 57] Reisinger (2018) states that if we want to have no further warming from livestock emissions, they would need to be reduced by 22% of the 2018 levels by the year 2050, with further reductions by 2100.[54] In 2020, $CH_4$ emissions were 43.5% of Aotearoa New Zealand's total GHG emissions, with 90% of $CH_4$ emissions originating from agriculture.[58] Currently, Aotearoa New Zealand has a Methane Emissions Reduction Plan that proposes to reduce biogenic $CH_4$ emissions by 10% below 2017 levels by 2030, and reduce all other GHG emissions (including anthropogenic $CH_4$ emissions) to net-zero by 2050.[58] They aim to do this by implementing policies like pricing agricultural emissions by 2025, requiring $CH_4$ capture from landfill sites, and improving organic household food and garden waste collection – which is a good start.[58]

Whilst there are already strategies for reducing $CO_2$ (as discussed in section 1.4), there are fewer available that target $CH_4$ specifically. By targeting $CH_4$ instead of $CO_2$, a trade off in the rate of $CO_2$ emissions reduction can be applied, as the mitigation effect is on the decadal timescale instead of the century timescale for $CO_2$ mitigation.[55] This means that $CH_4$ is an easy and actionable target for emissions reduction and can reduce the warming effect of increased overall GHG emissions with effects of reduced concentrations being seen within a decade of action. This quick turnaround would then give us time and act as a bridge between current and net-zero $CO_2$ emissions or could lessen the steepness of the reduction curve required to stay within target.

Part of $CH_4$'s importance in emissions reduction is its variability in concentration and difficulty in modelling emissions. Since it reacts with ·OH quickly (short lifetime) it is more concentrated closer to sources.[55] The amounts of emissions from natural sources have large uncertainties, specifically for emissions from wetlands and inland waters, which are also lacking in observations for accurate modelling.[55] $CH_4$ can also be unintentionally leaked from fossil-fuel productions and agricultural practices, or from sources like $CH_4$ hydrates that melt as GSAT increases.[55] On top of this, depending on what type of modelling is used to sum $CH_4$ sinks and sources, the imbalance can differ by a factor of 10 – Saunois et al. (2020) give a bottom-up estimate of 120 Tg $CH_4$ $yr^{-1}$ and a top-down estimate of 12 Tg $CH_4$ $yr^{-1}$ (where Tg = $1x10^{12}$ g).[55]

Since $CH_4$ is abundant in both concentration and rate of growth of emissions, a decrease in concentration will have a large impact. However, it is important to note that the impact of radiation absorption is dependent on multiple factors, including concentration of gas itself. For weak-line absorptions like $O_3$ and CO the impact is linear with increasing concentration but for strong absorbers like $CH_4$ the effect is non-linear as a saturation point is reached.[12] This means that as $CH_4$ is removed from the atmosphere,  further removal becomes more effective.

Reducing emissions and removing $CH_4$ has other indirect effects beyond just reducing the direct forcing, as summarised in Figure 1.5. Reducing $CH_4$ concentration will also reduce tropospheric $O_3$, contribute less $CO_2$ and water vapour from oxidation products to the atmosphere (both of which are strong GHGs), and potentially increase ·OH concentration since there will be fewer reactions between ·OH and $CH_4$, allowing for greater removal of other pollutants. It is important to also note that when considering the impact of $CH_4$ and the additional $CO_2$ load it represents, biogenic sources are not included, as the additional $CO_2$ is already involved in a cycle and is not considered “new” to the atmosphere. For anthropogenic $CH_4$, the $CO_2$ produced by its oxidation is “new” to the atmosphere and so represents additional forcing. There are other and more uncertain effects like the interaction between $CH_4$ and aerosols or the potential to perturb the carbon cycle, but overall $CH_4$ is a strong contender for emissions reduction and atmospheric removal due to its co-benefits and relatively quick turnaround time.

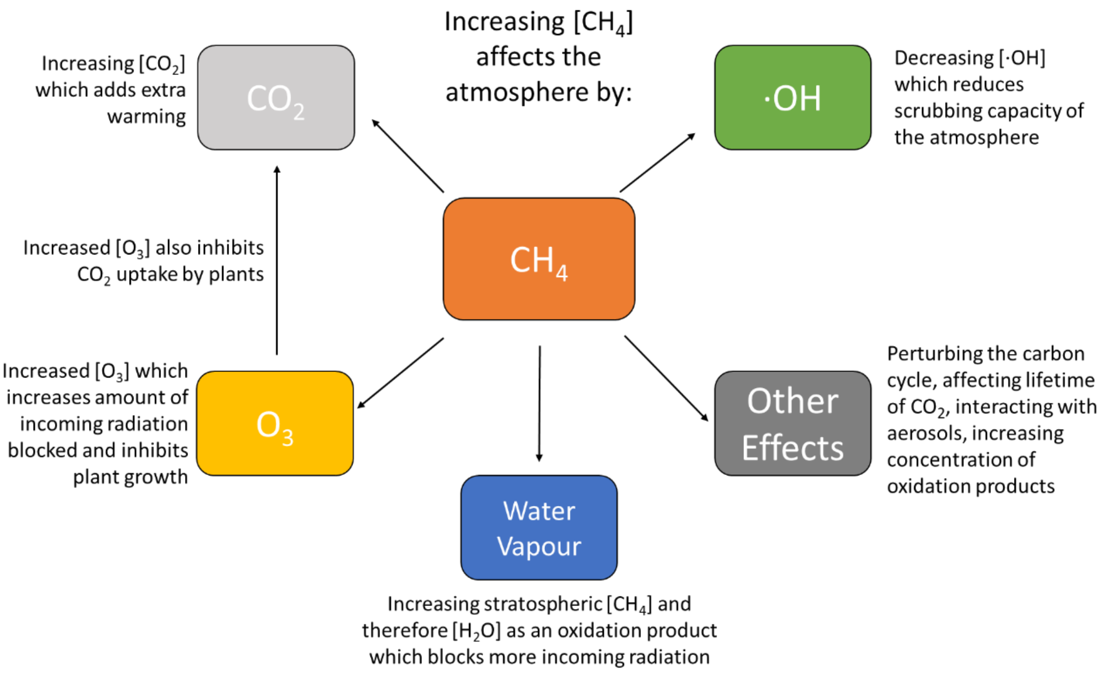

Figure 1.5 Summary of how increasing $CH_4$ concentrations will affect the atmosphere. Notably, [·OH] would be reduced from an increase in reactions with $CH_4$ which would extend $CH_4$'s atmospheric lifetime. An increase in $CH_4$ also would mean a greater amount migrating to the stratosphere, where the impact of water vapour (produced as an oxidation product) would have a greater impact in blocking radiation than the water vapour produced in the troposphere by the same reaction. Data summarised from Reisinger (2018).[54]

## 1.6 The Hydroxyl Radical

The hydroxyl radical (·OH) is considered the most important oxidizer of the atmosphere, often called the "detergent" of the atmosphere.[59] It is involved in a number of atmospheric reaction cycles that remove pollutants and other species, and is often involved in the first and rate-determining step of these reactions.[60] ·OH is found in the atmosphere at a relatively high concentration of the order of $10^6$ molecules $cm^{-3}$ due to the recycling nature of radical chain reactions.[59, 60] This is despite its high reactivity and lifetime of less than a second, meaning the atmosphere has a large capacity to recycle and produce ·OH as it is consumed.[59]

The formation of atmospheric ·OH is predominantly initiated by photolysis of $O_3$ into a singlet oxygen atom ($O^1D$):

$$O_3 + hv \ \rightarrow \ O^1D + \ O_2 \ \ (\lambda \leq 320 \, nm) \tag{1.1}$$

The majority of $O^1D$ formed ends up colliding with other molecules (M) and being quenched to ground-state oxygen ($O^3P$), but the small amount (~ 10%) that remains can react with water to form ·OH[59-61]:

$$O^1D + M \ \rightarrow \ O^3P + \ M \tag{1.2}$$

$$O^1D + H_2O \ \rightarrow \ OH \cdot + OH \cdot \tag{1.3}$$

Since the primary source of ·OH is dependent on photolysis and $O_3$ concentration, it is subject to diurnal and regional seasonal cycles for both factors. Concentration of ·OH is then also indirectly subject to factors that influence the concentration of tropospheric $O_3$. Due to the difference in $O_3$ concentration between hemispheres, the global distribution of ·OH is thus not even, with slightly more ·OH found in the Northern Hemisphere.[59, 62, 63] Globally, there has been no indication of large-scale changes in ·OH concentration due to sinks and sources increasing concurrently, although there is contention around this topic.[18, 59, 63]

Other important sources of ·OH are the photolysis of hydrogen peroxide ($H_2O_2$) and the reaction of hydroperoxyl radicals (referred to as HOO·) with $O_3$ or nitric oxide (NO·):[59, 60, 63]

$$H_2O_2 + hv \ \rightarrow OH \cdot + OH \cdot \ \ (\lambda \leq 248 \, nm) \tag{1.4}$$

$$HOO \cdot + NO \cdot \rightarrow \ OH \cdot + NO_2 \cdot \tag{1.5}$$

$$HOO \cdot + O_3 \ \rightarrow \ OH \cdot + 2O_2 \tag{1.6}$$

Additionally, ·OH and HOO· quickly interconvert (grouped together as $HO_x$), as do NO· and $NO_2$· (grouped together as $NO_x$). A $HO_x$ radical is recycled every 28 s.[60] In a high-$NO_x$ environment, HOO· is able to react and form ·OH, but in a low-$NO_x$ environment, HOO· destroys $O_3$, meaning $NO_x$ abundance is important in the balance of $O_3$ destruction and ·OH formation.[59, 60, 64] ·OH chemistry can therefore not be considered in isolation, as it is interconnected with $HO_x$, $NO_x$, and $O_3$ cycles (as pictured in Figure 1.6), as well as being indirectly dependent on factors influencing source reagents.[60] Even just from discussion of the six reactions above, one can see how complex and intricately interconnected atmospheric chemistry is.

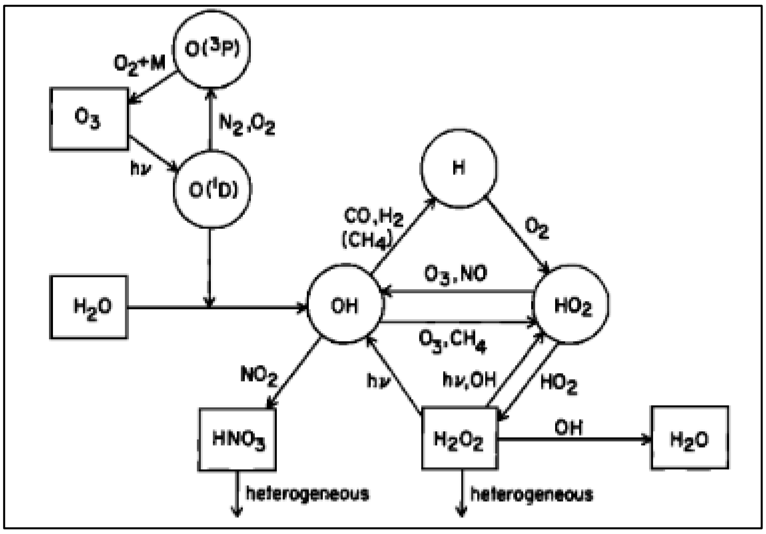

Figure 1.6 Major reactions affecting $HO_X$ in the troposphere. Interconversion between ·OH and HOO· is rapid and mediated by reactions with $O_3$ and NO·. Reproduced with permission from Logan et al. (1981).[65]

The targeted reaction for this research is the reaction of ·OH with $CH_4$, where ·OH first abstracts a hydrogen atom to give the methyl radical, $CH_3$· (1.7); $CH_3$· reacts to form the methylperoxy radical, $CH_3O_2$· (1.8); $CH_3O_2$· reacts with NO· to form the methoxy radical, $CH_3O$· (1.9); $CH_3O$· reacts to form formaldehyde, $H_2CO$, and a hydroperoxyl radical (1.10), which can be recycled back into ·OH, giving no net change to $HO_x$ or $NO_x$ due to recycling between HOO· and ·OH and NO· and $NO_2$·:

$$OH\cdot + CH_4 \rightarrow CH_3\cdot + H_2O \tag{1.7}$$

$$CH_3\cdot + O_2 + M \rightarrow CH_3O_2\cdot + M \tag{1.8}$$

$$CH_3O_2\cdot + NO\cdot \rightarrow CH_3O\cdot + NO_2\cdot \tag{1.9}$$

$$CH_3O\cdot + O_2 \rightarrow H_2CO + HOO\cdot \tag{1.10}$$

Formaldehyde ($H_2CO$) also reacts with ·OH, ultimately forming carbon monoxide (CO) and hydroperoxyl radicals, and the CO then reacts with $O_2$ to form $CO_2$. The initial abstraction reaction is the rate-determining step, so in theory by increasing ·OH concentration we can increase the rate of reaction and therefore reduce $CH_4$ concentration.

In practice, and as has been demonstrated above, ·OH is involved in a swathe of reactions. Changing the concentration of such an impactful atmospheric scrubber could perturb the atmospheric system in negative as well as positive ways. This research aims to investigate this potential by modelling the effects of increasing ·OH concentration on the atmosphere, as laid out in Chapter 5. Any “positive” or heating effects that come from an increase in [·OH] will need to be offset and lesser than the “negative” or cooling effects from an increased destruction in pollutants and other GHGs. Prior research on the production of ·OH using photocatalysis and on detection of ·OH is discussed in Chapter 4.

## 1.7 Titanium Dioxide as a Photocatalyst

Titanium dioxide ($TiO_2$) is a well-known and well-used photocatalyst, with a large volume of research on its use focused on photocatalytic splitting of water or on environmental pollutant remediation in both gaseous and aqueous phases.[66, 67] It has been used in multiple forms, including coatings like thin films on various supports, powders, on supports like non-woven paper and metal mesh, nanoparticles and nanoparticle suspensions, nanotubes, and aerosols or as airborne particles.[68-80] It is non-toxic, inexpensive, and can be activated by near-UV light.[66] It has three main crystalline stable forms: anatase, rutile, and brookite.[66] This research uses the anatase form as it is the most photocatalytically active of the three and it has been suggested that for the anatase phase, ·OH can desorb from the surface to react, making it useful for proposed applications.[66, 75]

Photocatalysts tend to be semiconductors due to the need for a band gap, which is the gap or "void space" in energy levels between the filled valence band (VB) and the empty conduction band (CB).[67] For photocatalysis to occur, the catalyst must absorb light of an energy greater than or equal to its band gap.[66] Anatase $TiO_2$ has a band gap of ~ 3.2 eV which corresponds to $\lambda \sim 390$ nm. Absorbing a photon excites an electron ($e^-$) from the valence band to the empty conduction band and leaves behind a hole ($h^+$) in the valence band, creating an electron-hole pair.[66, 69] These pairs can then undertake one of a few pathways: recombination (or quenching), or reaction with adsorbed molecules on the catalyst surface via reduction by an electron or oxidation by a hole.[66] This process is visualised in Figure 1.7. Catalysts can be modified to have charge-carrier traps on

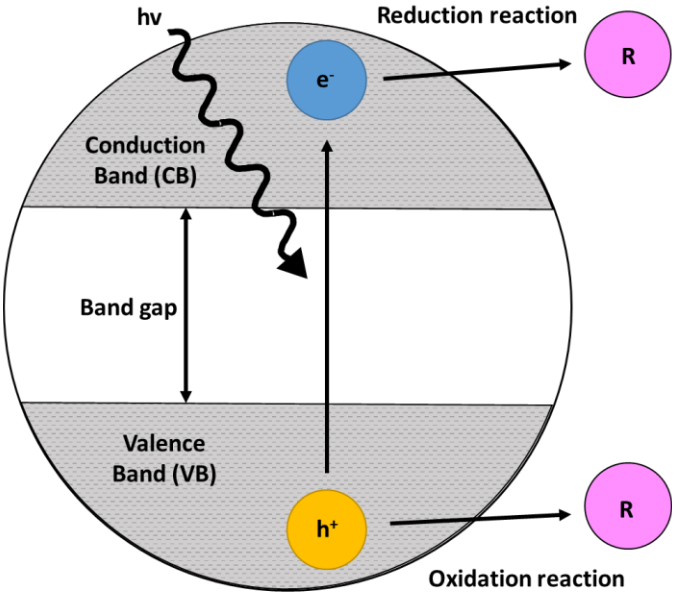

Figure 1.7 Representation of the photocatalysis process, where a semiconductor (represented by the large circle) absorbs a photon of wavelength greater than or equal to its bandgap, creating an electron-hole pair which can react with other molecules (R).

the surface, which prevent recombination and promote reaction.[67] Charge-carrier traps also occur naturally as point defects (visualised in Figure 1.8), which are oxygen vacancies and their neighbouring $Ti^{3+}$ atoms.[81, 82] Oxygen vacancies can then react to trap charge or can dissociate water.[81]

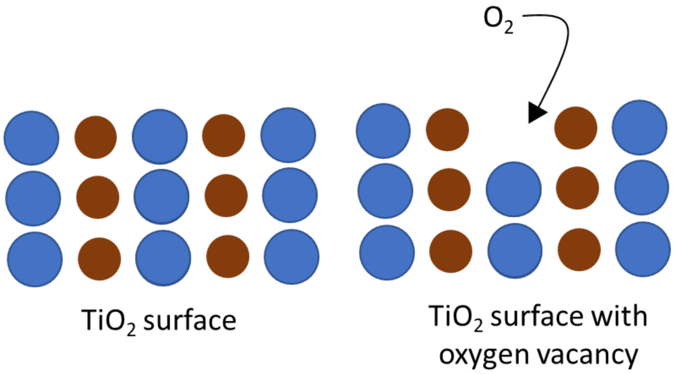

Figure 1.8 Simplified diagram of a $TiO_2$ surface with and without an oxygen vacancy. Blue circles are oxygen, red are titanium. Surface vacancies can act as charge traps or can react themselves with molecules like oxygen to form adsorbed OH or other products.

For a typical photocatalysis reaction with $TiO_2$, the photon is absorbed to promote the electron-hole pair (1.11)[66, 69, 90]. The $e^-$ can then reduce $O_2$ to form the superoxide radical $O_2{\cdot}^-$ (1.12)[69, 71, 90, 91], which further reacts to form HOO·, $H_2O_2$, and ·OH (1.13 - 1.15)[69, 71, 83, 90, 91]. The $h^+$ oxidises water and surface adsorbed OH groups ($OH_s$) to form ·OH (1.16 - 1.17)[69, 71, 83, 91], which is known to desorb from the surface and react.

$$TiO_2 + hv \rightarrow e^- + h^+ \tag{1.11}$$

$$e^- + O_2 \rightarrow O_2^{\cdot -} \tag{1.12}$$

$$O_2^{\cdot -} + H^+ \rightarrow HOO\cdot \tag{1.13}$$

$$2HOO\cdot \rightarrow H_2O_2 + O_2 \tag{1.14}$$

$$H_2O_2 + e^- \rightarrow OH_s^- + OH\cdot \tag{1.15}$$

$$h^+ + OH_s^- \rightarrow OH\cdot \tag{1.16}$$

$$h^+ + H_2O \rightarrow OH\cdot + H^+ \tag{1.17}$$

Since reactions occur on the surface of the catalyst, reactants must be adsorbed on the surface. The way the reactant binds to the surface, where it binds, how many sites are available, the type of site it is bound to, and many other factors influence how it can react.[81] Particularly for the formation of ·OH the number and nature of adsorbed molecules can have both positive and negative effects. $H_2O$ acts as both a reactant source for formation of ·OH and is considered “indispensable” in $TiO_2$ photocatalysis, but also blocks sites on the surface, preventing reactions from occurring.[69, 81] Relative humidity is thus often a controlled variable in photocatalyst experiments. Specifically, $H_2O$ can block access to the reactants adsorbed on the surface by forming a layer, or can block sites required for reactants or products to bind, whilst also needing to be present in high enough concentrations to form ·OH or participate in reactions itself.[81] Reactants also have to be adsorbed on the surface, and $O_2$, $H_2$, $H_2O$, NO·, and $CH_4$ are known to photoadsorb, or show an increase in adsorption in the presence of the light, to the $TiO_2$ surface.[81] Studies have proven that reactive $HO_x$ species ·OH, HOO·, and $H_2O_2$ can be formed on the surface of the catalyst, so using $TiO_2$ as a catalyst for formation of ·OH is a viable pathway.[73, 77, 83-87]

## 1.8 Research Statement

This thesis aims to investigate the feasibility of reducing $CH_4$ concentration in the troposphere by increasing the concentration of ·OH using an *in-situ* $TiO_2$ based photocatalyst. By using a $TiO_2$ catalyst, the required energy is supplied by solar radiation. Increasing the concentration of ·OH will cause more atmospheric reactions overall, including $CH_4$ removal reactions, and therefore will reduce the overall $CH_4$ concentration. $CH_4$ was chosen as a target molecule over $CO_2$ due to its short lifetime and high impact as a GHG, as well as the lack of mitigation strategies specifically targeting $CH_4$. $TiO_2$ was chosen as the photocatalyst due to its well-researched state, proven ability to split water and produce $HO_x$ radicals, and ability to be easily deployed on a large scale (non-toxic and inexpensive). ·OH was chosen as a target reagent due to its atmospheric importance and dominant role in the removal of $CH_4$ and its oxidation products.

This strategy poses one large issue in that ·OH reacts indiscriminately and therefore will affect not only $CH_4$ concentrations but other gases present in the troposphere. This can have a "positive" or warming effect, in that ·OH is interconverted to odd oxygen ($O_x$, e.g. $O_3$, $O^1D$) in the atmosphere, but also a "negative" or cooling effect, in that it could enhance production of reaction products that are involved in depleting $O_3$. These effects must be carefully considered and investigated, with the balances between "positive" and "negative" effects weighed up before any practical application of a $TiO_2$ photocatalyst. As summarised by Brasseur (1991):

> *"A modification of the oxidizing capacity of the troposphere will affect the destruction rate and consequently lifetime and the density of a variety of species, including the greenhouse gases and chemical pollutants."*[14]

In Chapter 2, a reference library of atmospheric molecules of importance is created using a combination of experimental, computational, and literature data. Using matrix-isolation (MI) spectroscopy in combination with Fourier-Transform Infra-Red (FTIR) spectroscopy, a library of experimental spectra is obtained, giving clear and sharp vibrational information. The spectra are then assigned using literature and calculated data. Theoretical vibrations and spectra are calculated using Gaussian-16 software.[88] A correction factor and a scaling factor is created using this data that can be applied to data obtained in Chapter 3, allowing for ease and confidence of assignment.

In Chapter 3, a variety of techniques are used in attempts to create and detect ·OH radicals. Matrix-isolation and FTIR spectroscopy are used to detect radicals created using a flow of water vapour excited by a Tesla-coil. Experiments are run using hydrocarbons to detect radical reaction products.

In Chapter 4, a combination of UV irradiation is used to create radicals and a residual gas analyser (RGA) to detect reaction products. $TiO_2$ is coated onto slides and held in a fluorescence cell (built in-house) to react with water vapour and hydrocarbons. The $TiO_2$-coated slide is tested for photocatalytic ability and the rate of formation of ·OH is determined from this.

In Chapter 5, a simple atmospheric model is created to investigate the effect of increasing ·OH concentrations on the concentrations of important atmospheric molecules. A perturbation rate is calculated for a chosen particle density of $TiO_2$ and added to the model to determine the effect on the other concentrations modelled.

## 1.9 References

1. Gulev, S. K.; Thorne, P. W.; Ahn, J., et al., Changing State of the Climate System. In *Climate Change 2021: The Physical Science Basis. Contribution of Working Group I to the Sixth Assessment Report of the Intergovernmental Panel on Climate Change*, Masson-Delmotte V.; Zhai, P.; Pirani, A., et al., Eds. Cambridge University Press: Cambridge, United Kingdom, 2021; pp 287-422.
2. Ministry for Primary Industries Environment and climate change research. https://www.mpi.govt.nz/funding-rural-support/environment-and-natural-resources/environment-and-climate-change-research/ (accessed 5/4/23).
3. Reynolds, J. L., Solar geoengineering to reduce climate change: a review of governance proposals. *Proceedings of the Royal Society A: Mathematical, Physical and Engineering Sciences* **2019,** *475* (2229), 20190255.
4. Climate Analytics and New Climate Institute 2100 Warming Projections: Emissions and expected warming based on pledges and current policies. https://climateactiontracker.org/global/temperatures/ (accessed 22/03/23).
5. Canadell, J. G.; Monteiro, P. M. S.; Costa, M. H., et al., Global Carbon and other Biogeochemical Cycles and Feedbacks. In *Climate Change 2021: The Physical Science Basis. Contribution of Working Group I to the Sixth Assessment Report of the Intergovernmental Panel on Climate Change*, Masson-Delmotte, V.; Zhai, P.; Pirani, A., et al., Eds. Cambridge University Press Cambridge, United Kingdom; New York, NY, USA, 2021; pp 673-816.
6. Forster, P.; Storelvmo, T.; Armour, K., et al., Chapter 7: The Earth's Energy Budget, Climate Feedbacks, and Climate Sensitivity. In *Climate Change 2021: The Physical Science Basis. Contribution of Working Group I to the Sixth Assessment Report of the Intergovernmental Panel on Climate Change*, Zhai, P.; Pirani, A.; Connors, S. L., et al., Eds. Cambridge University Press: Cambridge, United Kingdom, 2021; pp 923-1054.
7. Berger, A., Basic Concepts of Climate Modelling. In *Climatic Change and Impacts: A General Introduction*, Fantechi, R.; Maracchi, G.; Almeida-Teixeira, E., Eds. Luxembourg, 1991.
8. Morel, P., An Overview of the Climate System. In *Climatic Change and Impacts: A General Introduction*, Fantechi, R.; Maracchi, G.; Almeida-Teixeira, E., Eds. Luxembourg, 1991.
9. Barry, R.; Chorley, R.; Barry, R. G., et al., Atmospheric Composition, Mass and Structure. In *Atmosphere, Weather and Climate*, 8th ed.; 2003.
10. Finlayson-Pitts, B. J.; Pitts, J. N., Chapter 1: Overview of the Chemistry of Polluted and Remote Atmospheres. In *Chemistry of the Upper and Lower Atmosphere*, Finlayson-Pitts, B. J.; Pitts, J. N., Eds. Academic Press: San Diego, 2000; pp 1-14.
11. Berger, A.; Tricot, C., Simple Climate Models. In *Climatic Change and Impacts: A General Introduction*, Fantechi, R.; Maracchi, G.; Almeida-Teixeira, E., Eds. Luxembourg, 1991.
12. Finlayson-Pitts, B. J.; Pitts, J. N., Chapter 14: Global Tropospheric Chemistry and Climate Change. In *Chemistry of the Upper and Lower Atmosphere*, Finlayson-Pitts, B. J.; Pitts, J. N., Eds. Academic Press: San Diego, 2000; pp 762-843.
13. Bolle, H.-J., Radiative Transfer and Greenhouse Effect. In *Climatic Change and Impacts: A General Introduction*, Fantechi, R.; Maracchi, G.; Almeida-Teixeira, E., Eds. Luxembourg, 1991.
14. Brasseur, G., Atmospheric Chemistry and Climate. In *Climatic Change and Impacts: A General Introduction*, Fantechi, R.; Maracchi, G.; Almeida-Teixeira, E., Eds. Luxembourg, 1991.
15. Siegenthaler, U., Carbon Dioxide: Its Natural Cycle and Anthropogenic Peturbation. In *Climatic Change and Impacts: A General Introduction*, Fantechi, R.; Maracchi, G.; Almeida-Teixeira, E., Eds. Luxembourg, 1991.
16. Mikolajczyk, J.; Bielecki, Z.; Bugajski, M., et al., Analysis of Free-Space Optics Development. *Metrol. Meas. Syst.* **2017,** *24*.
17. Myhre, G.; Shindell, D.; Bréon, F.-M., et al., Anthropogenic and Natural Radiative Forcing. In *Climate Change 2013 – The Physical Science Basis: Working Group I Contribution to*

*the Fifth Assessment Report of the Intergovernmental Panel on Climate Change*, Stocker, T. F.; Qin, D.; Plattner, G.-K., et al., Eds. Cambridge University Press: Cambridge, United Kingdom; New York, NY, USA, 2013; pp 659-740.

18. Turner, A. J.; Frankenberg, C.; Wennberg, P. O., et al., Ambiguity in the causes for decadal trends in atmospheric methane and hydroxyl. *Proc Natl Acad Sci U S A* **2017,** *114* (21), 5367-5372.

19. Finlayson-Pitts, B. J.; Pitts, J. N., Chapter 2: The Atmospheric System. In *Chemistry of the Upper and Lower Atmosphere*, Finlayson-Pitts, B. J.; Pitts, J. N., Eds. Academic Press: San Diego, 2000; pp 15-42.

20. Ritchie, H.; Rosado, P.; Roser, M. CO2 and Greenhouse Gas Emissions. https://ourworldindata.org/co2-and-greenhouse-gas-emissions.

21. Andrew, R. M.; Peters, G. P., The Global Carbon Project's fossil CO2 emissions dataset (2023 v36). 2023.

22. Jones, M. W.; Peters, G. P.; Gasser, T., et al., National contributions to climate change due to historical emissions of carbon dioxide, methane and nitrous oxide In *Scientific Data*, 2024.

23. Szopa, S.; Naik, V.; Adhikary, B., et al., Short-Lived Climate Forcers. In *Climate Change 2021: The Physical Science Basis. Contribution of Working Group I to the Sixth Assessment Report of the Intergovernmental Panel on Climate Change*, Masson-Delmotte, V.; Zhai, P.; Pirani, A., et al., Eds. Cambridge University Press: Cambridge, United Kingdom; New York, NY, USA, 2021; pp 817-922.

24. Logan, J. A., Nitrogen-Oxides in the Troposphere - Global and Regional Budgets. *J. Geophys. Res. Oceans.* **1983,** *88* (Nc15), 785-807.

25. Finlayson-Pitts, B. J.; Pitts, J. N., Chapter 6: Rates and Mechanism of Gas Phase Reactions in Irradiated Organic - NOx- Air Mixtures. In *Chemistry of the Upper and Lower Atmosphere*, Finlayson-Pitts, B. J.; Pitts, J. N., Eds. Academic Press: San Diego, 2000; pp 179-263.

26. Dutton, E. G.; Christy, J. R., Solar radiative forcing at selected locations and evidence for global lower tropospheric cooling following the eruptions of El Chichón and Pinatubo. *Geophys. Res. Lett.* **1992,** *19* (23), 2313-2316.

27. Finlayson-Pitts, B. J.; Pitts, J. N., Chapter 5: Kinetics and Atmospheric Chemistry. In *Chemistry of the Upper and Lower Atmosphere*, Finlayson-Pitts, B. J.; Pitts, J. N., Eds. Academic Press: San Diego, 2000; pp 130-178.

28. Graedel, T. E.; Crutzen, P. J., *Atmospheric Change: An Earth System Perspective*. W. H. Freeman & Co.: 1993.

29. Ministry for the Environment Paris Agreement. https://environment.govt.nz/what-government-is-doing/international-action/about-the-paris-agreement/ (accessed 23/3/23).

30. IPCC Summary for Policymakers. In *Global Warming of 1.5°C. An IPCC Special Report on the impacts of global warming of 1.5°C above pre-industrial levels and related global greenhouse gas emission pathways, in the context of strengthening the global response to the threat of climate change, sustainable development, and efforts to eradicate poverty*, Masson-Delmotte, V.; Zhai, P.; Pörtner, H.-O., et al., Eds. Cambridge University Press,: Cambridge, UK, 2018; pp 3-24.

31. Hoegh-Guldberg, O.; Jacob, D.; Taylor, M., et al., Impacts of 1.5ºC Global Warming on Natural and Human Systems. . In *Global Warming of 1.5°C. An IPCC Special Report on the impacts of global warming of 1.5°C above pre-industrial levels and related global greenhouse gas emission pathways, in the context of strengthening the global response to the threat of climate change, sustainable development, and efforts to eradicate poverty*, Masson-Delmotte, V.; Zhai, P.; Pörtner, H.-O., et al., Eds. Cambridge University Press: Cambridge, UK, 2018; pp 175-312.

32. *COP26 Glasgow Climate Pact*; 2021, 2021.

33. Ritchie, H.; Roser, M.; Rosado, P. $CO_2$ and Greenhouse Gas Emissions By Sector. https://ourworldindata.org/co2-and-greenhouse-gas-emissions (accessed 3/5/23).
34. Fawzy, S.; Osman, A. I.; Doran, J., et al., Strategies for mitigation of climate change: a review. *Environ. Chem. Lett.* **2020,** *18* (6), 2069-2094.
35. Stocker, T. F.; Qin, D.; Plattner, G.-K., et al., Technical Summary. In *Climate Change 2013: The Physical Science Basis. Contribution of Working Group I to the Fifth Assessment Report of the Intergovernmental Panel on Climate Change*, Stocker, T. F.; Qin, D.; Plattner, G.-K., et al., Eds. Cambridge University Press: Cambridge, UK; New York, NY, USA, 2013.
36. REN21 *Renewables in Energy Demand* Paris, 2023.
37. REN21 *Renewables 2022 Global Status Report*; Paris, 2022.
38. Thornes, J. E.; Pope, F. D., Why do we need Solutions to Global Warming. In *Geoengineering of the Climate System*, Hestor, R. E.; Harrison, R. M., Eds. Royal Society of Chemistry: 2014; Vol. 38, pp 1-21.
39. Moriarty, P.; Honnery, D., Chapter 14 - Bioenergy with carbon capture and storage in a future world. In *Bioenergy with Carbon Capture and Storage*, Magalhães Pires, J. C.; Da Cunha Gonçalves, A. L., Eds. Academic Press: 2019; pp 273-287.
40. Harvey, F.; Ambrose, J., UK government gambles on carbon capture and storage tech despite scientists' doubts. *The Guardian* 2023.
41. Ministry for Primary Industries One Billion Trees Programme. https://www.mpi.govt.nz/forestry/funding-tree-planting-research/one-billion-trees-programme/ (accessed 23/3/23).
42. The England Trees Action Plan 2021-2024. Department for Environment, F. R. A., Ed. UK, 2021.
43. England's Community Forests Trees for Climate. https://englandscommunityforests.org.uk/trees-for-climate (accessed 23/3/23).
44. Bandilla, K. W., Carbon Capture and Storage. In *Future Energy (Third Edition)*, Letcher, T. M., Ed. Elsevier: 2020; pp 669-692.
45. Southern Green Gas Our Technology. https://www.southerngreengas.com.au/our-technology/ (accessed 23/3/23).
46. Robock, A., Stratospheric Aerosol Geoengineering. In *Geoengineering of the Climate System*, The Royal Society of Chemistry: 2014; pp 162-185.
47. Pope, F. D.; Braesicke, P.; Grainger, R. G., et al., Stratospheric aerosol particles and solar-radiation management. *Nat. Clim. Change.* **2012,** *2* (10), 713-719.
48. Smith, W.; Wagner, G., Stratospheric aerosol injection tactics and costs in the first 15 years of deployment. *Environ. Res. Lett.* **2018,** *13* (12).
49. Office of Energy Efficiency and Reneweable Energy, NREL Study Identifies the Opportunities and Challenges of Achieving the U.S. Transformational Goal of 100% Clean Electricity by 2035. https://www.energy.gov/eere/articles/nrel-study-identifies-opportunities-and-challenges-achieving-us-transformational-goal#:~:text=To%20decarbonize%20the%20grid%20by,%24330%20billion%20to%20%24740%20billion. (accessed 23/3/23).
50. Tollefson, J., Can artifically altered clouds save the Great Barrier Reef? *Nature* **2021,** *595*, 476-498.
51. Tollefson, J., First sun-dimming experiment will test a way to cool Earth. *Nature* **2018,** *563*, 613-615.
52. Keutsch Group SCoPEx. https://www.keutschgroup.com/scopex (accessed 23/03/23).
53. Shepherd, J.; Caldeira, K.; Cox, P., et al., *Geoengineering the climate: science, governance, and uncertainty*. The Royal Society: London, UK; New York, Rutledge, 2009.
54. Reisinger, A., The contribution of methane emissions from New Zealand livestock to global warming. New Zealand Agricultural Greenhouse Gas Research Centre Ed. Palmerston North, 2018.

55. Saunois, M.; Stavert, A. R.; Poulter, B., et al., The Global Methane Budget 2000–2017. *Earth. Syst. Sci. Data.* **2020,** *12* (3), 1561-1623.
56. Te Tai Ohanga The Treasury, FEU Special Topic: Medium-term outlook for dairy exports. https://www.treasury.govt.nz/publications/research-and-commentary/rangitaki-blog/feu-special-topic-medium-term-outlook-dairy-exports (accessed 14/4/23).
57. Melhem, Y. B., New Zealand's troubled waters. *ABC News* 2021.
58. Ministry for the Environment Aotearoa New Zealand's Methane Emissions Reduction Action Plan. Ministry for the Environment Ed. New Zealand Government: New Zealand, 2022.
59. Lelieveld, J.; Dentener, F. J.; Peters, W., et al., On the role of hydroxyl radicals in the self-cleansing capacity of the troposphere. *Atmos. Chem. Phys.* **2004,** *4*, 2337-2344.
60. Monks, P. S., Gas-phase radical chemistry in the troposphere. *Chem Soc Rev* **2005,** *34* (5), 376-95.
61. Ehhalt, D. H.; Dorn, H. P.; Poppe, D., The Chemistry of the Hydroxyl Radical in the Troposphere. *P. Roy. Soc. Edinb. B* **1990,** *97*, 17-34.
62. Fishman, J.; Crutzen, P. J., The distribution of the hydroxyl radical in the troposphere. *J. Atmos. Sci.* **1978,** *284*.
63. Lu, Y.; Khalil, M. A. K., Tropospheric OH: model calculations of spatial, temporal, and secular variations. *Chemosphere.* **1991,** *23* (3), 397-444.
64. Rohrer, F.; Lu, K.; Hofzumahaus, A., et al., Maximum efficiency in the hydroxyl-radical-based self-cleansing of the troposphere. *Nat. Geosci.* **2014,** *7* (8), 559-563.
65. Logan, J. A.; Prather, M. J.; Wofsy, S. C., et al., Tropospheric chemistry: A global perspective. *J. Geophys. Res.* **1981,** *86* (C8).
66. Chen, H.; Nanayakkara, C. E.; Grassian, V. H., Titanium Dioxide Photocatalysis in Atmospheric Chemistry. *Chem. Rev.* **2012,** *112* (11), 5919-5948.
67. Linsebigler, A. L.; Lu, G.; Yates Jr, J. T., Photocatalysis on $TiO_2$ surfaces: principles, mechanisms, and selected results. *Chem. Rev.* **1995,** *95* (3), 735-758.
68. Anpo, M.; Dohshi, S.; Kitano, M., et al., The Preparation and Characterization of Highly Efficient Titanium Oxide–Based Photofunctional Materials. *Annu. Rev. Mater. Res.* **2005,** *35* (1), 1-27.
69. Gaya, U. I.; Abdullah, A. H., Heterogeneous photocatalytic degradation of organic contaminants over titanium dioxide: A review of fundamentals, progress and problems. *J. Photochem. Photobiol. C.* **2008,** *9* (1), 1-12.
70. Molina-Reyes, J.; Romero-Moran, A.; Uribe-Vargas, H., et al., Study on the photocatalytic activity of titanium dioxide nanostructures: Nanoparticles, nanotubes and ultra-thin films. *Catal. Today.* **2020,** *341*, 2-12.
71. Bahrini, C.; Parker, A.; Schoemaecker, C., et al., Direct detection of $HO_2$ radicals in the vicinity of $TiO_2$ photocatalytic surfaces using cw-CRDS. *Appl. Catal. B.* **2010,** *99* (3), 413-419.
72. Harbour, J. R.; Tromp, J.; Hair, M. L., Photogeneration of hydrogen peroxide in aqueous TiO2 dispersions. **1985,** *63* (1), 204-208.
73. Ishibashi, K.-I.; Fujishima, A.; Watanabe, T., et al., Detection of active oxidative species in $TiO_2$ photocatalysis using the fluorescence technique. *Electrochem. Commun.* **2000,** *2* (3), 207-210.
74. Moon, D. R.; Ingham, T.; Whalley, L. K., et al., Production of $HO_2$ and OH radicals from near-UV irradiated airborne $TiO_2$ nanoparticles. *Phys Chem Chem Phys* **2019,** *21* (5), 2325-2336.
75. Nosaka, Y.; Nosaka, A., Understanding Hydroxyl Radical (•OH) Generation Processes in Photocatalysis. *ACS Energy Lett.* **2016,** *1* (2), 356-359.
76. Schwarz, P. F.; Turro, N. J.; Bossmann, S. H., et al., A New Method To Determine the Generation of Hydroxyl Radicals in Illuminated $TiO_2$ Suspensions. *J. Phys. Chem. B.* **1997,** *101* (36), 7127-7134.
77. Thiebaud, J.; Thevenet, F.; Fittschen, C., OH Radicals and H2O2 Molecules in the Gas Phase near to $TiO_2$ Surfaces. *J. Phys. Chem. C* **2010,** *114* (7), 3082-3088.

78. Jaeger, C. D.; Bard, A. J., Spin trapping and electron spin resonance detection of radical intermediates in the photodecomposition of water at titanium dioxide particulate systems. *J. Phys. Chem.* **1979,** *83* (24), 3146-3152.
79. Lugo-Vega, C. S.; Serrano-Rosales, B.; de Lasa, H., Immobilized particle coating for optimum photon and $TiO_2$ utilization in scaled air treatment photo reactors. *Appl. Catal. B.* **2016,** *198*, 211-223.
80. Lien, C.-F.; Chen, M.-T.; Lin, Y.-F., et al., Photooxidation of Methane over $TiO_2$. *JCCS.* **2004,** *51* (1), 37-42.
81. Henderson, M. A., A surface science perspective on $TiO_2$ photocatalysis. *Surf. Sci. Rep.* **2011,** *66* (6), 185-297.
82. Nowotny, J.; Bak, T.; Nowotny, M. K., et al., TiO2 Surface Active Sites for Water Splitting. *J. Phys. Chem. B.* **2006,** *110* (37), 18492-18495.
83. Diesen, V. Heterogeneous TiO2 Photocatalysis - Fundamental Chemical Aspects and Effects of Solid Phase Alterations. KTH Royal Institute of Technology, Stockholm, 2013.
84. Yi, J.; Bahrini, C.; Schoemaecker, C., et al., Photocatalytic Decomposition of $H_2O_2$ on Different $TiO_2$ Surfaces Along with the Concurrent Generation of $HO_2$ Radicals Monitored Using Cavity Ring Down Spectroscopy. *J. Phys. Chem. C.* **2012,** *116* (18), 10090-10097.
85. Murakami, Y.; Endo, K.; Ohta, I., et al., Can OH Radicals Diffuse from the UV-Irradiated Photocatalytic $TiO_2$ Surfaces? Laser-Induced-Fluorescence Study. *J. Phys. Chem. C.* **2007,** *111* (30), 11339-11346.
86. Kubo, W.; Tatsuma, T., Detection of $H_2O_2$ Released from $TiO_2$ Photocatalyst to Air. *Anal. Sci.* **2004,** *20* (4), 591-593.
87. Uchino, T.; Tokunaga, H.; Ando, M., et al., Quantitative determination of OH radical generation and its cytotoxicity induced by TiO2–UVA treatment. *Toxicol. In Vitro.* **2002,** *16* (5), 629-635.
88. Frisch, M. J.; Trucks, G. W.; Schlegel, H. B., et al. *Gaussian 16, Revision A.03*, Gaussian, Inc.: Wallingford, CT, USA, 2016.
89. Berger, A.; Tricot, C., The greenhouse effect. *Surv. Geophys.* **1992,** *13* (6), 523-549.
90. Fujishima, A.; Zhang, X.; Tryk, D. A., $TiO_2$ photocatalysis and related surface phenomena. *Surf. Sci. Rep.* **2008,** *63* (12), 515-582.
91. Coral, J. A. Measuring and Predicting Hydroxyl Radical Generation From Irradiated $TiO_2$ Nanoparticles Under Simulated Environmental Conditions and Correlations to Daphnia magna Toxicity. Clemson University, 2018.

# 2.0 Establishing a MI-FTIR Correction Function

## 2.1 Introduction

The initial technique chosen for the detection of radicals and reaction products generated from the use of a $TiO_2$ catalyst was matrix-isolation (MI) Fourier-Transform Infra-Red (FTIR) spectroscopy. This technique was chosen over other potential methods as it was the most appropriate available technique. MI is a technique that uses an inert carrier (host) gas, in this case argon, at high concentrations compared to sample (guest), to build a thin layer of molecules over a $CaF_2$ window cooled to < 20 K, as shown in Figure 2.1. By heavily diluting the sample with weakly interacting argon, intermolecular interactions are minimised. Cooling the sample reduces the likelihood of vibrational, rotational, and translational motions by freezing the guest molecules in place in a host lattice, giving clear and sharp spectra of only vibrational transitions of singular sample molecules.[1] The MI system used was built in-house. Experimental layout is discussed further in section 2.3.1.

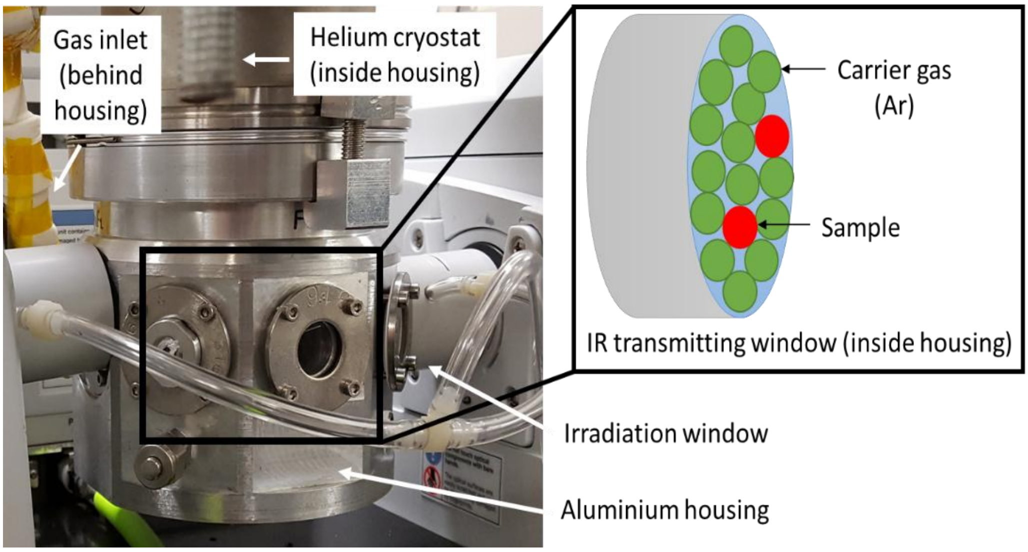

Figure 2.1 Image of the matrix-isolation setup, specifically the vacuum chamber housing, with an inset diagram of how the sample and carrier gas are distributed on the $CaF_2$ window.

Most radical lifetimes in ambient terrestrial conditions are very short, making investigation of the radical itself difficult. Radical detection can be done either indirectly (by converting to more stable products) or directly (detecting the radical itself). Common techniques include spin trapping, which converts ·OH to a stable product by reaction, electron paramagnetic resonance (EPR),[2] pulse radiolysis, laser induced fluorescence (LIF), and continuous-wave cavity-ring-down (cw-CRD) spectroscopy.[2-4] MI has advantages over these other techniques when it comes to investigating specifically radicals and reaction intermediates. By immobilising molecules, reactions are hindered from occurring, so radicals can last longer than their usual short lifetimes and reaction intermediates can be isolated.[1] MI also allows direct investigation of the radical itself when coupled with FTIR by allowing the radical or intermediate to be trapped immediately after formation. MI by nature gives very clear and sharp spectra; for neon and argon matrices Jacox (2002) gives line widths (FWHM) at around 1 $cm^{-1}$.[1]

When using MI, it is well known there is a shift or offset in wavenumber between the experimentally collected data and literature or computational data.[1] This shift is dependent on the carrier gas used to form the matrix;[5] for example, neon gives the smallest shift of 1%, and argon a 2% shift for diatomic molecules.[1] When comparing raw calculated vibrational frequencies to experimental data, the difference is conventionally mitigated by use of a scaling factor, which is specific to computational level of theory.[6, 7] Because the scaling factors are specific to the chosen level of theory and basis set used, the factor accounts for both the assumptions made when using computational methods as well as the variation inherent to the use of the matrix isolation technique. To combat these differences, a library of atmospherically important molecules and reaction products was analysed using MI-FTIR and calculations run using the Gaussian-16 software suite, in order to determine a correction function and a scaling factor for each spectral region, and to establish a reference library of experimental spectra for similar atmospherically important molecules.[8]

This reference library and its calculated functions were fundamental to the work carried out in Chapter 3. Firstly, the correction function has been applied when assigning reaction products and radical peaks to improve accuracy, as the latter are much harder to detect and assign due to a lack of, and conflicting, literature information. This function is also specific to the MI setup and types of molecules investigated. Scaling factors are commonly calculated using gas-phase data and applied to gas-phase experimental data; herein, the correction and scaling functions have been calculated using MI-phase data to give a function more appropriate to apply to the subsequently collected MI spectra. The functions are also usually calculated from a larger library of molecules with a range of different functional groups; in this case, the chosen library of molecules is specific to the types of molecules expected as reaction intermediates or products for atmospheric reactions (see section 2.2.1 for further detail). By including only functional groups relevant to the experiments that will be undertaken, the correction function will be only weighted towards the offset experienced by those functional groups, instead of correcting shifts for irrelevant functional groups that could change the offset, making the correction less accurate. The library also includes large molecules like terpenes, which are computationally expensive and so aren’t always included. Secondly, the reference library gives a baseline for any reactions attempted, as it contains experimental spectra of the reactants as well as computational data for expected products or intermediates. Finally, the process of creating a correction function also gives insight to the accuracy of computed spectra. Computed intensities are known to be inaccurate, depending on the level of theory employed.[6, 9] This, coupled with the known shift in vibrational frequency, makes comparison of experimental peaks with the computed spectra somewhat difficult, and having a correction function to apply to congested, or unknown to literature, spectral peaks gives an increased confidence in the peak assignments.

## 2.2 Computational Procedure

To assign experimental peaks and compare to literature, calculations were run for each reference library molecule using the Gaussian-16 (G16) software suite, visualised in Gaussview-6.[8 10]

MP2 and B3LYP levels of theory were used for the calculations. MP2[11] is the second-order Møller-Plesset perturbation, which adds to Hartree-Fock (HF) theory by adding a small perturbation (to a specific order) which accounts for electron correlation. B3LYP is a hybrid exchange-correlation functional, so it adds to HF methods by specifying exchange and correlation functionals. In this case, it uses Becke's 3-parameter exchange functional[12] and the Lee-Yang-Parr correlation functional,[13] which also accounts for electron correlation. These two methods were used as they are computationally less intensive than other available theories yet still provide results that accord closely to experimental data. Roy et al. (2014) found that B3LYP and MP2 methods, when applied with the cc-pVTZ basis set, gave good approximations to experimental frequencies and intensities for anharmonic calculations.[14] They found MP2 calculations were marginally more accurate, and that frequencies were shifted +2% compared to the –2% shift for B3LYP results.[14] In contrast, Jacox (2002) found that HF and MP2 gave erratic results and that B3LYP was more reliable, with basis set choice of less consequence.[1] As such, both levels of theory were used, since MP2 calculations were found to be more computationally taxing but historically tended to be closer to experimental and literature data, and B3LYP provided a good baseline and will converge at higher basis sets compared to some MP2 calculations. It was particularly important to use methods that account for electron correlation as they accord more accurately with experimental results.

Basis sets of cc-pVDZ, cc-pVTZ, and cc-pVQZ were used (referred to herein as DZ, TZ, and QZ respectively).[15, 16] These are correlation-consistent polarised valence double/triple/quadruple zeta basis sets.[17] The correlation-consistent term refers to grouping together the basis functions that contribute the same correlation energy within a calculation. The polarised term refers to the additional basis functions that are added to the orbitals, which allows the electron density more space to occupy. This is closer to real bonding, which is polarised. The valence term refers to the set dealing with only valence electron orbitals and not core orbitals, which makes them less computationally expensive. The zeta term refers to the number of extra basis functions used to describe atomic orbitals. Overall, these basis sets were used as they account for electron correlation, are not too computationally expensive, and work well with the chosen MP2 and B3LYP levels of theory.

Calculations were all run using the same procedure. An initial harmonic “optfreq” job was run, which calculates the optimised geometry of the molecule from an initial input “guess” geometry created in Gaussview 6, then calculates the vibrations of the optimised molecule acting as a harmonic oscillator. Then an anharmonic frequency calculation was run using the optimised output of the previous optfreq calculation, calculating the vibrations of the optimised molecule acting as an anharmonic oscillator (i.e. a real-world molecule). The initial calculations at B3LYP and MP2 level started at DZ, then would go up to TZ and QZ as each harmonic calculation converged. Due to computational limits, some molecules have had harmonic calculations converge at a higher-level basis set than when using the anharmonic correction. This means the highest converged anharmonic calculation for some molecules may be at a low basis set level, like DZ. The anharmonic calculations are used when assigning experimental peaks and therefore creating the functions since they more closely model experimental data, even if there were higher-level converged harmonic calculations.[18] Convergence issues were encountered frequently for large molecules as these are computationally expensive – often calculations would ‘time-out’ if they had not finished after 30 days. This usually indicated that the system was unlikely to converge within reasonable timeframes, as although calculations can be restarted from the point they were terminated, many calculations that timed-out after a month would not finish even after further months of calculation. These errors or computational limits are why not every molecule has been calculated to the anharmonic QZ level; however, as will be seen in section 2.4 below, this has not had a significant impact on the creation of the correction function.

For calculations of molecules, the decision to use an anharmonic correction is a balance between computational resources and accuracy. Typically, harmonic (uncorrected) calculations are used as they are much cheaper in computational time and resources, and can be scaled to be close to experimental data using an already established scaling factor.[6, 18, 19] Scaling factors are weakly dependent on the basis set chosen, with MP2 having a stronger basis set dependence than B3LYP, due to the use the virtual orbitals which are more affected by increasing basis set size.[6] Anharmonic calculations give raw results that are close to experimental data but at the cost of significantly increased computation time. When modelling the potential energy surface of a molecule, a harmonic (parabolic) model gives energy levels that are equally spaced, whereas using an anharmonic model gives energy levels that become closer together at higher excitations, up to the point where a bond in the molecule will break (see Figure 2.2). Using the anharmonic correction allows the calculation to more accurately model the real-world molecule. Computations adding in anharmonic corrections by default in G16 includes effects such as Fermi resonance which can cause issues in matching calculated data to experimental data.[6, 18] However, anharmonic data has been chosen in this work to create the functions since they will act to scale the results as is conventionally done.

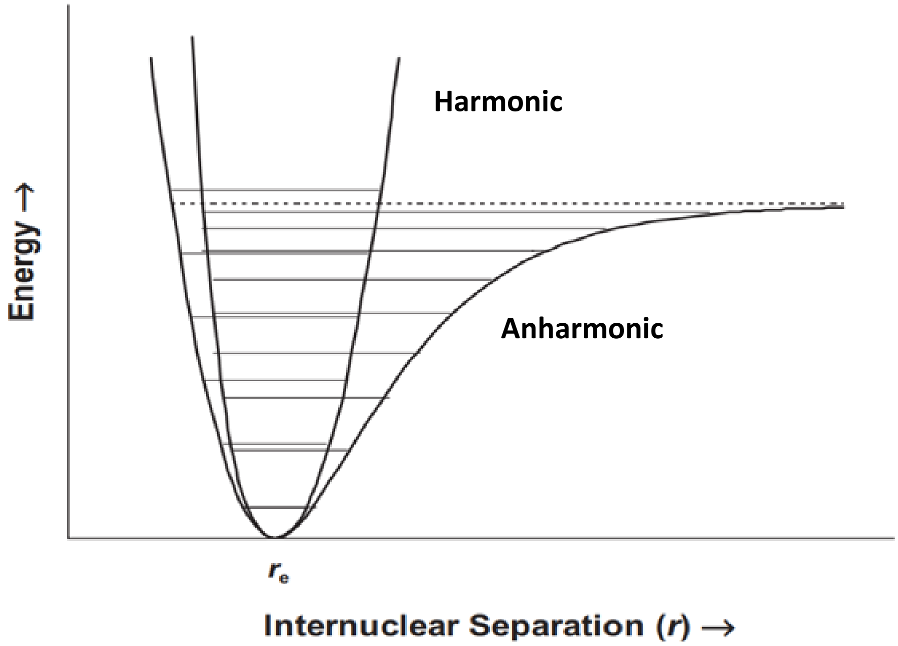

Figure 2.2 Harmonic and anharmonic potentials for bond stretching. Reproduced with permission from Allinger (2010).[31]

It is also known that computationally predicted IR intensities have a minimum 10 – 15% uncertainty compared to experimental data.[7] In one study comparing different basis sets and levels of theory, Galabov et al. (2002) found that MP2/cc-pVTZ had an average percentage error of 20 – 40% for predicted IR intensities for molecules with less than 5 atoms.[9] Additionally, experimental intensities can be higher than predicted intensities due to overlapping of fundamentals with overtones (Fermi resonance) or degenerate frequencies.[9] Whilst some studies find that predicted intensities converge toward experimental intensities as electron correlation is increased, computed intensities have not been considered when assigning computational data, with the exception of any IR inactive bands that have been calculated.[6, 9]

Typically, scaling factors have already been computed for given levels of theory and basis sets, so databases like the Computational Chemistry Comparison and Benchmark Database (CCCBDB), authored by the National Institute of Standards and Technology (NIST), hold the factors. NIST find their scaling factors using least squares theory:

$$s = \frac{\Sigma(v_i * w_i)}{\Sigma({w_i}^2)} \tag{2.1}$$

where $v_i$ is the experimental vibrational frequency and $w_i$ is the computational equivalent.[6, 19] A scaling factor for each molecule has been calculated for comparison, using equation 2.1 (see section 2.4.3). Additionally, a correction function was found by establishing the linear relationship between $v_i$ and $w_i$ for all molecules in the reference library. The correction function was calculated by level of theory, basis set, and spectral region, discussed in more detail in section 2.4.2.

### 2.2.1 Reference Library Molecules

There were 18 molecules selected for the reference library, listed in Table 2.1. By having a range of $M_w$ and classes of compounds in the reference library, the shifts determined and therefore the correction and scaling functions created can be used across a range of expected products and reaction intermediates.

Molecules were selected based on how atmospherically important they are. The first group of molecules selected are terpenes. Terpenes are volatile organic compounds (VOCs) emitted by vegetation and are involved in atmospheric reactions with ·OH and in reactions that produce $O_3$, aerosols and haze, organic nitrates, and CO.[20] They have lifetimes of ~ 1 day and therefore are stronger near the source – the "haze" that can be seen over forests like the Great Smoky Mountains is due to terpene-produced ozone.[21] Isoprene is the most important of the terpenes listed as it forms ~ 50% of emitted biogenic non-methane hydrocarbons.[21-23] Other terpenes chosen are α-pinene and its oxide, β-pinene, limonene, geraniol, and myrcene. The second group of selected compounds were chosen by size to balance out the large $M_W$ terpenes. These are propyne, ethylene, acetylene, cyclopropylacetylene, methane, and ethane.

Table 2.1 Reference library molecules, structures, and highest basis set used for anharmonic calculations for B3LYP and MP2 levels of theory.

| **Molecule** | **Structure** | **Highest Level of Theory Calculated (Anharmonic)** |
|---|---|---|
| 2-methyl-2-butene | 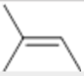 | B3LYP/cc-pVQZ; MP2/cc-pVTZ |
| Acetylene | $HC \equiv CH$ | B3LYP/cc-pVQZ; MP2/cc-pVQZ |
| α-pinene | 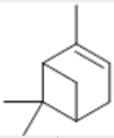 | B3LYP/cc-pVTZ; MP2/cc-pVDZ |
| α-pinene oxide | 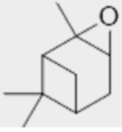 | B3LYP/cc-pVTZ; MP2/cc-pVDZ |
| B-pinene | 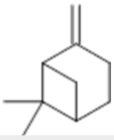 | B3LYP/cc-pVTZ; MP2/cc-pVDZ |
| Benzene |  | B3LYP/cc-pVQZ; MP2/cc-pVQZ |
| Cyclopropylacetylene |  | B3LYP/cc-pVQZ; MP2/cc-pVQZ |
| Ethylene | $H_2C{=}CH_2$ | B3LYP/cc-pVQZ; MP2/cc-pVQZ |
| Geraniol | 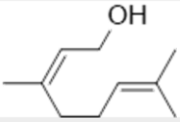 | B3LYP/cc-pVDZ; MP2/cc-pVDZ |
| Limonene | 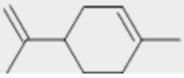 | B3LYP/cc-pVTZ; MP2/cc-pVTZ |
| Isoprene | 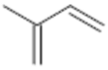 | B3LYP/cc-pVQZ; MP2/cc-pVQZ |
| Methacrolein | 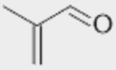 | B3LYP/cc-pVQZ; MP2/cc-pVQZ |
| Myrcene | 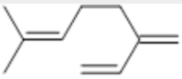 | B3LYP/cc-pVTZ; MP2/cc-pVTZ |
| Natural Gas | $CH_4$ & $H_3C{-}CH_3$ | B3LYP/cc-pVQZ; MP2/cc-pVQZ |
| Propyne |  | B3LYP/cc-pVQZ; MP2/cc-pVQZ |
| Toluene | 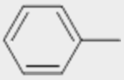 | B3LYP/cc-pVQZ ; MP2/cc-pVTZ |
| t-Butyl hydroperoxide | 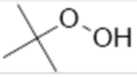 | B3LYP/cc-pVTZ; MP2/cc-pVTZ |

## 2.3 Experimental Procedure

### 2.3.1 Experimental Details

2-methyl-2-butene, acetone, α-pinene, α-pinene oxide, β-pinene, benzene, cyclopropylacetylene, geraniol, isoprene, (R)-limonene, methacrolein, myrcene, 2-propanol, toluene, and t-butyl hydroperoxide were purchased from Sigma Aldrich and underwent at least 3 freeze-pump-thaw (FPT) cycles before use. Acetylene, ethylene, propyne, oxygen, and nitrogen (for atmospheric purging) were all purchased from BOC. Natural gas was taken from a natural-gas line in the laboratory, and milli-Q water from a Milliq Reference Water Purification System. Zero-grade argon (99.999%) from BOC was used as the carrier gas and was further purified by an SGT-B1010-B8 triple filter**.** Pressure in the purification manifold is measured by an MKS baratron capacitance manometer (model number 622A1TBE), with readout on an SRS ion gauge controller (model IGC100). The lines are pumped by an Edwards RV5 pump.

The matrix-isolation system was built in-house. The vacuum chamber and cryo-mount (SHI CH-204SFF-N) are custom engineered and controlled by a Lakeshore 325 temperature controller. The inlet tip is heated by a temperature controller built in-house. The tubing system was built in-house, using ¼-inch stainless-steel and black nylon gas tubing, or thick-walled borosilicate glass tubing. Swagelok connectors, unions, and quarter-turn plug valves were used, with one PTFE union tee and all other connectors stainless steel (316). An iS50R FT-IR spectrometer was used to record data at 0.125 $cm^{-1}$ resolution, and OMNIC 9 software used to analyse data.[24] The gas lines are rough pumped by an Edwards RV5 rotary-vane pump. The vacuum chamber is pumped by a Turbovac SL80 pump with an attached Turbo.Drive TD400 controlled by a Turbocontrol 300. This is backed by a second Edwards RV5 pump. The backing vacuum from the Edwards RV5 was monitored by an Edwards PRM10 Pirani gauge with an Edwards 1101 controller. The chamber pressure was measured by an ion gauge with readout displayed on a Leybold-Heraeus Ionivac IM 210. MDC fine-leak valves (model E-MLV-21), attached in the argon and water lines, are used to set pressures precisely.

### 2.3.2 Matrix-Isolation Spectroscopy

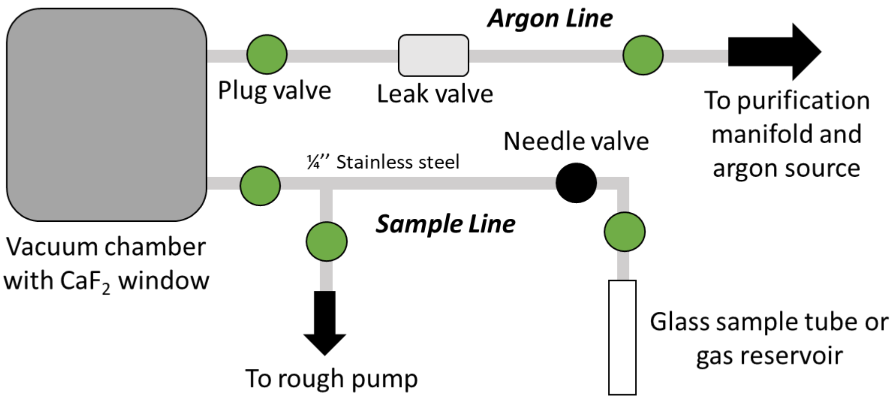

Figure 2.3 Schematic diagram of gas-handling layout for MI setup. The argon and sample lines are separate to avoid sample in the argon line and therefore in the 'baseline' spectrum. Both lines are connected to the vacuum housing such that the gas stream will contact the ~ 20 K $CaF_2$ window to form the matrix.

Experimental spectra were collected for each library molecule using the following procedure and the gas-handling layout as shown in Figure 2.3. For liquid samples, approximately 0.5 – 1 mL was placed in a glass tube, which was then immersed in liquid nitrogen until frozen. The headspace of the glass tube was then evacuated ("rough pumped") by an Edwards RV5 pump, and the sample was then allowed to thaw. This freeze-pump-thaw (FPT) cycle was repeated at least three times to degas the sample. Gas samples did not undergo FPT cycles and were instead connected to the sample line either directly from source or from a prefilled reservoir (Swagelok 304L-HDF4-15000). The pressure of sample vapour and argon was set to achieve a sufficient dilution so as to eliminate, as much as possible, broad absorptions due to guest molecules interacting. The system was then cooled to 20 K and the iS50R MCT detector cooled to 77 K with liquid nitrogen. An atmospheric purge of the IR beam path using $N_2$ was run

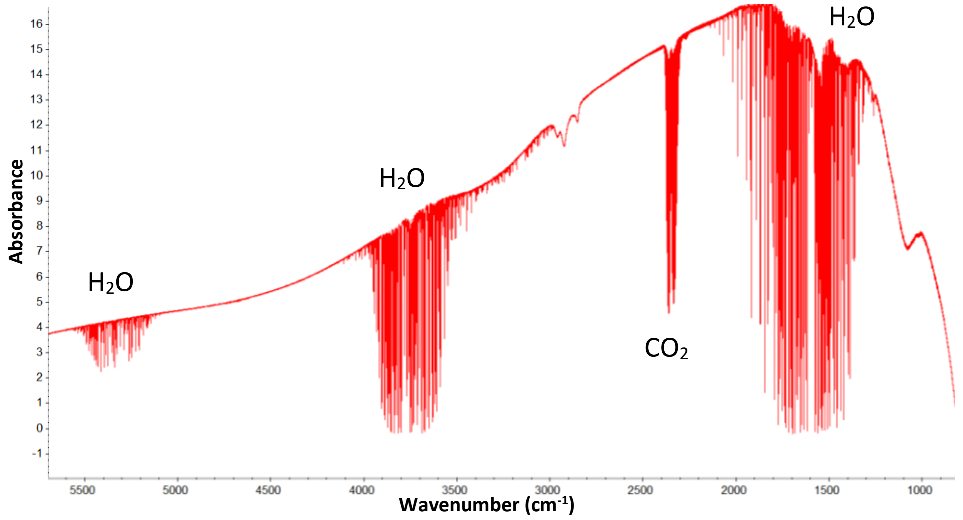

Figure 2.4 Background spectrum of benzene matrix-isolation experiment. This spectrum is automatically subtracted from the collected data to remove any atmospheric background peaks. Peaks from water and $CO_2$ are often still seen in sample spectra but at a much lesser intensity due to the automatic subtraction.

for at least an hour before data collection and remained purging throughout the experiment. Once cooled to 20 K, a single beam background spectrum (example in Figure 2.4) was taken to enable a subtraction of an atmospheric baseline of gases like $H_2O$ and $CO_2$. There is a small drift seen in the background spectrum over time due to equipment limitations. The background spectrum is automatically subtracted from further spectra collected during the experiment.

Argon was then flowed into the cell and allowed to deposit on the $CaF_2$ window for around 5 minutes, during which scans were taken to determine the baseline and what impurities were present (example in Figure 2.5). The sample was then flowed into the cell and allowed to deposit on the 20 K $CaF_2$ window for anywhere between half an hour to two hours, with scans taken periodically (section of an example spectrum in Figure 2.6). This resulted in an optically clear matrix, which was measured without annealing since this would cause the matrix to fracture, losing transmission. However, not annealing may cause issues with site splitting occurring. Site splitting occurs due to conformational differences in how guest molecules are trapped in the matrix, and are included in the 'matrix shift' since it refers to changes to the spectrum from host-guest interactions and so are corrected for by the applied correction functions.

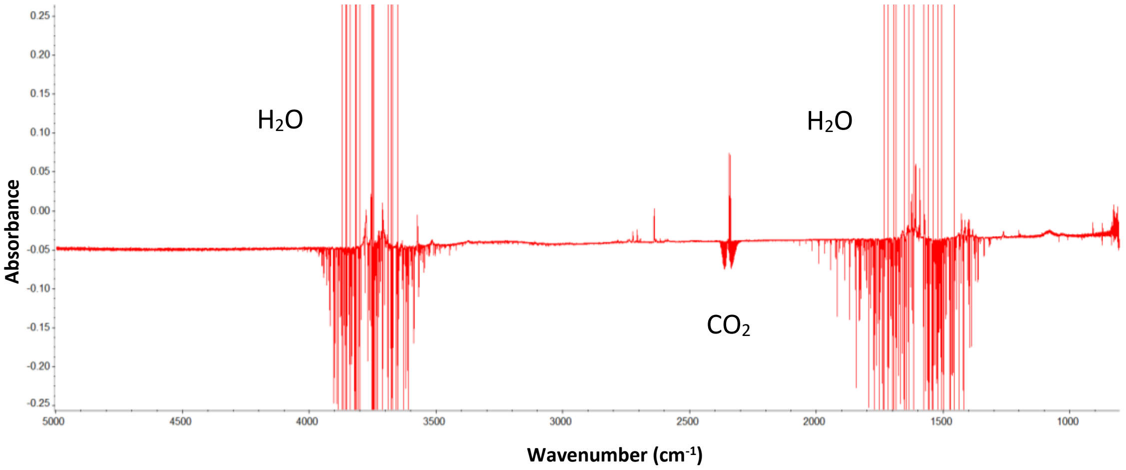

Figure 2.5 Argon baseline for benzene matrix-isolation experiment. Even though an atmospheric baseline is automatically subtracted from the sample spectrum, small changes in the atmospheric background cause the presence of peaks from $CO_2$ and $H_2O$. The presence of these peaks can make it difficult to see sample peaks in these areas. There are also clearly peaks in the argon spectrum that are not from the atmospheric background; these peaks are noted in the sample spectrum and will not be assigned as they were present before the introduction of the sample.

Collected data were analysed by comparing sample spectra taken to the argon "baseline" spectrum to find peaks that appeared after the addition of sample to the system. Any pre-existing peaks in the argon baseline were not assigned to the sample molecule since they were present before any introduction of the sample to the system. The peaks found were then assigned to computational data with anharmonic corrections or literature data (see section 2.4.1

or appendix A for assignments). Sections of annotated spectra for each molecule can be found in appendix A.

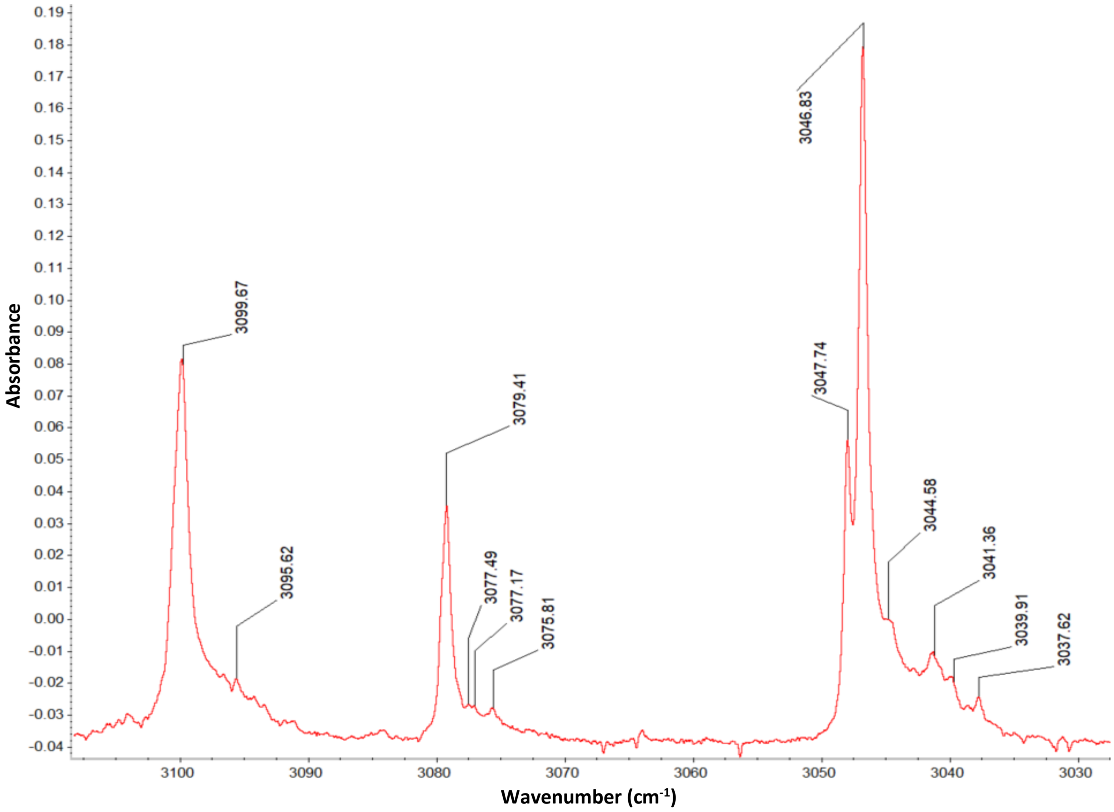

Figure 2.6 Annotated section from ~ 3100 - 3000 $\text{cm}^{-1}$ of the benzene matrix-isolation spectrum. These are a few of the peaks that are seen when the sample is introduced to the system. These peaks are then assigned using a combination of literature and computational data.

The section of the annotated benzene spectrum shown in Figure 2.6 is a good example of the difficulties experienced in assigning spectra. Each of the three intense, sharp peaks have associated less intense shoulder peaks. These shoulder peaks are due to multimer formation, which occurs when there isn't sufficient dilution of sample, and are due to either host-guest or guest-guest interactions.[25] With low dilution, there will be peaks present in the experimental spectrum that aren't in the computed data, along with peaks that are broad due to originating from molecular interactions, which may overlap or obscure other peaks in the area. Additionally, the three intense peaks are subject to Fermi resonance effects, where the peak at ~ 3099 $\text{cm}^{-1}$ is attributed to a fundamental band ($\nu_{20}$), and the other two peaks are combination bands that have mixed with another fundamental (3079 $\text{cm}^{-1}$: $\nu_1 + \nu_6 + \nu_8$; 3046 $\text{cm}^{-1}$: $\nu_8 + \nu_{19}$).[25, 26, 30] Fermi resonance alters the combination peaks' intensity, making the computed intensity inaccurate. This effect contributes to the decision to not use computed intensities when assigning frequencies in this work.

## 2.4 Establishing the Functions

### 2.4.1 Peak Assignments

To create the scaling and correction functions, first the observed experimental peaks in section 2.3.2 were assigned to the corresponding literature vibrational frequency where available, as well as to the corresponding computational frequency from B3LYP and MP2 calculations at the highest converged level of basis set. Every calculated frequency assigned in this work has had anharmonic corrections applied. Tables of assignments for each molecule are found in appendix A, with an example table of assignments given as Table 2.2.

Table 2.2 Table of assigned literature and calculated frequencies to experimental data for benzene. Calculations are anharmonic and at QZ level. Not all calculated or experimental peaks are assigned.

| Literature Wavenumber (cm$^{-1}$)[30] | B3LYP QZ Wavenumber (cm$^{-1}$) | MP2 QZ Wavenumber (cm$^{-1}$) | Experimental | |
|---|---|---|---|---|
| | | | Wavenumber (cm$^{-1}$) | Shape |
| 3103 | | 3086.1 | 3099.7 | Sharp |
| 3080 | | 3079.2 | 3079.4 | Sharp |
| | | 3079.2 | 3077.2 | Sharp, shoulder |
| | | 3079.2 | 3075.8 | Sharp, shoulder |
| 3048 | | | 3046.8 | Sharp |
| 3044 | 3030.3 | 3030.9 | 3037.6 | Medium |
| 1481 | 1487.2 | 1481.1 | 1483.3 | Sharp |
| 1481 | 1487.6 | 1481.2 | 1483.0 | Broad, shoulder |
| | 1186.3 | 1182.0 | 1180.2 | Sharp |
| | | 1182.0 | 1180.2 | Sharp |
| 1178 | 1182.4 | 1156.1 | 1179.5 | Sharp |
| 1038 | | 1042.3 | 1040.7 | Sharp |
| 1038 | | 1042.3 | 1040.7 | Sharp |
| 1010 | | 1030.2 | 1039.1 | Sharp |

Peaks found in the experimental spectra were assigned to calculated or literature peaks based on several factors: whether calculated or literature peaks were expected in the area as well as how many were expected; size and shape of the experimental peak; and how close to the experimental value the calculated or literature data was. More intense peaks were assigned in preference to less intense peaks when present in the same region, since for a peak to become intense it must keep growing throughout the deposition process, a result of continuous sample addition. Computed intensities were not strongly considered when assigning experimental data, as discussed in section 2.2 above, except for any IR inactive bands that were calculated (intensity of 0). Sharp peaks (< 1 cm$^{-1}$ FWHM) were assigned in preference to broad peaks when present in the same region, as broad peaks are usually an indication of intermolecular interactions of multiple sample molecules, usually from inadequate dilution. For example, in regions where peaks were expected but only broad peaks were present, these peaks were assigned. For some samples, only broad peaks were attainable due to difficulty in getting a high dilution of sample.

For every molecule, not every experimentally determined peak was able to be assigned, as some peaks could be from overtone or combination bands, could be from background noise, or could be from other contaminant molecules present in the scan. Additionally, not all calculated or literature peaks could be seen in the experimental data, as peaks were often beyond the detection range of the iS50R MCT detector (below 800 cm$^{-1}$) or were obscured by background absorptions, usually due to atmospheric water.

### 2.4.2 Correction Function

For each molecule in the library, how well the calculated peaks were fit to the corresponding experimental peaks was analysed. Excel was used to fit and graph data. Graphing the corresponding experimental and calculated vibrations for each molecule and applying linear regression analysis gives a trendline with an adjusted $R^2$ between 0.9985 - 1.0000, with the lowest adjusted $R^2$ of 0.9985 for propyne (example graphs are given in Figure 2.6; see appendix B for graphs of the remaining molecules). Table 2.3 gives a list of the $R^2$ and adjusted $R^2$ values for each molecule in the library. Adjusted $R^2$ is used as it provides an indication of fit that is not biased by the number of data points added, as it doesn't increase with added data points like $R^2$ does. Although the trendline is linear it does not indicate a uniform shift in vibrational frequency

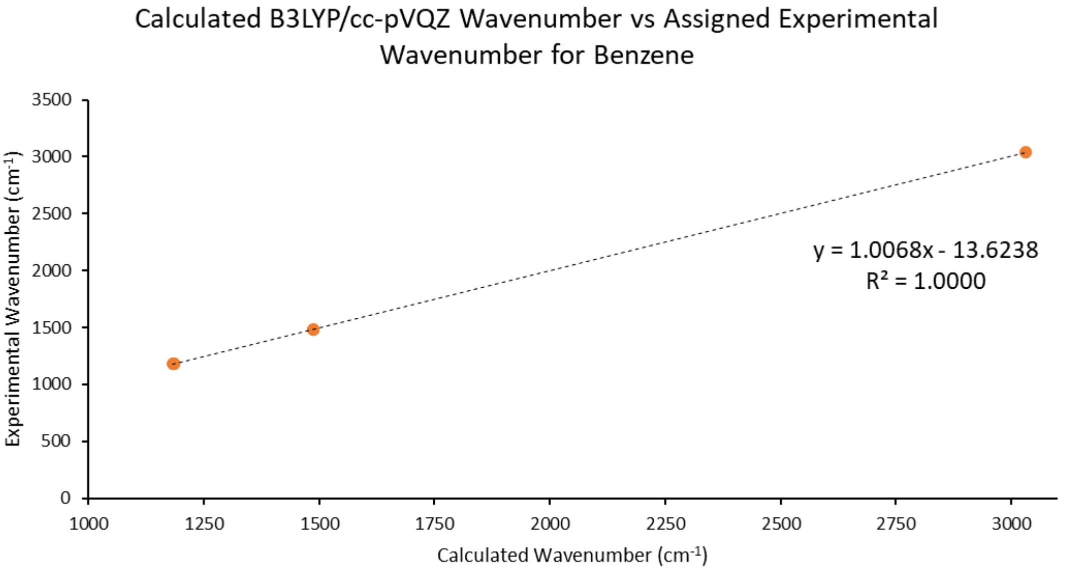

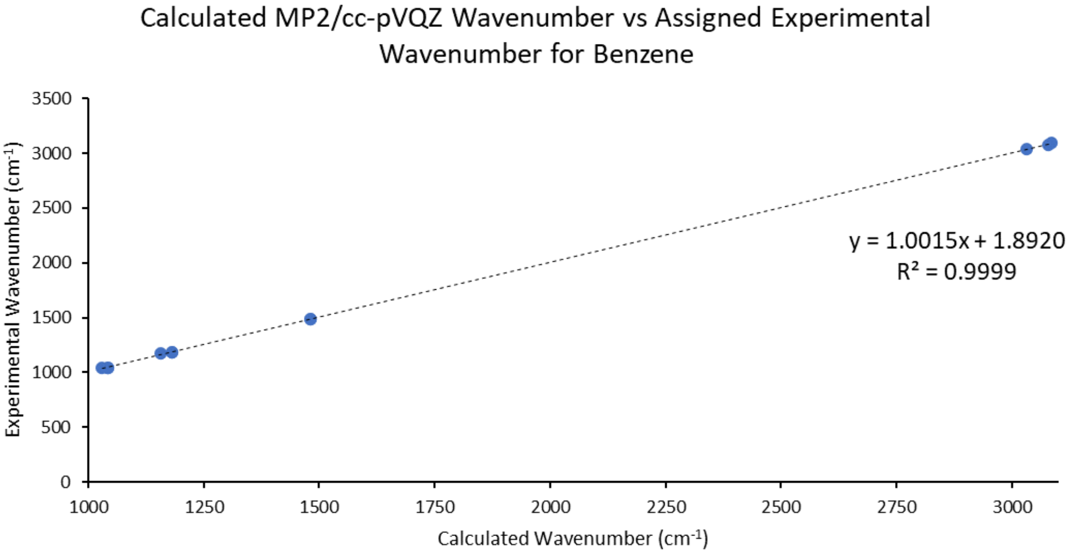

Figure 2.7 Graphs of assigned experimental wavenumber versus calculated wavenumber for benzene. Calculations are done with either B3LYP or MP2 levels of theory, and a cc-pVQZ basis set. Assigned frequencies are given in Table 2.2.

from experimental to calculated value; rather, the small spread and closeness to unity for all molecules indicates consistency in assignment of the spectra, as well as a good match between the experimental and calculated data sets. It allows confident use of the functions created when assigning data in Chapter 3. There is no statistically significant difference between the $R^2$ and adjusted $R^2$ values for B3LYP and MP2 assignments, indicating that the data is not subject to overfitting. The assigned literature data experiences larger differences between $R^2$ and adjusted $R^2$ values, especially for geraniol. However, these differences are still small (in the fourth decimal place excluding geraniol), indicating that the fit is still good. The indicated consistency in assigning peaks gives confidence to the creation of an accurate correction function.

Table 2.3 Table of $R^2$ and adjusted $R^2$ values for plotted graphs of calculated versus assigned experimental wavenumber (graphs in appendix A) for both levels of theory, as well as reference data where available for each molecule. Most $R^2$ values, if not 1.0000, are 0.9990 or higher. This tight spread indicates a consistency in the assignment of calculated to experimental wavenumbers.

| **Molecule** | **B3LYP** | | **MP2** | | **Reference Data** | |
|---|---|---|---|---|---|---|
| | **$R^2$** | **Adjusted $R^2$** | **$R^2$** | **Adjusted $R^2$** | **$R^2$** | **Adjusted $R^2$** |
| 2-methyl-2-butene | 0.9996 | 0.9995 | 0.9993 | 0.9993 | 0.9998 | 0.9997 |
| α-pinene | 0.9999 | 0.9999 | 0.9999 | 0.9999 | | |
| α-pinene oxide | 0.9999 | 0.9999 | 1.0000 | 1.0000 | | |
| β-pinene | 0.9997 | 0.9997 | 1.0000 | 0.9999 | | |
| Benzene | 0.9999 | 0.9999 | 0.9999 | 0.9999 | 0.9999 | 0.9999 |
| Cyclopropylacetylene | 0.9996 | 0.9996 | 0.9996 | 0.9996 | 1.0000 | 0.9999 |
| Ethylene | 1.0000 | 1.0000 | 1.0000 | 1.0000 | 0.9997 | 0.9996 |
| Geraniol | 0.9999 | 0.9999 | 1.0000 | 1.0000 | 0.9926 | 0.9852 |
| Isoprene | 0.9997 | 0.9997 | 0.9999 | 0.9999 | 0.9999 | 0.9999 |
| Limonene | 0.9998 | 0.9998 | 0.9998 | 0.9998 | | |
| Methacrolein AP | 0.9999 | 0.9999 | 0.9999 | 0.9999 | 1.0000 | 1.0000 |
| Methacrolein SP | 0.9989 | 0.9988 | 0.9998 | 0.9998 | 0.9997 | 0.9997 |
| Myrcene | 1.0000 | 1.0000 | 1.0000 | 1.0000 | | |
| Propyne | 0.9997 | 0.9997 | 0.9988 | 0.9985 | 0.9994 | 0.9992 |
| Toluene | 0.9998 | 0.9998 | 0.9998 | 0.9998 | 0.9999 | 0.9999 |
| **Average $R^2$** | 0.9998 | 0.9997 | 0.9998 | 0.9997 | 0.9991 | 0.9983 |
| **Minimum** | 0.9989 | 0.9988 | 0.9988 | 0.9985 | 0.9926 | 0.9852 |

Due to the nature of the data, multiple correction and scaling functions will be found instead of one globally applied function. By analysing the data here in finer detail, functions that are more representative of the actual shifts experienced are found and are therefore more accurate than one globally applied function as is conventionally used. The most accurate and appropriate function will be applied to the work in Chapter 3 to assign spectra.

From the linear relationship established in Figure 2.7, it is assumed that the relationship between the experimental frequencies ($v_i$) and corresponding computational values ($w_i$) determined here is given by the equation of the linear trendline of a plot of $v_i$ vs $w_i$, equation 2.2:

$$v_i = mw_i + c \tag{2.2}$$

where m is the gradient and c is the intercept of the plot.

This relationship allows for a "corrected" computed value (the expected experimental value, $v_i$) to be determined by solving for $v_i$ using the corresponding $w_i$. Plotting all assigned $v_i$ and corresponding $w_i$ by level of theory gives the graph shown in Figure 2.8, with trendline equations 2.3 and 2.4, and no difference between $R^2$ and adjusted $R^2$ values.

$$(B3LYP)\ v_i = 1.0008w_i - 2.7036 \tag{2.3}$$

$$(MP2)\ v_i = 0.9993w_i - 0.0317 \tag{2.4}$$

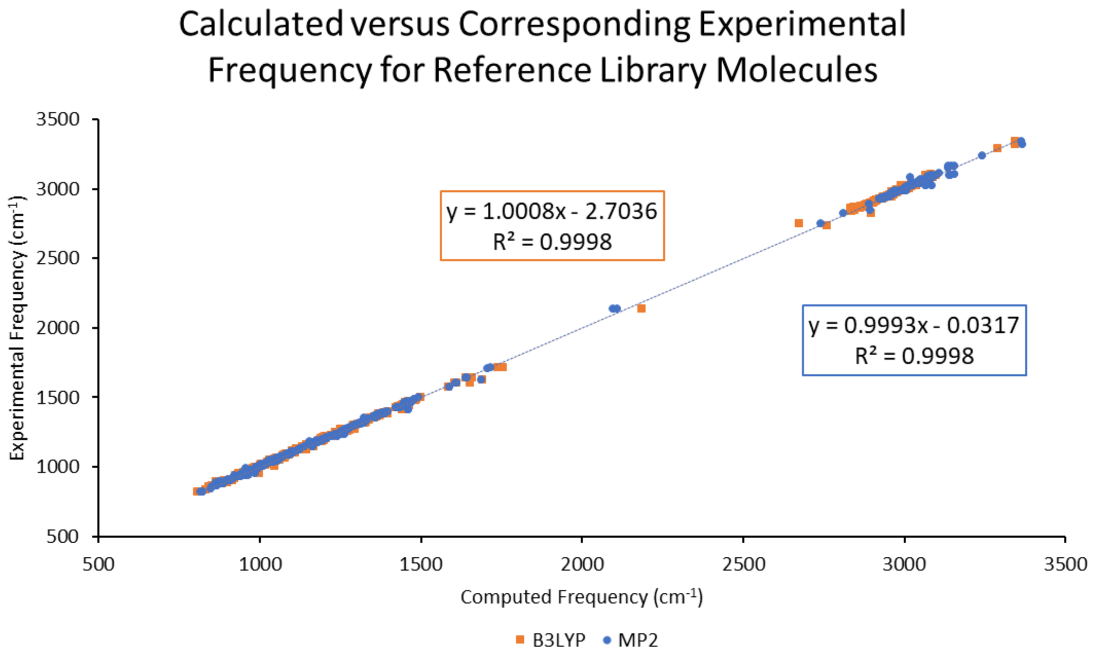

Figure 2.8 Plot of experimental frequency versus corresponding computed value for molecules in the reference library, by level of theory. It is assumed that the relationship between the two values is given by the linear regression trendline.

The data can be analysed in finer detail to give a more accurate correction. In principle, as the basis set increases the accuracy of the calculation should increase, and therefore scaling functions are basis set specific. In practice there is only a slight dependence on basis set choice for correction function.[6]

The data broken down into basis sets are visualised in Figures 2.9, 2.10, and 2.11, and the relationships are given in Table 2.4. B3LYP/QZ level has the greatest offset (intercept value) of ~ 12 cm$^{-1}$, where all other relationships have an offset of ~ 4 cm$^{-1}$ or less. MP2/DZ has a gradient of 1.0000, meaning the only correction applied to that data is the offset given by the intercept of the line. For both levels of theory, the TZ calculation is the closest to unity in terms of gradient. All given relationships are within the ~ 2 % expected offset given in literature (between 0.98 – 1.02 cm$^{-1}$ gradient and ~ 16 – 60 cm$^{-1}$ maximum intercept), and split into basis set are more representative of the data than equations 2.3 and 2.4 as it does not imply a uniform offset across all peaks within a level of theory.[1] There is no difference for any relationship between the R$^2$ and adjusted R$^2$ values, indicating the data is not subject to overfitting. The RMSE is similar between levels of theory with a ~ 2 cm$^{-1}$ difference or less, except for at the cc-pVDZ basis set level, where the MP2 fitted data RMSE is half that of the B3LYP data.

Table 2.4 Linear regression values, adjusted R$^2$, and RMSE for plots of experimental frequency versus corresponding computational value, split into level of basis set.

| **Basis Set Level** | **B3LYP** | | | **MP2** | | |
|---|---|---|---|---|---|---|
| | **Linear Regression Values** | **Adjusted R$^2$** | **RMSE (cm$^{-1}$)** | **Linear Regression Values** | **Adjusted R$^2$** | **RMSE (cm$^{-1}$)** |
| cc-pVDZ | m = 0.9980<br>c = + 2.7536 | 0.9999 | 10.32 | m = 1.0009<br>c = - 0.8873 | 1.0000 | 5.77 |
| cc-pVTZ | m = 1.0017<br>c= - 3.5143 | 0.9998 | 11.77 | m = 1.0000<br>c = - 1.1217 | 0.9998 | 12.53 |
| cc-pVQZ | m = 1.0046<br>c = - 11.7760 | 0.9996 | 17.06 | m = 0.9968<br>c = + 1.6909 | 0.9996 | 18.67 |

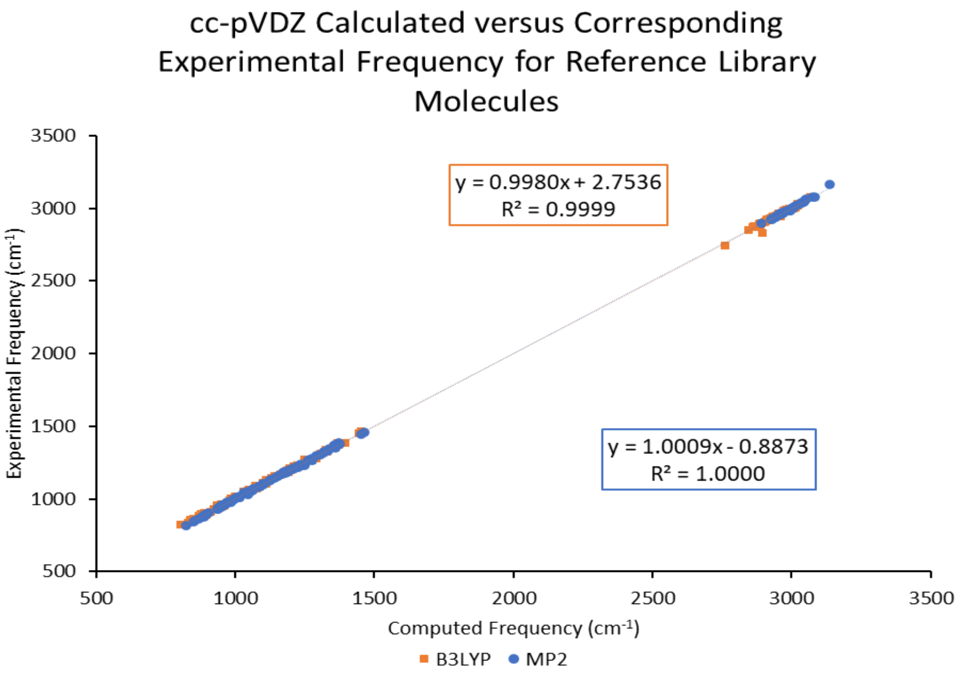

Figure 2.9 Plot of experimental frequency versus corresponding computed value for molecules in the reference library, by level of theory calculated at the cc-pVDZ level. It is assumed that the relationship between the two values is given by the linear regression trendline.

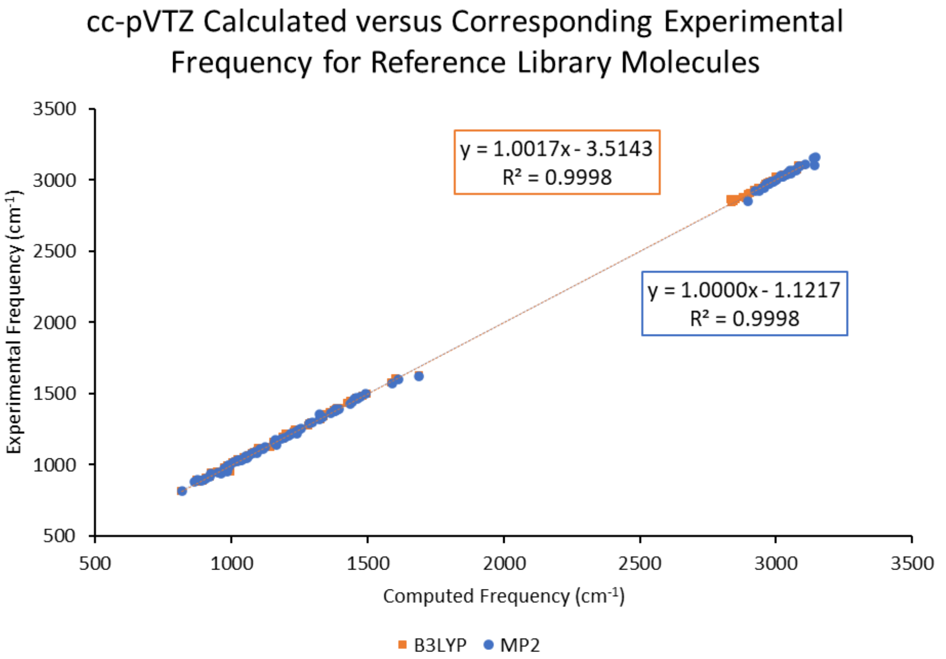

Figure 2.10 Plot of experimental frequency versus corresponding computed value for molecules in the reference library, by level of theory calculated at the cc-pVTZ level. It is assumed that the relationship between the two values is given by the linear regression trendline.

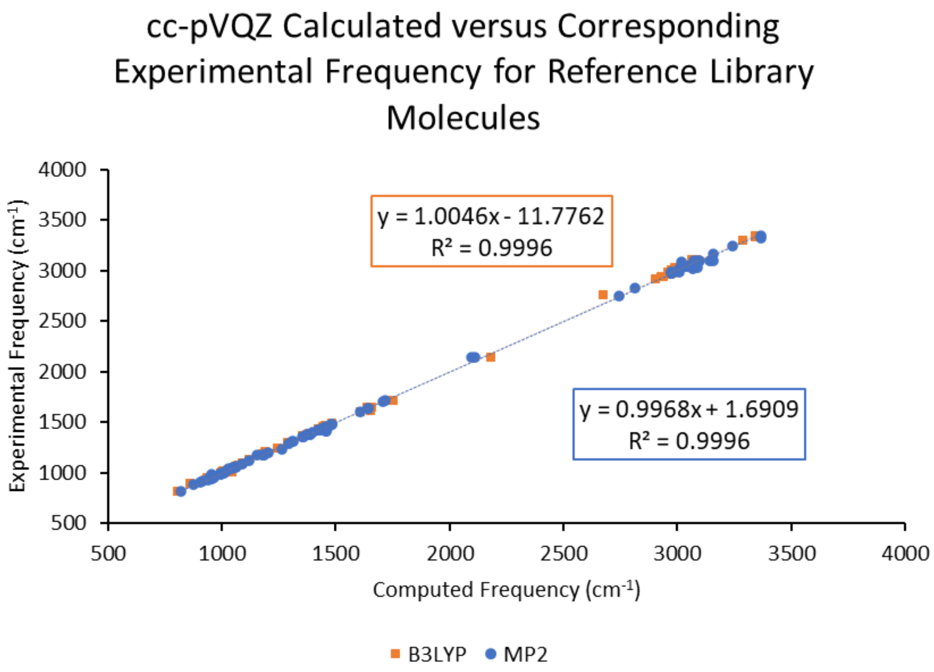

Figure 2.11 Plot of experimental frequency versus corresponding computed value for molecules in the reference library, by level of theory calculated at the cc-pVQZ level. It is assumed that the relationship between the two values is given by the linear regression trendline.

The data can be analysed in further detail by breaking it down into spectral regions. These are the high frequency range ( > 3000 – 2000 $cm^{-1}$), the mid-frequency range (2000 – 1000 $cm^{-1}$), and the low frequency range (1000 – 650 $cm^{-1}$). Applying the correction by spectral region is expected to give more accurate peak assignments within each region, as has been noted by Zapata Trujillo et al.'s (2023) work.[27] The equations for this level of detail are given in Table 2.5 below, and an example graph is given in Figure 2.12 (see appendix B for remaining graphs). There is a large variation in offset, with the smallest being ~ 5 $cm^{-1}$ and the largest ~ 265 $cm^{-1}$. The B3LYP/cc-pVTZ gradients are closest to unity and therefore the closest $w_i$ to corresponding $v_i$, confirmed by both Jacox (2002) and Zapata Trujillo et al. (2023), who found that B3LYP and cc-pVTZ calculations respectively gave computed frequencies closest to corresponding experimental frequencies.[1, 27]

Table 2.5 Linear regression analysis outputs for plots of experimental frequency versus corresponding computational value, split into spectral region by level of basis set.

| Spectral Region ($cm^{-1}$) | cc-pVDZ | | cc-pVTZ | | cc-pVQZ | |
|---|---|---|---|---|---|---|
| | B3LYP | MP2 | B3LYP | MP2 | B3LYP | MP2 |
| > 3000 - 2000 | m = 0.9181<br>c = + 242.85 | m = 0.9466<br>c = + 158.34 | m = 1.0008<br>c = - 4.5836 | m = 0.9123<br>c = + 264.92 | m = 0.9821<br>c = + 50.07 | m = 1.0468<br>c = - 134.38 |
| 2000 - 1000 | m = 1.0131<br>c = - 15.124 | m = 0.9938<br>c = + 6.1157 | m = 1.0210<br>c = - 24.891 | m = 1.0145<br>c = - 16.383 | m = 1.0191<br>c = - 17.039 | m = 1.0092<br>c = - 8.2015 |
| 1000 - 650 | m = 1.0040<br>c = - 5.9751 | m = 0.9645<br>c = + 35.386 | m = 1.0174<br>c = - 12.710 | m = 1.0480<br>c = - 44.057 | m = 1.0968<br>c = - 90.306 | m = 0.9603<br>c = + 39.419 |

Table 2.6 gives the RMSE for the assignments broken down into spectral region, alongside the overall RMSE that was given in Table 2.4. For B3LYP assignments and MP2/cc-pVQZ assignments, the RMSE has a significant variation between spectral regions, increasing in size as basis set level increases. However, the overall RMSE is not significantly different to the largest RMSE by spectral region ( less than ~ 3 cm$^{-1}$ with the exception of MP2/cc-pVQZ data), indicating that the accuracy improvement that can be achieved in each spectral region by assigning multiple factors is not worth the effort or time it takes to do so.

Table 2.6 RMSE for plots of experimental frequency versus corresponding computational value, split into spectral region by level of basis set. The overall RMSE for each basis set by level of theory is given for comparison (data from Table 2.4).

| Spectral Region (cm$^{-1}$) | cc-pVDZ RMSE (cm$^{-1}$) | | cc-pVTZ RMSE (cm$^{-1}$) | | cc-pVQZ RMSE (cm$^{-1}$) | |
|---|---|---|---|---|---|---|
| | **B3LYP** | **MP2** | **B3LYP** | **MP2** | **B3LYP** | **MP2** |
| > 3000 - 2000 | 12.772 | 5.835 | 9.054 | 12.802 | 20.903 | 27.641 |
| 2000 - 1000 | 8.793 | 6.021 | 12.324 | 12.000 | 15.725 | 11.933 |
| 1000 - 650 | 8.868 | 4.952 | 14.893 | 13.469 | 9.360 | 12.776 |
| Overall | 10.32 | 5.77 | 11.77 | 12.53 | 17.06 | 18.67 |

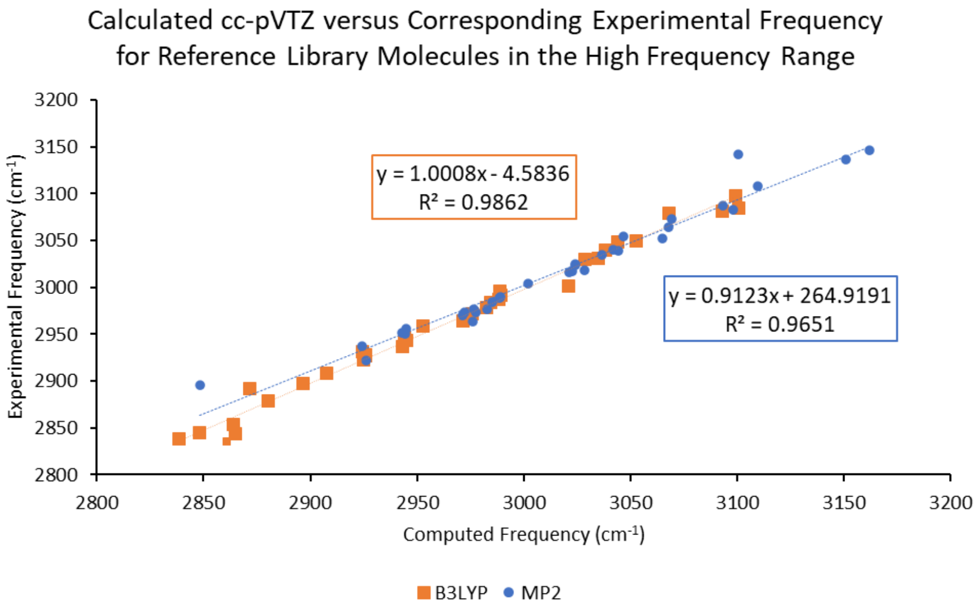

Figure 2.12 Plot of experimental frequency versus corresponding computed value in the high frequency range for molecules in the reference libray, by level of theory calculated at the cc-pVTZ level.

### 2.4.3 Scaling Factor

A scaling factor for each molecule in the reference library was also calculated using equation 2.1:

$$s = \frac{\Sigma(v_i * w_i)}{\Sigma(w_i^2)} \tag{2.1}$$

where s is the scaling factor, $v_i$ is the experimental vibration and $w_i$ is the computed vibration.[19, 27, 28] Assigned frequencies that have a ratio of experimental frequency over calculated frequency outside of the range 0.85 - 1.1 have been excluded from the calculation to give the same conditions as reference factors, specifically from the CCCBDB.[19] Table 2.6 below gives the calculated scaling factors for each molecule; here, the literature column refers to the scaling factor calculated using the literature values as $w_i$ in equation 2.1.

Table 2.7 Table of calculated scaling factors for each molecule in the reference library. Here, "literature" refers to the scaling factor calculated using the literature data assigned in section 2.4.1.

| Molecule | Basis Set | Scale Factor | | |
|---|---|---|---|---|
| | | Literature | B3LYP | MP2 |
| 2-methyl-2-butene | TZ | 0.9982 | 0.9982 | 0.9972 |
| α-pinene | DZ | | 1.0001 | 1.0007 |
| α-pinene oxide | DZ | | 0.9991 | 1.0007 |
| acetylene | QZ | 0.9999 | 0.9993 | 0.9985 |
| β-pinene | DZ | | 0.9985 | 1.0003 |
| Benzene | QZ | 1.0035 | 0.9999 | 1.0024 |
| Cyclopropylacetylene | QZ | 0.9964 | 1.0015 | 0.9899 |
| Ethylene | QZ | 1.0031 | 1.0023 | 1.0084 |
| Geraniol | DZ | 1.0042 | 0.9992 | 0.9993 |
| Limonene | TZ | | 1.0002 | 0.9972 |
| Isoprene | QZ | 0.9994 | 0.9978 | 0.9997 |
| Methacrolein (AP) | QZ | 0.9987 | 0.9981 | 0.9984 |
| Methacrolein (SP) | QZ | 0.9994 | 1.0011 | 0.9984 |
| Myrcene | TZ | | 1.0010 | 1.0010 |
| Propyne | QZ | 0.9960 | 0.9963 | 0.9927 |
| Toluene | TZ | 1.0012 | 0.9997 | 1.0014 |

The scaling factors calculated here are given to 4dp as is conventional in literature.[28] Interestingly, they are all very close to unity, with the MP2 scaling factor for cyclopropylacetylene the furthest from unity and the B3LYP scaling factor for benzene the closest to unity. Table 2.7 gives scaling factors calculated using reference data (and the scale factor calculator tool) from the CCCBDB.[19] For the 15 molecules above, only 5 molecules had available data for calculation. These reference scaling factors are all further from unity than the factors calculated in this work. This could be due to the experimental vibrations coming from gas-phase IR data, which would indicate that calculated vibrations are closer to matrix-phase than gas-phase experimental data. This seems reasonable since the calculations are run on a singular molecule at 0 K, making conditions closer to matrix-phase than experimental gas-phase conditions; however, the reference data will have been corrected to account for this difference. The reference scaling factor is further from unity for the MP2 calculations than the B3LYP calculations, which is reflected in the scaling factors calculated in this work.

Table 2.8 Scaling factors calculated in this work for B3LYP and MP2 levels of theory with scaling factors calculated using the CCCBDB data.[29] Note only TZ level calculations for isoprene were available in the CCCBDB; all other reference scale factors were calculated using QZ level data, in line with those calculated in this work.

| Molecule | Scale Factor | | Reference Scale Factor[29] | |
|---|---|---|---|---|
| | B3LYP | MP2 | B3LYP | MP2 |
| Acetylene | 0.9993 | 0.9985 | 0.9606 ± 0.0047 | 0.9621 ± 0.0160 |
| Benzene | 0.9999 | 1.0024 | 0.9683 ± 0.0084 | 0.9580 ± 0.0213 |
| Ethylene | 1.0023 | 1.0084 | 0.9641 ± 0.0060 | 0.9491 ± 0.0125 |
| Isoprene | 0.9978 | 0.9997 | 0.9616 ± 0.0154 | 0.9494 ± 0.0187 |
| Propyne | 0.9963 | 0.9927 | 0.9672 ± 0.0097 | 0.9581 ± 0.0148 |

The scaling factor has also been calculated by level of basis set and spectral region, as was done previously for the correction function in section 2.4.2. The data for the scaling factor calculated by basis set are given in Table 2.8 below. Again, these values are all very close to unity. Interestingly, the scaling factors indicate that the TZ data for B3LYP are the closest fit to experimental data across the three methods used here, with the DZ and QZ B3LYP data fitting exactly the same. Zapata Trujillo et al. (2023) found that TZ level calculations employed in their study gave the lowest basis set incompleteness error, meaning TZ level calculations will be approximating closest to experimental data and therefore should fit the best.[27] There is little variation across the calculated scaling factors, indicating the use of a global scaling factor across a level of theory is reasonably accurate compared to using a scaling factor for each level of basis set as well. There is a stronger basis set dependence displayed in the MP2 scaling factors, as

Table 2.9 Table of scaling factor calculated by basis set, using the data from all molecules in the reference library, along with reference scaling factors, calculated using data from the CCCBDB (reference 1) and Sinha et al. (2004) (reference 2).[28, 29] Here, "literature" refers to the scaling factor calculated using the literature data assigned in section 2.4.1.

| Basis Set | Scale Factor | | | Reference 1[29] | | Reference 2[28] | |
|---|---|---|---|---|---|---|---|
| | Literature | B3LYP | MP2 | B3LYP | MP2 | B3LYP | MP2 |
| cc-pVDZ | 1.0042 | 0.9993 | 1.0004 | 0.970 ± 0.025 | 0.953 ± 0.028 | 0.9709 | 0.9543 |
| cc-pVTZ | 1.0004 | 1.0001 | 0.9994 | 0.967 ± 0.018 | 0.950 ± 0.072 | 0.9691 | 0.9575 |
| cc-pVQZ | 0.9992 | 0.9993 | 0.9975 | 0.969 ± 0.021 | 0.948 ± 0.030 | 0.9751 | 0.9624 |

noted by Irikura et al. (2005).[6] In comparison to the two literature sources of scaling factors, the functions calculated in this work are much closer to unity. Again, this is likely due to the use of gas-phase IR data used to calculate the reference scaling factors.

The scaling factor has also been calculated by spectral region and level of basis set for each method of theory, given in Table 2.9. Again, there is little variation across the calculated scaling factors, with the factors also very close to unity. There is no real trend evident bar the general and slight decrease from unity seen for the MP2 scaling factors as basis set increases, which would be expected to increase instead. Generally, the furthest scaling factor from unity is that for the mid-range and the closest to unity is that for the high range. The mid-range is influenced by the lower number of data points assigned and significant difficulty in assigning within regions of significant atmospheric water interference.

Table 2.10 Table of calculated scaling factor by spectral region and basis set level.

| Spectral Region ($cm^{-1}$) | cc-pVDZ | | cc-pVTZ | | cc-pVQZ | |
|---|---|---|---|---|---|---|
| | B3LYP | MP2 | B3LYP | MP2 | B3LYP | MP2 |
| 3250 - 2000 | 0.9990 | 1.0004 | 1.0007 | 0.9998 | 1.0013 | 0.9977 |
| 2000 - 1000 | 0.9990 | 1.0011 | 0.9979 | 0.9982 | 0.9933 | 0.9969 |
| 1000 - 650 | 1.0024 | 0.9973 | 0.9968 | 0.9977 | 0.9975 | 0.9978 |

Comparisons between the scaling factors calculated in this work to those in the work of Zapata Trujillo et al. (2023) are given in Table 2.10 for DZ and TZ level, as no QZ data was available in Zapata Trujillo et al.’s work. Again, the scaling factors calculated in this work are much closer to unity than the reference scaling factors. Interestingly, scaling factors furthest from unity for Zapata Trujillo et al.’s work are in the high range, and the scaling factors closest to unity are the low range. This could be due to a different set of molecules used to create the scaling factor between the two sets of work. Depending on the types of molecules used, there may be a greater number of points in the low and mid-range in Zapata Trujillo et al.’s work compared to the reference library created here. Zapata Trujillo et al.’s work uses a library of 141 molecules that vary more in type and in atoms involved than the library collated here. Both data sets find

Table 2.11 Table of scale factors (SF) by spectral region calculated in this work and in the work of Zapata Trujillo et al. (2023) for each B3LYP and MP2 levels of theory at cc-pVDZ and cc-pVTZ basis sets.[27]

| Spectral Region ($cm^{-1}$) | Calculated SF cc-pVDZ | | Reference SF cc-pVDZ[27] | | Calculated SF cc-pVTZ | | Reference SF cc-pVTZ[27] | |
|---|---|---|---|---|---|---|---|---|
| | B3LYP | MP2 | B3LYP | MP2 | B3LYP | MP2 | B3LYP | MP2 |
| 3250 - 2000 | 0.9990 | 1.0004 | 0.9622 | 0.9446 | 1.0007 | 0.9998 | 0.9634 | 0.9420 |
| 2000 - 1000 | 0.9990 | 1.0011 | 0.9829 | 0.9742 | 0.9979 | 0.9982 | 0.9747 | 0.9712 |
| 1000 - 650 | 1.0024 | 0.9973 | 0.9963 | 0.9938 | 0.9968 | 0.9977 | 0.9927 | 0.9841 |

that B3LYP calculations are closer to experimental data than MP2 calculations, with the scaling factors found for B3LYP generally closer to unity than for MP2.

### 2.4.4 Comparison of Functions

To determine which of the functions created above is most appropriate for use, MI-FTIR data for acetone and 2-propanol was collected and the peaks found assigned to calculated vibrational frequencies using both the correction and scaling functions determined above. The computed frequencies were also transformed using a literature factor from Sinha et al.'s (2004) work.[28] Acetone and 2-propanol were used as they were not included in the reference library already, were readily available materials, and are already characterized in literature with simple spectra, with some matrix phase data available for comparison.[32,33]

To transform the raw computed values, equation 2.5 is applied when using the correction function, and equation 2.6 is applied when using either the scaling factor or the literature scaling factor:

$$w_{corr} = m * w_i + c \tag{2.5}$$

$$w_{corr} = w_i * s \tag{2.6}$$

where $w_{corr}$ is the corrected computed frequency, $w_i$ is the raw computed value, s is the scaling or literature factor, and m and c are the gradient and intercept of the correction function relationship determined in section 2.4.2. The functions found in this work are specific to level of theory and basis set (in this case using the cc-pVQZ basis set) and are applied by spectral region. The literature factor is applied globally (i.e. not by spectral region but overall). The functions used are given in Table 2.12 below.

Table 2.12 Correction function, and scaling and literature factors used to transform raw computed frequencies for assigning experimental spectra of acetone and 2-propanol. The scaling and literature factors are multiplicative, and the correction function is applied as an equation. Literature factors are from Sinha et al.'s (2004) work.[28]

| **Spectral Region ($cm^{-1}$)** | **Correction Function** | | **Scaling Factor** | | **Literature Factor[28]** | |
|---|---|---|---|---|---|---|
| | **B3LYP** | **MP2** | **B3LYP** | **MP2** | **B3LYP** | **MP2** |
| > 3000 - 2000 | y = 0.9821x + 50.0700 | y = 1.0468x - 134.3800 | 1.0013 | 0.9977 | 0.9751 | 0.9624 |
| 2000 - 1000 | y = 1.0191x - 17.0390 | y = 1.0092x - 8.2015 | 0.9933 | 0.9969 | | |
| < 1000 | y = 1.0968x - 90.3060 | y = 0.9603x + 39.4190 | 0.9975 | 0.9978 | | |

Tables 2.13 and 2.14 give the $R^2$ and adjusted $R^2$ for the assignments of computed ($w_i$) and experimental frequencies ($v_i$) for acetone and 2-propanol. For the 2-propanol assignments, there is no significant difference between the $R^2$ and adjusted $R^2$ values, indicating the data have not been overfit. For the acetone assignments, there is no significant difference between the $R^2$

and adjusted $R^2$ values for MP2 data. For B3LYP assignments, there is a 0.0001 difference for the correction function data and a 0.0007 for then literature factor data. These differences are insignificant, indicating a good fit. Tables 2.15 and 2.16 give the RMSE for the acetone and 2-propanol assignments. The data are visualised in Figures 2.12 and 2.13. For acetone assignments, the computed data corrected by the correction function has the lowest RMSE for both B3LYP and MP2 data. For the B3LYP assignments, the correction function RMSE is lower than the scaling and literature factor RMSE by ~ 8 $cm^{-1}$. For the MP2 assignments, the difference is ~ 24 $cm^{-1}$, which is a significant difference. For 2-propanol, the lowest RMSE is different depending on the computed data that has been corrected. For B3LYP assignments, the literature factor has the lowest RMSE by ~ 8 $cm^{-1}$; for MP2 assignments, the correction function has the lowest RMSE by ~ 7 $cm^{-1}$; and for the literature data assignments, the scaling factor has the lowest RMSE by ~ 1 $cm^{-1}$. Overall, data assigned using the correction function gives a lower RMSE and therefore gives a better fit to experimental data.

Table 2.13 $R^2$ and adjusted $R^2$ values for the assigned experimental and corresponding cc-pVQZ computed values for acetone.

| Function Applied | B3LYP | | MP2 | |
|---|---|---|---|---|
| | $R^2$ | Adjusted $R^2$ | $R^2$ | Adjusted $R^2$ |
| Literature Factor | 0.9983 | 0.9977 | 0.9998 | 0.9998 |
| Scale Factor | 0.9998 | 0.9998 | 0.9999 | 0.9999 |
| Correction Function | 0.9998 | 0.9997 | 0.9999 | 0.9999 |

Table 2.14 $R^2$ and adjusted $R^2$ values for the assigned experimental and corresponding cc-pVQZ computed values for 2-propanol.

| Function Applied | B3LYP | | MP2 | | Literature | |
|---|---|---|---|---|---|---|
| | $R^2$ | Adjusted $R^2$ | $R^2$ | Adjusted $R^2$ | $R^2$ | Adjusted $R^2$ |
| Literature Factor | 1.0000 | 1.0000 | 0.9998 | 0.9998 | 0.9998 | 0.9998 |
| Scale Factor | 0.9999 | 0.9999 | 0.9999 | 0.9999 | 0.9999 | 0.9999 |
| Correction Function | 0.9999 | 0.9999 | 0.9999 | 0.9999 | 0.9998 | 0.9998 |

Table 2.15 RMSE error for the assigned experimental and corresponding cc-pVQZ computed values for acetone.

| Function Applied | B3LYP RMSE ($cm^{-1}$) | MP2 RMSE ($cm^{-1}$) |
|---|---|---|
| Literature Factor | 19.2513 | 30.7166 |
| Scale Factor | 13.9603 | 8.0283 |
| Correction Function | 11.6589 | 6.5831 |
| Lowest RMSE | Correction Function | Correction Function |

Table 2.16 RMSE error for the assigned experimental and corresponding cc-pVQZ computed values for 2-propanol.

| Function Applied | B3LYP RMSE (cm$^{-1}$) | MP2 RMSE (cm$^{-1}$) | Literature RMSE (cm$^{-1}$) |
|---|---|---|---|
| Literature Factor | 4.2047 | 12.9458 | 7.9968 |
| Scale Factor | 12.5801 | 10.4958 | 6.7158 |
| Correction Function | 9.5170 | 6.0489 | 7.9968 |
| Lowest RMSE | Literature Factor | Correction Function | Scale Factor |

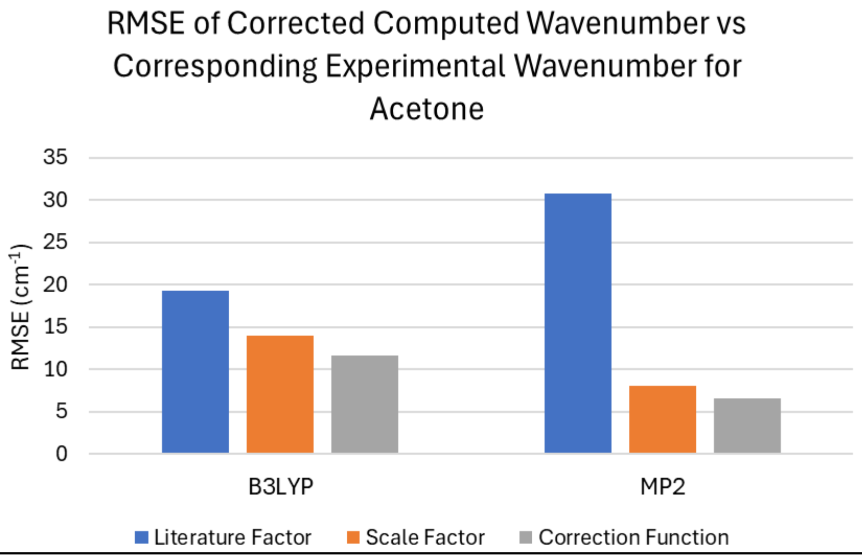

Figure 2.13 RMSE between the corrected computed wavenumbers and the corresponding assigned experimental wavenumbers for acetone. The corrections applied are the correction and scaling factors calculated in this work, and the literature factors given by Sinha et al. (2004).[28] The assignments are split into B3LYP and MP2 levels of theory and are calculated using the cc-pVQZ basis set.

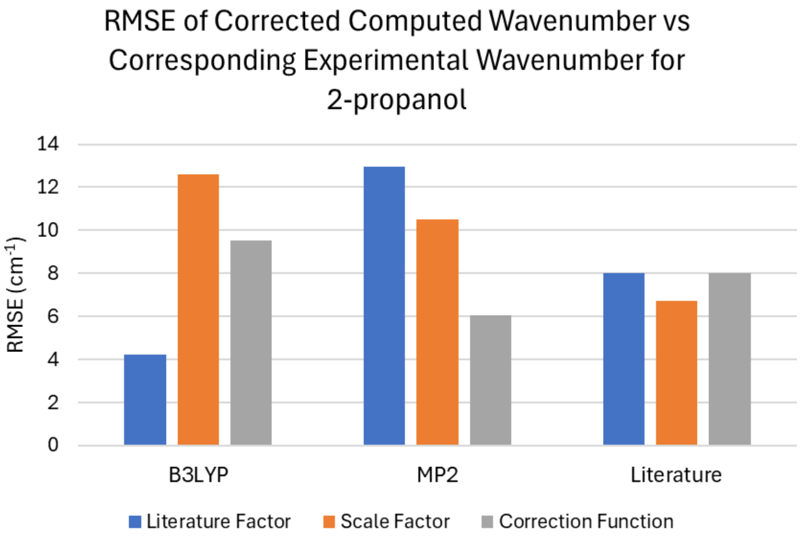

Figure 2.14 RMSE between the corrected computed wavenumbers and the corresponding assigned experimental wavenumbers for 2-propanol. The corrections applied are the correction and scaling factors calculated in this work, and the literature factors given by Sinha et al. (2004).[28] The wavenumbers are calculated using the cc-pVQZ basis set.

Zapato Trujillo et al. (2023) found that applying a general scaling factor gave worse agreement than applying a factor by spectral region.[27] Roy et al. (2014) found that for low frequencies, both B3LYP and MP2 calculations underestimated values, whereas for high frequencies, MP2 overestimates and B3LYP underestimates them, which correlates with the improved agreement by spectral region.[14] Application of a correction function by spectral region is more feasible for small datasets like those used in this work, which is why conventionally a global scaling factor is applied. For this work, the functions used in the following chapter are applied by spectral region as it gives more insight into the potential differences between the calculated and experimental data and is not an infeasible task due to the small number of molecules and calculated vibrations. However, were the data set used in this work to be any bigger, a general function applied not by spectral region but by level of theory and basis set only would be more appropriate.

Overall, the correction function determined in this work gave lower RMSE when used to assigned corrected computed frequencies to experimental frequencies, compared to data corrected by a literature factor and by the scaling factor determined in this work. The correction function will be used to correct the computed frequencies in Chapter 3 before analysing reaction spectra.

## 2.5 Conclusion

To begin the process of determining the effectiveness of $TiO_2$ as a catalyst for ·OH formation, MI-FTIR correction and scaling functions were determined by assigning experimental and computed frequencies using a library of collected spectra of atmospherically important molecules. The correction and scaling functions were developed to correct the known offset observed in matrix-isolation (MI) systems compared to literature data so that experimental results for radical formation and reaction products could be assigned with confidence and ease in the research carried out in Chapter 3. It was determined that applying the correction function by level of basis set and by spectral region was the most appropriate and accurate use of the functions created above, as applying the functions by spectral region gave more accurate results than the conventional 'blanket' application of one singular function.

## 2.6 References

1. Jacox, M. E., The spectroscopy of molecular reaction intermediates trapped in the solid rare gases. *Chem Soc Rev* **2002,** *31* (2), 108-15.

2. Rice-Evans, C. A.; Diplock, A. T.; Symons, M. C. R., The detection and characterization of free radical species. In *Laboratory Techniques in Biochemistry and Molecular Biology*, Rice-Evans, C. A.; Diplock, A. T.; Symons, M. C. R., Eds. Elsevier: 1991; Vol. 22, pp 51-100.

3. Bahrini, C.; Parker, A.; Schoemaecker, C., et al., Direct detection of $HO_2$ radicals in the vicinity of TiO2 photocatalytic surfaces using cw-CRDS. *Appl. Catal. B.* **2010,** *99* (3), 413-419.

4. Vincent, G.; Aluculesei, A.; Parker, A., et al., Direct detection of OH radicals and indirect detection of $H_2O_2$ molecules in the gas phase near a $TiO_2$ photocatalyst using LIF. *J. Phys. Chem. C* **2008,** *112* (25), 9115-9119.

5. Mitra, H.; Roy, T. K., Comprehensive Benchmark Results for the Accuracy of Basis Sets for Anharmonic Molecular Vibrations. *J. Phys. Chem. A.* **2020,** *124* (44), 9203-9221.

6. Irikura, K. K.; Johnson, R. D.; Kacker, R. N., Uncertainties in Scaling Factors for ab Initio Vibrational Frequencies. *J. Phys. Chem. A.* **2005,** *109* (37), 8430-8437.

7. Thomas, J. R.; DeLeeuw, B. J.; Vacek, G., et al., The balance between theoretical method and basis set quality: A systematic study of equilibrium geometries, dipole moments, harmonic vibrational frequencies, and infrared intensities. *J. Chem. Phys.* **1993,** *99* (1), 403-416.

8. Frisch, M. J.; Trucks, G. W.; Schlegel, H. B., et al. *Gaussian 16, Revision A.03*, Gaussian, Inc.: Wallingford, CT, USA, 2016.

9. Galabov, B.; Yamaguchi, Y.; Remington, R. B., et al., High Level ab Initio Quantum Mechanical Predictions of Infrared Intensities. *J. Phys. Chem. A.* **2002,** *106* (5), 819-832.

10. Dennington, R.; Keith, T.; Millam, J. *GaussView, Version 6.1.1*, Semichem Inc.: Shawnee Mission, KS, USA, 2019.

11. Møller, C.; Plesset, M. S., Note on an Approximation Treatment for Many-Electron Systems. *Phys. Rev.* **1934,** *46* (7), 618-622.

12. Becke, A. D., Density-functional thermochemistry. III. The role of exact exchange. *J. Chem. Phys.* **1993,** *98* (7), 5648-5652.

13. Lee, C.; Yang, W.; Parr, R. G., Development of the Colle-Salvetti correlation-energy formula into a functional of the electron density. *Phys. Rev. B.* **1988,** *37* (2), 785-789.

14. Roy, T. K.; Carrington, T., Jr.; Gerber, R. B., Approximate first-principles anharmonic calculations of polyatomic spectra using MP2 and B3LYP potentials: comparisons with experiment. *J Phys Chem A* **2014,** *118* (33), 6730-9.

15. Dunning, T. H., Jr., Gaussian basis sets for use in correlated molecular calculations. I. The atoms boron through neon and hydrogen. *J. Chem. Phys.* **1989,** *90* (2), 1007-1023.

16. Woon, D. E.; Dunning, T. H., Jr., Gaussian basis sets for use in correlated molecular calculations. III. The atoms aluminum through argon. *J. Chem. Phys.* **1993,** *98* (2), 1358-1371.

17. Hill, J. G., Gaussian basis sets for molecular applications. *Int. J. Quantum Chem.* **2013,** *113* (1), 21-34.

18. Jacobsen, R. L.; Johnson, R. D.; Irikura, K. K., et al., Anharmonic Vibrational Frequency Calculations Are Not Worthwhile for Small Basis Sets. *J. Chem. Theory Comput.* **2013,** *9* (2), 951-954.

19. National Institute of Standards and Technology Vibrational Scaling Factors. https://cccbdb.nist.gov/vibnotesx.asp (accessed 21/8/23).

20. Fehsenfeld, F.; Calvert, J.; Fall, R., et al., Emissions of volatile organic compounds from vegetation and the implications for atmospheric chemistry. *Global Biogeochem. Cy.* **1992,** *6* (4), 389-430.

21. Guenther, A.; Hewitt, C. N.; Erickson, D., et al., A Global-Model of Natural Volatile Organic-Compound Emissions. *J. Geophys. Res. Atmos.* **1995,** *100* (D5), 8873-8892.

22. Berndt, T.; Hyttinen, N.; Herrmann, H., et al., First oxidation products from the reaction of hydroxyl radicals with isoprene for pristine environmental conditions. *Commun. Chem.* **2019,** *2* (1).

23. Campuzano-Jost, P.; Williams, M. B.; O'Ottone, L., et al., Kinetics of the OH-initiated oxidation of isoprene. *Geophys. Res. Lett.* **2000,** *27* (5), 693-696.

24. Thermo Scientific *OMNIC*, Thermo Electron Corporation.

25. Kim, H. S.; Kim, K., Infrared Spectra of Benzene in Solid Argon. *Spectrosc. Lett.* **1996,** *29* (4), 667-675.

26. Snavely, D. L.; Walters, V. A.; Colson, S. D., et al., FTIR spectrum of benzene in a supersonic expansion. *Chem. Phys. Lett.* **1984,** *103* (5), 423-429.

27. Zapata Trujillo, J. C.; McKemmish, L. K. Model Chemistry Recommendations for Scaled Harmonic Frequency Calculations: A Benchmark Study 2023, p. arXiv:2302.04448. https://ui.adsabs.harvard.edu/abs/2023arXiv230204448Z (accessed February 01, 2023).

28. Sinha, P.; Boesch, S. E.; Gu, C., et al., Harmonic Vibrational Frequencies: Scaling Factors for HF, B3LYP, and MP2 Methods in Combination with Correlation Consistent Basis Sets. *J. Phys. Chem. A.* **2004,** *108* (42), 9213-9217.

29. Johnson, R. D. NIST Computational Chemistry Comparison and Benchmark Database, NIST Standard Reference Database Number 101. http://cccbdb.nist.gov/.

30. Brown, K. G.; Person, W. B., Infrared spectrum of benzene isolated in argon and krypton matrices. *Spectrochimica Acta Part A: Molecular Spectroscopy* **1978,** *34* (2), 117-122.

31. Allinger, N. L., Experimental Molecular Structures. In *Molecular Structure*, 2010; pp 7-27.

32. Han, S. W.; Kim, K., Infrared Matrix Isolation Study of Acetone and Methanol in Solid Argon. *J. Phys. Chem.* **1996,** *100* (43), 17124-17132.

33. Dobrowolski, J. C.; Ostrowski, S.; Kołos, R., et al., Ar-matrix IR spectra of 2-propanol and its OD, D7 and D8 isotopologues. *Vibrational Spectroscopy* **2008,** *48* (1), 82-91.

# 3.0 Radical Formation and Detection

## 3.1 Introduction

With the correction function established (see Table 2.12), the next step was to investigate a radical source and a formation method. First, the use of Tesla-coil discharge as a method of radical formation was validated for use with the experimental setup available. The same system used in Chapter 2 was used in this work with additional modifications included as experiments were conducted. A radical source was established using a series of mixtures of water, oxygen, and argon which were subjected to Tesla-coil discharge to see if any $HO_x$ radicals could be formed and then trapped in the matrix. Second, the radicals were attempted to be reacted with chosen hydrocarbons, and their radical intermediates detected in the matrix.

## 3.2 Establishing the Tesla-Coil Method of Radical Formation

Detecting ·OH directly in the matrix is difficult as it is very reactive and has high mobility, so can potentially move in the matrix at 20 K instead of being trapped.[1] To determine whether a reaction and radical production is occurring using the chosen technique of Tesla-coil discharge, the method can be tested on a well-characterised molecule with distinct products. Acetone was chosen as carbon monoxide (CO) is a distinct product with a sharp and intense IR peak.[2] The main known reaction products for the photolysis of acetone (which will have the same products as ionization) are the acetyl radical ($CH_3CO\cdot$), the methyl radical ($CH_3\cdot$), carbon monoxide (CO), ketene ($CH_2CO$), and methane ($CH_4$), as shown in Scheme 3.1.[2-4] The primary focus of this experiment was to determine if CO was produced, as it has a clear and sharp spectrum that is characterised in literature and doesn't overlap with any regions that other products or acetone itself will be present.

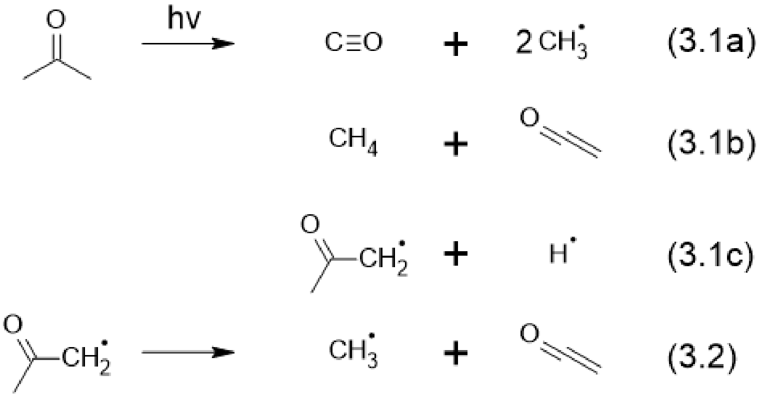

Scheme 3.1 Photolysis of acetone, and subsequent formation of ketene.[2-4]

The experiment is run like those in Chapter 2, using the method as described in section 2.3.2. The acetone sample was subjected to 3 freeze-pump-thaw cycles and sufficient dilution was achieved to minimise interaction between molecules. As shown in Figure 3.1, the argon and sample lines (in this case, acetone) combine before being subjected to Tesla-coil discharge. The Tesla-coil is positioned so the tip touches the borosilicate glass tubing that the gas flows through, with the tubing passing through the Faraday cage in which the Tesla-coil is housed. Immediately after being subjected to discharge, the sample gas flows through a PTFE (polytetrafluoroethylene, or Teflon) union and into the vacuum chamber where it deposits onto the 20 K $CaF_2$ window.

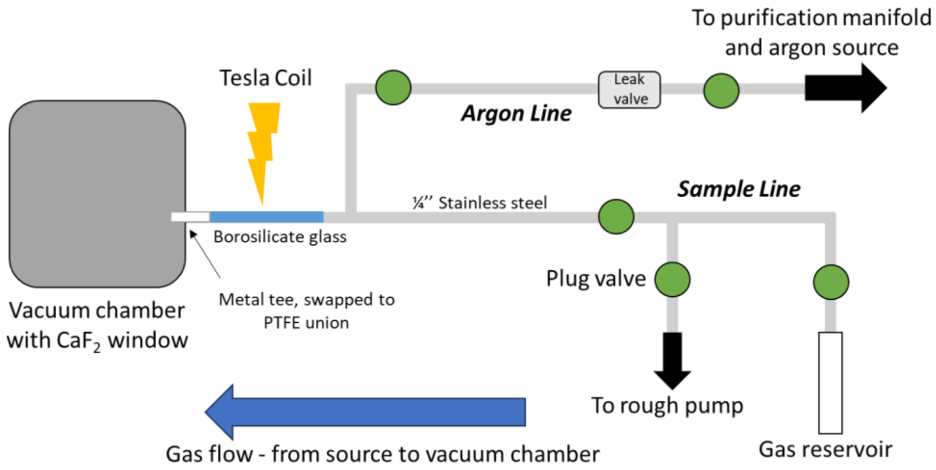

Figure 3.1 Gas-handling layout used for the acetone Tesla-coil test experiment. The Tesla-coil discharges to the sample through a borosilicate glass tube, which is connected to the vacuum chamber by initially a metal tee, and then subsequently a PTFE union with rubber o-rings to prevent radical scavenging. This is a modified layout of the one used in section 2.4.

Initially, argon is allowed to deposit for five minutes and a "baseline" spectrum is collected to filter any pre-existing peaks from the reaction spectra, then the argon and acetone mixture is allowed to deposit for ten minutes to give a reference spectrum of un-reacted acetone. Table 3.1 lists the experimental peaks assigned to literature and transformed calculated peaks for acetone in an argon matrix. Literature peaks, established by Han et al. (1996), within the instrument range of detection ( > 800 cm$^{-1}$) are all seen in the experimental data, within

Table 3.1 Table of assigned calculated and literature wavenumbers to experimental data for acetone, before being subjected to Tesla-coil discharge. Calculations are anharmonic, at QZ level, and are transformed using the correction factor established in Chapter 2. Literature data (Han et al., 1996) is in an argon matrix and is expected to match to experimental data.[5]

| **Literature Wavenumber (cm$^{-1}$)[5]** | **Corrected B3LYP QZ Wavenumber (cm$^{-1}$)** | **Corrected MP2 QZ Wavenumber (cm$^{-1}$)** | **Experimental** | |
|---|---|---|---|---|
| | | | **Wavenumber (cm$^{-1}$)** | **Shape/Size** |
| 3018.6 | | 3027.4 | 3018.4 | Sharp |
| | 2995.8 | | 3009.5 | Broad, shoulder |
| 2972.6 | 2993.6 | 2973.8 | 2972.8 | Sharp |
| 2932.2 | 2936.7 | | 2932.8 | Broad, shoulder |
| | 1785.1 | | 1768.8 | Broad |
| 1721.4 | | 1731.5 | 1721.5 | Medium |
| 1429.4 | 1436.7 | 1435.5 | 1429.2 | Broad |
| 1361.6 | 1365.5 | 1367.1 | 1361.4 | Sharp |
| 1354.1 | | 1358.7 | 1354.0 | Sharp |
| 1216.6 | | 1225.5 | 1223.6 | Sharp |
| | 1206.9 | | 1216.6 | Sharp |
| 1092.7 | 1097.2 | 1095.1 | 1091.6 | Sharp |
| 882.4 | | 884.2 | 882.6 | Sharp |

~ 1 $cm^{-1}$.[5] The calculated peaks are transformed using the correction function established in Chapter 2 before being assigned. This establishes the spectrum of acetone in the argon matrix.

After being subjected to Tesla-coil discharge, new peaks appeared in the spectrum that are not able to be assigned to the acetone reference spectrum. These peaks are listed in Table 3.2 and shown in Figure 3.2. The appearance of the peaks can be assigned to the formation of CO. No other peaks for the other reaction products listed in Scheme 3.1 could be definitively assigned. Literature for CO trapped in an argon matrix gives two main peaks assigned to the presence of CO, at ~ 2149 and 2138 $cm^{-1}$.[4, 6-9] It is noted in some works that the ~ 2149 $cm^{-1}$ peak is due to the $CO{\cdot}H_2O$ complex formed.[8] In the present work, the formation of this complex is possible due to the background presence of water in the vacuum chamber and piping – water is very difficult to get out of the physical system, so it is very likely there was water available to complex with the formed CO. In any case, the peaks formed between ~ 2138 – 2150 $cm^{-1}$ after the sample was subjected to Tesla-coil discharge can be assigned to the formation of CO, a reaction product of acetone photolysis, proving that using the system built in-house with Tesla-coil discharge as an excitation source is an appropriate method for causing reactions and forming radicals in this work.

Table 3.2 Table of significant peaks that appeared after acetone was subjected to Tesla-coil discharge. These peaks are associated with the formation of CO and its aggregates or complexes with water.

| Wavenumber ($cm^{-1}$) | Shape |
|---:|---|
| 2150.6 | Medium, shoulder |
| 2150.3 | Medium, shoulder |
| 2149.3 | Sharp |
| 2148.6 | Sharp |
| 2146.7 | Medium, shoulder |
| 2145.6 | Medium, shoulder |
| 2143.3 | Medium, shoulder |
| 2142.2 | Broad, shoulder |
| 2141.7 | Sharp, shoulder |
| 2138.7 | Broad |

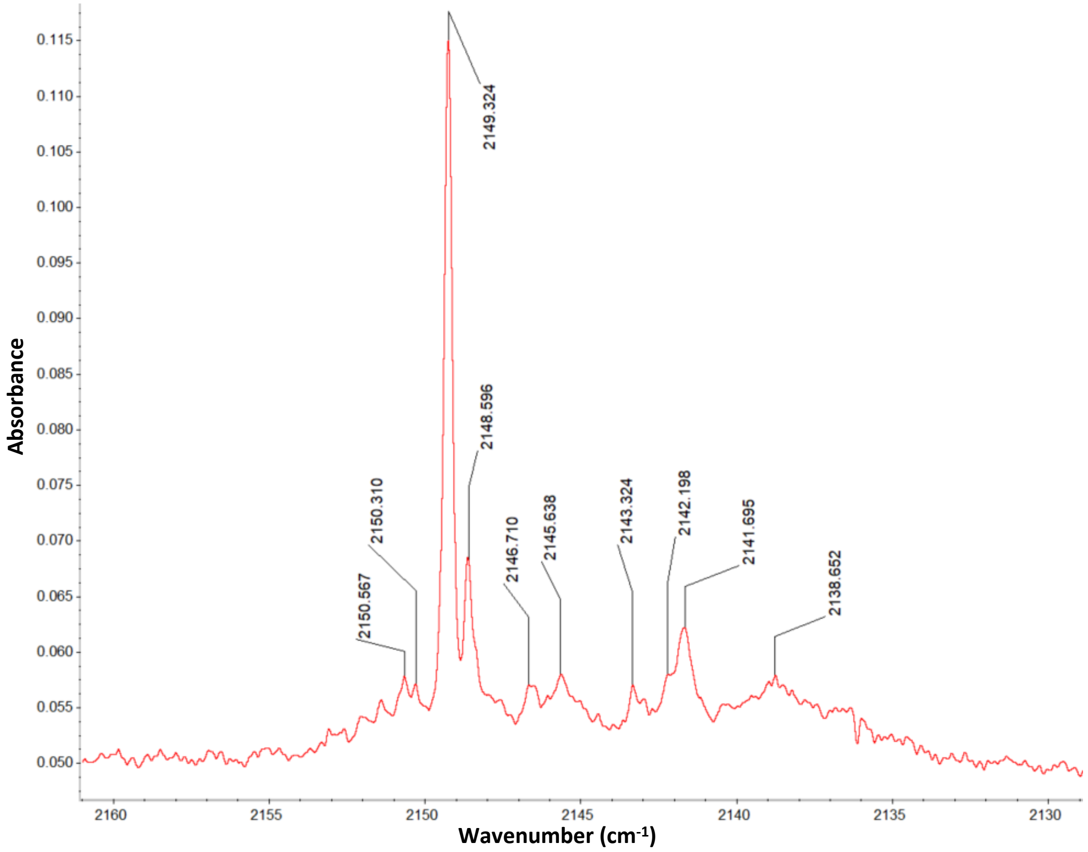

Figure 3.2 Peaks assigned to CO from a spectrum of acetone subject to Tesla-coil discharge.

## 3.3 Direct Detection of Formed Radicals Using the Tesla-Coil Method

With the method of Tesla-coil discharge established as a valid technique for our system to cause reactions and form radicals, the radicals were attempted to be directly detected, as opposed to detecting reaction products like CO. The source investigated will be water.

The ·OH radicals must be formed *in-situ* due to their atmospheric lifetime being less than a second.[32] This is beneficial as it minimises wall loss of the radicals due to transfer between vessels. Radicals for MI reaction spectra will be created using discharge from a Tesla-coil (CENCO BD10) that is situated inside a Faraday cage (built in-house) and further insulated by PTFE sheets. Initially, the radical source was intended to be concentrated $H_2O_2$, as this is a proven successful ·OH source when subjected to light of $\lambda \leq 360$ nm.[10, 11-13] However, there are explosion risks when using $H_2O_2$, and a more concentrated solution than the standard 30% would be required to produce significant radicals. Thus, water was investigated as an alternative radical source since it is much safer, and it was found that using a low pressure of degassed milli-Q water subjected to Tesla-coil discharge produced peaks indicating the presence of radicals (see section 3.3.2). Using water as a radical source does mean there is potential for formation of complexes with itself and with ·OH, so these “reaction products” must be considered when assigning the data.

### 3.3.1 Literature Studies

·OH radicals have been formed using a Tesla-coil excitation source in combination with an argon matrix by Langford et al. (1997) and Langford et al. (2000). Langford et al. (1997) made ·OH in an argon matrix using a 1:100 mol ratio of $H_2O$ vapour to argon, passed through a pipe subjected to Tesla-coil discharge.[14] Within 15 mins of discharge depositing onto a ~ 15 K window they positively identified the presence of the radical using the technique of magnetic circular dichroism. Langford et al. (2000) identified and assigned the $H_2O{\cdot}OH$ complex using a similar technique of flowing a mix of $H_2O$ in argon through a pyrex tube subject to Tesla-coil discharge that was then deposited onto a ~ 11.5 K window.[15] They identified the radical, the complex, and a number of multimers of $H_2O$ in their experiment. As such, Tesla-coil discharge combined with MI-FTIR is proven by literature to be a valid way of producing and detecting radicals and related complexes from a water source.

·OH radicals have also been trapped in argon matrices previously. Cheng et al. (1988) use two non-photolytic methods to create the radicals and subsequently trap them on a ~ 12 K window, using thermal dissociation on a tungsten filament or microwave discharge to create radicals from the reaction of $H_2$ with $NO_2{\cdot}$, $O_3$, and $O_2$.[16] Engdahl et al. (2003) used hydroperoxyl (HOO·) radicals in a hydrogen-doped argon matrix to form the ·OH radicals inside the matrix itself after UV irradiation.[1] They are specifically detecting the $OH{\cdot}H_2O$ complex, but still form the ·OH radical within the matrix.

Using water as a radical source means that complexes of water with itself and with ·OH and other radicals are possible. These complexes are well studied in the literature, using MI-FTIR spectroscopy as the detection technique. Common complexes seen are $H_2O$ dimers, trimers, and multimers, $H_2O{\cdot}OH$, $H_2O{\cdot}HOO$, $H_2O{\cdot}O_3$, $H_2O{\cdot}O$, and $H_2O{\cdot}H_2O_2$. Summarised in Table 3.3 are studies that cover these complexes using similar techniques to those employed in this work, either by computation or by experimental methods. These studies are run between 5 – 20 K and at 0.5 - 1 $cm^{-1}$ resolution. They give a reference for identification of the complexes that can form, making it easier to pinpoint the peaks associated with the ·OH radical and other expected products.

Table 3.3 Literature studies that make or detect ·OH radicals or water complexes. Most use MI-FTIR or calculational methods for detection, and a range of techniques for radical formation.

| Ref. | Radical Formation Technique | Molecules Detected | Detection Method |
|---|---|---|---|
| 1 | Irradiation by YAG laser of $H_2$/Ar and O/$H_2$/Ar mixtures subjected to microwave discharge and deposited on a cold window; calculations using HF/SCF methods | HOO·, ·OH, $H_2O$.OH | MI-FTIR, 0.5 – 1 $cm^{-1}$ resolution, 9 – 12 K window; matrix is hydrogen doped so ·OH forms within it |
| 14 | Tesla-coil discharge using $H_2O$:Ar in a 1:100 mole ratio | ·OH | Magnetic circular dichroism, sapphire window at 15 K |
| 15 | Tesla-coil discharge with $H_2O$:Ar mixtures | $H_2O$ dimer, trimer, multimer, ·OH, $H_2O$.OH, HOO· | MI-FTIR, 0.5 $cm^{-1}$ resolution, 11.5 ± 0.5 K sapphire window |
| 16 | Microwave discharge and W filament, using combinations of $H_2$ with $O_2$, $NO_2$·, and $O_3$ in argon | ·OH, HOO·, $H_2O$ | MI-FTIR, 0.5 $cm^{-1}$ resolution, 12 K CsBr window |
| 17 | Calculation, 6-31+G(d,p) and 6-311+G(d,p) basis sets using BLYP, BP86, B3LYP, B3P86, B3PW91 and MP2 methods | $H_2O_2$.$H_2O$ | |
| 18 | Calculation using MP2/6-311+G(d,p) | $H_2O_2$.$H_2O$ | |
| 19 | Tesla-coil discharge using $H_2O$:Ar mixtures in different ratios, calculations at QCISD/6-311++G(2d,2p) | $H_2O$.OH | MI-FTIR, 0.5 $cm^{-1}$ resolution, at 11.5 ± 5 K KBr window |
| 20 | Calculation, 6-31G** and 6-311G** basis sets using HF and MP2 theory | $H_2O_2$.$H_2O$ complexes | |
| 21 | Vacuum UV photolysis of $H_2O$:Ne at 1:3000 ratios deposited in a neon matrix, calculations using aug-cc-pVDZ and TZ basis sets for B3LYP, B98, MP2, and MP4(SDQ) methods | $H_2O$ clusters, OH.$(H_2O)_n$ | MI-FTIR, neon matrix, 0.25 $cm^{-1}$ resolution, 5 K CsI window |
| 22 | Combination of calculations and experimental data<br>Review (covers some studies listed) | $H_2O$.$O_2$, $H_2O$.O, $H_2O$.$O_3$, $H_2O$.OH, $H_2O$.HOO, $H_2O$.HOOO, $H_2O$.$H_2O_2$ | Range of techniques including MI-FTIR using an argon matrix |
| 23 | Photolysis of $H_2O_2$ in argon matrices by excimer laser | $H_2O$.O, ·OH | MI-FTIR, 1 $cm^{-1}$ resolution, 18 K CsI or KBr window |

### 3.3.2 Results

Mixtures of milli-Q water, oxygen (BOC), and argon (BOC) were subjected to Tesla-coil discharge to create ·OH. The mixture, held in a Swagelok 304L-HDF4-15000 reservoir, generally had a composition of ~ 20 Torr water vapour, ~ 20 Torr of oxygen, and then were made up to ~ 800 Torr with argon, with specific compositions found in Table 3.4. To make the mixtures, the reservoir would be pumped out using an Edwards RV5 pump. Degassed milli-Q water vapour was then allowed to flow into the reservoir up to ~ 20 Torr, and then ~ 20 Torr of $O_2$ was flowed in. The mixture was then made up to ~ 760 – 860 Torr with 99.999% argon (further purified by an SGT-B1010-B8 triple filter).

Table 3.4 Table of experiments run to test water and oxygen mixtures for use as a radical source when subjected to Tesla-coil discharge. The amount of each gas in the mixture is given. The total pressure in the mixture was ~ 1 atm. The amount of time the sample was subjected to Tesla-coil discharge is also given.

| Sample Name | Mixture | Mixture Composition | Temperature | Coil-On Time (mins) |
|---|---|---|---|---|
| W1 | $H_2O$, $O_2$, argon | $H_2O$ 20.4 Torr, $O_2$ 26.3 Torr, argon 820 Torr | 20 K | 60 |
| W2 | $H_2O$, $O_2$, argon | $H_2O$ 20.4 Torr, $O_2$ 26.3 Torr, argon 820 Torr | 20 K argon,<br>8 K sample | 80 |
| W3 | $H_2O$, $O_2$, argon | $H_2O$ + $O_2$ 47 Torr,<br>argon 800 Torr | 20 K argon,<br>8 K sample | 120 |
| W4 | $H_2O$, $O_2$, argon | $H_2O$ + $O_2$ 47 Torr,<br>argon 800 Torr | 20 K argon,<br>8 K sample | 30 |
| W5 | $H_2O$, $O_2$, argon | $H_2O$ + $O_2$ 47 Torr,<br>argon 800 Torr | 20 K argon,<br>8 K sample | 30 |
| W6 | $H_2O$ | $H_2O$ | 20 K argon,<br>8 K sample | 20 |
| W7 | $H_2O$, $O_2$, argon | $H_2O$ + $O_2$ 47 Torr,<br>argon 800 Torr | 8 K | 180 |
| METAL TEE SWAPPED FOR PTFE UNION | | | | |
| W8 | $H_2O$, $O_2$, argon | $H_2O$ + $O_2$ 47 Torr,<br>argon 800 Torr | 8 K | 135 |
| W9 | $H_2O$, argon | $H_2O$ ~ 20 Torr,<br>argon 788 Torr | 8 K | 60 |
| W10 | $H_2O$, argon | $H_2O$ ~ 20 Torr,<br>argon 788 Torr | 15 – 18 K | 90 |
| W11 | $H_2O$ | $H_2O$ | 15 K | 120 |

The same MI procedure as outlined in sections 2.3.2 and 3.2 is followed, with the milli-Q water subjected to degassing before being used to create the mixtures. The sample and argon pressures are set to ensure sufficient dilution to minimise interactions between molecules. Flow rates of sample and argon were kept constant throughout the experiment. Once an argon baseline is established, the mixture is allowed to build up on the window for between 20 – 60 minutes to give a reference spectrum of the mixture before subjected to discharge. The mixture was then subjected to Tesla-coil discharge and allowed to deposit on the window, same as in section 3.2. The experiments were run at different temperatures, as initial experiments at 20 K didn't give any conclusive product peaks, and it's been noted that ·OH can move in the matrix even at 15 – 20 K;[1] as a result, the lowest temperature reachable by the cryostat of 8 K was used for sample deposition for most of the latter experiments (and was more reflective of literature conditions), whereas the argon baseline was deposited at 20 K.

There is a specific difficulty associated in assigning these spectra due to the high water background. Water 'sticks' to the metal and is difficult to remove even after baking out the system, so over time the water background grew more intense, potentially obscuring any small peaks expected in those areas. The mixtures were allowed to deposit for up to an hour before being subjected to discharge so that a baseline of the mixture was established. Additionally, at least an hour of deposition time was allowed with the Tesla-coil active to give the product peaks time to build in intensity, but transmission was lost over time when the coil was active, thus there was an upper limit to how long it could be left on to deposit. Figure 3.3 and Table 3.5 show the peaks in the ~ 3600 – 3300 cm$^{-1}$ range typical of water and its multimers seen in each mixture spectrum before Tesla-coil discharge. Water and water dimers, trimers, and multimers are present for each spectra. There is additional difficulty in assigning peaks associated with radical formation as they are found within this range and are often less intense than the water multimer peaks; however, the same shape is seen for the peaks listed across all experiments, which helps to reduce difficulty.

Table 3.5 Peaks assigned for water and its complexes typical to mixture pre-discharge spectra. The experimental data has come from W6 but the peaks listed are typical to all water/oxygen/argon mixture experiments run.

| Molecule/ Complex | Expected Peak (cm$^{-1}$) | Reference | Experimental Data | |
|---|---|---|---|---|
| | | | Wavenumber (cm$^{-1}$) | Shape |
| $H_2O$ | 1586.0 | 15 | 1593.223 | Sharp |
| $H_2O$ dimer | 3573.6 | 23 | 3573.614 | Sharp |
| $H_2O$ trimer | 3528 | 23 | 3527.880 | Broad, shoulder |
| | 3516 | 23 | 3516.831 | Broad |
| $H_2O$ multimer | 3566.5 | 23 | 3567.040 | Sharp |
| $O{\cdot}H_2O$ | 3633 | 24 | 3633.031 | Sharp |

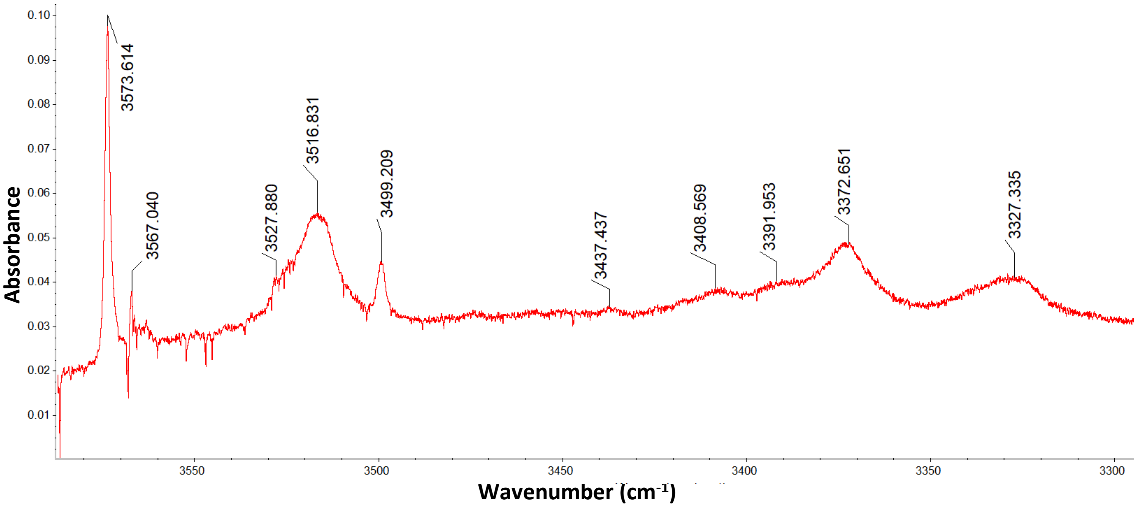

Figure 3.3 Typical peaks seen for water and its multimers in water/oxygen/argon mixture experiments. The section of the spectra shown is from W6 but is typical to the "baseline" established for mixtures before being subjected to Tesla-coil discharge.

In experiments W1 – W7, although different mixture compositions, deposition temperatures, and lengths of time subject to the Tesla-coil discharge were tested (as detailed in Table 3.4), no radicals were directly detected. It was suspected that the metal tee, positioned after the Tesla-coil but before the vacuum chamber, was scavenging most of the radicals being formed, giving no conclusive peaks in the spectra. However, a reaction was indicated to still be occurring by presence of peaks associated with CO formation, also seen in section 3.2. For these peaks to be present in these experiments, a radical reaction is suspected to be occurring with a source of carbon within the gas-handling lines. This is expected to be the rubber o-ring positioned in the metal union. This indicates that radicals are being formed, even though they are not directly detected within the spectra, as some have likely reacted with the rubber o-ring and the remainder been scavenged by the metal tee itself. Subsequently, the metal tee was replaced with a PTFE union to prevent further scavenging. Table 3.6 gives a summary of peaks assigned to the presence of radicals for experiments after the metal tee was removed (experiments W8 – W11). These experiments give evidence of radical formation from the presence of the radicals themselves; an ·OH precursor, $H_2O_2$; the presence of $O_3$ (which is formed from $O_2$ reactions and is an ·OH precursor, detailed in section 1.6); and their complexes with water. In every spectrum, the presence of ·OH and HOO· is given by peaks at ~ 3548 – 3549 cm$^{-1}$ and peaks at ~ 3412, 1388, and 1101 cm$^{-1}$, respectively. There is also evidence of the $OH{\cdot}H_2O$ complex in each spectrum.

Table 3.6 Peaks assigned to $HO_x$ radicals and $O_3$, and their complexes with water for Tesla-coil discharge experiments using a mixture of water, oxygen, and argon. Each experiment gives evidence of radical formation occurring, either by the presence of $HO_x$ radicals or their precursor $H_2O_2$, or by water complexes with the radicals.

| Molecule/ Complex | Literature Peak ($cm^{-1}$) | Ref. | Experimental Peak ($cm^{-1}$) | | | |
|---|---|---|---|---|---|---|
| | | | W8 | W9 | W10 | W11 |
| ·OH | ~ 3548 - 3549 | 23, 16, 15 | 3548.1 | 3548.8 | 3549.7 | 3549.3 |
| OH·$H_2O$ | 3718.6 | 1 | | 3718.4 | | |
| | 3711.5 | 1 | | 3711.2 | | |
| | 3634.6 | 1 | 3633.3 | 3633.2 | | |
| | 3452.2 | 22 | 3452.4 | | 3452.4 | 3452.4 |
| | 3417 | 22 | | | | 3415.8 |
| HOO· | 3412.8 | 23 | 3412.7 | 3414.3 | 3414.1 | 3412.4 |
| | 1388.5 | 23 | 1388.3 | 1388.3 | 1388.5 | 1388.5 |
| | 1101.1 | 23 | 1100.8 | | 1100.8 | 1100.3 |
| HOO·$H_2O$ | 3489.82 | 22 | | | | 3489.0 |
| $H_2O_2$ | 3597 | 23 | | | 3596.9 | 3597.0 |
| | 3588 | 22 | | | | 3589.8 |
| | 1272.51 | 22 | 1272.3 | | | |
| $O_3$ | 1110.82 | 24 | | | 1109.7 | 1110.9 |
| | 1044 | 24 | 1039.9 | | 1039.7 | 1039.6 |
| $H_2O$·$O_3$ | 3709 | 22 | | 3707.0 | | 3707.1 |

To see if any additional radical products were formed matrices were annealed, which involves turning the flow of gas off and heating the matrix up to ~ 35 K at a rate of ~ 1 K/min. It can then be cooled back down to deposition temperature but often a large decrease in transmission is experienced from cracking in the matrix. Annealing allows any trapped radicals or small molecules to move around in the matrix as it relaxes at higher temperatures, meaning radical peaks could decrease as they move and react further with other trapped molecules, causing product peaks to increase or new peaks to form. Matrices W2, W3, W5, W6, and W8 were annealed to ~ 35 K. Of these, W8 is the only experiment that has evidence of radical products beyond formation of CO, as discussed above. This means that much of the annealing data only indicates what is occurring to the water molecules trapped in the matrix. The most intense (and easily discerned) peaks attributed to water and its multimers are found in the 3600 – 3000 $cm^{-1}$ range, and when heated up to 35 K these peaks are all absorbed into a very broad peak that covers this range, indicating a lot of interactions between water molecules in the matrix. Additionally, the peaks at ~ 2149 and 2138 $cm^{-1}$, attributed to CO and $H_2O$·CO, also change during annealing, seen in Figure 3.4. Once heated to 35 K the 2138 $cm^{-1}$ peak reduced in intensity, if not disappearing altogether, and the 2149 $cm^{-1}$ peak experienced a shift to a lower wavelength of < 1 $cm^{-1}$, usually accompanied by an increase or appearance of a shoulder peak at ~ 2151 $cm^{-1}$. When annealing W8 to 35 K, the peaks assigned to radicals were all buried by the appearance of the broad peak in the water multimer area (3600 – 3000 cm$^{-1}$) or were buried by the increase in noise that occurred during annealing due to their low intensity to begin with. The annealing process thus tells us that the water molecules shift positions in the matrix when it is heated and interact with themselves, if not other molecules present.

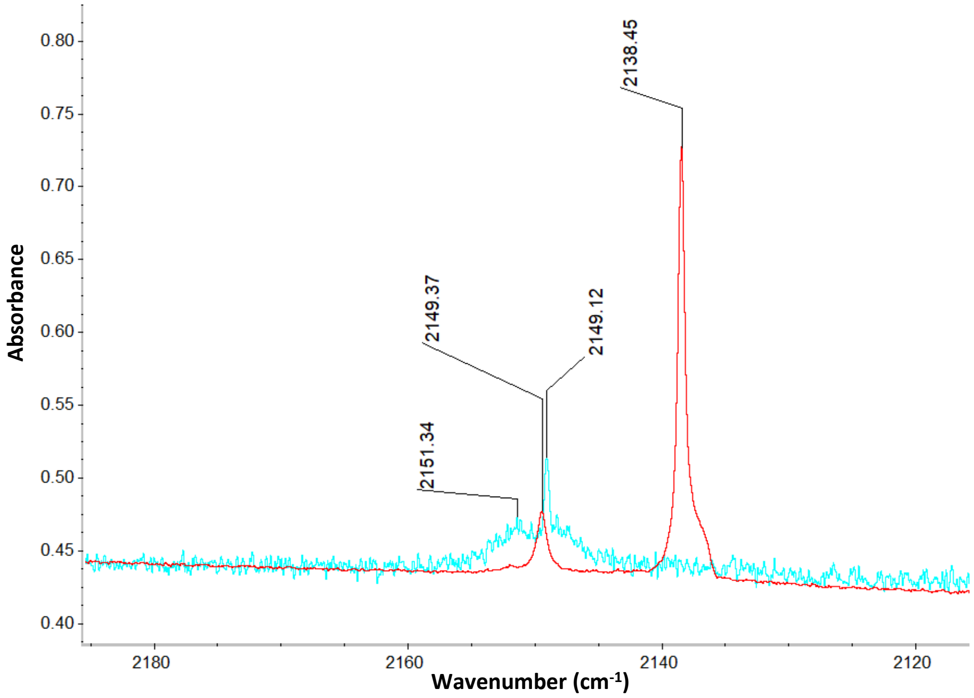

Figure 3.4 Behaviour of the CO attributed peaks during annealing. This section comes from the spectra of W8, with the red being deposited at 8 K and the blue having been annealing slowly up to 35 K. The 2138 cm$^{-1}$ peak completely disappears at 35 K, and a shoulder peak appears at 2151 cm$^{-1}$.

Overall, these experiments have proven the validity of using milli-Q water subjected to Tesla-coil discharge as a source of radicals that can be detected using the MI-FTIR system. The presence of radicals and their complexes with water is seen in experiments using both a mixture of milli-Q water, oxygen, and argon (W8), and a mixture of just milli-Q water and argon (W9 – W10). For the radical reaction experiments in section 3.4, only a mixture of water and argon will be used to reduce the potential products that could be formed by including oxygen in the mixture.

## 3.4 Radical Reaction Experiments

Once the radical source was established and the method for radical formation validated, radical reactions with chosen molecules from the reference library were run. Simple molecules with clear reference spectra and well-characterised, easy to determine, or few intermediates and potential products were preferred. These experiments were run to establish whether the radicals produced by the method defined in section 3.3 could react with hydrocarbons, and that the reaction between these molecules could be detected via the presence of reaction intermediates or products trapped in the matrix. This would allow for confident detection of products when applying the $TiO_2$ catalyst to the ·OH formation process, such that the increase in formation of ·OH and subsequent reaction intermediates and products could be determined to prove catalytic ability. Isotopic substitution, whilst typically employed for this kind of work, was not used here as it was not available.

Experiments were run using a similar MI setup as described in section 3.2 above, but with an additional gas line included for the sample that added downstream of the irradiated water and argon mixture (see Figure 3.5). This means that only the water and argon will be subjected to Tesla-coil discharge and therefore only ·OH be formed. Thus, reaction products and intermediates isolated in the matrix should have come only from reaction of the unexcited sample with the irradiated flow of water and argon. This minimises possible products, as well as reactions of the sample with itself if it were to be subject to Tesla-coil discharge. There is potential for background contaminants like $O_2$ or previously used samples to be present, but they should be low in concentration and therefore have an insignificant effect compared to the amount of ·OH produced. For the isoprene sample specifically, the sample was kept in an ethanol

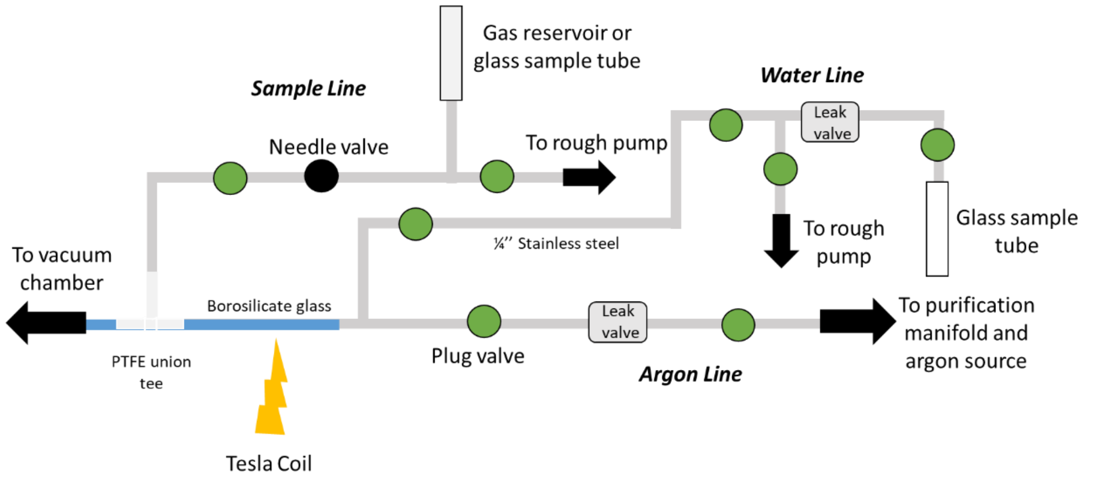

Figure 3.5 Final gas-handling layout for matrix-isolation radical reaction experiments. There are three lines; the water and argon line connect before being subjected to Tesla-coil discharge, after which the sample line connects by way of a PTFE union tee (to avoid radical scavenging). Each line can be valved off and rough pumped individually.

bath at – 60℃ to reduce the vapour pressure and give better control for setting sample pressure. Each sample was degassed before use.

Each radical reaction matrix was annealed to allow for any mobile trapped molecules to move within the matrix, since it relaxes at higher temperatures. A spectrum is recorded at deposition temperature; the matrix is then warmed to 35 K in 5 K increments, at a rate of ~ 1 K/min, with a spectrum recorded at each increment; and then the matrix is cooled back to deposition temperature in 5 K increments at a rate of ~ 1 K/min, with a spectrum recorded at each increment. This means any trapped radicals should be able to move and react further, and additionally any trapped molecules can rearrange to a more favourable position. Peaks that disappear indicate the corresponding molecule has been used up in reactions within the matrix or rearranged to a more favourable position. New peaks could be from further reactions in the matrix creating new products.

### 3.4.1 ·OH + Propyne

The first molecule chosen for reaction with ·OH was propyne, as it is small, has only two possible sites of ·OH addition or H abstraction, gives a reference spectrum with clear and sharp peaks, and has well-characterised reaction products.[25]

Oxidation of propyne by ·OH has two pathways it can follow:

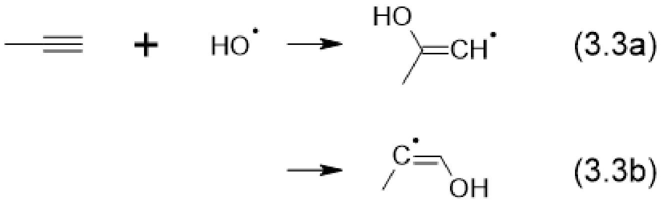

Scheme 3.2 Reaction of ·OH and propyne.[25]

Reaction 3.3a occurs from attack at the central carbon, and 3.3b from attack at the terminal carbon. Following this, in the presence of oxygen the two intermediates form a carbonyl radical and a carboxylic acid as products, or the intermediate from 3.3b can undergo rearrangement to give ketene and the methyl radical as products (3.5b).[25]

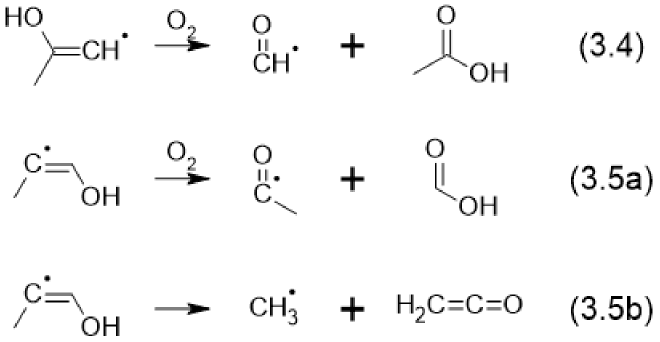

Scheme 3.3 Reactions of propyne intermediates from Scheme 3.2 in the presence of $O_2$ or undergoing rearrangement.[25]

The oxidation pathways in Scheme 3.3 give the oxidation products ethanoic acid and the formyl radical (3.4), formic acid and the acetyl radical (3.5a), and ketene and the methyl radical (3.5b).[25] No oxygen was added to the vacuum chamber, so reaction products from reactions 3.4 and 3.5a are unlikely to form at detectable concentrations. As such, the reaction products shown in Scheme 3.2 are investigated instead. Calculations for the intermediates given in scheme 3.2 were calculated at B3LYP/cc-pVTZ level with anharmonic corrections and transformed using the correction function determined in Chapter 2.

For the propyne radical reaction experiment, after a background and an argon baseline was established, water vapour from a glass sample tube of milli-Q water was allowed to flow through the water line, mixing with the argon in line before entering the vacuum chamber, for ~ 20 minutes to give a background. The mixture of water vapour and argon was subsequently subjected to Tesla-coil discharge for ~ 20 minutes before propyne was added to the system, downstream of the Tesla-coil discharge point. This was then allowed to deposit for ~ 2 hours to allow peaks to build up, giving a spectrum referred to herein as the "Tesla-coil discharge (TCD) spectrum". Once gas flow was stopped, the matrix was annealed by heating from 15 K to 35 K, then cooling to 8 K. A separate "blank" experiment was run in which only propyne and argon was subjected to Tesla-coil discharge with no water added. This was used as a reference spectrum for assigning peaks in the TCD spectrum.

For the calculated radical intermediates (3.3a and 3.3b), each has 9 unique peaks that can be considered a definitive assignment to that specific radical. Since the intermediates differ from the reactant only by addition of ·OH, a significant number of the corrected calculated peaks are very similar and so would be difficult to differentiate between when assigning. Of these unique peaks, only 5 can be assigned, given in Table 3.7. Two peaks can be uniquely assigned to each intermediate. Annealing the matrix did not give any new peaks but did have 3 of the assigned peaks below (3639.98, 1388.43, and 1382.92 cm$^{-1}$) shift or disappear when heated to 35 K and then return to their original state when cooled back to 8 K, which indicates a conformational shift or change in lattice position and therefore is not related to radicals. This means that presence of radical intermediates is only uniquely identified for 4 peaks, since 2 of the assigned peaks in Table 3.7 can be assigned to multiple molecules, but does overall indicate the presence of reaction intermediates and therefore a radical reaction occurring.

Table 3.7 Table of assigned experimental peaks from the TCD spectrum. There is one vibrational frequency that could be assigned to both intermediates and propyne, and one that can be assigned to either propyne itself or an intermediate.

| Experimental | | Assigned | |
|---|---|---|---|
| Wavenumber (cm$^{-1}$) | Shape | Wavenumber (cm$^{-1}$) | Molecule |
| 3640.0 | Broad | 3639.2 | 3.3b |
| 2940.4 | Broad, shoulder | 2938.3 | 3.3b |
| 2940.4 | Broad, shoulder | 2939.0 | Propyne |
| 2940.4 | Broad, shoulder | 2940.2 | 3.3a |
| 2914.1 | Broad | 2914.0 | Propyne |
| 2914.1 | Broad | 2911.8 | 3.3b |
| 1382.9 | Broad | 1374.7 | 3.3a |
| 1348.8 | Broad | 1335.2 | 3.3b |
| 1282.8 | Sharp | 1284.9 | 3.3a |

### 3.4.2 ·OH + Isoprene

Isoprene was chosen as the second molecule for radical reaction experiments. There are four possible points for ·OH to add:

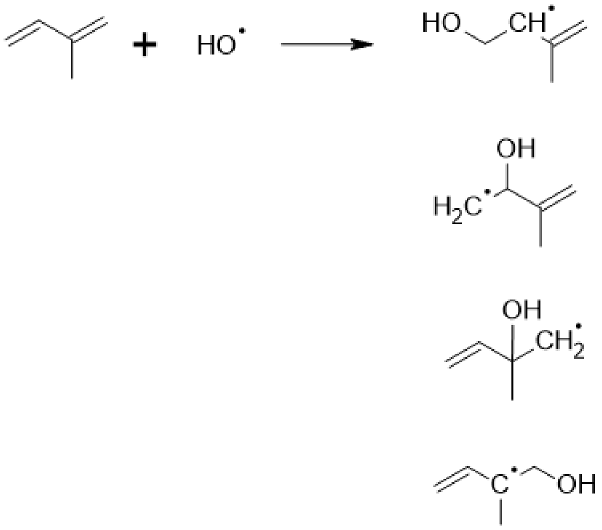

(3.6a)
(3.6b)
(3.6c)
(3.6d)

Scheme 3.4 Reaction of ·OH addition to isoprene, producing four radical intermediates.[26]

However, only 3.6a and 3.6d occur as they are more stable radicals, with a ratio of 0.37:0:0:0.63 for 3.6a:3.6b:3.6c:3.6d given by Wennberg et al. (2018).[26] Calculations for these four intermediates were run at B3LYP/cc-pVTZ level with anharmonic corrections. The calculated frequencies were transformed using the correction function determined in Chapter 2.

For the isoprene radical reaction experiment, after a background and argon baseline was established, isoprene was allowed to build up in the chamber for ~ 40 minutes. The flow of argon was then subjected to Tesla-coil discharge and allowed to mix with the isoprene which was added to the system downstream of the Tesla-coil discharge, depositing for ~ 30 minutes. This was to establish if any reaction occurred between with no radical source present. Then, water vapour from a glass sample tube was allowed to flow through the water line, mixing with the argon in line. This water vapour and argon mixture was subjected to Tesla-coil discharge, depositing for ~ 2 hours (“TCD spectrum”). Once gas flow was stopped, the matrix was annealed by heating from 15 K to 35 K, then cooling to 8 K.

Of the radical intermediates calculated, only two (3.6a and 3.6d) are considered for peaks present in the reaction spectrum. Because the intermediates and the reactant are similar in structure, they have similar expected frequencies, which makes it difficult to distinguish in the spectra which molecule is associated with specific peaks. The molecules do have a certain number of frequencies that differ significantly enough (~ 10 cm$^{-1}$) from the frequencies expected for the other molecules, that the presence of these unique frequencies would allow for confident identification of that specific intermediate or reactant. Intermediates 3.6a and 3.6d have 11 – 12 unique expected frequencies. Unfortunately, many of the unique frequencies are present in congested areas that have peaks present that aren't assigned to the reactant. Table 3.8 gives a list of assigned frequencies present in the TCD spectrum. These vibrational frequencies indicate presence of both radical intermediates, with 4 unique peaks for intermediate 3.6a and 6 unique peaks for intermediate 3.6d.

Table 3.8 Table of assigned peaks for the isoprene TCD spectrum and behaviour during annealing (at 35 K and then cooled back to 8K).

| Experimental | | | Assigned | |
|---|---|---|---|---|
| **Wavenumber ($cm^{-1}$)** | **Behaviour at 35 K** | **Behaviour at 8 K** | **Wavenumber ($cm^{-1}$)** | **Molecule** |
| 3082.9 | Disappears | Disappears | 3081.1 | Isoprene |
| 3082.9 | Disappears | Disappears | 3082.7 | 3.6d |
| 2988.8 | | | 2989.8 | 3.6d |
| 2988.8 | | | 2982.2 | Isoprene |
| 2972.0 | | | 2972.0 | Isoprene |
| 2972.0 | | | 2973.6 | 3.6d |
| 2945.4 | Disappears | Disappears | 2941.5 | 3.6a |
| 2945.4 | Disappears | Disappears | 2945.6 | 3.6d |
| 2913.0 | Decreased | Reappears | 2906.4 | 3.6a |
| 2913.0 | Decreased | Reappears | 2916.1 | Isoprene |
| 1461.2 | | | 1459.3 | 3.6a |
| 1461.2 | | | 1463.5 | 3.6d |
| 1461.2 | | | 1466.6 | Isoprene |
| 1445.8 | | | 1440.1 | 3.6a |
| 1445.8 | | | 1439.9 | 3.6d |
| 1384.8 | | | 1385.0 | 3.6a |
| 1384.8 | | | 1382.0 | 3.6d |
| 1384.8 | | | 1385.4 | Isoprene |
| 1378.3 | | | 1377.2 | Isoprene |
| 1374.8 | | | 1372.9 | 3.6d |
| 1368.2 | | | 1364.6 | 3.6a |
| 1361.6 | | | 1364.6 | 3.6a |
| 1354.0 | | | 1349.4 | 3.6d |
| 1305.4 | | | 1303.8 | Isoprene |
| 1305.4 | | | 1300.9 | 3.6d |
| 1247.3 | | | 1246.5 | 3.6d |
| 1238.1 | | | 1230.1 | 3.6a |
| 1216.8 | | | 1206.0 | 3.6a |
| 1113.8 | | | 1115.4 | 3.6d |
| 1033.3 | | | 1029.5 | 3.6d |

Annealing the matrix affected 3 significant peaks, listed in Table 3.8. Two of these peaks disappeared when annealed to 35 K and remained gone even when cooled back to 8 K, and one disappeared at 35 K but returned at 8 K. All the peaks affected by annealing listed in Table 3.8 could be assigned to 2 molecules. Usually, when a peak experiences a change during the annealing process it is due to movement of the molecule in the matrix. In this case, it could be due to either a radical being able to move and react with other molecules, reducing a peak in intensity and remaining at this new reduced intensity even when cooled back down, or could be due a change in conformation or lattice site of a molecule, which would cause the peak to reappear or shift back to the original position once cooled down. The two peaks that did not return when cooled back to 8 K can thus be assigned to intermediates, and the peak that did return assigned to isoprene.

### 3.4.3 ·OH + β-pinene

β-pinene was the third molecule chosen for radical reaction experiments, so that reactions with a large molecule could be attempted, representing a significant portion of the reference library established in Chapter 2. β-pinene has two sites that ·OH can add to (3.7a and 3.7b), as well as one site of H abstraction (3.7c)[27]:

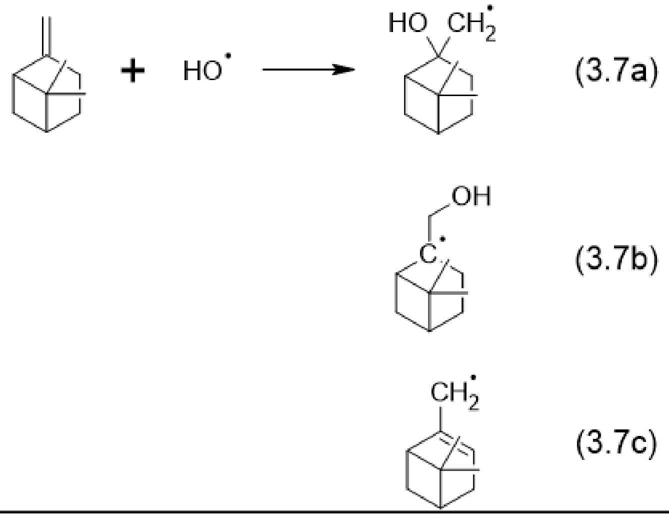

Scheme 3.5 Reaction of ·OH with β-pinene, producing two addition products and one H abstraction product.[27]

Calculations for these intermediates were run at B3LYP/cc-pVTZ levels with anharmonic corrections applied. The calculated frequencies were transformed using the correction function determined in Chapter 2.

For the β-pinene experiments, after a background and argon baseline was established, sample was allowed to build up in the chamber for ~ 40 minutes – 2 hours. The flow of argon was then subjected to Tesla-coil discharge and allowed to mix with the sample which was added in downstream of the Tesla-coil discharge, depositing for ~ 30 minutes. This was to establish if any reaction occurred without inclusion of the radical source (water). Then, water vapour from a glass sample tube was allowed to flow through the water line, mixing with argon in line. This mixture of water vapour and argon was subjected to Tesla-coil discharge, depositing for ~ 2 hours (“TCD spectrum”). Once gas flow was stopped, the matrix was annealed by heating from 15 K to 35 K, then cooling to 8 K. The first experiment run had significant peaks in the baseline from the previous isoprene experiment, so a second experiment was run after swapping o-rings in the sample line (which historically have retained isoprene after experiments) to try and get a ‘clean’ spectrum.

The intermediates given in 3.7a and 3.7b have 12 – 14 unique frequencies that can be used to establish their presence in the TCD spectrum, with 3.7c having only 3 unique frequencies. Of these, only 3 can be assigned, and are seen only during the annealing process. Table 3.9 gives assigned peaks from the TCD spectrum. Unfortunately, each assigned peak can be attributed to either an intermediate or β-pinene itself, since the peaks are similar between the intermediate molecules and the reactant, especially for 3.7c. Expected peaks for the intermediates are all in congested areas so are difficult to identify, especially since they are likely to be at a much lower intensity than the present reactant peaks.

Table 3.9 Table of assigned experimental peaks from the TCD spectrum.

| Experimental | | | Assigned | |
|---|---|---|---|---|
| **Wavenumber ($cm^{-1}$)** | **Behaviour at 35 K** | **Behaviour at 8 K** | **Wavenumber ($cm^{-1}$)** | **Molecule** |
| 2993.0 | Increase | Decrease | 2999.5 | 3.7a |
| 2970.0 | Increase | Decreased to 0 | 2978.5 | β-pinene |
| 2970.0 | Increase | Decreased to 0 | 2978.6 | 3.7a |
| 2875.8 | No change | Decreased to 0 | 2872.3 | 3.7a |
| 2259.2 | | | 2863.0 | 3.7c |
| 2259.2 | | | 2862.2 | β-pinene |
| 1414.3 | Decrease | Increase | 1414.7 | β-pinene |
| 1414.3 | Decrease | Increase | 1412.1 | 3.7b |
| 1361.5 | | | 1361.2 | 3.7b |
| 1361.5 | | | 1358.1 | β-pinene |
| 1322.3 | New peak | Increase | 1327.9 | β-pinene |
| 1265.9 | Decrease | Increase | 1264.8 | 3.7b |
| 998.7 | Increase | Decreased/merged with existing 999.6 $cm^{-1}$ peak | 998.4 | β-pinene |
| 991.2 | Decrease | Increase | 995.6 | 3.7a |
| 946.9 | | | 946.1 | β-pinene |
| 946.9 | | | 945.9 | 3.7b |
| 946.9 | | | 944.8 | 3.7c |
| 915.5 | Decrease | Decrease | 917.7 | β-pinene |
| 882.1 | | | 885.0 | β-pinene |
| 882.1 | | | 885.0 | 3.7b |

Table 3.9 also gives assigned peaks that are affected by the annealing process. The presence of intermediate 3.7a is only given by these peaks, as there were no peaks before the annealing process that indicated the presence of 3.7a. It is expected that any peaks that appear during annealing would come from the product of reactions in the matrix, as at higher temperatures the trapped radicals would be able to move and thus react. Additionally, any peaks that decrease in intensity or disappear entirely (without reappearing when cooled back to 8 K) would indicate loss of the molecule attributed to it i.e. the molecule responsible is removed from the matrix, probably from reaction with radicals or from relaxation of the molecule in the lattice to a more favourable position. Three peaks assigned to intermediate 3.7a exhibit this behaviour and

decrease in intensity when cooled back down to 8 K, indicating they can be attributed to the radical intermediate.

Ultimately, due to issues with collection of spectra for both β-pinene experiments – strong presence of isoprene in the first, and severe loss of transmission in the second – definitive assignment of peaks to prove presence of intermediates could not be made. From the peaks identified it is likely that they are present, with reactions confirmed to be occurring due to the presence of CO peaks. However, due to the broad and very intense peaks that β-pinene causes, any small peaks in these areas from intermediates will be buried.

### 3.4.4 Common Peaks Across Spectra

For the experiments discussed in section 3.4, the same series of peaks is seen in the ~ 2100 cm$^{-1}$ area which are associated with the presence of CO, as discussed in section 3.2. The peaks are seen at ~ 2149, 2142, 2138, and 2136 cm$^{-1}$. The same behaviour is seen in all spectra when the matrices are annealed: the ~ 2149 cm$^{-1}$ peak shifting to a lower wavelength at 35 K then back to the original position at 8 K; the addition of a new peak at ~ 2152 cm$^{-1}$ at 35 K that is retained when cooled to 8 K; and a decrease in intensity for the ~ 2138 cm$^{-1}$ peak at 35 K,

Table 3.10 Literature vibrational frequencies and the corresponding assigned experimental values for CO, its aggregates, and its complex with water, for the radical reaction experiments conducted in section 3.2.[5]

| Molecule[5] | Literature Frequency (cm$^{-1}$)[5] | Propyne Frequency (cm$^{-1}$) | Isoprene Frequency (cm$^{-1}$) | β-Pinene Run 1 Frequency (cm$^{-1}$) | β-Pinene Run 2 Frequency (cm$^{-1}$) |
|---|---|---|---|---|---|
| CO·$H_2O$ cluster | 2151 | 2151.8 | 2151.3 | 2151.8 | 2152.2 |
| CO·$H_2O$ 1 - 1 | 2149 | 2149.3 | 2149.4 | 2149.3 | 2149.7 |
| CO dimer | 2142 | 2142.4 | 2142.3 | 2142.2 | 2142.3 |
| CO | 2138 | 2138.3 | 2138.3 | 2138.7 | 2138.2 |
| CO multimer | 2136 | 2136.8 | 2137.1 | 2136.7 | 2136.9 |

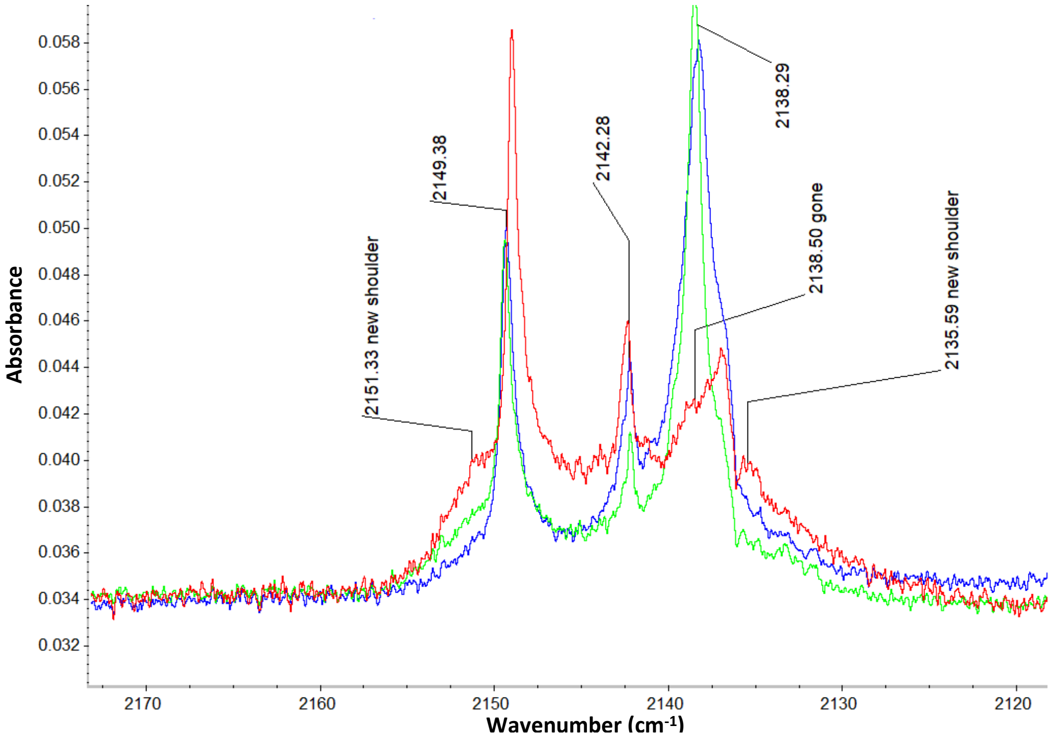

Figure 3.6 Behaviour of CO attributed peaks during annealing process. These spectra are taken from the isoprene experiment. Blue: Mixture deposited at 8 K subject to Tesla-coil discharge. Red: Annealed to 35 K. Green: Cooled to 8 K.

which then returns to the original intensity or thereabouts at 8 K, shown in Figure 3.6. Table 3.10 gives the assignments of these peaks.

There is some conflicting literature information about the assignment of the 2149 and 2138 cm$^{-1}$ peaks. The majority of literature assigns the 2149 cm$^{-1}$ peak to the complex CO·$H_2O$ and the 2138 cm$^{-1}$ peak to the CO monomer, attributing the temperature dependence exhibited during annealing by the monomer peak to librational motion, a kind of constricted rotation. When looking at the propyne blank run, which had no water added to the gas stream, the most intense and sharpest peak is at 2136 cm$^{-1}$, with the 2138 cm$^{-1}$ peak the second most intense (Figure 3.7). Since there is no additional water added to the system, peaks attributed to the presence of CO and its aggregates would be expected in greater intensity than that of the CO·$H_2O$ complex. If this is the case, the 2138 cm$^{-1}$ peak can be attributed to the CO monomer, in agreement with the majority of literature data. However, when looking at the peaks in this range found in the acetone experiment in section 3.2, the most intense peak present is at ~ 2149 cm$^{-1}$, with a much less intense and broad peak barely present at ~ 2138 cm$^{-1}$, which would indicate the 2149 cm$^{-1}$ peak is attributed to the monomer CO and the 2138 cm$^{-1}$ peak to an aggregate or complex.

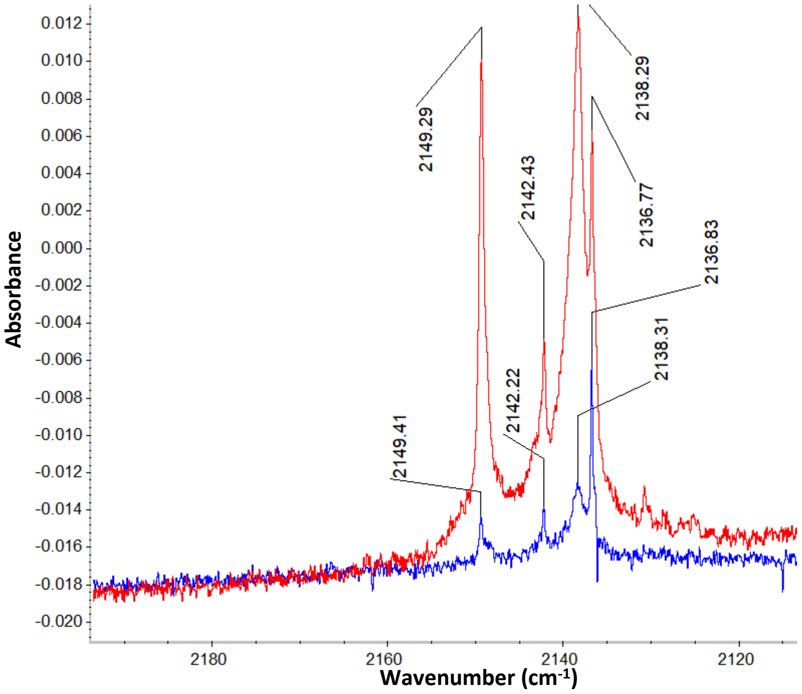

Figure 3.7 CO attributed peaks for the propyne blank experiment (blue) and propyne TC-discharge experiment (red). For the TC-discharge experiment, the 2149 cm$^{-1}$ and 2138 cm$^{-1}$ peaks are of similar intensity, but for the blank experiment, the 2138 cm$^{-1}$ peak is more intense, second only to the 2136 cm$^{-1}$ peak.

Evidence for the divergent assignment of peaks – 2149 cm$^{-1}$ being monomeric CO and 2138 cm$^{-1}$ an aggregate – is given by Leroi et al. (1964) and Nxumalo et al. (2006).[6, 9] Nxumalo et al. give spectra that show a decrease in peak height ratio between the 2138 and 2149 cm$^{-1}$ peaks as the ratio of CO deposited increases, indicating the peak at 2149 cm$^{-1}$ is attributable to the CO monomer since as deposition ratio increases, the sample becomes more dilute and therefore the peak due to an isolated CO molecule would increase in intensity, whereas a peak due to aggregates would decrease in intensity, as the 2138 cm$^{-1}$ peak does. Leroi et al. also argue that since the 2149 cm$^{-1}$ peak becomes less intense but maintains its shape as deposition ratio increases, it must be attributed to the CO monomer, whereas the peak at 2138 cm$^{-1}$, which broadens and increases in intensity with increasing deposition ratio, must be attributed to the CO aggregate. They deposit at a temperature of 17 - 20 K, which Givan et al. (1996) has shown gives a broader peak at 2138 cm$^{-1}$, with the explanation that at higher temperatures the CO monomer is able to rotate more and therefore broadens and flattens the peak (becomes "smeared out").[28]

Givan et al. (1996) find both a deposition temperature and deposition ratio dependence on the peak intensity and presence.[28] They use a deposition ratio of 100:1:1 Ar:CO:$H_2O$, similar to that in section 3.2 of this work, which has a ratio of ~ 100:1:1 Ar:Sample:$H_2O$ (with the acknowledgement that not all sample will be converted to CO and therefore a lower ratio will occur in this work). Despite this, a similar peak intensity and shape is seen in Figure 3.8 to the spectrum labelled C in Figure 3.9. Both this spectrum and the spectra in this work are deposited at 15 K. Givan et al. also note that CO is able to rotate in the matrix and observe a change in shape for the corresponding 2138 cm$^{-1}$ peak when annealed to higher temperatures that reverts back when cooled to 5 K. In this work, the 2138 cm$^{-1}$ peak reduces in intensity and in some cases disappears completely when annealed to higher temperatures but does revert back when cooled to 8 K, exhibiting similar behaviour. Similarly the presence of new peaks at 2136, 2142, and 2151 cm$^{-1}$ when annealed to higher temperatures that are retained once cooled to 8 K occurs in this work and in Givan et al.'s work, which they assign to either CO aggregates or CO·$H_2O$ complexes. Given the similarities in the spectra recorded in this work and those detailed in Givan et al.'s, as well as a lack of spectra with differing deposition rates to allow comparison to Leroi et al. and Nxumalo et al.'s spectra, Givan et al.'s assignments are employed in this work, attributing the 2149 cm$^{-1}$ peak to the CO·$H_2O$ complex and the 2138 cm$^{-1}$ peak to the CO monomer. A majority of literature reviewed in this work agrees with this assignment.[7, 28, 30, 31]

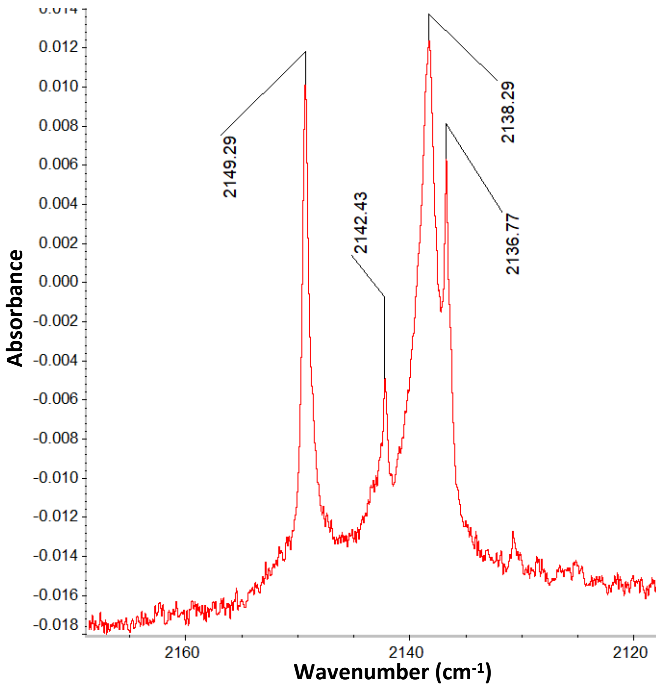

Figure 3.8 CO attributed peaks for the propyne TC-discharge experiment. Similar peak shape and behaviour is experienced as noted in Givan et al. (1996).[25]

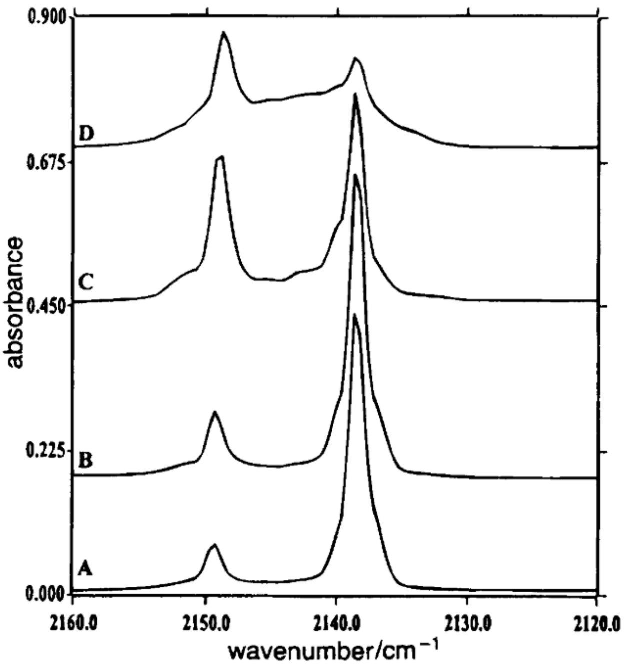

Figure 3.9 2120 – 2160 cm$^{-1}$ section of spectra of 100:1:1 Ar:$H_2O$:CO mixtures. Spectra are recorded at 5 K but are deposited at different temperatures: A. 5 K, B. 10 K, C. 15 K, and D. 20 K. Reproduced from Givan et al. (1996).[25]

When comparing the radical reaction spectra, there are a number of peaks in common across multiple spectra. Listed in Table 3.11 are the peaks that can be assigned to $HO_x$ radicals and their complexes with water, as well as CO, $CO_2$, and their complexes with water. The presence of $\cdot OH$, $HOO\cdot$, $H_2O_2$, and their complexes with water are confirmed across the spectra, as well as the presence of $O_3$. Additionally, as discussed above, the presence of CO and $CO_2$ complexes with water is also confirmed, along with the simple hydrocarbon oxidation product ketene ($H_2CCO$), which is a possible product for the propyne reaction 3.5b. The presence of these products indicates a reaction is occurring, confirmed also by the presence of the reaction intermediates assigned in the subsections above.

Table 3.11 List of assigned frequencies in the radical reaction spectra that relate to $HO_x$ radicals and their complexes with water, as well as the presence of CO and $CO_2$.

| **Molecule/ Complex** | **Literature Peak ($cm^{-1}$)** | **Reference** | **Experimental Peak ($cm^{-1}$)** | | |
|---|---|---|---|---|---|
| | | | **Propyne** | **Isoprene** | **β-pinene** |
| $\cdot OH$ | 3554 | 23 | 3553.3 | | |
| | ~ 3548 - 3549 | 15, 16, 23 | 3549.6 | | |
| $H_2O\cdot OH$ | 3535.419 | 22 | 3535.3 | 3533.9 | 3533.6 |
| | 1593.4 | 1 | | | 1593.0 |
| $HOO\cdot$ | 3412.8 | 23 | 3413.6 | | |
| | 1388.5 | 23 | 1388.4 | | |
| $HOO\cdot H_2O$ | 3230.224 | 22 | | | 3231.7 |
| $H_2O_2$ | 1272.506 | 22 | 1271.1 | | |
| | 1267.607 | 22 | | | 1265.9 |
| $H_2O\cdot H_2O_2$ | 1240.169 | 17 | | 1238.1 | |
| $H_2O\cdot CO$ | 2149.2 | 26 | 2149.3 | 2149.4 | 2149.7 |
| | 1595.4 | 26 | 1589.6 | 1589.4 | 1589.5 |
| $H_2O\cdot CO_2$ | 1620.566 | 26 | | | 1623.8 |
| $H_2CCO$ | 1383.235 | 24 | 1382.9 | 1384.8 | |
| $O_3$ | 1110.823 | 24 | 1111.7 | 1113.8 | |

### 3.4.5 Radical Reaction Conclusions

For each radical reaction experiment in section 3.4, the presence of radical intermediates has been indicated by assigned peaks in the reaction spectra. Reactions have been confirmed to be occurring by the presence of peaks attributed to CO and its aggregates and water complexes, as well as the presence of peaks attributed to $HO_x$ radicals and their water complexes. Although the presence of intermediates hasn't been able to be assigned to peaks as desired, definitive assignment of expected peaks to the radical intermediates is difficult due to a few reasons: the intermediates differ in composition from the reactants only by the addition of an ·OH, meaning many of their expected vibrational frequencies are very similar to that of the reactants; and since the reactants are found in much higher concentrations than the intermediates, it is difficult to find peaks attributed to the intermediates in congested areas or areas where reactant peaks are present.

If these experiments were to be conducted again, there are some modifications to procedure which could improve results and make assigning spectra easier. Separate 'blank' experiments should be run, as was done for propyne, as this gives a spectrum to compare to of the reactant with argon subjected to Tesla-coil discharge. Blanks were run for each experiment, but they were not run with a consistent method or separate to the reaction experiment, which would have improved data collection. Running blanks separately would reduce the amount of deposition time required and therefore reduce the intensity of the peaks that could be burying expected intermediate peaks, as instead of beginning the experiment by allowing the sample or water to build, reaction could immediately occur giving the intermediate peaks a chance to build in intensity. A greater ratio of water to sample could be used to increase the amount of ·OH formed and therefore increase the intensity of intermediate peaks, although this could create more congested areas where water peaks are present. The system should also be "baked out" between experiments to remove as much water as possible from the system, reducing the background significantly, as it was seen to build up over the experiments run. Additionally, each experiment in which suspected radical peaks are seen should be repeated to test reproducibility of results.

## 3.5 Conclusion

A radical source was established in this chapter. Experiments using a mixture of milli-Q water and argon subjected to Tesla-coil discharge were seen to produce peaks in the MI-FTIR spectrum that indicated the presence of $HO_x$ radicals like ·OH and HOO·, as well as complexes of the radicals with water. Once this radical source was established, radical reactions were run, in which three hydrocarbons were added downstream of an excited water and argon mixture and then trapped in the matrix using MI-FTIR. Radical intermediates and potential reaction products for these reactions of ·OH with propyne, isoprene, or β-pinene were investigated, using a combination of calculated corrected frequencies and the peaks seen in the MI-FTIR spectra. The presence of intermediates was seen for propyne and isoprene, but difficulties in collecting data for the β-pinene reactions meant no substantive evidence was seen. Additionally, the presence of CO peaks and those related to the CO and water complexes is also seen, also indicating reactions are occurring (a small carbon source could be from o-rings downstream of the excitation source). The presence of $HO_x$ radicals and their water complexes are also noted within the radical reaction experiments.

Due to the difficulties in using this technique to detect the radicals, the detection method will be changed in further research, since the encountered issues are intrinsic to the method – examples are low signal of intermediates versus high signal of reactants, issues with the signal-to-noise ratio, difficulty with appropriate dilution causing broad peaks, and loss of transmission during experiments when annealing. However, this work was not done at a loss, as it indicated that a different ·OH detection technique was required. Instead of attempting to detect radical intermediate products or directly detect ·OH itself, which is known to be difficult, a more sensitive technique or an indirect technique like spin-trapping can be used instead.

## 3.6 References

1. Engdahl, A.; Karlström, G.; Nelander, B., The water–hydroxyl radical complex: A matrix isolation study. *J. Chem. Phys.* **2003,** *118* (17), 7797-7802.
2. Lin, L. J.-T.; Ausloos, P., Gas phase photolysis of acetone in the far ultra-violet. *J. Photochem.* **1972,** *1* (6), 453-462.
3. Saheb, V.; Zokaie, M., Multichannel Gas-Phase Unimolecular Decomposition of Acetone: Theoretical Kinetic Studies. *J. Phys. Chem. A.* **2018,** *122* (28), 5895-5904.
4. Zhang, X. K.; Parnis, J. M.; Lewars, E. G., et al., FTIR spectroscopic investigation of matrix-isolated isomerization and decomposition products of ionized acetone: Generation and characterization of 1-propen-2-ol. *Can. J. Chem.* **1997,** *75* (3), 276-284.
5. Han, S. W.; Kim, K., Infrared Matrix Isolation Study of Acetone and Methanol in Solid Argon. *J. Phys. Chem.* **1996,** *100* (43), 17124-17132.
6. Leroi, G. E.; Ewing, G. E.; Pimentel, G. C., Infrared Spectra of Carbon Monoxide in an Argon Matrix. *J. Chem. Phys.* **1964,** *40* (8), 2298-2303.
7. Dubost, H.; Abouafma, L., Infrared-Spectra of Carbon-Monoxide Trapped in Solid Argon - Double-Doping Experiments with $H_2O$, $NH_3$ and $N_2$. *Chem. Phys. Lett.* **1972,** *17* (2), 269-273.
8. Parnis, J. M.; King, K. A.; Thompson, M. G., The chemistry of ionized acetone/Ar mixtures under varying gas flow and mole ratio conditions: a matrix-isolation study. *J Mass Spectrom* **2009,** *44* (5), 652-61.
9. Nxumalo, L. M.; Ngidi, E. K.; Ford, T. A., The structures of some dimers of carbon monoxide—an infrared matrix isolation spectroscopic and ab initio molecular orbital study. *J. Mol. Struct.* **2006,** *786* (2-3), 168-174.
10. Vione, D.; Maurino, V.; Minero, C., et al., The atmospheric chemistry of hydrogen peroxide: a review. *Ann Chim* **2003,** *93* (4), 477-88.
11. Gill, K. J.; Hites, R. A., Rate Constants for the Gas-Phase Reactions of the Hydroxyl Radical with Isoprene, α- and β-Pinene, and Limonene as a Function of Temperature. *J. Phys. Chem. A.* **2002,** *106* (11), 2538-2544.
12. Hites, R. A.; Turner, A. M., Rate constants for the gas-phase β-myrcene + OH and isoprene + OH reactions as a function of temperature. *Int. J. Chem. Kinet.* **2009,** *41* (6), 407-413.
13. Campuzano-Jost, P.; Williams, M. B.; O'Ottone, L., et al., Kinetics of the OH-initiated oxidation of isoprene. *Geophys. Res. Lett.* **2000,** *27* (5), 693-696.
14. Langford, V. S.; Williamson, B. E., Magnetic circular dichroism of the hydroxyl radical in an argon matrix. *Journal of Physical Chemistry A* **1997,** *101* (17), 3119-3124.
15. Langford, V. S.; McKinley, A. J.; Quickenden, T. I., Identification of $H_2O.HO$ complexes in argon matrices. *J. Am. Chem. Soc.* **2000,** *122* (51), 12859-12863.
16. Cheng, B. M.; Lee, Y. P.; Ogilvie, J. F., The Infrared-Absorption Spectrum of Hydroxyl Radicals in Solid Argon. *Chem. Phys. Lett.* **1988,** *151* (1-2), 109-115.
17. Gonzalez, L.; Mo, O.; Yanez, M., High-level ab initio versus DFT calculations on $(H_2O_2)_2$ and $H_2O_2$-$H_2O$ complexes as prototypes of multiple hydrogen bond systems. *J. Comput. Chem.* **1997,** *18* (9), 1124-1135.
18. Mo, O.; Yanez, M.; Rozas, I., et al., Structure, Vibrational Frequencies and Thermodynamic Properties of Hydrogen Peroxide-Water Dimers - an Ab-Initio Molecular-Orbital Study. *Chem. Phys. Lett.* **1994,** *219* (1-2), 45-52.
19. Cooper, P. D.; Kjaergaard, H. G.; Langford, V. S., et al., Infrared measurements and calculations on $H_2O.HO$. *J Am Chem Soc* **2003,** *125* (20), 6048-9.
20. Dobado, J. A.; Molina, J. M., Ab-Initio Molecular-Orbital Study of the Hydrogen Peroxide-Water Complex (HOOH ... $H_2O$). *J. Phys. Chem.* **1994,** *98* (7), 1819-1825.

21. Tsuji, K.; Shibuya, K., Infrared spectroscopy and quantum chemical calculations of OH-$(H_2O)_n$ complexes. *J Phys Chem A* **2009,** *113* (37), 9945-51.
22. Sennikov, P. G.; Ignatov, S. K.; Schrems, O., Complexes and clusters of water relevant to atmospheric chemistry: $H_2O$ complexes with oxidants. *ChemPhysChem* **2005,** *6* (3), 392-412.
23. Khriachtchev, L.; Pettersson, M.; Tuominen, S., et al., Photochemistry of hydrogen peroxide in solid argon. *J Chem Phys* **1997,** *107*.
24. Johnson, R. D. NIST Computational Chemistry Comparison and Benchmark Database, NIST Standard Reference Database Number 101. http://cccbdb.nist.gov/.
25. Lockhart, J.; Blitz, M. A.; Heard, D. E., et al., Mechanism of the reaction of OH with alkynes in the presence of oxygen. *J Phys Chem A* **2013,** *117* (26), 5407-18.
26. Wennberg, P. O.; Bates, K. H.; Crounse, J. D., et al., Gas-Phase Reactions of Isoprene and Its Major Oxidation Products. *Chem. Rev.* **2018,** *118* (7), 3337-3390.
27. Kaminski, M.; Fuchs, H.; Acir, I. H., et al., Investigation of the β-pinene photooxidation by OH in the atmosphere simulation chamber SAPHIR. *Atmos. Chem. Phys.* **2017,** *17* (11), 6631-6650.
28. Givan, A.; Loewenschuss, A.; Nielsen, C. J., FTIR studies of CO-water complexes in argon matrices and in porous ices. *J. Chem. Soc. Faraday. T.* **1996,** *92* (24), 4927-4933.
29. Lundell, J.; Rasanen, M., The 193-nm Induced Photodecomposition of HCOOH in Rare-Gas Matrices - the $H_2O$-CO 1/1-Complex. *J. Phys. Chem.* **1995,** *99* (39), 14301-14308.
30. Abe, H.; Takeo, H.; Yamada, K. M. T., Infrared spectroscopy of CO trapped in an argon matrix revisited. *Chem. Phys. Lett.* **1999,** *311* (3-4), 153-158.
31. Abe, H.; Yamada, K. M. T., Infrared spectra of the CO–$H_2O$ 1–1 cluster trapped in an argon matrix. *J. Chem. Phys.* **2001,** *114* (14), 6134-6141.
32. Lelieveld, J.; Dentener, F. J.; Peters, W., et al., On the role of hydroxyl radicals in the self-cleansing capacity of the troposphere. *Atmos. Chem. Phys.* **2004,** *4*, 2337-2344.

# 4.0 Photochemistry and $TiO_2$ Experiments

## 4.1 Introduction

With the difficulty in using MI-FTIR as a detection method for the formation of ·OH radicals, a different detection method of a Residual Gas Analyser (RGA) was employed. The RGA is a gas phase specific mass spectrometer with a quadrupole probe that can measure pressures to the $10^{-9}$ Torr scale. It allows for targeted detection of mass fragments, with the ability to measure the pressure of chosen mass fragments over time or to measure the pressure of a range of mass fragments in a series of scans. This technique is therefore more complementary to the specific aims of the research than FT-IR, which was largely impacted by the low intensity of the peaks of interest, and the presence of these peaks of interest being obfuscated by complex and noisy regions of the spectra. The RGA would in theory allow these peaks to be singled out from the noise by specifically tracking the peaks, instead of measuring the entire spectrum. Alongside this new detection method, $TiO_2$ was employed as the photocatalyst to generate ·OH from water vapour, as discussed in section 1.7. This process was conducted inside of a fluorescence cell that was built in-house, using a spectrofluorophotometer as the excitation source.

Before implementing these new methods, several preliminary studies were required. Firstly, the fluorescence cell was designed to house a slide, requiring development of a method for coating a flat surface with $TiO_2$. A flat surface is preferred to other forms, such as powder, as it provides a large surface area for irradiation and contact with gas-phase reactants. Secondly, the photoactivity of the $TiO_2$ slides was confirmed in a probe study, to determine the slides' ability to photocatalyse the formation of ·OH. Thirdly, the infrastructure for the final experiments of the chapter were built in-house, including the fluorescence cell and the gas-handling structures. Finally, the use of these methods was employed in section 4.5 to detect gas-phase radicals and reaction products by RGA, with the aim to simulate atmospheric conditions.

## 4.2 Depositing $TiO_2$

Several different methods were investigated to find the best available method to disperse the $TiO_2$ across a flat surface. Initially, the simplest method of drop-casting was used. A glass slide (super white glass) was cleaned with 36% HCl and rinsed with milli-Q water to remove organic material. Then, a slurry of 2.5 mg $mL^{-1}$ $TiO_2$ (Sigma Aldrich, 248576, anatase, average particle size 44 µm) in milli-Q water was deposited onto the slides, as previously used by van den Berg (2019).[1] The slides were then annealed at 250 ℃ for 24 hours. However, the coating was powdery and detached from the substrate.

Following this, the Rapid Annealing Self-Solution-Shearing (RASSS) method was investigated.[2] This method heats the substrate to above the boiling point of the solvent used (in this case, 195 ℃) on a slightly angled surface. When the solution is deposited onto the hot substrate, the solvent evaporates as the solution pools down the slide (due to the angle), leaving a film of solvate behind. A thick coating was achieved with minimal cracking or gaps using this technique. Different concentrations of $TiO_2$ suspensions were made during the testing process to obtain a thick and uniform coating. Initially a layered approach was employed in which a 1 mg $mL^{-1}$ suspension was deposited several times resulting in non-uniform surfaces (Figure 4.1), following which a single layer of a more concentrated 48.4 mg $mL^{-1}$ suspension gave increased surface coverage and a more uniform surface. However, when the slides were submerged in milli-Q water the coating flaked off. The probe study conducted in section 4.3 requires a slide that is stable when suspended in aqueous solution, so the spin-coating method was investigated instead.

Figure 4.1 Initial $TiO_2$ coating test with one layer (top) and two layers (bottom) deposited. Adding extra layers dissolved the preceding layers.

The spin-coating method, when compared to drop-casting and RASSS, involves more trial and error to find the optimum conditions. Solutions can be deposited either statically (not spinning) or dynamically (whilst the slide is spinning).[3, 4] When deposited, the solution is spun off at a set rpm, determined by the solvent used and the evaporation rate. When the substrate is spun, the solution spreads across the surface and evaporates, leaving a smooth film behind. A range of conditions were tested to find the optimum spin-coating conditions for the slides. Using an Ossila spin coater, slides were spun at 700 – 2000 rpm, with 50 - 400 µL additions of concentrations from ~ 1 mg/mL - 0.5 g/mL $TiO_2$ suspensions, using both glass and quartz films that had been cleaned with piranha solution and stored in milli-Q water. The slides were sized from 75x25 mm (microscope slide size) to smaller ~ 9x9 mm sized. Slides that were run at 1000 rpm with higher concentrations of solution produced slides with the best coverage. All suspensions were dispensed statically and spun for 10 seconds. Once coated, the slides were transferred to a hotplate in an ambient environment to anneal. The slides that were ramped up from room temperature to 500 ℃ gave better annealed films in comparison to those that were put on a pre-heated hotplate directly at 500 ℃, giving more consistent coverage and retention.

Figure 4.2 shows the slides in order of film retention after being submerged in distilled water and agitated. The RASSS-deposited slide, slide 1, immediately dissolved upon contact with the water, whereas other slides retain some amount of film. Primarily, the thinner the coating of $TiO_2$, the more $TiO_2$ was retained once submerged. Slides 4 and 5 have had the thickest part of the coating come off in the water, but have retained the thinnest section, giving the uneven coating observed. The film that gave the best retention and coverage was formed using a ~ 0.5 g/mL suspension, dispensed statically and spun at 1000 rpm for 10 s, then immediately spun at 2000 rpm for 10 s, followed by annealing by ramping up from room temperature to 500 ℃ for 10 mins, then cooled to ambient temperature. This method also gave films that were thinner and more uniform than the RASSS method, as well as able to retain film when submerged in aqueous solution. These were the films used in the experiments in this chapter. The thicknesses of these films were not determined as they were optically dense and did not transmit, and therefore analysis could be based on the total absorption of incident light flux.

Figure 4.2 Slides in order of film retention after being submerged in distilled water. 1: RASSS-deposited slide. 2 & 3: 1 mg/mL suspension spun at 700 rpm. 4: 1 mg/mL suspension spun at 1000 rpm. 5 & 6: 0.5g/mL suspension spun at 1000 rpm. 7: 0.5g/mL suspension spun at 1000 rpm, then 2000 rpm. Slides 5 & 6 are glass, all other slides are quartz. All slides are cleaned with piranha solution and then stored in milli-Q water before depositing.

## 4.3 Fluorescent Probe Studies

### 4.3.1 Introduction

To confirm whether the $TiO_2$ slides were photochemically active, a fluorescent probe study was conducted based on literature methods using coumarin and terephthalic acid (TPA) probes.[5-10] Fluorescence probe studies work off the basis that the reaction between the probe molecule and ·OH form one strongly fluorescent product (and no other fluorescing products if multiple can form). The probe studies track the increase in emission intensity at a wavelength attributed to the fluorescent product (460 nm for coumarin and 425 nm for TPA) while the probe solution is excited ($\lambda_{ex}$ = 332 nm for coumarin and $\lambda_{ex}$ = 315 nm for TPA). The increase in emission intensity of the peak of interest over time has been found to be directly correlated to the production of ·OH in the system when exposed to an excitation source.[5] As a result, the rate of formation of the fluorescent product can be determined, and from that the total rate of production of ·OH can be back-calculated.

Coumarin and TPA are common fluorescent probes. Both coumarin and TPA form only one strongly fluorescent reaction product, shown in Figure 4.3, when reacted with ·OH.[5] Due to TPA's symmetry, only one reaction product can form, 2-hydroxyterephthalic acid (referred to as 2TPA);

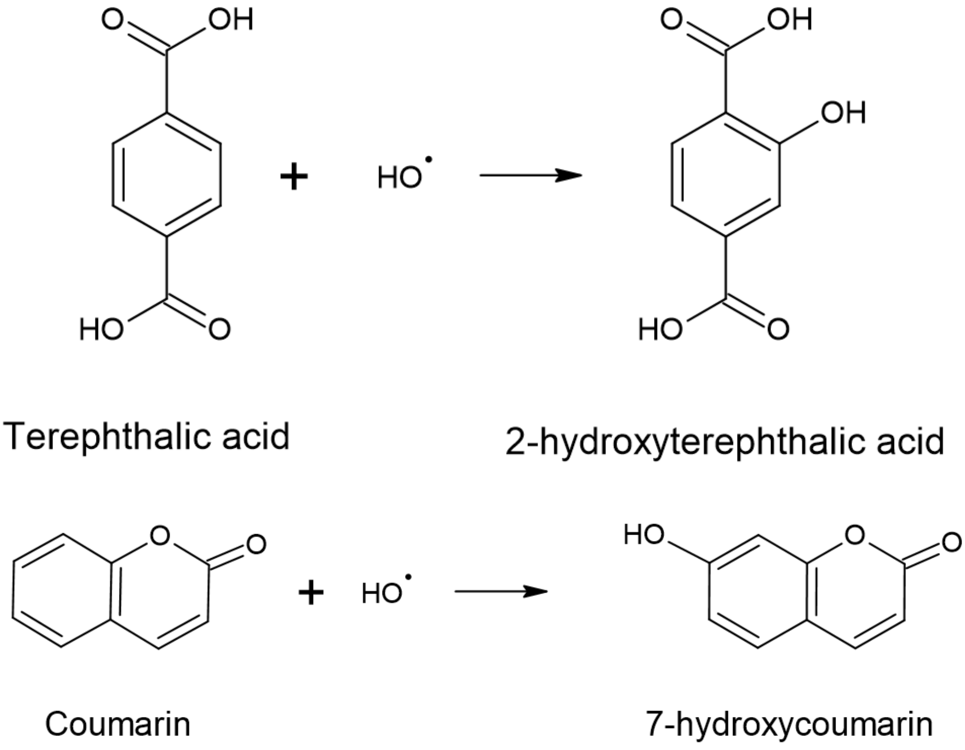

Figure 4.3 Top: Reaction of terephthalic acid (TPA) with ·OH to form the fluorescent product, 2-hydroxyterephthalic acid (2TPA). Bottom: Reaction of coumarin with OH· to form the only fluorescent product, 7-hydroxycoumarin (7HC). Source: Ishibashi, 2000.[5]

for coumarin, multiple products can form but only 7-hydroxycoumarin (referred to as 7HC) is significantly fluorescent.[11] Additionally, TPA does not fluoresce itself, so there is no interference in measurement from unreacted starting material, and coumarin is considered "essentially non-fluorescent".[22] It is known that for a 1 mM solution of coumarin, 6.1% of ·OH produced can be detected as the 7HC product, meaning that the concentration of ·OH produced by photocatalysis can be calculated from the amount of 7HC formed.[8,12] Similarly, for TPA an approximate 31 - 35% conversion rate to 2TPA is known.[13]

Two probe studies considered here use $TiO_2$-coated slides instead of the aqueous suspension that is common to other studies. Ishibashi et al. (2000) used dip-coated soda-lime glass plates along with both coumarin and TPA as their probe molecules.[5] They found the optimum concentrations of both molecules ($1 \times 10^{-4}$ M for coumarin and $5 \times 10^{-4}$ M for TPA in $2 \times 10^{-3}$ M NaOH) that are used throughout much of the literature. They determined that the UV-light intensity and concentrations of product are linearly related and that thus zero-order reaction kinetics are followed for ·OH formation on the surface of the slide, a finding that is echoed through the rest of the studies. Zero-order kinetics typically occur for reactions on a surface, where the concentration of the reactant remains constant and the rate depends on the absorption of the reactant onto the surface and not the concentration of the reactant itself.[23] Cernigoj et al. (2009) also used slides for their $TiO_2$ source but used a range of soda-lime glass slides with differing numbers of layers coated onto them to investigate effects of thickness and amount of $TiO_2$ on the slide.[14] They found that the ratio between degraded coumarin and formed 7HC is constant between the different slides. These studies show that the fluorescent-probe method is applicable for experiments with a $TiO_2$-coated slide source.

Coumarin is used as a probe molecule in other studies covered here, all using aqueous suspensions of $TiO_2$ as their catalyst. Czili et al. (2008) investigated the reaction in the presence of added oxygen, and found that when oxygen was added to the system it reacted with 7HC, leading to the disappearance of the 7HC peak within 60 minutes of photolysis.[10] They also found that only ·OH that is not adsorbed to the catalyst surface reacted with coumarin due to a low redox potential of surface ·OH groups. Zhang et al. (2013) and Zhang et al. (2014) have similar findings in their probe studies, determining a 6.1% conversion rate of ·OH to 7HC, as well as generation rates of total ·OH.[8, 9]

For TPA, only one study gives a rate of ·OH formation or of formation of reaction product 2TPA. Jimenez-Relinque et al. (2018) use a calibration curve to determine the rate of formation of 2TPA and the amount produced.[7] They assume a 35% trapping factor for this reaction. They also investigate the effect of phase of $TiO_2$ on rate and find that a mixed phase gives the best results. This is similar to Lv et al.'s (2010) study, which finds that a 6:4 anatase:rutile phase mixture gives the best formation rate.[6]

Coumarin and TPA have also been investigated using techniques that don't necessarily look into rates of formation of product. Louit et al. (2005) use coumarin and gamma radiolysis to investigate the product distribution, finding that 5-hydroxycoumarin (5HC) is the major product, 3-hydroxycoumarin (3HC) is the minor product, and 7HC is the only fluorescent product, thus making coumarin applicable as a fluorescent probe molecule.[11] De-Nasri et al. (2021) use coumarin and HPLC to determine the products being made, and to investigate whether the rate found is applicable across all circumstances.[12] Gonzalez et al. (2018) use TPA and investigate how it reacts with different metals, finding that the conversion factor is dependent on pH but that it ranges between 31 - 35%, and finally Li et al. (2015) use TPA and the transient plasma spark technique to find that intensity is directly related to concentration of the product, which is in turn directly related to ·OH produced.[15]

However, there are a large number of assumptions used in these calculations, as is pointed out by De-Nasri et al. (2021).[12] They state that, the total ·OH in the system that reacts with the probe molecule, $[\cdot\mathrm{OH}]_{TOT}$, is the sum of all the ·OH that has reacted to form each product, where $[\cdot\mathrm{OH}]_n$ is the concentration of ·OH that reacted to form product n:

$$[\cdot\,\mathrm{OH}]_{TOT} = [\cdot\,\mathrm{OH}]_1 + [\cdot\,\mathrm{OH}]_2 + \cdots [\cdot\,\mathrm{OH}]_n$$

$[\cdot\mathrm{OH}]_n$ differs between processes, and De-Nasri et al. claim that it is more appropriate and accurate to calculate $[\cdot\mathrm{OH}]_n$ than it is to calculate $[\cdot\mathrm{OH}]_{TOT}$ as it involves other factors that can't all be quantified. Assumptions are therefore made during these calculations that: 100% of the monitored product is formed by the reaction of ·OH with the probe molecule; that decay via other pathways of both the probe molecule and reaction product is insignificant compared to that of the monitored reaction; and that the conversion factors are applicable to the current conditions. Additional assumptions of no interfering absorption processes from the excitation and fluorescent emission processes are also made when doing calculations in section 4.3.2.

### 4.3.2 Experimental Details and Results

A 1 x $10^{-3}$ M solution of coumarin was made in milli-Q water. A 5 x $10^{-4}$ M solution of terephthalic acid was made in 2 x $10^{-3}$ M NaOH. $TiO_2$ slides were made for these experiments using the same methods outlined in section 4.2 but using a smaller (~ 9 x 9 mm) quartz substrate so that the slides could be suspended inside a 3 mL quartz cuvette inside the Shimadzu RF-6000 spectrofluorophotometer, using the LabSolutions RF software for data collection and analysis (see Figure C.3 in Appendix for diagram). Ideally, a different source would be used to monitor emissions and excite the reagents, but this was not an available option.

The following general method was used for probe experiments: 2 - 3 mL of probe solution was added to a quartz cuvette containing a $TiO_2$-coated slide. The slide was then exposed to light $\lambda < 387$ nm (332 nm and 315 nm for coumarin and TPA respectively) and emission monitored. The solution was stirred continuously (except during measurement) by a magnetic flea and a MST magnetic stirrer to ensure contact with the photocatalyst, and emission was measured periodically, every 5 – 10 minutes. An emission peak at 460 nm and 425 nm for coumarin and TPA respectively was seen to appear and increase with illumination time. In “blank” tests run with the same conditions but with no $TiO_2$ slide present, no significant peak was seen to appear, indicating the peak comes from a reaction product.

In initial tests using RASSS-coated slides, the slides did not remain coated with $TiO_2$. Instead, the $TiO_2$ flaked off into solution. This meant initial fluorescent probe experiments were essentially done with an aqueous suspension of $TiO_2$ that was continually stirred since the slides disintegrated over time. Additionally, these tests also used 20 nm slit widths for both emission and excitation, giving large intensity signals and saturating the measurement in the case of TPA. These trial experiments thus confirmed the method used by literature and that the powder in suspension was photochemically active but required finetuning to be able to successfully and quantitively apply to films of $TiO_2$ used in this work.

Spin-coated slides were thus used as they retained the coating after being submerged in solution. The slide was suspended in a cuvette containing 2 mL of probe solution above a magnetic stir bar so that the stir bar wouldn’t hit the slide, but the slide was still in solution whilst being irradiated. 5 nm slit widths were used for both excitation and emission. As expected, this method gave similar results to the attempts with the RASSS-deposited slides but retained the catalyst as a film, with the peaks at 460 nm and 425 nm for coumarin and TPA respectively appearing after irradiation and continuing to grow with irradiation time (Figures 4.4 and 4.5). The emission plots in Figures 4.4 and 4.5 are given with normalised intensity values to compare the increase in intensity seen at the monitored wavelength of interest. The raw, un-normalised data can be found in Appendix C. Figure 4.4 gives spectra taken at 30-minute intervals during continuous irradiance for a 1 mM coumarin solution, and a plot of the intensity over time at 460 nm. Table 4.1 gives the linear regression details for this plot. A clear increase in intensity is seen at 460 nm over irradiance time. When monitoring this peak, a linear relationship is observed, which is confirmed by literature. The same relationship was observed in the TPA experiment (Figure 4.5, Table 4.2). When excited with $\lambda_{ex}$ = 315 nm light, a significant increase in emission intensity was observed at 425 nm (Figure 4.5). Since TPA isn't fluorescent by itself, this peak is due to a reaction product. When monitoring the emission intensity at 425 nm, a linear relationship is also observed. Although it may be more accurate to have fitted only the first 60 minutes of data, where the linear relationship is stronger and less likely to have been affected by factors like inner filter effects from high concentrations of products, the fit and adjusted $R^2$ values of both plots monitoring the wavelength of interest is acceptable to allow a linear relationship to be used.

Table 4.1 Slope, intercept, standard errors for each, and adjusted $R^2$ value for the plot of intensity vs irradiation time at 460 nm (Figure 4.4).

| Property | Value |
|---|---:|
| m | 18.31 |
| c | 337.41 |
| Standard error of m | 0.29 |
| Standard error of c | 34.76 |
| Adjusted $R^2$ | 0.9936 |

Table 4.2 Slope, intercept, standard errors for each, and adjusted $R^2$ value for the plot of intensity vs irradiation time at 425 nm (Figure 4.5).

| Property | Value |
|---|---:|
| m | 18.94 |
| c | 1109.55 |
| Standard error of m | 0.96 |
| Standard error of c | 54.49 |
| Adjusted $R^2$ | 0.9916 |

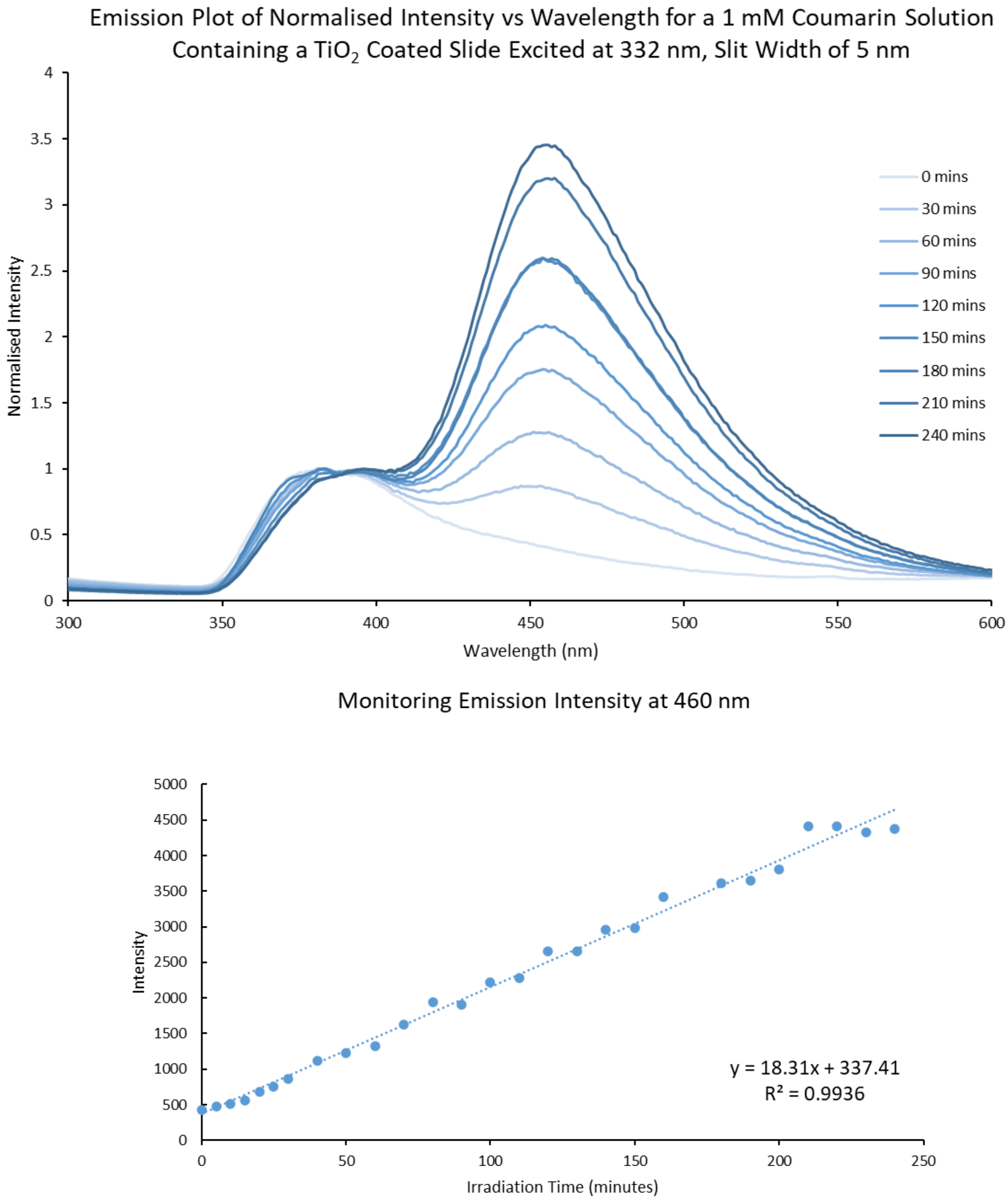

Figure 4.4 Top: Emission plot for the 1 mM coumarin solution containing a $TiO_2$-coated slide undergoing continuous UV irradiation ($\lambda_{ex}$ = 332 nm). Data were recorded every 10 minutes but for simplicity scans taken every 30 minutes are shown. Slit widths were 5 nm, and a 360 nm filter was used. The intensity is normalised to the highest intensity for each scan. There is a clear increase in intensity at 460 nm with irradiance time. Bottom: Monitoring emission intensity at 460 nm. There is an increase in intensity with irradiation time.

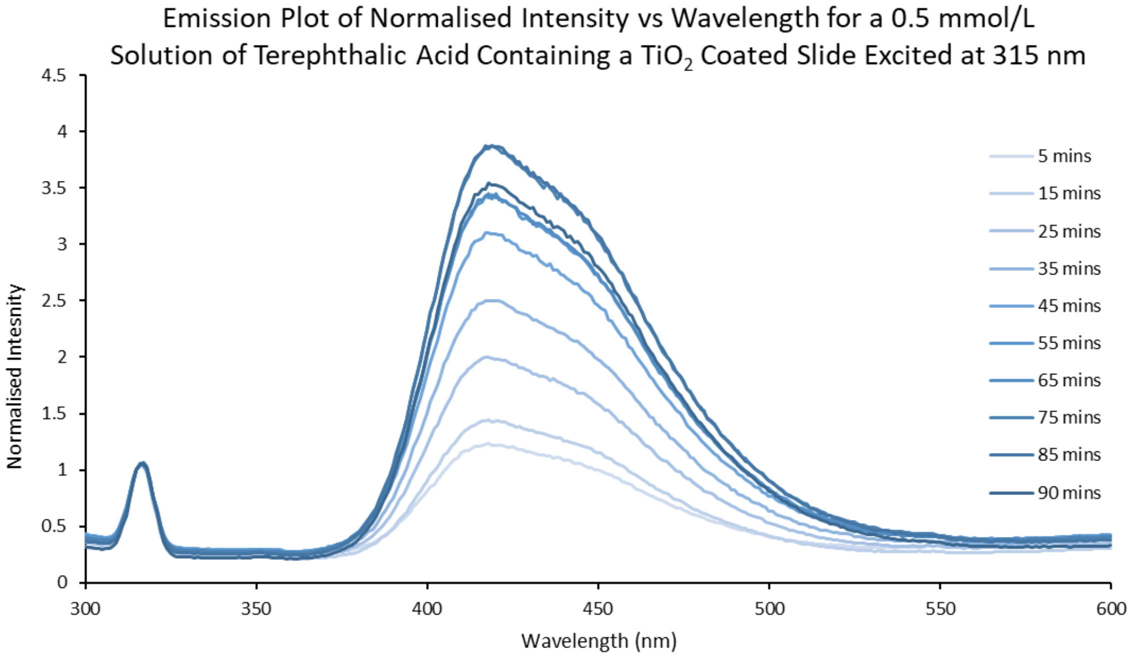

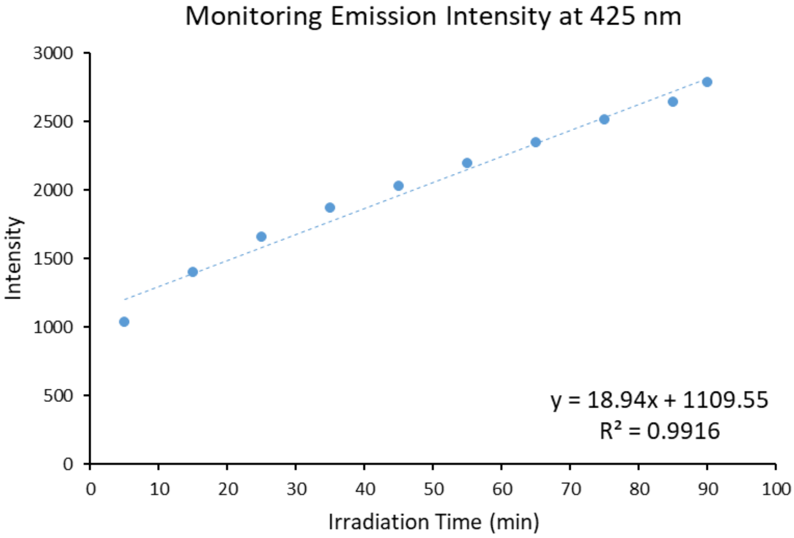

Figure 4.5 Top: Emission plot for the 0.5 mM terephthalic acid solution containing a $TiO_2$-coated slide undergoing continuous UV irradiation ($\lambda_{ex}$ = 315 nm). Slit widths were 5 nm, and a 340 nm filter was used. The data were normalised to the peak present at 315 nm which corresponds to the excitation light. There is a clear increase in intensity at 425 nm with irradiance time. Bottom: Monitoring emission intensity at 425 nm. There is an increase in emission intensity with irradiation time.

The same results are observed when using 10 nm slit widths to excite a 1 mM coumarin solution, but additionally this experiment was allowed to sit in the dark for 150 minutes after illumination was stopped to see if any further reactions would occur (see Figure 4.6). The intensity after being left in the dark increases marginally, but this could be due to small amounts of radical species in the solution after illumination was stopped, and no significant growth occurs when compared to growth between each 30 minute measurement. Additionally, there was no decay of intensity, meaning the product is stable and that no significant decrease in intensity would be occurring over time and introducing error.

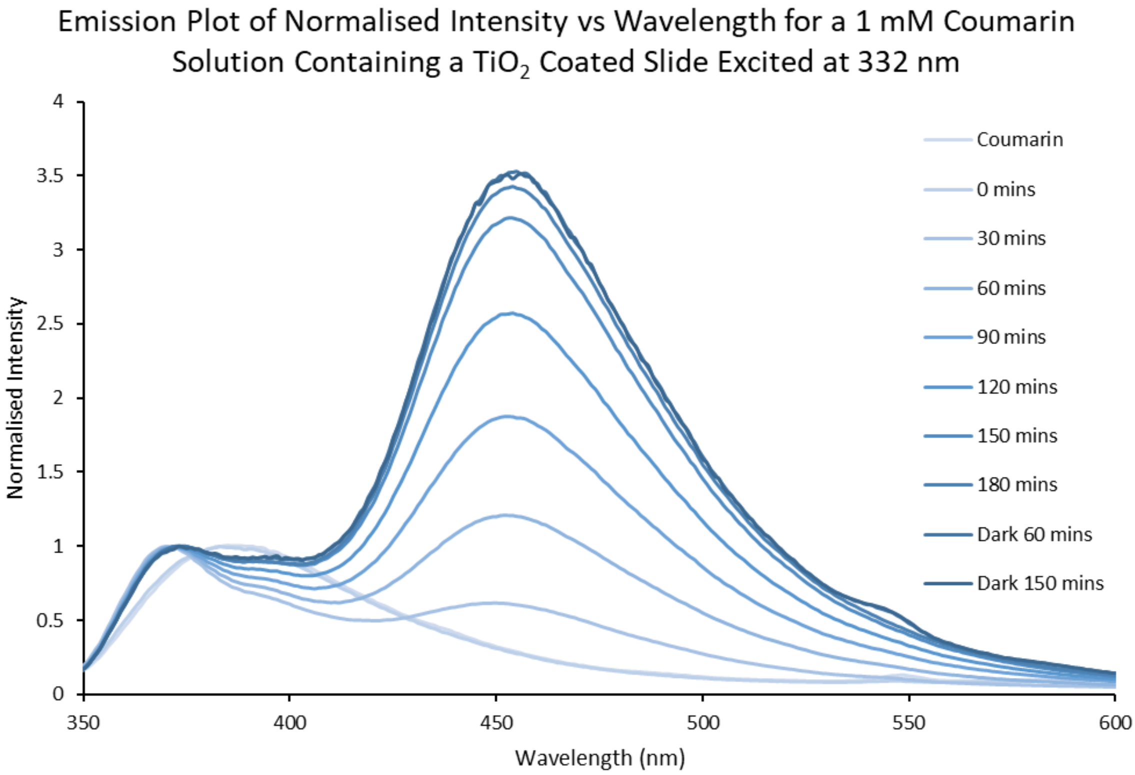

Figure 4.6 Emission plot for the 1 mM coumarin solution containing a $TiO_2$-coated slide undergoing continuous UV irradiation ($\lambda_{ex}$ = 332 nm). Slit widths were 10 nm, and a 360 nm filter was used. The intensity is normalised to the highest intensity for each scan. There is a clear increase in intensity at 460 nm with irradiance time, as well as little significant change seen when the solution was left to stir in the dark for 150 minutes, indicating reactions only occur when an excitation source is present.

A “blank” was run of both probe solutions, using the same method as above but without a slide in the cuvette to determine whether the product peak would appear without the presence of $TiO_2$. The spectra remain much the same with a small and broad increase between 400 - 500 nm but no significant increase at the wavelengths associated with product formation as seen previously (see Figure 4.7 for an example, and Appendix C for the raw intensity graphs). The slight increase in intensity for the shoulder in Figure 4.7 could be due to background shift, or a background reaction like excimer formation, but is not significant compared to the increase in intensity seen in Figures 4.5 and 4.6. This confirms that the peaks monitored are due to product formation catalysed by the UV irradiation, and that the $TiO_2$ is photochemically active in this form.

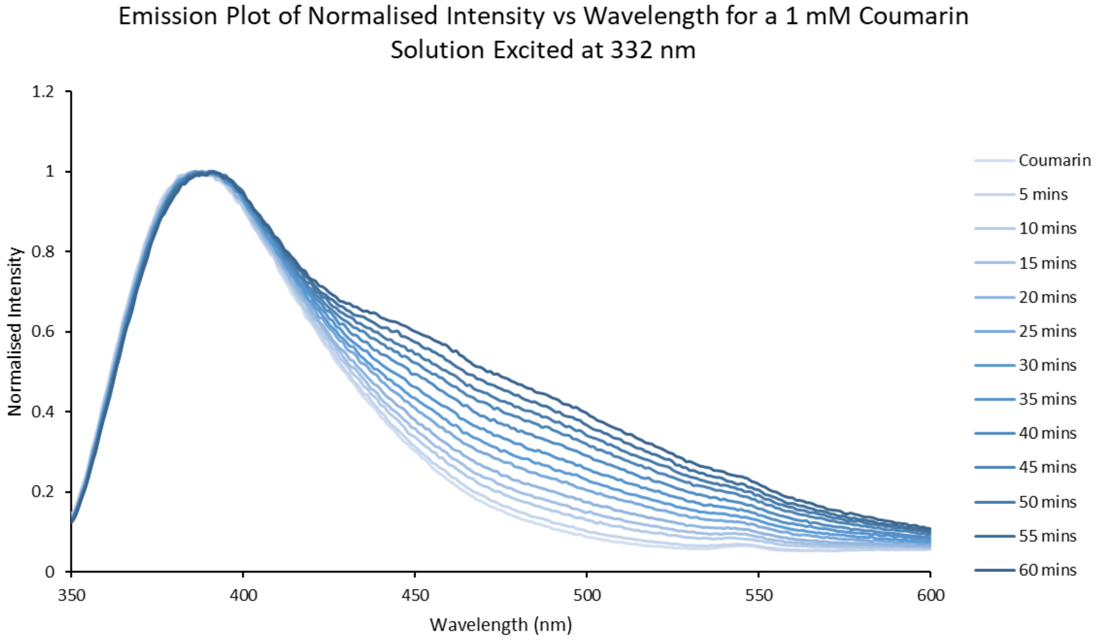

Figure 4.7 “Blank” run of the 1 mM coumarin probe solution, run without a $TiO_2$ slide. There is no significant increase observed in the 460 nm region, proving the increase observed in probe tests is due to a reaction involving the $TiO_2$. Slit width 10 nm, $\lambda_{ex}$ = 332 nm.

To determine the amount of either 7HC or 2TPA formed from photooxidation, a calibration curve of emission intensity for each molecule was established. Nine solutions of each fluorescent product were made, ranging from $1 \times 10^{-6} – 1 \times 10^{-10}$ mol/L in milli-Q water. An emission spectrum was collected for each concentration, and Figures 4.8 and 4.9 plot emission intensity for each molecule at the monitored wavelength. To account for the inner-filter effect (self-absorption), all solutions were dilute ($\leq 1 \times 10^{-6}$ mol/L) and had an absorption < 0.01 at the monitored wavelength of interest (see appendix C).[16] Table 4.3 gives the details of the linear regression analysis conducted for both graphs. Fluorescent emission intensity was found to be linearly related to concentration between $1 \times 10^{-10}$ - $5 \times 10^{-7}$ mol/L solutions for 7HC and between $1 \times 10^{-10}$ - $1 \times 10^{-6}$ mol/L solutions for 2TPA.

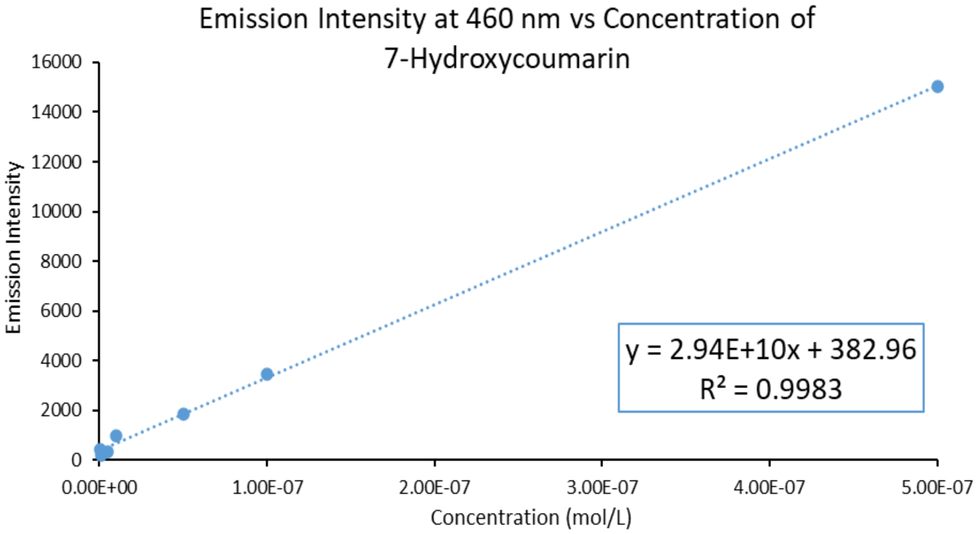

Figure 4.8 Plot of emission intensity vs concentration, monitored at 460 nm, for different concentrations of 7-hydroxycoumarin. $\lambda_{ex}$ = 332 nm, slit widths of 5 nm. The slope of the line is the rate of production of 7-hydroxycoumarin.

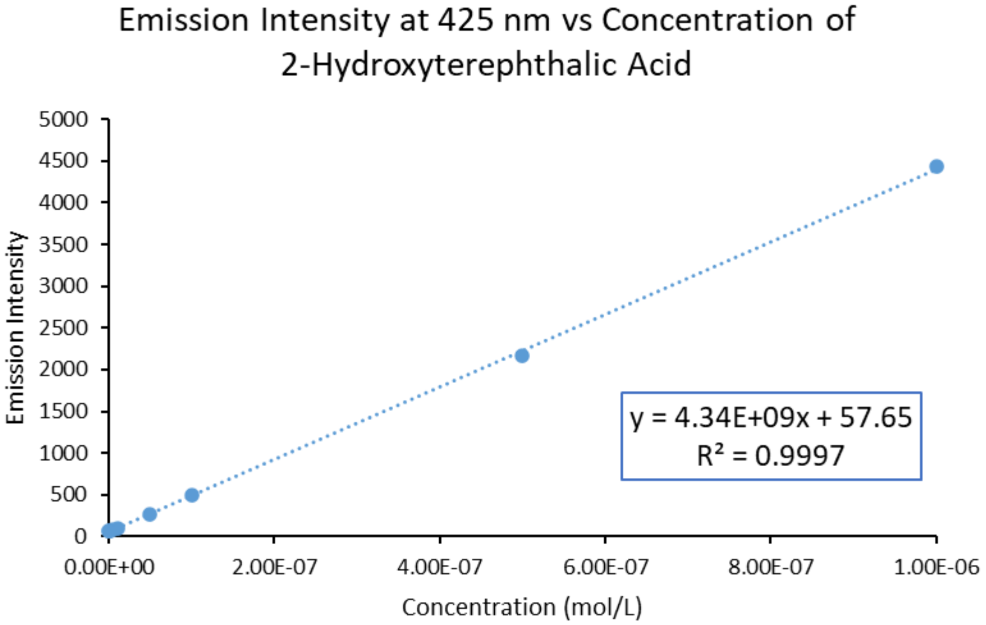

Figure 4.9 Plot of emission intensity vs concentration, monitored at 425 nm, for different concentrations of 2-hydroxyterephthalic acid. $\lambda_{ex}$ = 332 nm, slit widths of 5 nm. The slope of the line is the rate of production of 2-hydroxyterephthalic acid.

Table 4.3 Slope, intercept, standard errors for each, and adjusted $R^2$ value for the calibration curves (Figures 4.8 and 4.9) of emission intensity vs concentration for both 7-hydroxycoumarin and 2-hydroxyterephthalic acid solutions.

| Property | 7-Hydroxycoumarin (L/mol) | 2-Hydroxyterephthalic Acid (L/mol) |
|---|---:|---:|
| m | $2.94\times10^{10}$ | $4.34\times10^{9}$ |
| c | 382.96 | 57.65 |
| Standard error of m | 1.00 | $2.77\times10^{7}$ |
| Standard error of c | 210.83 | 10.39 |
| Adjusted $R^2$ | 0.9983 | 0.9997 |

From these calibration curves, the relationship between fluorescent intensity ($F_I$) and concentration is given by the equation of the line (equation 4.1), where c is concentration in mol/L.

$$F_I = slope * c + intercept \tag{4.1}$$

By substituting in the $F_I$ measured from the experiments of probe solutions containing a continuously excited $TiO_2$-coated slide, using the non-normalised intensity values, the concentration of product formed at given time intervals can be calculated by rearranging to equation 4.2:

$$c = \frac{(F_I - intercept)}{slope} \tag{4.2}$$

From this, a graph of either 7HC or 2TPA produced over time can be plotted (Figure 4.10 and 4.11, details of linear regression analysis in Table 4.4). From the linear fit of these graphs, the rate of product formation is given by the slope of the graph. This rate is then divided by a conversion factor to find the total production rate of ·OH; for coumarin, 6.1% of total ·OH is converted to 7HC, and for TPA, ~ 30% of total ·OH is converted to 2TPA.[8, 13] This therefore gives an approximate rate for total production of ·OH from the system. This rate is only applicable if the same conditions are used, as the conversion factors can be affected by factors as discussed in section 4.3.1, so it is considered only an approximation of the total rate of production. The calculated rate of ·OH formation for photooxidation of coumarin is 0.9762 x $10^{-8}$ M/min and for TPA is 1.455 x $10^{-8}$ M/min.

The probe study conducted therefore establishes the photoactivity of the $TiO_2$ slides used in this work, as well as their ability to catalyse ·OH formation and further photooxidation in solution. This knowledge can then be applied when using the fluorescence cell in combination with the RGA to do gas-phase studies. It also validates the spectrofluorophotometer as an excitation source.

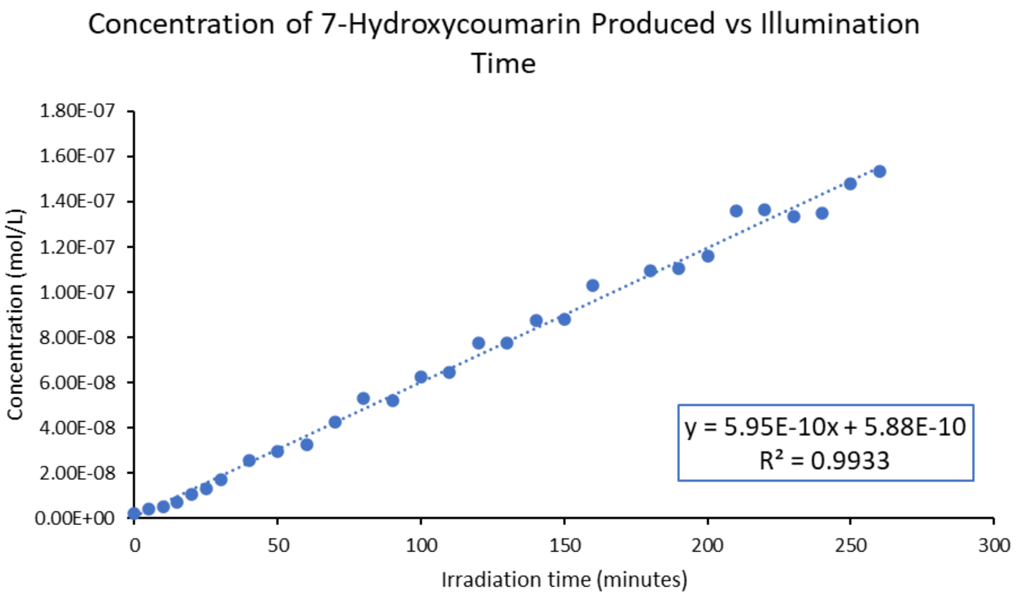

Figure 4.10 Plot of concentration of 7-hydroxycoumarin produced from photooxidation of coumarin vs illumination time.

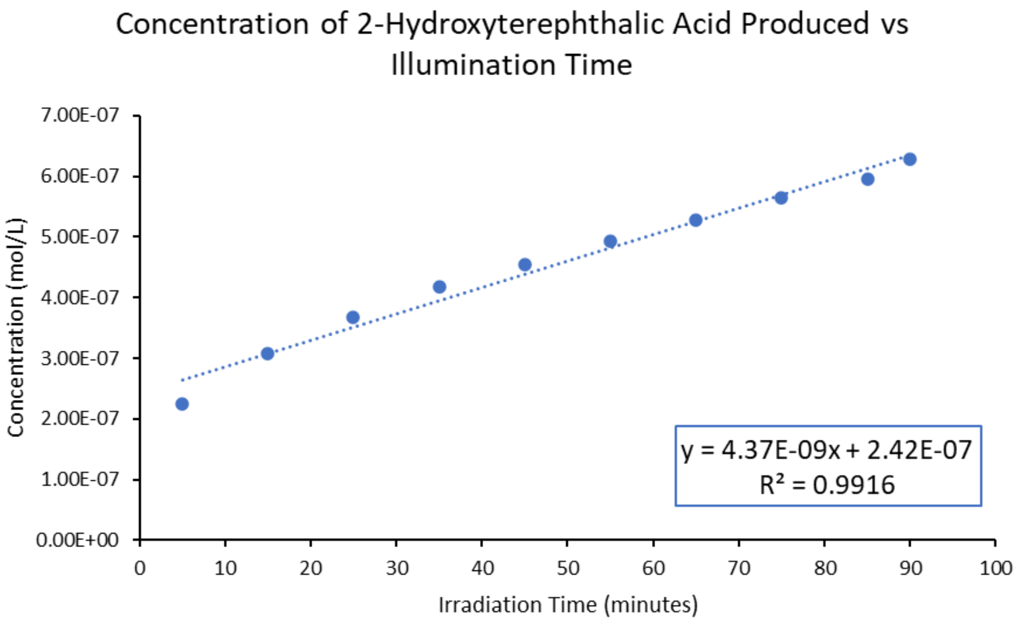

Figure 4.11 Plot of concentration of 2-terephthalic acid produced from photooxidation of terephthalic acid vs illumination time.

Table 4.4 Slope, intercept, standard errors for each, and adjusted R$^2$ value for the calculated concentration vs irradiation time plots (Figures 4.10 and 4.11) for both 7-hydroxycoumarin and 2-hydroxyterephthalic acid solutions.

| Property | 7-Hydroxycoumarin (mol/L) | 2-Hydroxyterephthalic Acid (mol/L) |
|---|---|---|
| m | $5.95\text{x}10^{-10}$ | $4.37\text{x}10^{-9}$ |
| c | $5.88\text{x}10^{-10}$ | $2.42\text{x}10^{-7}$ |
| Standard error of m | $8.93\text{x}10^{-12}$ | $2.21\text{x}10^{-10}$ |
| Standard error of c | $1.28\text{x}10^{-9}$ | $1.26\text{x}10^{-8}$ |
| Adjusted R$^2$ | 0.9933 | 0.9916 |

## 4.4 Experimental Infrastructure

Having established the photoactivity of the $TiO_2$ slides and the ability of the spectrofluorophotometer to be used as an excitation source, RGA experiments were undertaken.

### 4.4.1 RGA Infrastructure and Experimental Conditions

The RGA setup was built in house using stainless steel ultra high-vacuum (UHV) vacuum chambers, seen in Figure 4.12.

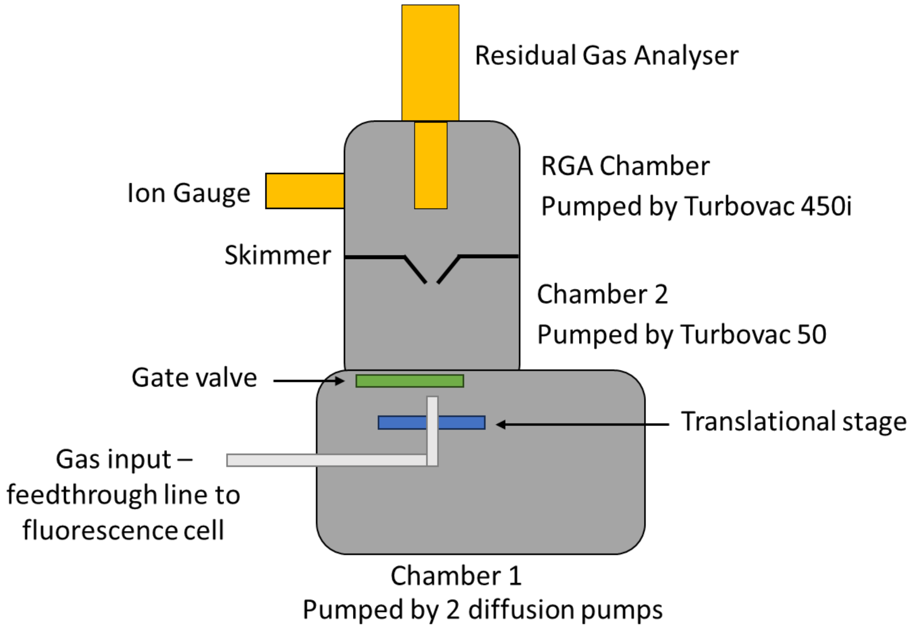

Figure 4.12 Diagram of vacuum chamber setup (top-down view). The translational stage can bring the gas line closer to the vacuum chamber entrance, which has an adjustable size entry hole.

The first chamber is pumped by two water-cooled diffusion pumps (an Edwards Diffstak model 100 DN2 backed by an Edwards R5 rotary-vane pump, and an Alcatel Crystal 160E backed by an Edwards E2M18 rotary-vane pump), with pressure monitored by a thermocouple gauge and an MKS Type 286 readout, readout on an SRS IGC100. The chamber pressure was measured using an Edwards Penning model 6 gauge and readout. The second chamber is pumped by a Leybold Turbovac 50 turbopump controlled by a Turbotronik NT 10. The RGA chamber was pumped by a Turbovac 450i. Both the second and third (RGA) chambers are backed by an Edwards R5 rotary-vane pump, and chamber pressure was measured by an ion gauge via the readout on the SRS IGC100. The RGA is connected at the end of the third chamber. Pressure is measured by a Pirani gauge (SRS PG105 UHV) and an ion gauge in each chamber, readout on either an Edwards Penning 8 or the SRS IGC100. The feedthrough line from the fluorescence cell is positioned in front of the gate valve separating the chambers on a translational stage, which moves the line closer or further away from the entrance to the second chamber. The entrance can be closed or adjusted in size using the gate valve. When running experiments, the pressures of each chamber are: $10^{-6}$ Torr in the first chamber, $10^{-7}$ Torr in the second chamber, and $10^{-8}$ Torr in the third (RGA) chamber.

The mass spectrometer used during experiments was either an SRS Residual Gas Analyser (RGA) 300 or 200 – during the experiments the RGA 300 was swapped out for the 200 due to detection difficulties and issues with tuning to specific mass peaks. During the process of swapping the RGA over, corrosion was discovered on the connection pins of the RGA300, so the RGA200 was installed, as the pins were too delicate to clean. After replacement, the RGA200 was tuned to both argon and $H_2O$ peaks. RGAs are used specifically for low-pressure experiments and can be mounted in vacuum chambers. The RGA is controlled by the RGA software, which is also used to analyse the data. The RGA settings are: electron energy 90 eV, ion energy 1 eV, focus plate voltage 120 V, electron emission current (filament) 2.5 mA, electron multiplier high voltage 2000 V.

During experiments, difficulties were encountered with detection and tuning. As a result, an SRS SR430 MultiChannel Scaler (MCS) was used to collect the data instead of using the RGA software. The MCS works by counting the ions as they come in to the detector and integrating the counts over the chosen time period. The MCS allows for only one mass to be tracked at a time, instead of tracking multiple masses like the RGA software can. It also allows a discriminator to be set, which means the signal-to-noise ratio can be adjusted, as a discriminator allows a level (or number of counts) to be set, below which the signal is ignored and above which it is counted as data. Initial tests indicated that the MCS behaved as expected to, detecting an increase in peaks for argon and water when the feedthrough line was open versus when it was closed. The MCS was connected to an SRS DG535 Pulse Generator to trigger collection. The MCS was set to record 100 records per bin with a bin width of 1.3107 ms, and the discriminator was set to 58 – 60 mV.

### 4.4.2 Fluorescence Cell

The fluorescence cell was built in house, using stainless steel chambers and piping, and Swagelok unions and quarter-turn plug valves, with a combination of o-rings greased with high-vacuum grease or copper flanges in between joins. Quartz windows (2.5 cm diameter) were mounted on 3 sides, so that light could pass through or emission could be measured (see Figure 4.13). A feedthrough of Ultrachem tubing (Leda) runs from inside the cell to entry of the vacuum chamber of the RGA. The tubing is connected to 0.005 inch internal diameter polyether ether ketone tubing that sits just above the surface of the mounted slide, siphoning reaction products to the RGA directly from the surface and point of illumination, shown in Figures 4.13 and 4.14. The slide holder, also seen in Figure 4.14, can be rotated so that the incidence angle of the excitation source can be changed. The cell can be valved off at both the gas input side and at the feedthrough line to the RGA for static experiments, allowing gas to build up inside, or it can have gas flowed through it continuously for dynamic experiments.

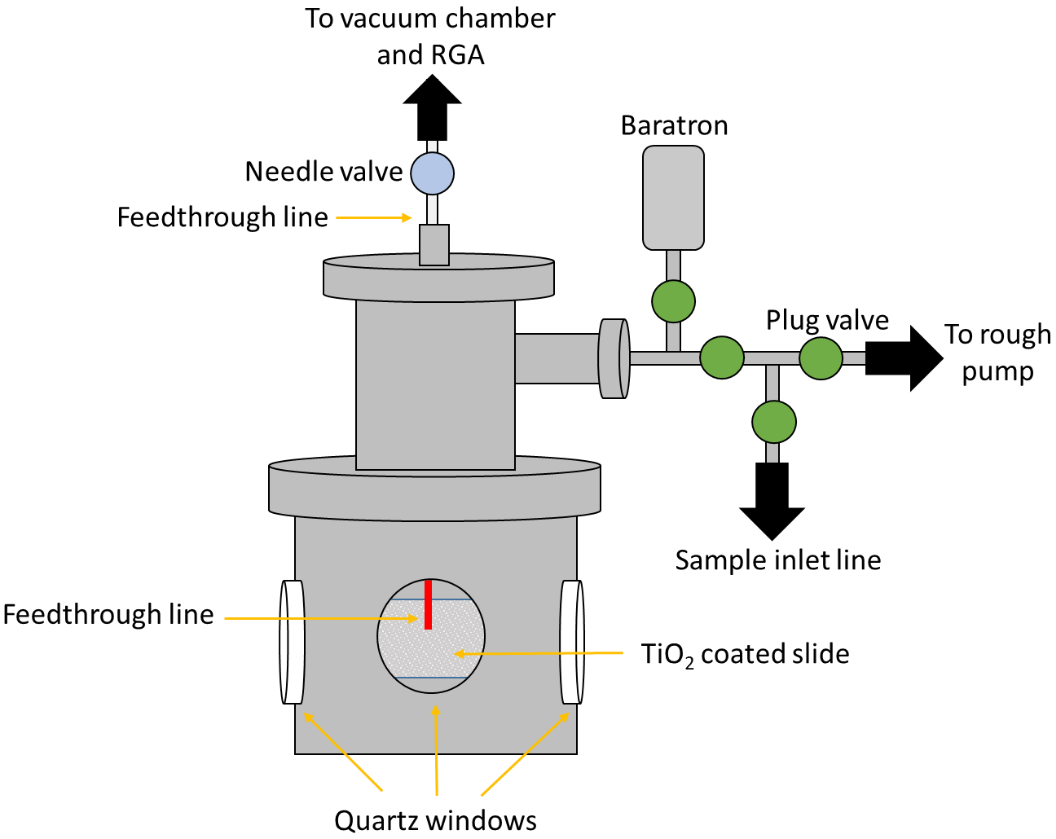

Figure 4.13: Schematic representation of the fluorescence cell and associated gas-handling for RGA experiments. The cell is connected to both a gas source and rough pump which can be valved off individually, and to the vacuum chamber.

Pressure in the fluorescence cell is measured using an MKS baratron (model 622A13TBE) attached to the purification manifold and the SRS IGC100 controller as used in Chapter 2. After swapping the RGA from the 300 to the 200, a MKS baratron (model 722B13TGA2FA, readout on an MKS PDR2000) was attached closer to the cell to measure cell pressure more accurately (shown in Figure 4.13).

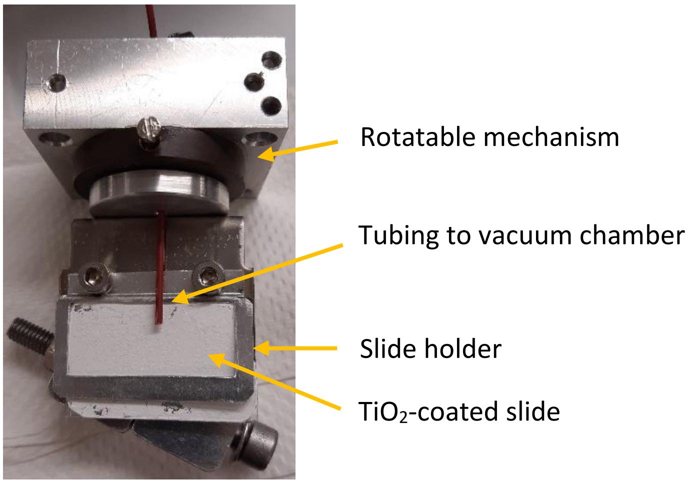

Figure 4.14 Slide holder inside the fluorescence cell. The holder can be rotated so that angle of incidence can be changed.

Water was added to the fluorescence cell via a bubbler attached to the manifold using argon as the carrier gas, as shown in Figure 4.15. The argon is purified via the manifold as previously described in Chapter 2, and is used since at 40 m/z it won't interfere with expected peaks of interest. It can also be used to tune the RGA and test whether any gas is flowing into the cell.

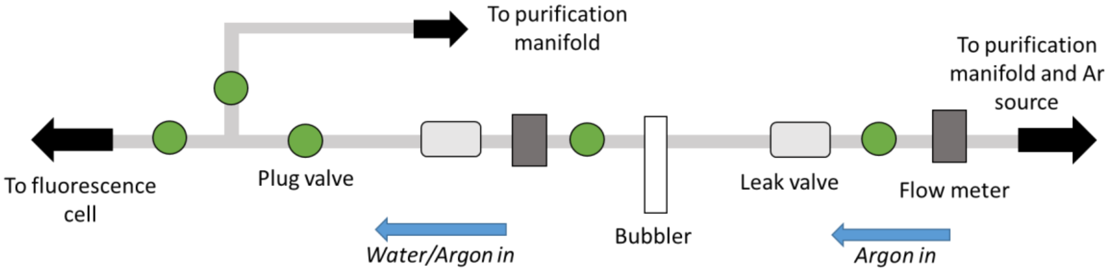

Figure 4.15 Simplified layout of gas-handling for the fluorescence cell. Leak valves allow for precise flow control.

After attempts to finetune the pressure of gas being fed through to the vacuum chamber, a Swagelok SS-1RS4 needle valve and a SS-4P4T-KZ quarter-turn plug valve were also added to the feedthrough line of the fluorescence cell. This has the potential to increase wall loss of radicals for the experiment but allows the flow of gas from the cell to be more finely controlled, and also allows for the cell to be isolated so that static experiments can be run. The plug valve also has more chemically resistant o-rings.

### 4.4.3 Sensitivity Test for RGA 300

First, the RGA300 was tested for sensitivity to $H_2O_2$ since it is the most likely reaction product that would be seen in water photolysis experiments, since the ·OH are likely to recombine during the time it takes to traverse from the cell to the detector. A glass vial of 30% $H_2O_2$ was connected to a glass tap (with a silicon-based vacuum grease to prevent reaction) which was fed through to the detector via the Ultrachem tube (Leda brand) (see Figure 4.16).

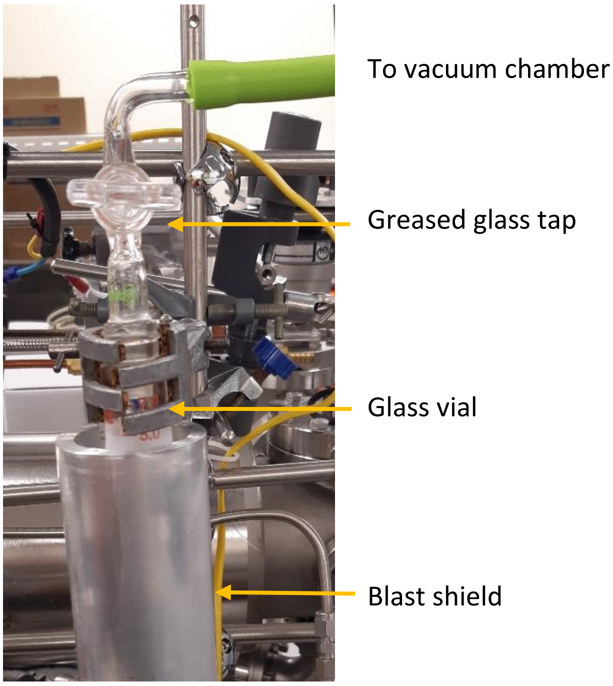

Figure 4.16 Experimental setup for $H_2O_2$ sensitivity testing.

The $H_2O_2$ was degassed by 3 FPT cycles and pumped on by an Edwards RV5 pump. Using the RGA mass spectrometry program, the background was taken with the glass tap closed, and then subtracted from the next scan, with the glass tap open so $H_2O_2$ was flowing into the chamber. Once ~ 0.5 – 1x$10^{-7}$ Torr increase in pressure was seen in the vacuum chamber by the ion gauge, there was a notable increase in the 34 m/z peak, along with other associated peaks like water (18 m/z), oxygen (32 m/z), nitrogen (28 m/z), and carbon dioxide (44 m/z). When the tap was open, and therefore $H_2O_2$ flowing into the cell, the peak at 34 m/z was the largest (once known atmospheric peaks were removed) and increased from background numbers (see Figure 4.17). The peak seen at 20 m/z is likely due to argon.[21] This means that the system, at low sensitivity and pressures, can detect $H_2O_2$, and therefore should be able to see reaction products in later experiments.

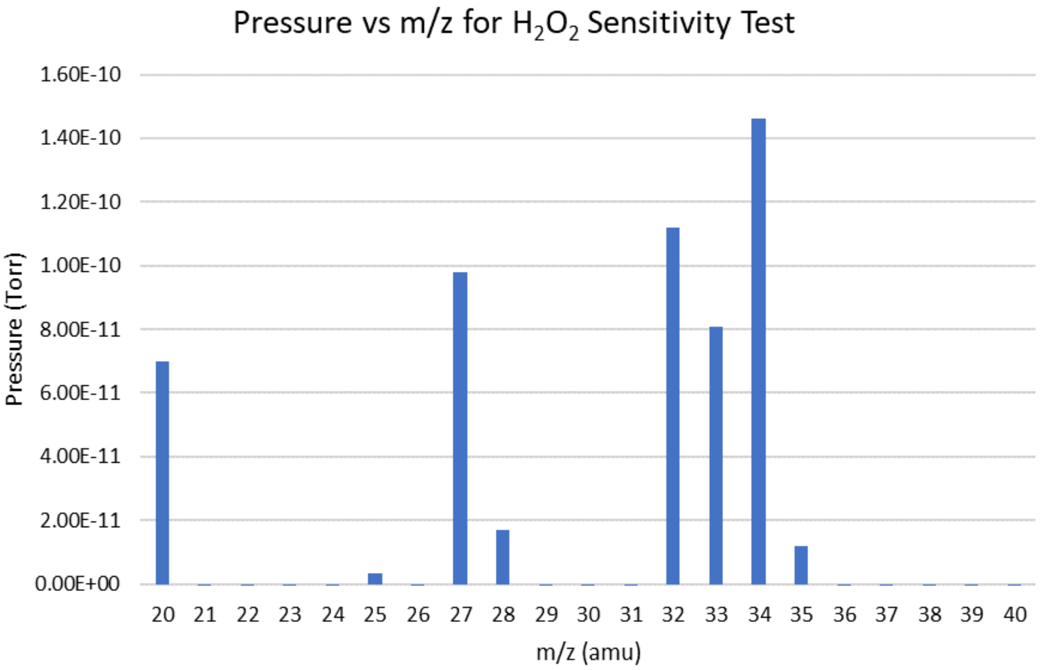

Figure 4.17 Mass spectrum whilst flowing $H_2O_2$ into the vacuum chamber. The large peak at 34 m/z indicates the detector is sensitive to $H_2O_2$, especially since the peak is insignificant in background data. This spectrum comes specifically from run 5.

## 4.5 Residual Gas Analyser Experiments

### 4.5.1 Using RGA Software to Collect and Visualise Data

Having established the photoactivity of the $TiO_2$ slides and the ability of the RGA300 to detect $H_2O_2$, experiments to photocatalyse ·OH formation from water vapour using a $TiO_2$ slide were undertaken, listed in Table 4.5. Multiple wavelengths were tested, with 530 nm used as a "blank" to determine if any peaks were produced using an excitation wavelength that shouldn't give ·OH, equating to 'dark' conditions. Particle size effects on the band gap were not considered as it acts on a nano-scale to increase photocatalytic ability with decreasing particle size, whereas the $TiO_2$ particle size used here is on the micro-scale (44 µm diameter).[24]

Table 4.5 List of experiments run using the RGA software to collect and visualise data. A series of experiments were run in attempts to optimise conditions.

| Name | Mixture | $\lambda_{ex}$ (nm) | Notes |
|---|---|---|---|
| R1 | $H_2O$/Ar | - | Peroxide sensitivity test (section 4.4.3) |
| R2 | $H_2O$/Ar | 250, 325, 532 | Dynamic experiment evaluating excitation wavelengths |
| R3 | $H_2O$/Ar | 350, 530 | Static experiment using pressure-vs-time mode to observe changes during measurement |
| R4 | $H_2O$/Ar | - | Altering concentrations and flow to observe change |
| R5 | $H_2O$/Ar, Ethylene/Ar | 250, 300 | Introducing ethylene probe |
| R6 | $H_2O$/Ar, Ethylene/Ar | 250 | Ethylene probe |

Experiment R2 used a mixture of argon and water to attempt to form ·OH and then detect $H_2O_2$ formed from the process of ·OH recombination. Argon was flowed through a bubbler filled with milli-Q water as a carrier gas for water vapour, which was passed through the fluorescence cell containing a $TiO_2$ slide, and then through to the vacuum chamber to the RGA. The RGA software was used on a histogram method to track the change in pressure across masses 1 – 64 m/z when the cell was opened to the vacuum chamber. Upon opening the cell feedthrough line to the vacuum chamber, an increase in 40 m/z for argon was observed, with no significant increase in 18 m/z for water observed despite the expected addition to the cell. This could be due to the low pressure of water being added in comparison to the pressure of the carrier gas. When the cell was then closed off, a corresponding signal drop was observed for 40 m/z, validating the ability to detect addition of gas to the chamber. The cell was then irradiated with light of $\lambda_{ex}$ = 350, 200, or 532 nm to see if an increase in 34 m/z would be observed from the production of $H_2O_2$, but no change in 34 m/z was observed; formation of ·OH and therefore recombination to $H_2O_2$ was expected at $\lambda_{ex}$ = 350 and 200 nm. At the time, the lack of products expected to be seen was attributed to the experiment being run dynamically, so that the gas was flowed through the cell and vacuum chamber. This means the gas has a low residence time in the cell and therefore only a small period of time where it can be irradiated and form radicals. In a static experiment, the gas is held inside the cell for a long period of time, ~ 30 – 60 minutes, which allows the build-up of reaction products to occur during irradiation. It was decided to run static experiments from this point forward.

Static experiments R3 and R4 were run, where the fluorescence cell was filled with a mixture of $H_2O$ and argon and then valved off. The cell was irradiated with $\lambda_{ex}$ = 350 nm or 530 nm whilst valved off to the vacuum chamber. Scans were then taken every 30 minutes, allowing stable reaction products to build up within the cell during the irradiation period, making detection easier as they are expected to be present in higher concentrations than in the dynamic experiment. The RGA software was run in pressure-vs-time mode, such that scans were started with the cell valved off to give a background pressure of the chosen masses in the vacuum chamber, then the cell opened midway through the scan, which should correlate to a rise in pressure. However, little significant change was observed in the data despite clear indication from the ion and Pirani gauges that gas was being fed from the cell into the vacuum chamber and therefore should be detected by the RGA. Investigating the RGA300 unearthed corrosion on the connection pins, which could have been interfering with measurements. Thus, the RGA300 was swapped to an RGA200, which was tuned to argon and water.

Due to the difficulties encountered in detecting radicals and $H_2O_2$, and the long metallic pathway from the cell to the detector, it was decided to use a probe molecule that would produce few reaction products from oxidation by ·OH. This way, both consumption of the reactant and increase in reaction products formed can be tracked. Ethylene was chosen since it is small and symmetric, so will produce few products when reacted with ·OH. Potential products (see Scheme 4.1) are the 2-hydroxyethyl radical (4.1a), formaldehyde and the methyl radical (4.1b), acetaldehyde and the hydrogen radical (4.1c), which are produced in a ratio of 21:44:35

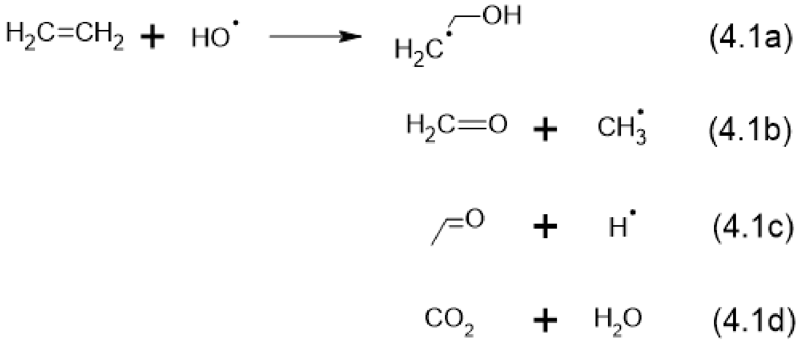

Scheme 4.1 Reaction of ethylene with ·OH.[17,18]

according to Bartels et al. (1982); or complete oxidation to $CO_2$ and water (4.1d) as seen by Fu et al. (1996).[17, 18] It should be noted that both reaction products formaldehyde and acetaldehyde undergo photolysis at $\lambda_{ex}$ = 269 – 339 nm and $\lambda_{ex}$ = 250 – 330 nm respectively.[19, 20] Since the maximum $\lambda_{ex}$ = 387 nm for $TiO_2$ to act as a photocatalyst, a $\lambda_{ex}$ = 360 nm is used in further experiments to avoid potentially destroying the reaction products with further photolysis reactions.

When using the RGA software to visualise the data in experiments R5 and R6, the CEM (Channel Electron Multiplier) had to be used to multiply the signal. However, the CEM was unable to be tuned, meaning that sensitivity couldn't be adjusted, and a repeating cyclical frequency was seen in the data recorded with the CEM on. Seen in Figure 4.18, the frequency repeats for all m/z measured. The increased flow of argon is evident as the argon line (orange dots) increases in pressure from the rest of the masses around 3000 s, but then continues with the same repeating frequency. This interference was determined to be most likely from an external electronic interference affecting the electrometer and therefore the CEM, as a separate scan was run for over an hour without the filament on, and therefore no data should be able to be recorded, but the same cyclical frequency was seen. Since the working pressures used cannot be seen using the RGA software without the multiplier, a Multichannel Scaler (MCS) was used instead to collect and readout the data.

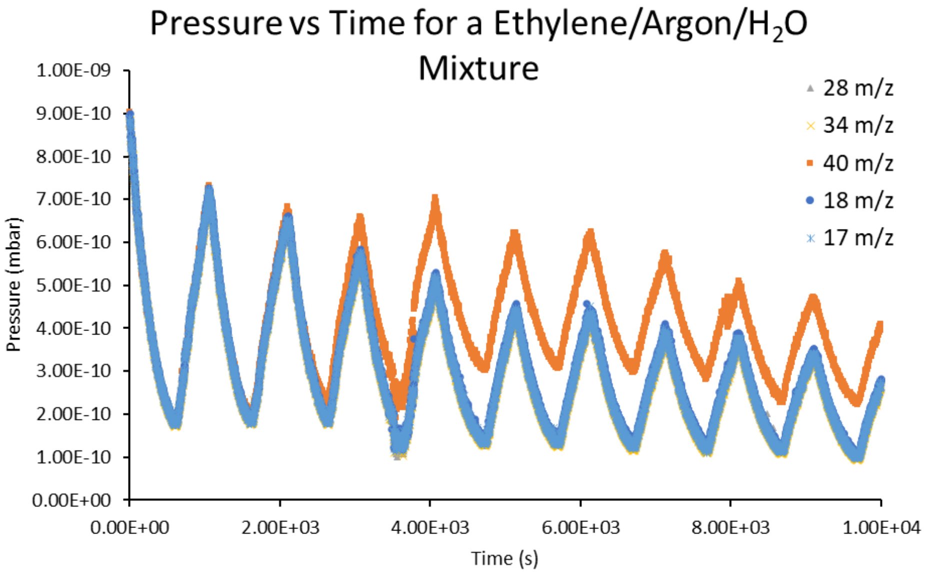

Figure 4.18 Plot of pressure-vs-time for a mixture of ethylene/argon/$H_2O$, monitoring chosen m/z peaks. This experiment was run using the CEM to give appreciable signal. The graph shows the repeating frequency experienced in all experiments when using the CEM which makes detecting small changes in pressure very difficult and resulted in changing methods for collecting and visualising data.

### 4.5.2 Using the RGA with MCS to Collect and Visualise Data

The MCS works by counting the ions as they come in to the RGA, integrating the counts over a specified time period. It also allows a discriminator level to be set, which adjusts the signal-to-noise ratio by setting a voltage level that must be surpassed to be considered data and not noise or background signal. This means that noise can be reduced, compared to the RGA software. However, the MCS can only track one mass at a time, compared to the RGA software which could track multiple. The experiments run using the MCS are listed in Table 4.6.

Table 4.6 List of experiments run using the MCS to visualise and collect data. More experiments were run but the data were lost in a hard-drive corruption event; the experiments lost consisted of a series of small changes to the mixture compositions, flow rates, or irradiation time to finetune conditions and so are not a significant loss.

| Name | Mixture | $\lambda_{ex}$ (nm) | Notes |
|---|---|---|---|
| M1 | $H_2O$/Ar, Ethylene/Ar | - | Observed pressure changes in MCS counts |
| M2 | $H_2O$/Ar, Ethylene/Ar | 300 | Varying conditions which established standard procedure |
| M3 | $H_2O$/Ar, Ethylene/Ar | 300 | Varying conditions which established standard procedure |
| M4 | $H_2O$/Ar, Ethylene/Ar | 300 | Scans taken with ion gauge off to mitigate interference |
| M5 | $H_2O$/Ar, Ethylene/Ar | 360 | Scans run in triplicate which reduced random error through averaging |
| M6 | $H_2O$/Ar, Ethylene/Ar | 360 | Discovered cell was open to atmosphere during experiment |
| M7 | $H_2O$/Ar, Ethylene/Ar | 360 | Fixed cell issues and re-ran previous experiment |
| M8 | $H_2O$/Ar, Ethylene/Ar | - | Blank, run with no irradiation light |
| M9 | $H_2O$/Ar, Ethylene/Ar | 360 | Blank, run with no catalyst slide in cell |
| M10 | $H_2O$/Ar, Ethylene/Ar | 360 | Ran for longer irradiation time |
| M11 | $H_2O$/Ar, Ethylene/Ar | 360 | Tracking only 2 masses to reduce scan time |

Experiments M1 – M7 account largely for finetuning of experimental conditions and are not subjected to a significant period of irradiation time compared to the later experiments and thus are not discussed in any further detail. Experiments M8 – M11 will be discussed below. Experiments M8 and M9 are “blanks”. M8 was run with no excitation light present, and M9 was run with no $TiO_2$ slide present to determine whether reactions were occurring without the catalyst or light.

After initially finetuning conditions with the MCS (experiments M1 – M7), a general method was established. For each mass of interest, scans were run in triplicate to average and thus reduce random errors. Scans were run, in order, on:

1. The empty fluorescence cell, with the feedthrough line to the vacuum chamber open (background scan)
2. The fluorescence cell filled with the gas mixture, with the feedthrough line to vacuum chamber open (baseline scan)
3. The fluorescence cell after 30-minute periods of irradiation with $\lambda_{ex}$ = 360 nm, with the feedthrough line to vacuum chamber open (experimental scan), repeating this scan after each subsequent 30 (or 60) minute period

By holding the cell in a static state, with the feedthrough line to the vacuum chamber closed while the cell is under irradiation, the final reaction products like $CO_2$ were expected to form in detectable concentrations. The consumption of reactants can also be tracked in this manner.

There are 7 masses tracked across the experiments conducted, listed in Table 4.7. The reactant masses were tracked to see an expected pattern of consumption, since the cell is filled to start with and then slowly decreases as the gas flows into the vacuum chamber and RGA (noting that water can be formed as a product so could potentially maintain a steady pressure). Reaction products were also tracked to see an expected trend of increase or no change over time. The initial scan, scan 0, gives a baseline of counts for each monitored mass when the vacuum chamber is empty. The data presented in Figure 4.19 and 4.20 has been “zeroed” by subtracting the count value from scan 0 from each of the subsequent count values measured for each scan, such that each monitored mass starts at 0 counts for scan 0.

Table 4.7 Table of mass fragments for each molecule measured in RGA experiments.

| Mass (m/z) | Molecule | Reactant/Product |
|---|---|---|
| 28 | Ethylene ($C_2H_4$) | Reactant |
| 40 | Argon (Ar) | Carrier Gas |
| 18 | Water ($H_2O$) | Reactant and Product |
| 30 | Formaldehyde ($H_2CO$) | Product |
| 15 | Methyl radical ($CH_3\cdot$) | Product |
| 16 | Methane ($CH_4$) | Product |
| 44 | Acetaldehyde ($CH_3CHO$) | Product |
| 44 | Carbon Dioxide ($CO_2$) | Product |

For experiment M10, a number of masses are tracked, including reactant and product masses. Figure 4.19, in which scan 0 is the empty cell, scan 1 is the full cell (t = 0), and scans 2 – 4 are conducted in 60-minute irradiation periods, shows the general decreasing trend. After the gas mixture is introduced into the cell (scan 1), there is as expected a greater count of 28 m/z (ethylene), 18 m/z ($H_2O$), and 16 m/z ($CH_4$) compared to 44 m/z ($CO_2$/$CH_3CHO$) and 30 m/z ($H_2CO$). The increase in counts for the product masses (44 m/z, 30 m/z, and 16 m/z) means they have been accidentally included in the gas mixture from the atmosphere. In further scans, after significant periods of irradiation, there is general decreasing trend in counts for all monitored masses, with counts all remaining below the value seen in scan 1. Compared to blank experiment M8, there is no significant difference in overall trend (see Figure 4.20) bar a spike in ethylene counts at scan 2, and a “negative” count for masses 44 m/z and 30m/z in M8, which is due to data processing to give zero counts at scan 0, as previously discussed. Otherwise, the same slight decreasing trend is seen for all masses. A greater decrease would be expected for 28 m/z (ethylene) in M10 compared to the blank (M8) as it would be consumed by both flowing out of the cell and by reaction. An increase in product mass counts would be expected in M10 compared to M8 since there should be no production in the blank. Even if the rate of product formation in M10 was similar to the rate of consumption (gas flow leaving the cell to the detector), the initial pressure seen in scan 1 would be maintained. However, a decrease is seen from the counts measured in scan 1, so this is not the case, suggesting a lack of product formation or inability to detect the products.

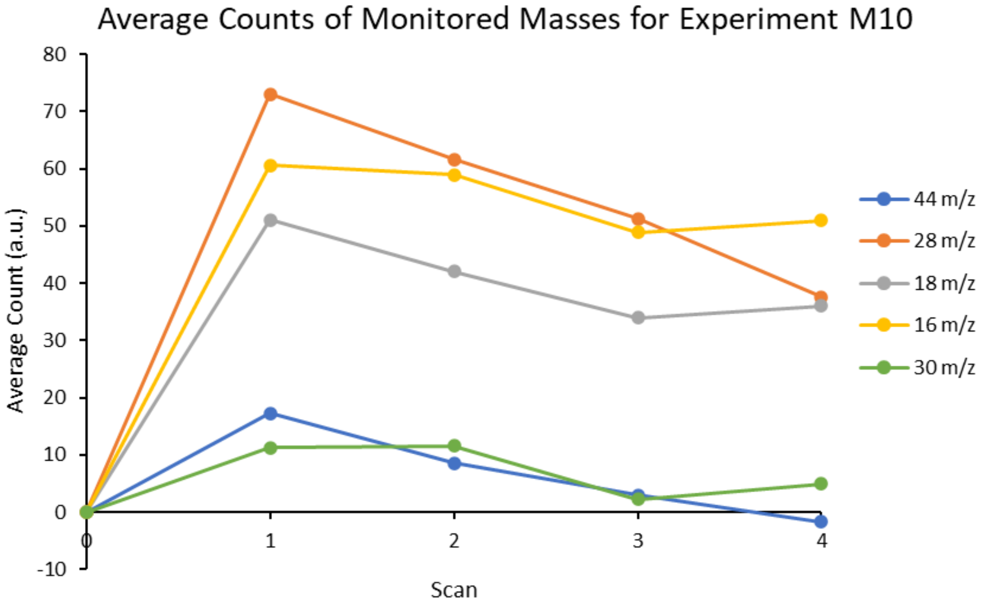

Figure 4.19 Plot of average counts for a mixture of ethylene/argon/$H_2O$, irradiated with $\lambda_{ex}$ = 360 nm in the presence of a $TiO_2$ slide (experiment M10). Scan 0 is the empty cell, 1 the cell containing the gas mixture, 2 after 60 minutes of irradiation, 3 after 120 minutes of irradiation, and 4 after 180 minutes of irradiation.

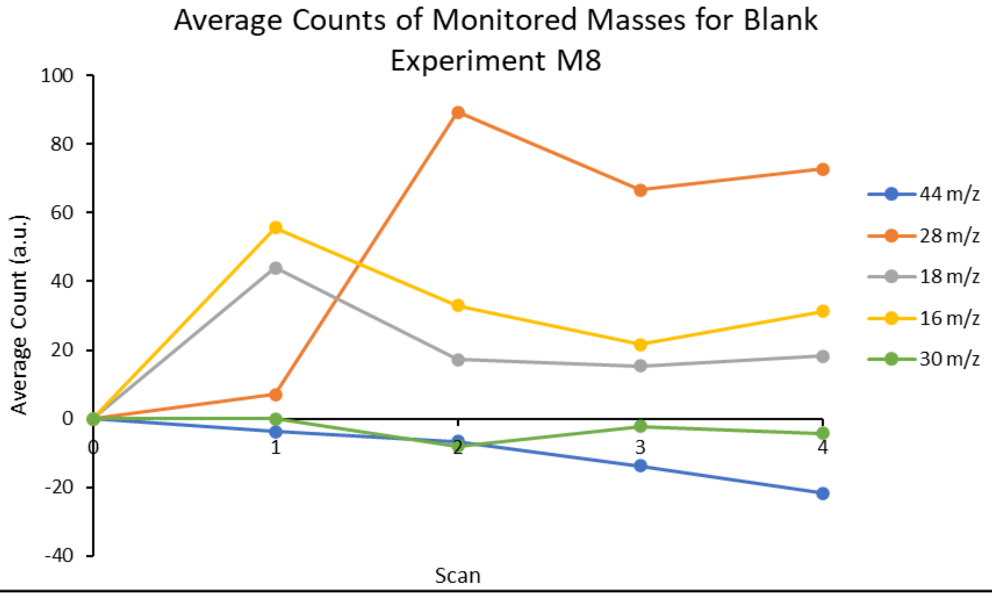

Figure 4.20 Plot of average counts for a mixture of ethylene/argon/$H_2O$ in the presence of a $TiO_2$ slide. The experiment, M8, is run as a blank so no excitation light is added. Scan 0 is the empty cell, 1 the cell containing the gas mixture, 2 after 60 minutes of irradiation, 3 after 120 minutes of irradiation, and 4 after 180 minutes of irradiation.

For the last experiment, M11, only two masses are tracked, 44 m/z for ($CO_2$/$CH_3CHO$) and 28 m/z for ethylene. This is so the time taken during scans is reduced, as it took ~ 2 mins to conduct a scan, giving a total scan time of ~ 12 mins to collect data on two masses in triplicate. The experiments were conducted such that the irradiation periods were greater than the time taken to collect data in order to allow build up of reaction products. Additionally, by reducing the time taken to conduct scans, the experiment could be run for a longer total time to give a better indication of the overall trend in counts. Seen in Figure 4.21, there is a general decreasing trend for 28 m/z (ethylene), which is expected since ethylene would be used up either in reactions or when flowed out of the cell. For 44 m/z ($CO_2$/$CH_3CHO$), the counts cycle around the initial value with no significant increasing or decreasing trend seen, maintaining a count around the initial value. This could indicate the product is being continually formed as if the product was not being formed, a lack or a decrease in signal would be observed, as seen in M10. The fact that the signal is relatively steady could be associated with the product being replenished by reactions after each scan. The blank experiment M9, seen in Figure 4.22, also tracks only 28 m/z (ethylene) and 44 m/z ($CO_2$/$CH_3CHO$), and shows a similar decreasing trend. In contrast, M11 has a much smoother trend, with the data seen in M9 subject to spikes, exhibiting greater variability. Both M9 and M11 do have a similar count value for each mass, ~ 350 counts for ethylene initially and ~ 100 counts for $CO_2$/$CH_3CHO$ initially. It is expected that a steeper decreasing trend in 44 m/z

($CO_2$/$CH_3CHO$) would be seen in the blank M9 compared to the M11, since there shouldn't be any production in the blank experiment.

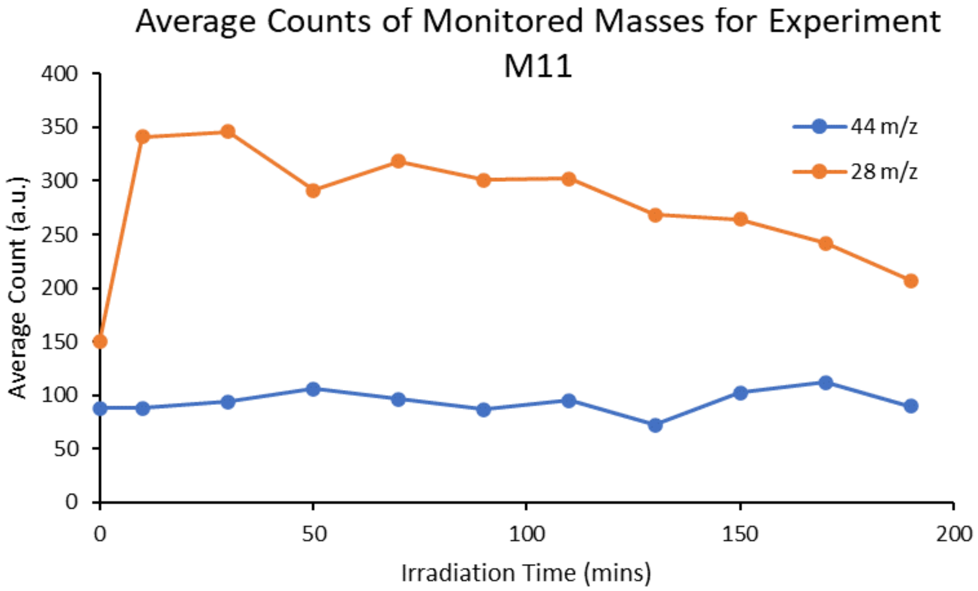

Figure 4.21 Plot of average counts vs irradiation time for a mixture of ethylene, argon, and $H_2O$ (experiment M11). The mixture is held in the fluorescence cell in the presence of a $TiO_2$ slide irradiated by $\lambda_{ex}$ = 360 nm. The masses tracked are $CO_2$ (44), a final oxidation product, and ethylene (28), to track reactant consumption. There is a general decrease in counts for mass 28, and little significant change for mass 44 over time.

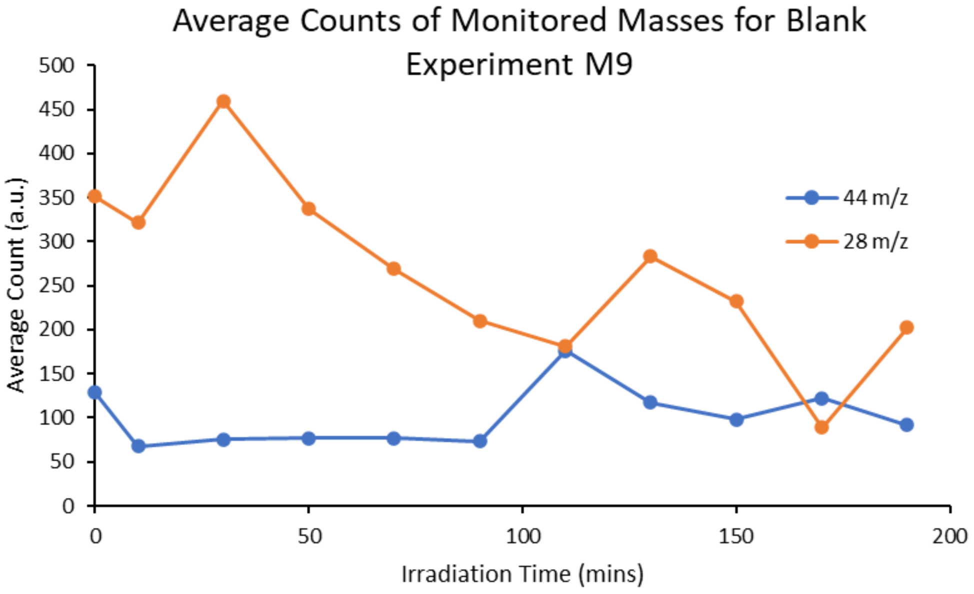

Figure 4.22 Plot of average counts vs irradiation time for a mixture of ethylene, argon, and $H_2O$ (experiment M9). The mixture is held in the fluorescence cell with no $TiO_2$ slide, irradiated by $\lambda_{ex}$ = 360 nm, to act as a blank. The masses tracked are $CO_2$ (44), a final oxidation product, and ethylene (28), to track reactant consumption. There is a general decrease in counts for mass 28, and little significant change for mass 44 over time.

Figure 4.23 shows the counts for both the blank (M9) and experiment M11 for mass 44 ($CO_2$/$CH_3CHO$), which clearly shows a similar lack of significant trend and maintenance of initial value in both experiments. There is larger variation in counts for M9, which could be due to random error. This lack of change could again indicate the products aren't being formed, with reaction occurring through a different mechanism to form different products, or that the products are being used up in other reactions. Alternatively, the formation rate of the products could be enough to maintain the count value as the gas is flowed out the cell over time, as the trend for 28 m/z (ethylene) is clearly decreasing, from potential reactions and being flowed out the cell. Overall, the results are inconclusive and cannot definitively indicate that the reaction is occurring as expected.

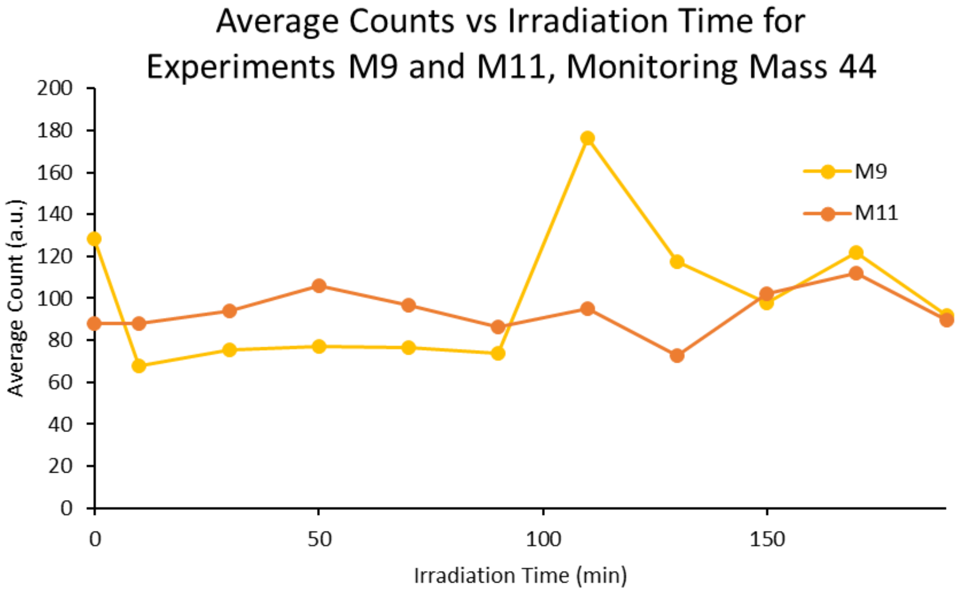

Figure 4.23 Plot of average counts vs irradiation time for experiments M9 and M11, monitoring mass 44. The gas mixture of $H_2O$/ethylene/argon is held in the fluorescence cell with a $TiO_2$ slide irradiated by $\lambda_{ex}$ = 360 nm (with no slide in the case of the blank). There is little significant change in counts for the experiment, with larger variation seen in the blank.

## 4.6 Conclusion

In this chapter, the ability of $TiO_2$ to photocatalyse the formation of ·OH from water vapour was investigated using an RGA detector. To do this, a series of preliminary investigations were undertaken before the experiments could be conducted.

First, a series of $TiO_2$-coated slides were produced through the techniques of RASSS and spin-coating. It was found that RASSS provided a thick and smooth coating, but that the coating would flake off the slide in aqueous solution. Spin-coating was thus found to produce slides with good coverage that were smooth and would remain coated in aqueous solution.

Second, the photoactivity of the $TiO_2$ slides was tested in a probe study that used both coumarin and terephthalic acid (TPA) as probe molecules. The slides, when illuminated with $\lambda_{ex} \leq 387$ nm and submerged in a solution of probe molecule, catalysed the oxidation of the probe molecules into their fluorescent products. The increase in emission seen from the product formation was then evaluated to give an approximate rate of formation of ·OH from photooxidation of coumarin ($9.762 \times 10^{-9}$ M/min) and TPA ($1.455 \times 10^{-8}$ M/min).

Third, the slides were then housed in a fluorescence cell that was built in-house, alongside other built in-house infrastructure required to conduct the experiments. The slides were subjected to irradiation in the presence of a mixture of gases such that the formation of radicals and reaction products could be tracked using the RGA. Initially, the gas mixture comprised of only water and argon, with the formation of $H_2O_2$ monitored, but due to lacking success in this endeavour the small and symmetric molecule ethylene was introduced to the mixture such that further oxidation products could be detected. During this process, a swap from the RGA software to an MCS occurred for collection and visualisation of data due to interference from the CEM, which was required to amplify the signal when using the RGA software. Using the MCS, further experiments were conducted, including two blank experiments conducted to observe if patterns seen in irradiation experiments were repeated without the presence of either a catalyst or excitation light. Unfortunately, the experiments gave no conclusive evidence that a reaction was occurring to produce the reaction products as expected, as a general decreasing trend in measured counts was seen for all masses tracked that was replicated in the blanks, with no significant deviation from initial counts seen where they would be expected. The exception to this was mass 44 in final experiments, which maintained the value measured at the initial scan, potentially indicating product formation; however, the data did not allow for the definitive conclusion of radical production.

In future, dynamic experiments could be run to measure the reactant consumption over time continuously. Dynamic (flowing) experiments would prevent build up in the cell, which could prevent recombination of any reaction products or radicals or any further oxidation reactions by immediately removing reaction products. This would allow investigation into whether the rate of consumption differs between irradiation experiments and blank experiments, which would indicate that a consumption source other than gas flow from the cell was occurring, which could confirm reaction occurrence. However, depending on the pressure of the products formed, detection could prove difficult. Static experiments as run in this chapter provide time for further reactions beyond the initial oxidation as well as time for the products to diffuse from the surface and mix within the volume of the cell, potentially giving a lower pressure than expected. Additionally, decreasing the distance between the cell and the detector could also help increase signal by funnelling products directly from the point of reaction to the detector and reducing the time available for recombination and further reactions. Ideally, these experiments, as well as those conducted within the chapter, would use the RGA and the RGA software, as it allowed for the detection of multiple mass fragments at the same time, whereas the MCS only allows for one mass to be tracked at once, requiring significant time to measure, alongside large random fluctuations in data which required scans to be run in triplicate to mitigate.

Further experiments were intended to be run using this setup, but due to time constraints and other issues perpetrated by the University, they were unable to be conducted. The goal was to create a mixture within the cell that mimicked the current percentage make-up of the atmosphere with regard to water and $CH_4$, with the rest of the cell's "atmosphere" being argon carrier gas, similar to the ethylene experiments run. This would then allow the consumption of $CH_4$ from reactions with ·OH using the $TiO_2$ slide to be measured. The consumption would be measured as a function of water vapour concentration in the cell, and of temperature, in order to determine the approximate rate when applied at atmospheric conditions. Blanks could also then be run to track what consumption occurred without the $TiO_2$ catalyst present. Further studies on the amount of $TiO_2$ used could also then be run to see if there is an optimal amount for reduction of $CH_4$ concentration. Further, the amount of $TiO_2$ required to remove specific amounts of $CH_4$ (e.g. 10% overall atmospheric decrease) by extrapolating out the amount of catalyst and the volume of the cell could be calculated.

## 4.7 References

1. van den Berg, J. Photon catalysis and microdroplet chemistry: Applications of electric fields to influence reaction dynamics. Stanford, CA, USA, 2019.
2. Li, Y.; Ji, D.; Liu, J., et al., Quick Fabrication of Large-area Organic Semiconductor Single Crystal Arrays with a Rapid Annealing Self-Solution-Shearing Method. *Sci. Rep.* **2015,** *5* (1), 13195.
3. Yilbas, B. S.; Al-Sharafi, A.; Ali, H., Chapter 3 - Surfaces for Self-Cleaning. In *Self-Cleaning of Surfaces and Water Droplet Mobility*, Yilbas, B. S.; Al-Sharafi, A.; Ali, H., Eds. Elsevier: 2019; pp 45-98.
4. O'Neil, A. Development of a molecular toolbox for multifunctional lanthanide-based supramolecular materials. Massey University, Auckland, New Zealand, 2022.
5. Ishibashi, K.-I.; Fujishima, A.; Watanabe, T., et al., Detection of active oxidative species in $TiO_2$ photocatalysis using the fluorescence technique. *Electrochem. Commun.* **2000,** *2* (3), 207-210.
6. Lv, K.; Yu, J.; Deng, K., et al., Effect of phase structures on the formation rate of hydroxyl radicals on the surface of $TiO_2$. *J. Phys. Chem. Solids.* **2010,** *71* (4), 519-522.
7. Jimenez-Relinque, E.; Castellote, M., Hydroxyl radical and free and shallowly trapped electron generation and electron/hole recombination rates in $TiO_2$ photocatalysis using different combinations of anatase and rutile. *Appl. Catal. A.* **2018,** *565*, 20-25.
8. Zhang, J.; Nosaka, Y., Quantitative Detection of OH Radicals for Investigating the Reaction Mechanism of Various Visible-Light $TiO_2$ Photocatalysts in Aqueous Suspension. *J. Phys. Chem. C.* **2013,** *117* (3), 1383-1391.
9. Zhang, J.; Nosaka, Y., Mechanism of the OH Radical Generation in Photocatalysis with $TiO_2$ of Different Crystalline Types. *J. Phys. Chem. C.* **2014,** *118* (20), 10824-10832.
10. Czili, H.; Horváth, A., Applicability of coumarin for detecting and measuring hydroxyl radicals generated by photoexcitation of $TiO_2$ nanoparticles. *Appl. Catal. B.* **2008,** *81* (3), 295-302.
11. Louit, G.; Foley, S.; Cabillic, J., et al., The reaction of coumarin with the OH radical revisited: hydroxylation product analysis determined by fluorescence and chromatography. *Radiat. Phys. Chem.* **2005,** *72* (2), 119-124.
12. De-Nasri, S. J.; Nagarajan, S.; Robertson, P. K. J., et al., Quantification of hydroxyl radicals in photocatalysis and acoustic cavitation: Utility of coumarin as a chemical probe. *J. Chem. Eng.* **2021,** *420*, 127560.
13. Gonzalez, D. H.; Kuang, X. M.; Scott, J. A., et al., Terephthalate Probe for Hydroxyl Radicals: Yield of 2-Hydroxyterephthalic Acid and Transition Metal Interference. *Anal. Lett.* **2018,** *51* (15), 2488-2497.
14. Černigoj, U.; Štangar, U. L.; Trebše, P., et al., Determination of catalytic properties of $TiO_2$ coatings using aqueous solution of coumarin: Standardization efforts. *J. Photochem. Photobiol. A.* **2009,** *201* (2), 142-150.
15. Li, S.; Timoshkin, I. V.; Maclean, M., et al., Fluorescence detection of hydroxyl radicals in water produced by atmospheric pulsed discharges. *IEEE. Trans. Dielectr. Electr. Insul.* **2015,** *22* (4), 1856-1865.
16. Valeur, B., *Molecular Fluorescence: Principles and Applications*. Wiley-VCH: Germany, 2001.
17. Bartels, M.; Hoyermann, K.; Sievert, R., Elementary reactions in the oxidation of ethylene: The reaction of OH radicals with ethylene and the reaction of C2H4OH radicals with H atoms. *Symp. Combust.* **1982,** *19* (1), 61-72.
18. Fu, X.; Clark, L. A.; Zeltner, W. A., et al., Effects of reaction temperature and water vapor content on the heterogeneous photocatalytic oxidation of ethylene. *J. Photochem. Photobiol. A.* **1996,** *97* (3), 181-186.

19. Smith, G. D.; Molina, L. T.; Molina, M. J., Measurement of Radical Quantum Yields from Formaldehyde Photolysis between 269 and 339 nm. *J. Phys. Chem. A.* **2002,** *106* (7), 1233-1240.
20. Moortgat, G. K.; Meyrahn, H.; Warneck, P., Photolysis of Acetaldehyde in Air: $CH_4$, CO and $CO_2$ Quantum Yields. *ChemPhysChem* **2010,** *11* (18), 3896-3908.
21. NIST Standard Reference Data Program Collection, Argon - Mass Spectrum (Electron Ionization). In *NIST Chemistry WebBook, NIST Standard Reference Database Number 69*, NIST Mass Spectrometry Data Centre; W. E. Wallace, Eds. Gaithersburg MD, 2025.
22. Taniguchi, M.; Lindsey, J. S., Database of Absorption and Fluorescence Spectra of >300 Common Compounds for use in PhotochemCAD. *Photochemistry and Photobiology* **2018,** *94* (2), 290-327.
23. Murzin, D. Y., On Langmuir kinetics and zero order reactions. *Catalysis Communications* **2008,** *9* (9), 1815-1816.
24. Lin, H.; Huang, C. P.; Li, W., et al., Size dependency of nanocrystalline $TiO_2$ on its optical property and photocatalytic reactivity exemplified by 2-chlorophenol. *Appl. Catal. B.* **2006,** *68* (1), 1-11.

# 5.0 Atmospheric Modelling

## 5.1 Introduction

With the intention of potentially adding $TiO_2$ to the atmosphere for the purpose of photocatalysing the removal of $CH_4$, consequences of this addition to the chemical cycles present in the atmosphere need to be determined. As discussed in Chapter 1, the atmosphere contains a number of chemical cycles that are all dependent on concentrations of the molecules involved and interconnected with other cycles. A rough atmospheric model was thus established to give an idea of the effect of adding different amounts of $TiO_2$ to the atmosphere on the concentrations of important gases, as well as give an idea of how much $TiO_2$ would be required to remove a given amount of methane (e.g. targeting a 10% removal rate).

Atmospheric models vary in complexity and accuracy, and therefore computational cost. The first item in the construction of the model to consider is the spatial dimension. Visualised in Figure 5.1, the simplest model that could be used is a box model (or zero-dimensional model), which doesn't consider transport in or out of the box but instead inputs an initial concentration to get a final concentration output for the species inside.[1] In a zero-dimensional model, concentrations are considered uniform across the space and are time dependent only.[1] Increasing the dimensionality of the model means adding further boxes in space with flow allowed between them. In a 1-D model, vertical columns of boxes are modelled with vertical transport and settling of gases allowed, making the concentrations dependent on both time and altitude.[1] 2-D models extend the boxes in the vertical columns of the 1-D models, assuming uniformity in one dimension (e.g. the y axis), thus making concentrations dependent on the other two axes and time.[1] In a 3-D model, the space is divided up into a series of boxes, with transport allowed both horizontally and vertically, making concentrations dependent on all three axes and time.[1] With increasing dimensionality comes increasing complexity and therefore increasing computational cost, so in this work a zero-dimensional box model was employed as with a small enough time step the results give a good estimate without requiring the complexity or computational time that a higher dimension model requires. Additionally, the level of detail supplied by a 3-D model, which can model transport between vegetation and the atmosphere in different environments or localised climate abnormalities, is not required for the indicative and approximate approach desired here.[1, 2]

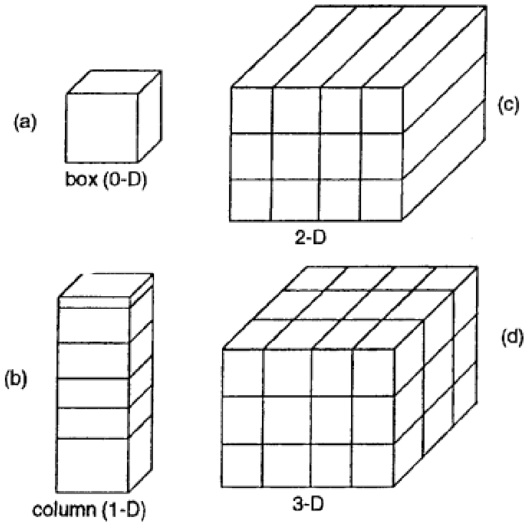

Figure 5.1 Representations of differing dimensions of models: a) zero-dimensional or box model, b) 1-D or column model, c) 2-D model, and d) 3-D model. Reproduced from Seinfeld et al. (2016).[1]

The second item to consider in the construction of a model is the variables that will be included and calculated. Atmospheric models calculate concentrations of a range of important atmospheric molecules. These can range from the well-known GHGs involved in $NO_x$, $HO_x$ and $O_x$ cycles, which can be long lived and well mixed throughout the atmosphere, to the more variable and source-specific biogenic volatile organic compounds and non-methane hydrocarbons and their reaction products. Atmospheric models also consider a swathe of other variables including stratospheric transport, deposition of particles, effects of aerosols through both deposition mechanisms and as a reaction surface, atmospheric transport, diurnal patterns, particulate matter, emissions from natural sources like the land or the ocean, and activity over different areas like urban, ocean, or land.[1] As more variables and molecules are added to the model, it becomes more complex and requires more computational resources. If the model can be simplified to an optimum number of variables, a balance can be struck between accuracy and computational cost. The model constructed here considers only the "big names" of atmospheric molecules involved in the $HO_x$ and $NO_x$ cycles, since these cycles are inter- and intra-dependent on each other (discussed in Chapter 1). Since a zero-dimensional model is used, the concentrations are considered uniform across the space being modelled; however, it must be acknowledged that concentrations of atmospheric constituents differ in space across the globe due to factors such as wind transport and lifetimes.[1] As a result, the concentrations employed here are assumed to be representative of global concentrations, since the study is indicative and not quantitative.

The third item to consider in the construction of the model is how, mathematically, the calculations will be solved. Different approaches to solving the equations can be taken, also varying in levels of complexity and time required. Solving iteratively is the least complex and computationally expensive, as it involves solving the equation for each time step using the previous solution as the input. Each time step ($\Delta t$) represents a small portion of the total time modelled, and by breaking up the total time into small time steps, a more accurate result is achieved. The calculations are usually calculated iteratively for each time step until convergence occurs. Using a smaller time step will give more accurate results than a larger one, but requires more calculations to be performed and so is more computationally expensive. The time step should be shorter than the shortest lifetime being modelled to ensure changes in concentration of all modelled concentrations can be captured within an iteration. A coupled differential approach is also commonly taken, which involves solving a series of coupled differential equations to find steady-state equations using partial derivatives. This allows for modelling on much larger time scales, upwards of an hour or day. Since the model employed here is only intended to be indicative of potential impacts a “plume” or injection of a substance will cause, the required time frame isn’t large so an iterative approach is the most appropriate and gives a good estimate.

## 5.2 Literature Studies

Three previous studies were heavily consulted during the construction of the model applied here, as they were similar in the variables they involved and the way they calculated the outputs. The first was constructed by Levy (1972).[3] It solves coupled differential equations that describe variables as either a function of time or in the steady-state approximation. Levy then simplifies these equations down to give equations for the concentration of each calculated variable only dependent on reaction rate and concentration of the other variables considered. Levy holds the concentrations of the major species of air, $O_2$, $H_2O$, $CH_4$, CO, $O_3$, and $NH_3$ constant, and calculates the concentration variables for NO·, $NO_2$·, $NO_3$·, $N_2O_5$, $HNO_3$, $HNO_2$, HOO·, OH·, $H_2O_2$, $CH_3O_2$·, $CH_3O$·, $CH_3OOH$, $H_2CO$, and HCO using 48 reactions. He considers reactions of first, second, and third order, but doesn't consider rainout or deposition of molecules, and so is the least complex of the models considered.

The second considered is by Logan et al. (1981), who use a numerical approach described by Wofsy et al. (1972).[4, 5] They use time-dependent continuity equations (which are equations that consider transport and sinks or sources of molecules), which are then adapted to be finite difference equations on which they impose boundary conditions. Logan et al.'s model is more sophisticated than that of Levy, as it considers vertical diffusion of long-lived gases, allows for variation with diurnal patterns, and uses 52 reactions that also consider loss of variables by aerosol scavenging or precipitation. Logan et al. (1981) calculate $CH_3CCl_3$ as a marker of ·OH production and to give a budget for ·OH distribution. Logan et al. (1981) also apply a 2-D column type model by finding rates as functions of altitude and latitude. Their inputs for $H_2O$, CO, $O_3$, $CH_4$, and $H_2$ are 2-D distributions that are functions of latitude and season, taken from observational data.

The final model considered is investigated by Pan (2000).[6] They use the zero-dimensional photochemical model from Logan et al. (1981), and attempt to use the steady-state approximation with "clean" tropospheric conditions to simplify equations for concentration of atmospheric molecules.[4] They use an iterative method to compute the steady-state concentration of their variables.

## 5.3 Model Details

Similar to those studies discussed in section 5.2, a zero-dimensional model was constructed using an iterative method to calculate the concentration of each variable at each time step. The concentrations of the major species of $H_2O$, $O_2$, $O_3$, CO, $CH_4$, $N_2$, $H_2$, $N_2O$, $HNO_2$, $HNO_3$, $HNO_4$, $N_2O_5$ were fixed, with further species of $O^3P$, $O^1D$, $H_2CO$, and HCO· becoming fixed in later iterations. Major species were chosen and fixed based on the literature consulted in section 5.2. The concentration of these species can be fixed as they present in large concentrations compared to other species that are being calculated for, so the concentrations of major species do not change appreciably over the small time scales calculated for. 79 total reactions, listed in Tables 5.1, 5.2, and 5.3, were used to construct the model, sourced from the Chemical Kinetics Database and compared to Levy (1972), Logan et al. (1981), and Pan (2000) to ensure similar construction.[3, 4, 6, 7] Reaction constants were sourced from the work with the most similar conditions to those employed in the model (atmospheric pressure and standard temperature), and reaction constants for photodissociation reactions were calculated as discussed in section 5.3.1. As the simulation was intended to be indicative, using kinetic parameters at 298K was appropriate, with the knowledge that further refining of the model and use of kinetic parameters at specific given pressures and temperatures for specific altitudes modelled at would need to occur later on. Table 5.4 lists the input values for fixed variables used, excluding those that became fixed during finetuning of the simulation's construction. The time step used was determined by the fastest reaction included in the calculation, as increasing the time step significantly above the lifetime of the fastest reaction would cause instabilities and prevent calculations from occurring. Deposition is accounted for in the reactions listed, but no atmospheric transport or diffusion is considered.

Table 5.1 Photolysis reactions and rate constants at 298K. A indicates the J value was calculated in this work, as discussed in section 5.3.1.

| # | Reaction | J ($s^{-1}$) | Rate Expression | Ref |
|---|---|---|---|---|
| 1 | $O_3 + hv \rightarrow O^1D + O_2$ | $4.05E^{-06}$ | $J_1[O_3]$ | A |
| 5 | $H_2O_2 + hv \rightarrow 2OH\cdot$ | $1.3E^{-06}$ | $J_5[H_2O_2]$ | A, 8 |
| 20 | $H_2CO + hv \rightarrow CO + H_2$ | $1.08E^{-05}$ | $J_{20}[H_2CO]$ | A, 9 |
| 22 | $H_2CO + hv \rightarrow H\cdot + HCO\cdot$ | $6.88E^{-06}$ | $J_{22}[H_2CO]$ | A |
| 37 | $NO_2\cdot + hv \rightarrow NO\cdot + O^3P$ | $2.02E^{-03}$ | $J_{37}[NO_2\cdot]$ | A |
| 38 | $HNO_3 + hv \rightarrow \cdot OH + NO_2\cdot$ | $8.9E^{-08}$ | $J_{38}[HNO_3]$ | A |
| 44 | $NO_3\cdot + hv \rightarrow NO\cdot + O_2$ | $5.25E^{-04}$ | $J_{44}[NO_3\cdot]$ | A |
| 45 | $NO_3\cdot + hv \rightarrow NO_2\cdot + O^3P$ | $9.30E^{-03}$ | $J_{45}[NO_3\cdot]$ | A |
| 46 | $HNO_2 + hv \rightarrow \cdot OH + NO\cdot$ | $3.58E^{-04}$ | $J_{46}[HNO_2]$ | A |
| 48 | $O_3 + hv \rightarrow O^3P + O_2$ | $8.47E^{-06}$ | $J_{48}[O_3]$ | A |
| 59 | $HNO_4 + hv \rightarrow HO_2\cdot + NO_2\cdot$ | $5.25E^{-07}$ | $J_{59}[HNO_4]$ | A |
| 60 | $HNO_4 + hv \rightarrow HO\cdot + NO_3\cdot$ | $3.65E^{-07}$ | $J_{60}[HNO_4]$ | A |
| 61 | $N_2O_5 + hv \rightarrow NO_3\cdot + NO_2\cdot$ | $8.65E^{-06}$ | $J_{61}[N_2O_5]$ | A |

Table 5.2 Unimolecular reactions and rate constants at 298K.

| # | Reaction | k ($s^{-1}$) | Rate Expression | Ref |
|---|---|---|---|---|
| 49 | $H_2O_2 \rightarrow M$ (deposition) | $4.00E^{-05}$ | $k_{49}[H_2O_2]$ | 10 |
| 50 | $CH_3OOH \rightarrow M$ (deposition) | $1.20E^{-05}$ | $k_{50}[CH_3OOH]$ | 10 |
| 51 | $H_2CO \rightarrow M$ (deposition) | $2.31E^{-06}$ | $k_{51}[H_2CO]$ | 4 |
| 56 | $HNO_4 \rightarrow HOO\cdot + NO_2\cdot$ | 0.39 | $k_{56}[HNO_4]$ | 11 |
| 57 | $N_2O_5 \rightarrow NO_2\cdot + NO_3\cdot$ | 2.52 | $k_{57}[N_2O_5]$ | 11 |
| 66 | $HNO_2 \rightarrow M$ (deposition) | $2.31E^{-06}$ | $k_{66}[HNO_2]$ | 4 |
| 67 | $HNO_3 \rightarrow M$ (deposition) | $2.31E^{-06}$ | $k_{67}[HNO_3]$ | 4 |
| 68 | $HNO_4 \rightarrow M$ (deposition) | $2.31E^{-06}$ | $k_{68}[HNO_4]$ | 4 |

Table 5.3 Bimolecular reactions and rate constants at 298 K.

| # | Reaction | k (L mol$^{-1}$ s$^{-1}$) | Rate Expression | Ref. |
|---|---|---|---|---|
| 2 | $O^1D + N_2 \rightarrow N_2 + O^3P$ | $2.59\text{x}10^{-11}$ | $k_2[O^1D][N_2]$ | 12 |
| 3 | $O^1D + O_2 \rightarrow O_2 + O^3P$ | $4.05\text{x}10^{-11}$ | $k_3[O^1D][O_2]$ | 12 |
| 4 | $O^1D + H_2O \rightarrow OH\cdot + OH\cdot$ | $2.01\text{x}10^{-10}$ | $k_4[O^1D][H_2O]$ | 13 |
| 6 | $H_2O_2 + OH\cdot \rightarrow HOO\cdot + H_2O$ | $1.7\text{x}10^{-12}$ | $k_6[H_2O_2][OH\cdot]$ | 14 |
| 7 | $2HOO\cdot \rightarrow H_2O_2 + O_2$ | $1.8\text{x}10^{-12}$ | $k_7[HOO\cdot][HOO\cdot]$ | 15 |
| 8 | $CO + \cdot OH \rightarrow CO_2 + H\cdot$ | $2.31\text{x}10^{-13}$ | $k_8[CO][OH\cdot]$ | 16 |
| 10 | $HOO\cdot + NO\cdot \rightarrow OH\cdot + NO_2\cdot$ | $8.41\text{x}10^{-12}$ | $k_{10}[HOO\cdot][NO\cdot]$ | 17 |
| 11 | $HOO\cdot + O_3 \rightarrow \cdot OH + 2O_2$ | $2.01\text{x}10^{-15}$ | $k_{11}[HOO\cdot][O_3]$ | 14 |
| 12 | $CH_4 + OH\cdot \rightarrow CH_3\cdot + H_2O$ | $6.34\text{x}10^{-15}$ | $k_{12}[CH_4][\cdot OH]$ | 18 |
| 13 | $HO\cdot + NO_2\cdot \rightarrow HNO_3$ | $3.6\text{x}10^{-11}$ | $k_{13}[HO\cdot][NO_2\cdot]$ | 19 |
| 15 | $CH_3O_2\cdot + HOO\cdot \rightarrow CH_3OOH + O_2$ | $5.21\text{x}10^{-12}$ | $k_{15}[CH_3O_2\cdot][HOO\cdot]$ | 20 |
| 16 | $CH_3OOH + M \rightarrow CH_3O\cdot + \cdot OH$ | $9.37\text{E}^{-07}$ | $k_{16}[CH_3OOH][M]$ | 8 |
| 17 | $CH_3O_2\cdot + NO\cdot \rightarrow CH_3O\cdot + NO_2\cdot$ | $7.53\text{x}10^{-12}$ | $k_{17}[CH_3O_2\cdot][NO\cdot]$ | 21 |
| 18 | $2CH_3O_2\cdot \rightarrow 2CH_3O\cdot + O_2$ | $1.29\text{x}10^{-13}$ | $k_{18}[CH_3O_2\cdot][CH_3O_2\cdot]$ | 22 |
| 19 | $CH_3O\cdot + O_2 \rightarrow H_2CO + HOO\cdot$ | $1.6\text{x}10^{-15}$ | $k_{19}[CH_3O\cdot][O_2]$ | 23 |
| 21 | $H_2CO + \cdot OH \rightarrow HCO\cdot + H_2O$ | $9.38\text{x}10^{-12}$ | $k_{21}[H_2CO][\cdot OH]$ | 20 |
| 23 | $HCO\cdot + O_2 \rightarrow CO + HOO\cdot$ | $5.2\text{x}10^{-12}$ | $k_{23}[HCO\cdot][O_2]$ | 20 |
| 24 | $O^1D + CH_4 \rightarrow \cdot CH_3 + \cdot OH$ | $1.13\text{x}10^{-10}$ | $k_{24}[O^1D][CH_4]$ | 24 |
| 25 | $O^1D + CH_4 \rightarrow H_2CO + H_2$ | $1.5\text{x}10^{-11}$ | $k_{25}[O^1D][CH_4]$ | 24 |
| 26 | $HOO\cdot + \cdot OH \rightarrow H_2O + O_2$ | $1.11\text{x}10^{-10}$ | $k_{26}[HOO\cdot][\cdot OH]$ | 20 |
| 28 | $CH_3OOH + \cdot OH \rightarrow CH_3O_2\cdot + H_2O$ | $3.59\text{x}10^{-12}$ | $k_{28}[CH_3OOH][\cdot OH]$ | 24 |
| 29 | $CH_3OOH + \cdot OH \rightarrow H_2O + CH_2OOH$ | $1.89\text{x}10^{-12}$ | $k_{29}[CH_3OOH][\cdot OH]$ | 20 |
| 30 | $2CH_3O_2\cdot \rightarrow (CH_3O)_2 + O_2$ | $3.01\text{x}10^{-14}$ | $k_{30}[CH_3O_2\cdot][CH_3O_2\cdot]$ | 22 |
| 31 | $2CH_3O_2\cdot \rightarrow H_2CO + CH_3OH + O_2$ | $3.35\text{x}10^{-13}$ | $k_{31}[CH_3O_2\cdot][CH_3O_2\cdot]$ | 25 |
| 32 | $O^1D + H_2 \rightarrow \cdot OH + H\cdot$ | $1.1\text{x}10^{-10}$ | $k_{32}[O^1D][H_2]$ | 20 |
| 33 | $H_2 + \cdot OH \rightarrow H_2O + H\cdot$ | $6.69\text{x}10^{-15}$ | $k_{33}[H_2][\cdot OH]$ | 20 |
| 35 | $\cdot OH + O_3 \rightarrow HOO\cdot + O_2$ | $7.25\text{x}10^{-14}$ | $k_{35}[\cdot OH][O_3]$ | 14 |
| 36 | $O^1D + N_2O \rightarrow NO\cdot + NO\cdot$ | $7.21\text{x}10^{-11}$ | $k_{36}[N_2O][O^1D]$ | 20 |
| 39 | $\cdot OH + HNO_3 \rightarrow H_2O + NO_3\cdot$ | $1.5\text{x}10^{-13}$ | $k_{39}[\cdot OH][HNO_3]$ | 14 |
| 40 | $NO\cdot + NO_3\cdot \rightarrow NO_2\cdot + NO_2\cdot$ | $2.6\text{x}10^{-11}$ | $k_{40}[NO\cdot][NO_3\cdot]$ | 14 |
| 41 | $O_3 + NO\cdot \rightarrow O_2 + NO_2\cdot$ | $1.73\text{x}10^{-14}$ | $k_{41}[O_3][NO\cdot]$ | 14 |
| 42 | $O_3 + NO_2\cdot \rightarrow O_2 + NO_3\cdot$ | $3.52\text{x}10^{-17}$ | $k_{42}[O_3][NO_2\cdot]$ | 14 |

| # | Reaction | k (L mol$^{-1}$ s$^{-1}$) | Rate Expression | Ref. |
|---|---|---|---|---|
| 52 | $HOO\cdot + NO_2\cdot \rightarrow O_2 + HNO_2$ | $3.01 \times 10^{-13}$ | $k_{52}[HOO\cdot][NO_2\cdot]$ | 26 |
| 54 | $\cdot OH + HNO_2 \rightarrow H_2O + NO_2\cdot$ | $6 \times 10^{-12}$ | $k_{54}[\cdot OH][HNO_2]$ | 14 |
| 55 | $\cdot OH + HNO_4 \rightarrow H_2O + NO_2\cdot + O_2$ | $5 \times 10^{-13}$ | $k_{55}[\cdot OH][HNO_4]$ | 4 |
| 64 | $M + N_2O_5 \rightarrow M + NO_2\cdot + NO_3\cdot$ | 3.24 | $k_{64}[N_2O_5][M]$ | 14 |
| 65 | $M + HNO_4 \rightarrow M + HOO\cdot + NO_2\cdot$ | 0.35 | $k_{65}[HNO_4][M]$ | 14 |
| 69 | $H_2O + N_2O_5 \rightarrow HNO_3 + HNO_3$ | $2.5 \times 10^{-22}$ | $k_{69}[H_2O][N_2O_5]$ | 14 |
| 70 | $HNO_3 + O^3P \rightarrow \cdot OH + NO_3\cdot$ | $3.01 \times 10^{-17}$ | $k_{70}[HNO_3][O^3P]$ | 12 |
| 72 | $H_2O_2 + NO\cdot \rightarrow \cdot OH + HNO_2$ | $5.2 \times 10^{-20}$ | $k_{72}[H_2O_2][O^3P]$ | 27 |
| 73 | $\cdot OH + HNO_2 \rightarrow H_2O + NO_2\cdot$ | $6 \times 10^{-12}$ | $k_{73}[\cdot OH][HNO_2]$ | 14 |
| 74 | $HOO\cdot + NO\cdot \rightarrow \cdot OH + NO_2\cdot$ | $8.91 \times 10^{-12}$ | $k_{74}[HOO\cdot][NO\cdot]$ | 14 |
| 75 | $\cdot OH + \cdot OH \rightarrow H_2O + O^3P$ | $1.88 \times 10^{-12}$ | $k_{75}[\cdot OH][\cdot OH]$ | 14 |
| 77 | $O^3P + H_2O_2 \rightarrow \cdot OH + HOO\cdot$ | $1.7 \times 10^{-15}$ | $k_{77}[O^3P][H_2O_2]$ | 22 |
| 78 | $HOO\cdot + NO_3\cdot \rightarrow O_2 + HNO_4$ | $4.3 \times 10^{-12}$ | $k_{78}[HOO\cdot][NO_3\cdot]$ | 22 |
| 79 | $HOO\cdot + NO_3\cdot \rightarrow HO\cdot + NO_2\cdot + O_2$ | $4.3 \times 10^{-12}$ | $k_{79}[HOO\cdot][NO_3\cdot]$ | 22 |

Table 5.4 Termolecular reactions and rate constants at 298 K. Rate constants and expressions listed are pseudo second order, using air density as M = $2.70 \times 10^{19}$ cm$^3$ molecule$^{-1}$.

| # | Reaction | k (L$^2$ mol$^{-2}$ s$^{-1}$) | Rate Expression | Ref. |
|---|---|---|---|---|
| 9 | $M + O_2 + H\cdot \rightarrow M + HOO\cdot$ | $1.48 \times 10^{-12}$ | $k_9[O_2][H\cdot][M]$ | 14 |
| 14 | $M + CH_3\cdot + O_2 \rightarrow CH_3O_2\cdot$ | $2.04 \times 10^{-11}$ | $k_{14}[CH_3\cdot][O_2][M]$ | 28 |
| 27 | $M + HOO\cdot + HOO\cdot \rightarrow H_2O_2 + O_2$ | $1.37 \times 10^{-12}$ | $k_{27}[HOO\cdot][HOO\cdot][M]$ | 11 |
| 34 | $M + O_2 + H\cdot \rightarrow HOO\cdot$ | $5.4 \times 10^{-32}$ | $k_{34}[H\cdot][O_2][M]$ | 11 |
| 43 | $M + \cdot OH + NO\cdot \rightarrow HNO_2$ | $2 \times 10^{-11}$ | $k_{43}[\cdot OH][NO\cdot][M]$ | 24 |
| 47 | $M + O_2 + O^3P \rightarrow O_3$ | $1.62 \times 10^{-14}$ | $k_{47}[O_2][O^3P][M]$ | 11 |
| 53 | $M + HOO\cdot + NO_2\cdot \rightarrow HNO_4$ | $4.86 \times 10^{-12}$ | $k_{53}[HOO\cdot][NO_2\cdot][M]$ | 11 |
| 58 | $M + NO_2\cdot + NO_3\cdot \rightarrow N_2O_5$ | $7.59 \times 10^{-11}$ | $k_{58}[NO_2\cdot][NO_3\cdot][M]$ | 11 |
| 62 | $M + \cdot OH + NO_2\cdot \rightarrow HNO_3$ | $8.91 \times 10^{-11}$ | $k_{62}[\cdot OH][NO_2\cdot][M]$ | 29 |
| 63 | $M + CH_3O_2\cdot + NO_2\cdot \rightarrow CH_3O_2NO_2$ | $6.75 \times 10^{-11}$ | $k_{63}[CH_3O_2\cdot][NO_2\cdot][M]$ | 20 |
| 71 | $H_2O + NO\cdot + NO_2\cdot \rightarrow HNO_2 + HNO_2$ | $6.07 \times 10^{-35}$ | $k_{71}[H_2O][NO\cdot][NO_2\cdot]$ | 30 |
| 76 | $M + \cdot OH + \cdot OH \rightarrow H_2O_2$ | $1.86 \times 10^{-11}$ | $k_{76}[\cdot OH][\cdot OH][M]$ | 11 |

Table 5.5 List of input concentrations for fixed variables used in simulations.

| **Molecule** | **Concentration (molecule cm$^{-3}$)** | **Reference** |
|---|---|---|
| $H_2O$ | $5.00x10^{17}$ | 3 |
| Air (M) | $2.50x10^{19}$ | 3 |
| $O_2$ | $5.15x10^{18}$ | 3 |
| $N_2$ | $1.92x10^{19}$ | 6 |
| $H_2$ | $1.35x10^{13}$ | 6 |
| $N_2O$ | $8.00x10^{12}$ | 31 |
| $HNO_2$ | $3.20x10^{8}$ | 3 |
| $HNO_3$ | $1.40x10^{10}$ | 3 |
| $HNO_4$ | $6.00x10^{5}$ | 6 |
| $N_2O_5$ | $3.00x10^{3}$ | 6 |
| CO | $1.72x10^{12}$ | 32 |
| $O_3$ | $5.24x10^{11}$ | 33 |
| $CH_4$ | $3.35x10^{13}$ | 34 |
| $H_2CO$ | $2.00x10^{10}$ | 3 |

The species: OH·, HOO·, $H_2O_2$, $CH_3$·, $CH_3O_2$·, $CH_3O$·, $CH_3OOH$, NO·, $NO_2$·, and $NO_3$·, had concentrations calculated iteratively. The change in concentration for one iteration was found according to equation 5.1, where P is the total production rate and L is the total loss rate:

$$\frac{d[x]_i}{dt} = P - L \tag{5.1}$$

The concentration at each time step was then calculated according to equation 5.2, where $[x]_i$ is the current concentration, $[x]_{i-1}$ is the concentration from the previous iteration, and Δt is the time step:

$$[x]_i = [x]_{i-1} + \Delta t * \frac{d[x]_i}{dt} \tag{5.2}$$

Using $CH_3$· as an example, the calculation process is as follows:

Production equations:

$$CH_4 + \cdot OH \rightarrow CH_3 \cdot + H_2O \tag{5.3}$$

$$CH_4 + O^1D \rightarrow CH_3 \cdot + \ \cdot OH \tag{5.4}$$

$$P = k_{12}[CH_4][\cdot OH]_{i-1} + k_{24}[CH_4][O^1D]_{i-1} \tag{5.5}$$

Loss equations:

$$CH_3 \cdot + O_2 \rightarrow CH_3O_2 \cdot \tag{5.6}$$

$$L = [CH_3 \cdot]_{i-1}(k_{14}[O_2]) \tag{5.7}$$

Iterative concentration equation:

$$[CH_3 \cdot]_i = [CH_3 \cdot]_{i-1} + \Delta t(P - L) \tag{5.8}$$

Once a variable no longer experienced significant change and had P ≈ L, it was considered to have reached "steady-state". Figure 5.2 shows an example of the variable $NO_2\cdot$ reaching steady-state in the V14 "spin-up" simulation, with the value maintained over a time period (flat line on graph).

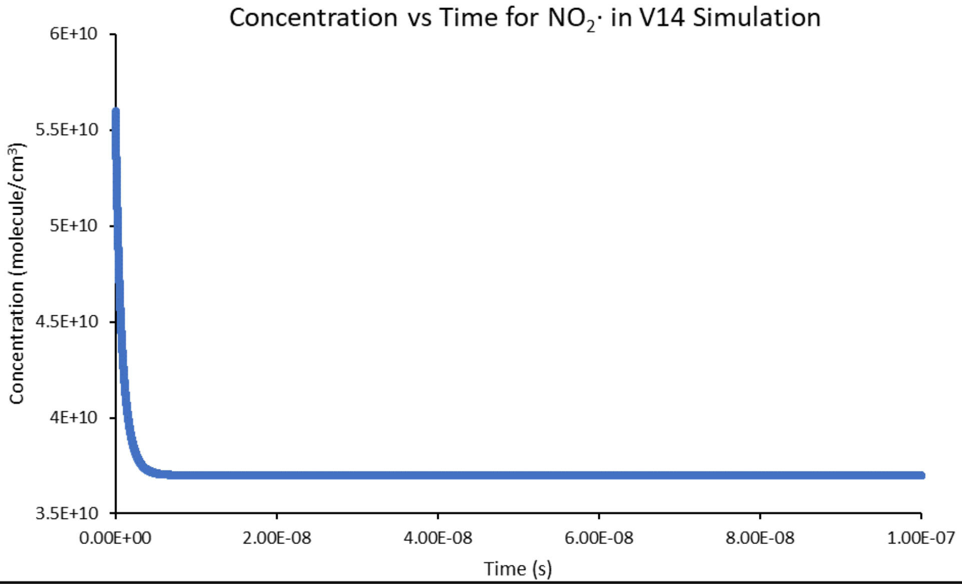

Figure 5.2 Graph of concentration vs time for $NO_2\cdot$ in the V14 simulation. $NO_2\cdot$ is considered to have reached steady-state as it remains at a constant value over a large time period as shown in the graph, as well as equal and unchanging production and loss values.

Multiple iterations of the model were run to determine its accuracy by allowing the "spin-up" of variables, where "spin-up" iterations have initial concentration inputs at 0 and the calculations are continued until a steady-state (SS) value is reached. The variable would then be fixed at the SS value for the remainder of the simulation, such that the timestep could be increased and thus other variables, specifically long-lived molecules like $H_2O_2$, could reach SS. The experimental SS values were then compared to literature values, as the model was considered to give a good estimate when experimental SS values were comparable with literature. During construction of the model, variables would be fixed or un-fixed and further equations or molecules added in to the system to improve accuracy.

More variables and reactions were added to the model during development, and some were removed in order to make the model less computationally taxing. HCO· and $H_2CO$ were found to be involved in only a handful of reactions, so by fixing them at the SS values calculated in previous iterations, computational complexity was lessened. Over time, other variables also became fixed as their values did not appreciably change between model iterations; $CH_4$, $O_3$, $O^1D$, $O^3P$ all became fixed variables. This makes sense for $O^3P$ and $O^1D$ as production of both is dependent on $O_3$, which in itself has only one major reaction considered.

### 5.3.1 SMARTS and Photolysis Rates

The model, being atmospheric, includes a number of photodissociation reactions. The J value is the rate of reaction specifically for photodissociation reactions, units $s^{-1}$.[35] It varies with light available as it is calculated by integrating over the absorption cross section σ, quantum yield ϕ, and actinic flux F (Equation 5.9).[35]

$$J = \int_{\lambda_2}^{\lambda_1} \sigma * \phi * F \, d\lambda \tag{5.9}$$

To get an accurate J value for the reactions included in the model, the SMARTS program was used. SMARTS is the Simple Model of the Atmospheric Radiative Transfer of Sunshine.[36] It calculates how changes in atmospheric conditions affect the available solar power or photon energy for each wavelength. It calculates the amount of photon energy received on a plane at a specified altitude and height, which is called the site. SMARTS is used in this model so that the rate (J) is specific to the site chosen (in this case, New Zealand in the summer at noon). It does so by allowing the conditions listed to be set by the user (see Table 5.5) and supplies outputs chosen by the user. The parameters were set to simulate a New Zealand specific environment. This was done by using input values that were taken from data measured at the NIWA base in Lauder, Otago for $O_3$ level, $CO_2$ concentration, and site pressure, temperature, and relative

Table 5.6 Parameters for SMARTS simulation and values chosen for each.

| Condition | Value |
|---|---|
| Site Pressure | 964 mb[33] |
| Altitude | 2 km |
| Atmosphere | 10.6 ̊C ground level air temperature,[33] 75% ground level relative humidity,[33] 16.1 ̊C average daily temperature[37] |
| Season | Summer |
| Water Vapour | Calculate from input |
| $[O_3]$ (site level) | 0.282 atm-cm[38] |
| Pollution level | Light |
| $[CO_2]$ | 407 ppmv[39] |
| Extra-terrestrial spectrum | Gueymard 2004[40] |
| Aerosol model | Urban (Shettle and Fenn)[41] |
| Turbidity | 0.05 aerosol optical depth at 500nm |
| Albedo | 0 |
| Spectral range | 280 – 700 nm |
| Solar constant | 1336.1 W $m^{-2}$ [40] |
| Solar constant distance correction factor | 1.0 [42] |
| Output values | Extra-terrestrial irradiance, direct normal irradiance, diffuse horizontal photon irradiance, beam-normal photon irradiance |

humidity.[33] A light pollution level and an urban aerosol model was chosen to simulate conditions over cities. Summer was chosen since it will experience the highest irradiance and therefore give an upper limit to the potential effects modelled. The albedo was set to 0 for simplicity. Outputs of irradiance (W $m^{-2}$ $nm^{-1}$) and spectral photon flux ($cm^{-2}$ $s^{-1}$ $nm^{-1}$), usually called actinic flux, were chosen. Using these outputs, the actinic flux can be found, allowing J to be calculated for each photolysis reaction.

Actinic flux (F) consists of direct, diffuse, and reflected components, as shown in Equation 5.10:

$$F = F_{diffuse} + F_{direct} + F_{reflected} \tag{5.10}$$

It is calculated from the incident radiation at the surface of the atmosphere, considering all scattering and absorption processes the radiation undergoes to reach the surface of the Earth.[35, 43, 44] However, it can be calculated in this case by finding the sum of the individual components. The direct component $F_{direct}$ can be found by Equation 5.11, where beam-normal photon irradiance (DNI, $cm^2$ $nm^{-1}$ $s^{-1}$) is calculated by SMARTS, and SZA is the solar zenith angle.[43] Beam-normal photon irradiance or direct normal irradiance excludes the diffuse irradiance experienced from the incident radiation.[43] SZA is the angle between the sun's rays and the surface modelled, which was chosen by SMARTS as 45°.[43]

$$F_{direct} = \frac{DNI}{cos\,(SZA)} \tag{5.11}$$

$F_{reflected}$ usually depends on the albedo (the amount of light reflected by the surface), which is set to 0 for simplification.[43] $F_{diffuse}$ is found by Equation 5.12, where DHI is diffuse horizontal irradiance, which is the portion of the incident irradiance from only scattering, and r is the ratio of diffuse irradiance to diffuse actinic flux. This ratio has been experimentally determined to be 0.5 when scattered radiation is isotropic, and is used as such in this work for simplification.[44]

$$F_{diffuse} = \frac{DHI}{r} \tag{5.12}$$

The calculated values for F using data from the SMARTS simulation are in the $10^{14}$ $cm^{-2}$ $s^{-1}$ $nm^{-1}$ range (λ = 280 – 700 nm), which are within the range of literature values ($1x10^{14}$ – $2x10^{16}$ $cm^{-2}$ $s^{-1}$ $nm^{-1}$), validating the calculation method.[43-45]

Using the calculated data for F, J can then be found for each photolysis reaction included in the model. To verify this method, the J for photolysis of $O^1D$ was found first and compared to literature values. The calculated value for J($O^1D$), using data from the SMARTS simulation, is $4.05x10^{-06}$ $s^{-1}$. The literature compiled in Table 5.6 ranges from $1x10^{-06}$ – $4.25x10^{-05}$ $s^{-1}$. The calculated value therefore falls within the range of literature data, validating this method of calculating J values (values can be found in appendix D, alongside the values of $\lambda_1$, $\lambda_2$, ϕ, and σ used in each calculation).

Table 5.7 Literature values of J($O^1D$) measured, along with conditions they were measured at. Most literature is from the Northern Hemisphere and measurements are done over summer at noon, which are the conditions considered in this simulation, so results are comparable.

| **Ref.** | **Conditions** | **J($O^1D$) ($s^{-1}$)** |
|---|---|---|
| 46 | Varying cloud cover, Sept - Nov (autumn) | Range: 1 - 14x$10^{-6}$, peak value of ~ 20x$10^{-6}$ in summer, 1.2x$10^{-6}$ in winter |
| 47 | August (summer); mix of clear, cloudy, and rainy days | Range: 0 - 1.0x$10^{-6}$, peak value of ~ 22x$10^{-6}$ |
| 48 | - | 8.5x$10^{-6}$ |
| 49 | Ireland, August (autumn) | $10^{-5}$ scale, peak value of 3.5x$10^{-5}$ |
| 32 | Spring and winter | 1.46x$10^{-5}$ in spring, 3.86x$10^{-7}$ in winter |
| 50 | Greece, March - July (spring - summer) | 4.25x$10^{-5}$ |
| 43 | Sunspec calculations | Peak value of ~ 2.3x$10^{-5}$ |
| 44 | Midday, June | 3.5x$10^{-6}$ from NIWA data, 3.5x$10^{-5}$ measured value |
| 51 | Colorado, June (summer); mix of cloudy and clear skies | Peak value of ~ 3.5x$10^{-5}$ |
| **Average** | Northern Hemisphere, American | Range: $10^{-6}$ - $10^{-5}$ scale, average value of ~ 2.2x$10^{-5}$ |

## 5.4 Results

Table 5.7 lists the different simulations run, along with the number of iterations of that simulation run and a list of the fixed variables in the simulation. Many simulations were conducted to finetune the conditions applied, including determining which variables reached the same steady-state (SS) value repeatedly, thus allowing them to become fixed, and which variables would not reach literature SS values, allowing further investigation into the construction of their production and loss equations or the decision to fix them at literature SS concentrations be made. During the process of finetuning the simulations, reactions were added to improve the $NO_x$ variables' ability to reach literature SS.

Table 5.8 List of simulations conducted, with number of iterations run and calculated variables for each. Most simulations were conducted to finetune conditions, changing things like which variables were fixed, input concentrations, time steps, or adding other reactions in.

| Name | Calculated Variables | Iterations | Notes |
|---|---|---|---|
| V1 | $OH\cdot$, $HOO\cdot$, $H_2O_2$, $CH_4$, $CH_3\cdot$, $CH_3O_2\cdot$, $CH_3OOH$, $CH_3O\cdot$, $NO\cdot$, $NO_2\cdot$, $NO_3\cdot$, $H_2CO$, $HCO\cdot$, $O^1D$, $O^3P$, $O_3$ | 1 | Testing model with new time step for instabilities and to see potential timeframe for variables to reach steady-state |
| V2 | $OH\cdot$, $HOO\cdot$, $H_2O_2$, $CH_4$, $CH_3\cdot$, $CH_3O_2\cdot$, $CH_3OOH$, $CH_3O\cdot$, $NO\cdot$, $NO_2\cdot$, $NO_3\cdot$, $H_2CO$, $HCO\cdot$, $O^1D$, $O^3P$, $O_3$ | 1 | Added to the $O_3$ emissions column and testing for steady-state |
| V3 | $OH\cdot$, $HOO\cdot$, $H_2O_2$, $CH_4$, $CH_3\cdot$, $CH_3O_2\cdot$, $CH_3OOH$, $CH_3O\cdot$, $NO\cdot$, $NO_2\cdot$, $NO_3\cdot$, $H_2CO$, $HCO\cdot$, $O^1D$, $O^3P$, $O_3$ | 1 | Calculated variables set to 0 initially to allow 'spin-up' of model, except $CH_4$, $O_3$, $NO\cdot$, and $NO_2\cdot$ which are set to literature steady-state concentrations |
| V4 | $OH\cdot$, $HOO\cdot$, $H_2O_2$, $CH_4$, $CH_3\cdot$, $CH_3O_2\cdot$, $CH_3OOH$, $CH_3O\cdot$, $NO\cdot$, $NO_2\cdot$, $NO_3\cdot$ | 1 | Calculated variables set to 0 initially except $CH_4$, $NO\cdot$, and $NO_2\cdot$, which are set to literature steady-state concentrations. |
| V5 | $HOO\cdot$, $H_2O_2$, $CH_3O_2\cdot$, $CH_3O\cdot$, $NO\cdot$, $NO_2\cdot$ | 6 | Rectified issue with inaccurate $HOO\cdot$ equations, testing impact of changed equations |
| V6 | $CH_3O\cdot$, $NO\cdot$, $NO_2\cdot$ | 5 | Concentrations set to 0 initially; added in many missing reactions and testing to see impact |
| V7 | $OH\cdot$, $HOO\cdot$, $H_2O_2$, $CH_4$, $CH_3\cdot$, $CH_3O_2\cdot$, $CH_3OOH$, $CH_3O\cdot$, $NO\cdot$, $NO_2\cdot$, $NO_3\cdot$ | 2 | Final concentrations from previous simulation used as initial inputs for all except $CH_3O\cdot$, which is set to 0, trying to reach steady-state |
| V8 | $OH\cdot$, $HOO\cdot$, $H_2O_2$, $CH_4$, $CH_3\cdot$, $CH_3O_2\cdot$, $CH_3OOH$, $CH_3O\cdot$, $NO\cdot$, $NO_2\cdot$, $NO_3\cdot$ | 3 | Calculated variables set to 0 initially except $CH_4$ which is set to literature concentration, trying to reach steady-state |

| Name | Calculated Variables | Iterations | Notes |
|---|---|---|---|
| V9 | $OH\cdot$, $HOO\cdot$, $H_2O_2$, $CH_3\cdot$, $CH_3O_2\cdot$, $CH_3OOH$, $CH_3O\cdot$, $NO\cdot$, $NO_2\cdot$, $NO_3\cdot$ | 56 | Calculated variables set to 0 initially except $NO\cdot$ and $NO_2\cdot$ which are set to literature steady-state concentrations, trying to reach steady-state |
| V10 | $OH\cdot$, $HOO\cdot$, $H_2O_2$, $CH_3\cdot$, $CH_3O_2\cdot$, $CH_3OOH$, $CH_3O\cdot$, $NO\cdot$, $NO_2\cdot$, $NO_3\cdot$ | 9 | Literature steady-state concentrations used as initial inputs except $CH_3\cdot$ and $CH_3O\cdot$ set at 0, trying to reach steady-state |
| V11 | $OH\cdot$, $HOO\cdot$, $H_2O_2$, $CH_3\cdot$, $CH_3O_2\cdot$, $CH_3OOH$, $NO\cdot$, $NO_2\cdot$, $NO_3\cdot$ | 25 | Literature steady-state concentrations used as initial inputs except $CH_3\cdot$ set at 0, fixed $CH_3O\cdot$, trying to reach steady-state |
| V12 | $OH\cdot$, $HOO\cdot$, $H_2O_2$, $CH_3O_2\cdot$, $CH_3OOH$, $NO\cdot$, $NO_2\cdot$, $NO_3\cdot$ | 15 | Literature steady-state concentrations used as initial inputs, fixed $CH_3\cdot$, trying to reach steady-state |
| V13 | $OH\cdot$, $HOO\cdot$, $H_2O_2$, $CH_3O_2\cdot$, $CH_3OOH$, $NO\cdot$, $NO_2\cdot$, $NO_3\cdot$ | 23 | Literature steady-state concentrations used as initial inputs, changed time step, trying to reach steady-state |
| V14 | $OH\cdot$, $HOO\cdot$, $H_2O_2$, $CH_3O_2\cdot$, $CH_3OOH$, $CH_3O\cdot$, $NO\cdot$, $NO_2\cdot$, $NO_3\cdot$ | 21 | Calculated variables set to 0 initially except $NO\cdot$ and $NO_2\cdot$ which are set to previous steady-state concentrations, unfixed $CH_3O\cdot$ |
| V15 | $OH\cdot$, $HOO\cdot$, $H_2O_2$, $CH_3O_2\cdot$, $CH_3OOH$, $CH_3O\cdot$, $NO\cdot$, $NO_2\cdot$, $NO_3\cdot$ | 11 | Literature steady-state concentrations used as initial inputs to test robustness of construction |
| V16 | $OH\cdot$, $HOO\cdot$, $H_2O_2$, $CH_3O_2\cdot$, $CH_3OOH$, $CH_3O\cdot$, $NO_2\cdot$, $NO_3\cdot$ | 7 | Literature steady-state concentrations used as initial inputs to test robustness of construction, fixed $NO\cdot$ value to see if it solved $NO_x$ instability |
| P1 | $OH\cdot$, $HOO\cdot$, $H_2O_2$, $CH_3O_2\cdot$, $CH_3OOH$, $CH_3O\cdot$, $NO_2\cdot$, $NO_3\cdot$ | 40 | Literature steady-state concentrations used as initial inputs, except for $CH_3O_2\cdot$, $CH_3OOH$, $CH_3O\cdot$, which are set to zero. Added term for $\cdot OH$ production by $TiO_2$ to simulate continuous production |
| P2 | $OH\cdot$, $HOO\cdot$, $H_2O_2$, $CH_4$, $CH_3\cdot$, $CH_3O_2\cdot$, $CH_3OOH$, $CH_3O\cdot$, $NO_2\cdot$, $NO_3\cdot$, $O^1D$, $O^3P$, $O_3$ | 80 | Literature steady-state concentrations used as initial inputs. Added term for $\cdot OH$ production by $TiO_2$ to simulate continuous production. Unfixed range of variables included in $CH_4$ reactions |
| P3 | $OH\cdot$, $HOO\cdot$, $H_2O_2$, $CH_4$, $CH_3\cdot$, $CH_3O_2\cdot$, $CH_3OOH$, $CH_3O\cdot$, $NO\cdot$, $NO_2\cdot$, $NO_3\cdot$, $O^1D$, $O^3P$, $O_3$ | 100 | Literature steady-state concentrations used as initial inputs. Calculated perturbation rate for $TiO_2$ added to $\cdot OH$ production equation. |

The final “spin-up” simulation, V14, had 18 fixed concentrations, 9 variable concentrations, and a final total of 21 iterations for all variables to reach SS concentrations that were close to expected values. Allowing the simulation to “spin-up” gave an idea as to how accurate it is, since an accurate simulation would have variables reach similar SS values to literature. Any variables that wouldn’t reach close to literature SS could then be fixed, or their equations modified to make them more accurate. Table 5.8 lists the input, output, and literature SS concentrations for the variables calculated. The $NO_x$ variables had a non-zero input since there is a known issue with the concentration of NO· reaching a SS value that is largely different from the literature SS concentration. Overall, OH·, HOO·, $NO_2$·, and $NO_3$· were within expected range for literature SS values. In future builds of this model, further equations would be added to improve modelling accuracy of the variables that didn’t reach SS values similar to literature values, but in this work these variables were instead fixed at literature values, as adding further equations, whilst increasing model accuracy, would significantly increase computational complexity and time requirements. This build of the model, with the fixed variables, was considered appropriate for the intended use of indicative, not quantitative, results, with the acknowledgement that further improvements could be made to the model in future.

Table 5.9 List of input, output, and literature concentrations for variables in the final "spin-up" simulation V14. NO·, $NO_2$·, and $NO_3$· had non-zero initial values so that their behaviour could be investigated as there were issues in getting the $NO_x$ concentration close to expected values.

| Molecule | Initial Concentration (molecule cm$^{-3}$) | Steady-State Concentration (molecule cm$^{-3}$) | Literature Concentration (molecule cm$^{-3}$) | Ref |
|---|---|---|---|---|
| ·OH | 0.00 | $2.63x10^{6}$ | $1.00x10^{6}$ | 6 |
| | | | $1.70x10^{7}$ | 3 |
| HOO· | 0.00 | $1.03x10^{7}$ | $3.20x10^{8}$ | 6 |
| | | | $1.20x10^{9}$ | 3 |
| $H_2O_2$ | 0.00 | $6.97x10^{6}$ | $1.50x10^{10}$ | 6 |
| $CH_3O$· | 0.00 | $1.39x10^{-6}$ | $1.00x10^{2}$ | 6 |
| $CH_3O_2$· | 0.00 | $2.12x10^{5}$ | $1.20x10^{8}$ | 6 |
| | | | $5.10x10^{8}$ | 3 |
| $CH_3OOH$ | 0.00 | $4.15x10^{5}$ | $1.40x10^{10}$ | 6 |
| NO· | $1.90x10^{10}$ | $7.82x10^{-2}$ | $1.60x10^{8}$ | 6 |
| $NO_2$· | $5.60x10^{10}$ | $3.70x10^{10}$ | $3.10x10^{8}$ | 6 |
| | | | $4.92x10^{10}$ | 45 |
| $NO_3$· | $1.80x10^{6}$ | $1.80x10^{6}$ | $1.80x10^{6}$ | 6 |

This build of the simulation was then used to conduct a further simulation, V16. V16 used inputs of literature SS values listed in Table 5.9. This simulation was run to test whether the variables would deviate from literature SS concentrations, as if the model was emulating atmospheric conditions to a good approximation, the final SS concentrations reached should not deviate significantly from the literature SS concentrations used as inputs. V16 had 19 fixed concentrations, 8 variable concentrations, and a final total of 7 iterations, with NO· fixed at literature SS concentrations compared to V14. Overall, the variables do not deviate largely from the literature SS concentrations used as their input values, deviating only by a factor of 10 except for $CH_3O$· which deviated by a factor of 100. This indicates that the simulation is stable at these values, as the total time elapsed for this simulation is $1.68x10^6$ s, or 467 hours, which is very significant on an atomic timeframe. This simulation thus emulates a good approximation of atmospheric conditions and concentrations reached, and achieves satisfactory results for the intended indicative purpose, and can therefore be used to investigate the impact of increasing the ·OH formation rate via photocatalysis using $TiO_2$ by adding in a perturbation term.

Table 5.10 List of input and output concentrations for variables in the final simulation V16. Input concentrations are taken from expected steady-state values to determine whether the simulation will deviate largely from them.

| Molecule | Initial Concentration (molecule $cm^{-3}$) | Final Concentration (molecule $cm^{-3}$) | Change (molecule $cm^{-3}$) | Ref. |
|---|---:|---:|---:|---:|
| ·OH | $1.70x10^7$ | $1.37x10^7$ | $3.30x10^6$ | 3 |
| HOO· | $1.20x10^9$ | $6.29x10^8$ | $5.71x10^8$ | 3 |
| $H_2O_2$ | $1.50x10^{10}$ | $1.11x10^{10}$ | $3.90x10^9$ | 6 |
| $CH_3O$· | $1.00x10^2$ | 1.87 | $9.81x10^1$ | 6 |
| $CH_3O_2$· | $5.10x10^8$ | $7.04x10^7$ | $4.40x10^8$ | 3 |
| $CH_3OOH$ | $1.40x10^{10}$ | $2.62x10^9$ | $1.14x10^{10}$ | 6 |
| $NO_2$· | $3.10x10^8$ | $3.23x10^7$ | $2.78x10^8$ | 6 |
| $NO_3$· | $1.80x10^6$ | $1.67x10^6$ | $1.30x10^5$ | 6 |

### 5.4.1 Targeting $CH_4$ Removal Rates

With the model established, the feasibility of the catalyst loading needs to be determined, along with the amount of catalyst required to remove targeted levels of $CH_4$. $CH_4$ levels in the atmosphere have increased by 149% from 750 ppb in ~ 1750 to 1866 ppb in 2019.[52] The IPCC AR5 report notes a ~ 3.5% increase in methane levels from 2011 to 2019, and the trend, despite being variable in the past, appears stable and as a linear increase.[52] If a consistent yearly growth rate of 0.4% is assumed, a targeted percentage of removal (e.g. 10% total volume of $CH_4$) can be chosen which accounts for this growth. If the relationship between the amount of $TiO_2$ used and the amount of $CH_4$ removed is known, the volume of $TiO_2$ catalyst for this targeted rate could thus be calculated.

A kinetic scheme for the process of generating hydroxyl radicals by water splitting on a $TiO_2$ photocatalyst surface is derived as follows (modified from Williamson, 2025).[53] R and κ are the rate and rate coefficients of surface reactions (per unit area per second), and r and k are the rate and rate coefficients for volume reactions. K is an equilibrium constant. Volume concentrations are given in square brackets and surface concentrations in curved brackets.

Electron/hole formation is given by Equation 1.11:

$$TiO_2 + h\nu \rightarrow h^+ + e^- \tag{1.11}$$

$$R_{form} = \frac{F_\nu \Phi_\nu}{N_A} \tag{R1}$$

where $F_\nu$ is the photon flux at frequency ν, $\Phi_\nu$ is the quantum yield at wavelength ν, and $N_A$ is Avogadro's constant ($6.022 \times 10^{23}$ $mol^{-1}$).

Holes can then be used up in a recombination reaction:

$$h^+ + e^- \rightarrow Heat \tag{5.13}$$

$$R_{rec} = \kappa_{rec}(h^+)(e^-) \tag{R2}$$

Water is adsorbed to the surface of the catalyst:

$$H_2O(free) + Site \rightarrow H_2O(ads) \tag{5.14}$$

$$K_{ads} = \frac{(H_2O)}{[H_2O](Site)} \tag{R3}$$

Hydroxyl radicals are then formed via a water-splitting reaction given by Equation 1.17:

$$H_2O(ads) + h^+ \rightarrow \cdot OH(ads) + H^+ \tag{1.17}$$

$$R_{hrf} = \kappa_{hrf}(h^+)(H_2O) \tag{R4}$$

The formed hydroxyl radicals can then undergo desorption from the catalyst surface to become free radicals:

$$\cdot OH(ads) \rightarrow \cdot OH(free) + Site \tag{5.15}$$

$$R_{des} = \kappa_{des}(\cdot OH) \tag{R4}$$

$$r_{des} = R_{des} * \frac{A_{cat}}{V_{sys}} \tag{R5}$$

These radicals can then be lost through reaction with scavengers or traps:

$$\cdot OH + Scav \rightarrow Dark \tag{5.16}$$

$$r_{scav} = k_{scav}[\cdot OH][Scav] \tag{R6}$$

$$\cdot OH + Trap \rightarrow Fluor \tag{5.17}$$

$$r_{trap} = k_{trap}[\cdot OH][Trap] \tag{R7}$$

By using the steady-state approximation for $h^+$:

$$R_{form} = R_{hrf} + R_{rec} \tag{5.18}$$

Which can be rearranged to:

$$R_{hrf} = f_{hrf}R_{form} \tag{5.19}$$

where $f_{hrf}$ is the percentage of $h^+$ used in the hydroxyl radical formation reaction:

$$f_{hrf} = \frac{R_{hrf}}{R_{form}} = \frac{R_{hrf}}{R_{hrf} + R_{rec}} \tag{5.20}$$

By using the steady-state approximation for ·OH(ads):

$$R_{hrf} = R_{des} \tag{5.21}$$

Which can be rearranged by substituting rate R5 and Equation 5.19:

$$r_{des} = \frac{A_{cat}}{V_{sys}} f_{hrf}R_{form} \tag{5.22}$$

By using the steady state approximation for ·OH(free):

$$r_{des} = r_{trap} + r_{scav} \tag{5.23}$$

Or, similar to equation 5.19, it can be written as:

$$r_{trap} = f_{trap} r_{des} = \frac{A_{cat}}{V_{sys}} f_{trap} f_{hrf} R_{form} \tag{5.24}$$

where $f_{trap}$ is the fraction of ·OH consumed in trapping reactions:

$$f_{trap} = \frac{r_{trap}}{r_{des}} = \frac{r_{trap}}{r_{trap} + r_{scav}} \tag{5.25}$$

The probe molecule studies in Chapter 4 can be represented by equation 5.17 as they are fluorescent traps. As such, the change in concentration of 7-hydroxycoumarin (7HC) or 2-hydroxyterephthalic acid (2TPA) can be given by:

$$\frac{d[Fluor]}{dt} = \frac{A_{cat}}{V_{sys}} f_{trap} f_{hrf} R_{form} = \frac{A_{cat}}{V_{sys}} f_{trap} f_{hrf} * (\frac{F_{\upsilon} \Phi_{\upsilon}}{N_A}) \tag{5.26}$$

Rearranging this equation for the quantum yield:

$$\Phi_{\upsilon} = \frac{d[Fluor]}{dt} \frac{V_{sys} N_A}{A_{cat} f_{trap} f_{hrf} F_{\upsilon}} \tag{5.27}$$

Therefore, if the values given in Table 5.11 for the coumarin probe system used in Chapter 4 are used, equation 5.27 can be solved for the quantum yield:

$$\Phi_{355\,nm} = \frac{1x10^{-14} * 6.022x10^{23} * 2.0}{0.81 * 0.061 * 0.1 * 3.54x10^{15}} = 6.89x10^{-4}$$

Table 5.11 Variables used for determination of the quantum yield of the coumarin probe system discussed in Chapter 4. Photon flux is used at a single wavelength below the catalyst bandgap to simulate the conditions in used in Chapter 4.

| Variable | Value | Source |
|---|---|---|
| $\frac{d[Fluor]}{dt}$ | 6 x $10^{-10}$ mol $L^{-1}$ $min^{-1}$<br>= 1 x $10^{-14}$ mol $cm^{-3}$ $s^{-1}$ | Slope of Figure 4.10 |
| $V_{sys}$ | 2.0 $cm^3$ | 2 mL of probe solution used |
| $N_A$ | 6.022 x $10^{23}$ $mol^{-1}$ | |
| $A_{cat}$ | 0.81 $cm^2$ | Area of the 9x9 mm slide |
| $f_{trap}$ | 6.1 % = 0.061 | 54, 55 |
| $f_{hrf}$ | 10 % = 0.1 | 56, $h^+$ formed that do not undergo recombination |
| $F_{332nm}$ | 3.54 x $10^{15}$ photon $cm^{-2}$ $s^{-1}$ | Measured by power meter |

Literature gives quantum yields on the 1 x $10^{-5}$ scale, so this determined yield can be considered as a maximum potential quantum yield for the system.[57] Additionally, this calculation assumes that the values used, which come from the aqueous probe system used in Chapter 4, are applicable to atmospheric gas-solid phase photocatalysis as will be modelled, such that an assumed atmospheric monolayer coverage of water on the $TiO_2$ surface is equivalent to the aqueous phase conditions and will provide the required water for reaction, alongside the other assumptions employed in Chapter 4 to derive the rates determined there.

From equation 5.15, the rate of formation of free hydroxyl radicals is equal to the rate of desorption of adsorbed hydroxyl radicals:

$$\frac{d[\cdot OH(free)]}{dt} = r_{des} = \frac{A_{cat}}{V_{sys}} f_{trap} f_{hrf} (\frac{F_v \Phi_v}{N_A}) \tag{5.28}$$

Since the model is simulating atmospheric conditions and effects, atmospheric dispersal of $TiO_2$ particles will be modelled, with the acknowledgement that actual catalyst deployment is more likely to be close to emission sources and in a form more similar to the slides used in Chapter 4. The chosen particle needs to be small enough that it will not rain out or deposit from the atmosphere too quickly, as it needs a lifetime that will allow for significant reactions to occur. Esmen et al. (1971) found that submicron particles have residence times of 100 – 1000 hours in urban air, and larger particles have smaller residence times (< 100 hours).[58] In these simulations, it is assumed that the chosen $TiO_2$ particle size allows for significant reaction time.

If the catalyst is assumed to be identical, spherical particles of radius $r_{cat} = 2.2x10^{-3}$ cm (44 µm diameter of $TiO_2$ used in Chapter 4, Sigma-Aldrich 248576), then:

$$A_{cat} = \pi r_{cat}^2 = 1.52x10^{-5}\ cm^2 \tag{5.29}$$

The volume of the system modelled across, $V_{sys}$, can be given by the volume of the spherical particles, multiplied by the particle per volume density $d_{cat}$:

$$d_{cat} = \frac{c_{cat}}{\rho_{cat}} \tag{5.30}$$

$$V_{sys} = \frac{3}{4} * \pi r_{cat}^3 * d_{cat} \tag{5.31}$$

From data recorded across sites in New Zealand over 2006 – 2021, the highest recorded concentration of $PM_{2.5}$ matter was used to give a benchmark of potential mass densities of small particles that could be achieved in the atmosphere.[59] $PM_{2.5}$, which is particulate matter of diameter less than 2.5 µm, was chosen as it was the smallest of the measured PM concentration data available as measured by the Ministry for the Environment across New Zealand, at a mass density of $1.21x10^{-10}$ g/cm$^3$. This metric was chosen as it gives a measured estimate of achievable atmospheric concentrations, were the catalyst to be deployed in the atmosphere as nanoparticles.

If a system wide mass density of $c_{cat}$ = 1.21 x $10^{-10}$ g $cm^{-3}$ is chosen to be modelled, equivalent to the $PM_{2.5}$ value for New Zealand in 2016, and the pure material density of anatase $TiO_2$ of ρ = 3.78 g $cm^{-3}$, then:

$$d_{cat} = \frac{c_{cat}}{\rho_{cat}} = 3.20x10^{-11}$$

$$V_{sys} = \frac{3}{4} * \pi r_{cat}^3 * d_{cat} = 8.03x10^{-19}$$

Assuming the quantum yield determined from equation 5.27 of $\Phi_{335nm}$ = 6.89 x $10^{-4}$, and that $f_{trap}$ is negligible and can therefore be omitted to give a maximum potential rate, the rate of hydroxyl radical formation from the surface of a $TiO_2$ catalyst by water splitting can be determined:

$$\frac{d[\cdot OH(free)]}{dt} = \frac{A_{cat}}{V_{sys}} f_{hrf} (\frac{F_v \Phi_v}{N_A}) \tag{5.32}$$

$$\frac{d[\cdot OH(free)]}{dt} = \frac{1.52x10^{-5}}{8.03x10^{-19}} * 0.1 * \left(\frac{3.54x10^{15} * 6.89x10^{-4}}{6.022x10^{23}}\right) = 7.66\, mol\, cm^{-3}\, s^{-1}$$

Therefore, the rate of r = 7.66 mol $cm^{-3}$ $s^{-1}$ can be added to the simulation to model the potential impact of adding this catalyst to the atmosphere. This rate is a maximum possible rate, as it assumes the same photon flux, and a uniform distribution of catalyst across the entire system, but it will suffice to give an indication of potential effects. It is assumed that the period over which the simulation acts is not long enough to be affected by any deposition effects, such that the concentration of $TiO_2$ and therefore the rate can be treated as constant. Table 5.12 lists the input and output values of this simulation, for which literature values or previous steady-state values were used as inputs. The total time elapsed for this simulation was 1.03x$10^8$ s, or ~ 29,000 hours, or ~ 3.3 years.

Table 5.12 Input and output values for P3 simulation which adds a term to the ·OH production equation to account for increased formation rate due to $TiO_2$ photocatalysis. Literature values or previous steady-state values were used for input. $CH_3O\cdot$, $NO\cdot$, and $NO_2\cdot$ values were fixed.

| Molecule | Initial Concentration (molecule cm$^{-3}$) | Steady-State Concentration (molecule cm$^{-3}$) | Percentage Change |
|---|---|---|---|
| $OH\cdot$ | $1.70x10^{7}$ | $1.45x10^{7}$ | -14.95% |
| $HOO\cdot$ | $1.20x10^{9}$ | $4.27x10^{8}$ | -64.41% |
| $H_2O_2$ | $1.50x10^{10}$ | $5.04x10^{9}$ | -66.38% |
| $O^1D$ | $2.63x10^{-3}$ | $2.63x10^{-3}$ | 0.00% |
| $O^3P$ | $3.79x10^{1}$ | $3.79x10^{1}$ | 0.00% |
| $O_3$ | $5.24x10^{11}$ | $1.63x10^{11}$ | -68.82% |
| $CH_4$ | $3.35x10^{13}$ | $1.57x10^{13}$ | -53.14% |
| $CH_3\cdot$ | $3.84x10^{-1}$ | $3.84x10^{-1}$ | -0.04% |
| $CH_3O_2\cdot$ | $1.20x10^{8}$ | $1.35x10^{8}$ | 12.63% |
| $CH_3OOH$ | $1.40x10^{10}$ | $3.26x10^{9}$ | -76.69% |
| $NO_3\cdot$ | $1.80x10^{6}$ | $9.53x10^{5}$ | -47.05% |

Since $O^1D$ and $O^3P$ are involved in few reactions for their production and loss, they experienced no change from their determined steady state value for the simulation. $CH_3\cdot$ also experienced very little change in concentration from the determined steady state value despite a significant change in $CH_4$ concentration. This could be due to the limited number of modelled reactions for $CH_3\cdot$ production and loss, which involve only $CH_4$ as a variable concentration. Since the timeframe at which $CH_3\cdot$ is modelled on ($1x10^{-9}$ s time step) is so small compared to the $CH_4$ lifetime, the $CH_4$ concentration will not have changed significantly during the time $CH_3\cdot$ is modelled. This is a specific consequence to taking an iterative approach to solving the model, as the timeframes at which concentrations of different molecules will change over are impacted by choice of timestep, the trade-off of which is computational time – the simulation was able to be run for 29,000 computed hours because once certain concentrations reached steady state and became fixed, the time step could be increased from $1 \times 10^{-9}$ s to 1 s. Other $CH_4$ breakdown products $CH_3O_2\cdot$ and $CH_3OOH$ experience a significant change in concentration, but $CH_3O_2\cdot$ increases where $CH_3OOH$ significantly decreases in concentration. The increase in $CH_3O_2\cdot$ concentration could be attributed to the decreased concentrations of $CH_3\cdot$ and $CH_3OOH$, as in combination with ·OH and $O_2$, they are the only modelled source of $CH_3O_2\cdot$, and the only modelled reaction product for the loss of $CH_3\cdot$. The $CH_4$ oxidation products modelled ($CH_3\cdot$, $CH_3O\cdot$, $CH_3O_2\cdot$, and $CH_3OOH$) would be expected to show this interdependence in concentration, with decreased concentrations in one molecule reflected in increased concentrations of others.

Interestingly, adding an extra term to the production rate of ·OH still resulted in an overall decrease of ~ 15 % of the starting concentration of ·OH. This could indicate that the simulation still hadn't reached a steady state for ·OH concentration before the perturbation term was added, or that further equations are required to improve model accuracy. If the loss of ·OH was due to increased consumption of ·OH, one could expect that to be reflected in an increased HOO· or $H_2O_2$ concentration due to $HO_x$ recycling; however, the concentrations of HOO· and $H_2O_2$ are also subject to a decrease in concentration, but a much more significant one than ·OH at ~ 65 %.

Concentrations of NO· and $NO_2$· were fixed for this simulation, due to some issues in attaining stable concentrations, likely due to model accuracy. Many of the modelled production and loss equations for $NO_3$· involve fixed concentrations, with the production impacted by ·OH and $O_3$, and loss impacted by HOO·. The impact of decreased concentrations of these molecules as modelled will have resulted in the significant decrease in $NO_3$· concentration. Additionally, $NO_3$· is usually higher at night-time, with NO· and $NO_2$· increasing during the day; however, this level of complexity was out of the scope of the model, which calculates for a day-time environment. This will also be impacting the chemistry of $NO_3$· that is modelled here.

The model predicts a significant decrease in $O_3$ over the modelled time period, at a ~ 69 % decrease in concentration. This significant decrease in $O_3$ concentration would have large scale ramifications if it occurred globally as has been modelled. The area that is considered the ozone hole measures under 220 Dobson Units (DU), compared to global average concentrations of 300 – 500 DU, which is only a ~ 30 % decrease in concentration.[60] As the loss of $O_3$ in the model is dependent on ·OH and HOO· concentrations, the significant decrease in these would have a flow-on effect to the $O_3$ concentration in the model. Additionally, the model does not consider transport to the stratosphere or other stratospheric processes, so this change is an indication of the maximum possible change that could occur, and would likely be significantly smaller in practical application. It does indicate a significant effect would occur and requires further detailed investigation in order to fully understand and characterise the effects of the proposed catalyst.

Lastly, the model predicts a significant decrease in $CH_4$ over the modelled time period, at a ~ 53% decrease in concentration. The decrease in concentration would be expected to result from the increase in ·OH production rate, but this does not align with the overall decrease in ·OH concentration observed. It does indicate the significance of ·OH concentration on the loss of $CH_4$ in the troposphere, and gives an indication on the impacts in terms of changing oxidation product concentrations. Removal of 10% of the initial starting concentration of $CH_4$ is achieved after ~ 765 hours, or ~ 1 month. The simulation thus indicates (roughly) that if $TiO_2$ concentration can be maintained at the modelled $1.21x10^{-10}$ g/cm$^3$ system wide mass density across an area, 10% of $CH_4$ in that area can be removed over the course of approximately one month. This is a maximum estimate, as the J values calculated and used in the simulation were calculated for summer conditions at noon, giving a maximum possible value.

Despite the simulation indicating that $CH_4$ removal is possible using a $TiO_2$ catalyst, the feasibility of practical application is low. The decrease in $CH_4$ concentration is specific to the area in which the $TiO_2$ is deposited in, and dependent on the concentration being maintained. It is not feasible nor sensible to attempt to maintain this concentration globally, and instead deployment on smaller localised areas must be targeted, meaning the reduction of $CH_4$ concentration would be significantly smaller than the modelled decrease seen. Depositing a large volume of $TiO_2$ in the atmosphere is complex not only scientifically but also politically, ethically, and financially. Deposition would have to occur over spaces uninhabited by humans to avoid any potential adverse effects or public opinion, like over an ocean surface or empty forestry space, or alternatively as a treatment for $CH_4$ leaks in areas like landfills. Additionally, particles in the atmosphere will agglomerate to form larger particles and then undergo deposition or rain out. This would affect the calculated rate, as it is dependent on the lifetime of the particles, potentially removing the catalyst before it has had significant time to achieve the targeted removal volume.

Financially, the cost of $TiO_2$ required to achieve the chosen concentration across the troposphere can be found. Knowing that the troposphere has an average height of 13 km and that Earth's surface area is 510 million $km^3$, the volume of the troposphere is 6.63 billion $km^3$, or $6.63x10^{24}$ $cm^3$. To achieve a concentration of $1.21x10^{-10}$ $g/cm^3$, $8.02x10^{14}$ g of $TiO_2$ is required. Using the cost of the $TiO_2$ used throughout this research, (Sigma Aldrich, 248576), at a cost of NZD$69 per 100g, this volume of $TiO_2$ would cost ~ NZD$550 trillion – this value excludes any equipment required for the deposition itself and only covers the $TiO_2$; however, industrial or bulk buying of chemicals is usually cheaper. Clearly, this is not a feasible cost. A balance between the cost and the amount of $CH_4$ targeted for removal would have to be determined. Alternatively, this calculation shows that this approach is more feasible for a targeted and localised treatment, as opposed to a global application. In comparison to literature, Pope et al. (2012) posited that, to match the effects of the 1991 Mt. Pinatubo eruption, which caused an average decrease in global temperature by 0.5 K over 2 years, using $TiO_2$ to increase albedo would allow the same effect to be gained at a lesser concentration when compared to the volcanically emitted aerosols that cause the observed cooling.[61] For a 10 km thick layer of 45 nm radius $TiO_2$ particles (twice as large as the amount of $TiO_2$ used by Pope et al.), $1.03x10^{13}$ g of $TiO_2$ would be required to achieve the same cooling effect as $H_2SO_4$ aerosols.[61]

## 5.5 Conclusion

In this chapter, an indicative model of the atmosphere and its important constituents was constructed to indicate the effects of increasing ·OH production on atmospheric reactions, specifically those involved with the $HO_x$ cycle and $CH_4$ oxidation. A zero-dimensional model was constructed, using 79 chemical equations. The concentration of the variables was calculated iteratively for each chosen time step, with concentrations becoming fixed when a steady-state value was reached (approximately equal production and loss rates and no significant change in concentration). The model was tested for robustness and found not to deviate from literature steady-state concentrations when they were used as inputs, indicating stability and the ability to simulate atmospheric conditions. The model was then used to simulate the effect of a perturbation, where an extra term for the rate of ·OH formation by $TiO_2$ photocatalysed water breakdown was added. This resulted in a decreased $CH_4$ concentration (by ~ 53 % over ~ 29,000 hours) and a decreased $O_3$ concentration.

Overall, the model was able to replicate some atmospheric concentrations for the variables calculated, reaching steady-state values similar to literature. Other variables consistently reached the same steady-state concentration across different simulations, but the value was very different to literature, potentially due to differences in the construction of the production and loss equations used here. With further opportunity, the model could have been optimised to improve accuracy by improving the production and loss equations or by fixing the variables at a literature steady-state concentration.

Significant difficulties were encountered in constructing and testing the simulation. Running or modifying the simulations was very computationally taxing and time consuming. Increasing computer power could help with this issue. Additionally, the time step used poses an issue in that it must be less than the shortest lifetime to prevent instabilities in the calculation appearing, so it takes a significant amount of CPU time to affect the concentrations of long-lived variables like $H_2O_2$. In fixing variables at steady-state concentrations during the simulation, the time step is able to be changed, but if the variable is fixed too early it can influence the final steady-state concentration reached of other variables, or remove flexibility of the system to respond to changes.

Future work with this model would address the assumptions used when constructing the model, as well as improving the production and loss equations used for each variable. The behaviour of NO· should be investigated and fixed such that a steady-state value close to literature is reached.

The calculation of the rate of ·OH formation for a given concentration of $TiO_2$ assumes that similar conditions to the probe system in section 4.3 are used in the atmosphere, by assuming a monolayer coverage of water on the $TiO_2$ surface in the atmosphere will have the same rate of ·OH production as the aqueous environment used in Chapter 4, and assumes that all produced holes react only in the reaction of interest. It also uses a particle size of $TiO_2$ that is not optimal for lifetime in the atmosphere. Additionally, the perturbation rate is added as a continuous factor, simulating a constant concentration of $TiO_2$, where it is more likely a set mass of $TiO_2$ would be released. Further simulations could model either a plume of $TiO_2$ added, or could account for deposition of the $TiO_2$ and therefore reduced concentration over time, allowing required replenishment rates to be determined.

The relationship between amount of $CH_4$ removed and $TiO_2$ particle size or particle density could also be determined. This would require further simulations using rates calculated with different particle densities of $TiO_2$, from which a plot of a particle density versus percentage of $CH_4$ removed could be established. This would then give the ability to choose an optimal particle density of $TiO_2$ for a chosen targeted removal percentage of $CH_4$. Due to time constraints, these further simulations could not be run.

## 5.6 References

1. Seinfeld, J. H.; Pandis, S. N., *Atmospheric Chemistry and Physics : From Air Pollution to Climate Change*. John Wiley & Sons, Incorporated: New York, United States, 2016.
2. Berger, A., Basic Concepts of Climate Modelling. In *Climatic Change and Impacts: A General Introduction*, Fantechi, R.; Maracchi, G.; Almeida-Teixeira, E., Eds. Luxembourg, 1991.
3. Levy, H., Photochemistry of the lower troposphere. *Planet. Space Sci.* **1972,** *20* (6), 919-935.
4. Logan, J. A.; Prather, M. J.; Wofsy, S. C., et al., Tropospheric chemistry: A global perspective. *J. Geophys. Res.* **1981,** *86* (C8).
5. Wofsy, S. C.; McConnell, J. C.; McElroy, M. B., Atmospheric $CH_4$, CO, and $CO_2$. *J. Geophys. Res.* **1972,** *77* (24), 4477-4493.
6. Pan, W., Steady State Analysis of Tropospheric Chemistry. **2000**.
7. Manion, J. A.; Huie, R. E.; Levin, R. D., et al. NIST Chemical Kinetics Database, NIST Standard Reference Database 17. https://kinetics.nist.gov/.
8. Baulch, D. L.; Cobos, C. J.; Cox, R. A., et al., Evaluated Kinetic Data for Combustion Modelling. **1992,** *21* (3), 411-734.
9. Troe, J., Theory of Multichannel Thermal Unimolecular Reactions. 2. Application to the Thermal Dissociation of Formaldehyde. *J. Phys. Chem. A.* **2005,** *109* (37), 8320-8328.
10. Slemr, F.; Tremmel, H. G., Hydroperoxides in the marine troposphere over the Atlantic Ocean. *J. Atmos. Chem.* **1994,** *19* (4), 371-404.
11. Atkinson, R.; Baulch, D. L.; Cox, R. A., et al., Evaluated Kinetic and Photochemical Data for Atmospheric Chemistry: Supplement VI. IUPAC Subcommittee on Gas Kinetic Data Evaluation for Atmospheric Chemistry. **1997,** *26* (6), 1329-1499.
12. Demore, W. B.; Sander, S. P.; Golden, D. M., et al. *Chemical kinetics and photochemical data for use in stratospheric modeling: Evaluation number 11*; United States, 1994-12-01, 1994.
13. Dunlea, E. J.; Ravishankara, A. R., Measurement of the rate coefficient for the reaction of $O^1D$ with $H_2O$ and re-evaluation of the atmospheric OH production rate. *Phys. Chem. Chem. Phys.* **2004,** *6* (13), 3333-3340.
14. Atkinson, R.; Baulch, D. L.; Cox, R. A., et al., Evaluated kinetic and photochemical data for atmospheric chemistry: Volume I - gas phase reactions of $O_x$, $HO_x$, $NO_x$ and $SO_x$ species. *Atmos. Chem. Phys.* **2004,** *4* (6), 1461-1738.
15. Kanno, N.; Tonokura, K.; Koshi, M., Equilibrium constant of the $HO_2$-$H_2O$ complex formation and kinetics of $HO_2$ + $HO_2$-$H_2O$: Implications for tropospheric chemistry. *J. Geophys. Res. Atmos.* **2006,** *111* (20).
16. Hofzumahaus, A.; Stuhl, F., Rate Constant of the Reaction HO + CO in the Presence of $N_2$ and $O_2$. **1984,** *88* (6), 557-561.
17. Bardwell, M. W.; Bacak, A.; Teresa Raventos, M., et al., Kinetics of the $HO_2$ + NO reaction: A temperature and pressure dependence study using chemical ionisation mass spectrometry. *Phys. Chem. Chem. Phys.* **2003,** *5* (11), 2381-2385.
18. Bonard, A.; Daële, V.; Delfau, J.-L., et al., Kinetics of OH Radical Reactions with Methane in the Temperature Range 295−660 K and with Dimethyl Ether and Methyl-tert-butyl Ether in the Temperature Range 295−618 K. *J. Phys. Chem. A.* **2002,** *106* (17), 4384-4389.
19. D'Ottone, L.; Campuzano-Jost, P.; Bauer, D., et al., A Pulsed Laser Photolysis−Pulsed Laser Induced Fluorescence Study of the Kinetics of the Gas-Phase Reaction of OH with $NO_2$. *J. Phys. Chem. A.* **2001,** *105* (46), 10538-10543.
20. Atkinson, R.; Baulch, D. L.; Cox, R. A., et al., Evaluated Kinetic, Photochemical and Heterogeneous Data for Atmospheric Chemistry: Supplement V. IUPAC Subcommittee on Gas Kinetic Data Evaluation for Atmospheric Chemistry. **1997,** *26* (3), 521-1011.

21. Bacak, A.; Bardwell, M. W.; Raventos, M. T., et al., Kinetics of the Reaction of $CH_3O_2$ + NO: A Temperature and Pressure Dependence Study with Chemical Ionization Mass Spectrometry. *J. Phys. Chem. A.* **2004,** *108* (48), 10681-10687.
22. Atkinson, R.; Baulch, D. L.; Cox, R. A., et al., Evaluated Kinetic and Photochemical Data for Atmospheric Chemistry: Supplement III. IUPAC Subcommittee on Gas Kinetic Data Evaluation for Atmospheric Chemistry. *J. Phys. Chem. Ref.* **1989,** *18* (2), 881-1097.
23. Chai, J.; Hu, H.; Dibble, T. S., et al., Rate Constants and Kinetic Isotope Effects for Methoxy Radical Reacting with $NO_2$ and $O_2$. *J. Phys. Chem. A.* **2014,** *118* (20), 3552-3563.
24. Atkinson, R.; Baulch, D. L.; Cox, R. A., et al., Evaluated Kinetic and Photochemical Data for Atmospheric Chemistry: Supplement IV. IUPAC Subcommittee on Gas Kinetic Data Evaluation for Atmospheric Chemistry. **1992,** *21* (6), 1125-1568.
25. Lu, Y.; Khalil, M. A. K., Tropospheric OH: model calculations of spatial, temporal, and secular variations. *Chemosphere.* **1991,** *23* (3), 397-444.
26. Simonaitis, R.; Heicklen, J., Reaction of hydroperoxyl radicals with nitrogen monoxide and nitrogen dioxide. *J. Phys. Chem.* **1974,** *78* (7), 653-657.
27. Gray, D.; Lissi, E.; Heicklen, J., Reaction of hydrogen peroxide with nitrogen dioxide and nitric oxide. *J. Phys. Chem.* **1972,** *76* (14), 1919-1924.
28. Kaiser, E. W., Pressure dependence of the rate constants for the reactions methyl + oxygen and methyl + nitric oxide from 3 to 104 torr. *J. Phys. Chem.* **1993,** *97* (45), 11681-11688.
29. Troe, J., Refined Representation of Falloff Curves for the Reaction HO + $NO_2$ + $N_2$ → ($HONO_2$, HOONO) + N2. *J. Phys. Chem. A.* **2012,** *116* (24), 6387-6393.
30. Wayne, L. G.; Yost, D. M., Kinetics of the Rapid Gas Phase Reaction between NO, $NO_2$, and $H_2O$. *J. Chem. Phys.* **1951,** *19* (1), 41-47.
31. Gulev, S. K.; Thorne, P. W.; Ahn, J., et al., Changing State of the Climate System. In *Climate Change 2021: The Physical Science Basis. Contribution of Working Group I to the Sixth Assessment Report of the Intergovernmental Panel on Climate Change*, Masson-Delmotte V.; Zhai, P.; Pirani, A., et al., Eds. Cambridge University Press: Cambridge, United Kingdom, 2021; pp 287-422.
32. Warneck, P., OH Production Rates in the Troposphere. *Planet. Space Sci.* **1975,** *23*, 1507-1518.
33. Network for the Detection of Atmospheric Composition Change (NDACC) Sonde Measurements At Lauder Station. NIWA, Ed. 2021.
34. Platt, U.; Perner, D.; Pätz, H. W., Simultaneous measurement of atmospheric $CH_2O$, $O_3$, and $NO_2$ by differential optical absorption. *J. Geophys. Res.* **1979,** *84* (C10).
35. Madronich, S., Photodissociation in the Atmosphere. 1. Actinic Flux and the Effects of Ground Reflections and Clouds. *J. Geophys. Res. Atmos.* **1987,** *92* (D8), 9740-9752.
36. Gueymard, C. A., Parameterized transmittance model for direct beam and circumsolar spectral irradiance. *J. Sol. Energy.* **2001,** *71* (5), 325-346.
37. Stats NZ, Temperature. https://www.stats.govt.nz/indicators/temperature (accessed 28/04).
38. National Institute of Water and Atmospheric Research (NIWA) Atmospheric ozone, state, 1979-2019. New Zealand's Environment Reporting Series: The Ministry for the Environment and Statistics New Zealand Ed. 2020.
39. National Institute of Water and Atmospheric Research (NIWA) Greenhouse gas concentrations, 1972-2019. New Zealand's Environment Reporting Series: The Ministry for the Environment and Statistics New Zealand Ed. 2020.
40. Gueymard, C. A., The sun's total and spectral irradiance for solar energy applications and solar radiation models. *J. Sol. Energy.* **2004,** *76* (4), 423-453.
41. Shettle, E.; Fenn, R., Models for the Aerosols of the Lower Atmosphere and the Effects of Humidity Variations on their Optical Properties. *Environ. Res.* **1979**, 94.
42. Gueymard, C., SMARTS code, version 2.9.5, User's Manual. 2006.

43. Cotte, H.; Devaux, C.; Carlier, P., Transformation of irradiance measurements into spectral actinic flux for photolysis rates determination. *J. Atmos. Chem.* **1997,** *26* (1), 1-28.
44. McKenzie, R.; Johnston, P.; Hofzumahaus, A., et al., Relationship between photolysis frequencies derived from spectroscopic measurements of actinic fluxes and irradiances during the IPMMI campaign. *J. Geophys. Res. Atmos.* **2002,** *107* (D5).
45. Hofzumahaus, A.; Kraus, A.; Kylling, A., et al., Solar actinic radiation (280–420 nm) in the cloud-free troposphere between ground and 12 km altitude: Measurements and model results. *J. Geophys. Res. Atmos.* **2002,** *107* (D18).
46. Müller, M.; Kraus, A.; Hofzumahaus, A., $O_3 \rightarrow O^1D$ photolysis frequencies determined from spectroradiometric measurements of solar actinic UV-radiation: Comparison with chemical actinometer measurements. *Geophys. Res. Lett.* **1995,** *22* (6), 679-682.
47. Kraus, A.; Hofzumahaus, A., Field Measurements of Atmospheric Photolysis Frequencies for $O_3$, $NO_2$, HCHO, $CH_3CHO$, $H_2O_2$, and HONO by UV Spectroradiometry. *J. Atmos. Chem.* **1998,** *31* (1), 161-180.
48. Crutzen, P. J., Photochemical reactions initiated by and influencing ozone in unpolluted tropospheric air. *Tellus* **1974,** *26* (1-2), 47-57.
49. Berresheim, H.; McGrath, J.; Adam, M., et al., Seasonal measurements of OH, $NO_x$, and $J(O^1D)$ at Mace Head, Ireland. *Geophys. Res. Lett.* **2013,** *40* (8), 1659-1663.
50. Kazadzis, S., Actinic flux and $O^1D$ photolysis frequencies retrieved from spectral measurements of irradiance at Thessaloniki, Greece. *Atmos. Chem. Phys.* **2004**.
51. Hofzumahaus, A., Photolysis frequency of $O_3$ to $O^1D$: Measurements and modeling during the International Photolysis Frequency Measurement and Modeling Intercomparison (IPMMI). *J. Geophys. Res.* **2004,** *109* (D8).
52. Szopa, S.; Naik, V.; Adhikary, B., et al., Short-Lived Climate Forcers. In *Climate Change 2021: The Physical Science Basis. Contribution of Working Group I to the Sixth Assessment Report of the Intergovernmental Panel on Climate Change*, Masson-Delmotte, V.; Zhai, P.; Pirani, A., et al., Eds. Cambridge University Press: Cambridge, United Kingdom; New York, NY, USA, 2021; pp 817-922.
53. Williamson, B., Kinetic Scheme. Pope, J., Ed. 2025.
54. Zhang, J.; Nosaka, Y., Quantitative Detection of OH Radicals for Investigating the Reaction Mechanism of Various Visible-Light $TiO_2$ Photocatalysts in Aqueous Suspension. *J. Phys. Chem. C.* **2013,** *117* (3), 1383-1391.
55. Zhang, J.; Nosaka, Y., Mechanism of the OH Radical Generation in Photocatalysis with $TiO_2$ of Different Crystalline Types. *J. Phys. Chem. C.* **2014,** *118* (20), 10824-10832.
56. Qian, R.; Zong, H.; Schneider, J., et al., Charge carrier trapping, recombination and transfer during $TiO_2$ photocatalysis: An overview. *Catal. Today.* **2019,** *335*, 78-90.
57. Ishibashi, K.-i.; Fujishima, A.; Watanabe, T., et al., Quantum yields of active oxidative species formed on $TiO_2$ photocatalyst. *J. Photochem. Photobiol. A.* **2000,** *134* (1), 139-142.
58. Esmen, N. A.; Corn, M., Residence time of particles in urban air. *Atmos. Environ.* **1971,** *5* (8), 571-578.
59. Ministry for the Environment Particulate matter 2.5 concentrations, 2006-2021. Minstry for the Environment, Ed. 2021.
60. NASA Ozone Watch, NASA Ozone Watch: Latest status of ozone. https://ozonewatch.gsfc.nasa.gov/statistics/annual_data.html.
61. Pope, F. D.; Braesicke, P.; Grainger, R. G., et al., Stratospheric aerosol particles and solar-radiation management. *Nat. Clim. Change.* **2012,** *2* (10), 713-719.

# 6.0 Conclusion and Future Work

The work has investigated the use of a $TiO_2$ catalyst to reduce the concentration of $CH_4$ in the atmosphere by increasing the formation of ·OH. This process has required a number of steps to investigate.

In Chapter 1, a background of the atmosphere and relevant information was covered. A look at climate drivers, their concentrations and increase in concentration over the years, and the chemical cycles they are involved in was covered. Mitigation strategies were also touched on. $CH_4$ and ·OH atmospheric chemistry was discussed, as was the use of $TiO_2$ as a photocatalyst.

In Chapter 2, a reference library of atmospherically important molecules was established, alongside a correction function to the data collected. MI-FTIR was used to collect spectra of the molecules, which were assigned using a combination of literature data (where available) and calculated data, using the Gaussian-16 software. From the assigned data, a correction function and a scaling factor was constructed, using the average shifts experienced across the different levels of theory calculated at, the different types of molecules assigned for, and the different spectral regions assigned in. Conventionally, a scaling factor is used and calculated according to a known equation, but in this case a correction function was also constructed so that it was specific to the experimental conditions in this work, specifically that this work is conducted using a matrix and is therefore solid phase and the literature factors are usually for gas-phase experiments. The two functions, calculated using data collected in this work, were then compared to the literature factors available, and it was found that the calculated functions gave more accurate results than the literature factors.

In Chapter 3, the same technique of MI-FTIR spectroscopy, combined with the correction function established in Chapter 2, was used to make and detect ·OH. A Tesla-coil was used as the excitation source to create the radicals, as it was established in the literature as being previously used for this purpose. A series of mixtures of water, oxygen, and argon were subjected to Tesla-coil discharge and deposited on the matrix-isolation window. When using a mixture of just water and argon, peaks associated with ·OH and their complexes with water, as well as other $HO_x$ radicals and their complexes with water, were present in the discharge spectrum. Subsequently, hydrocarbons were introduced to the experiment, downstream from the Tesla-coil discharge, to detect reaction products. Three hydrocarbons (propyne, isoprene, and β-pinene) were used. Ultimately, results from these experiments were unconvincing due to issues with seeing the radical product peaks, since they were much smaller in intensity than the background peaks from the reactants. Indications of a reaction occurring were seen in the form of peaks associated with CO and its aggregates with water, but definitive assignment of reaction intermediates or products proved difficult.

In Chapter 4, $TiO_2$ was introduced to the system. Methods to coat a slide with catalyst were investigated and it was found that spin-coating and annealing a slide gave the best coverage that was retained when in an aqueous environment. The photocatalytic ability of the $TiO_2$ slide was also tested, using the fluorescent-probe technique with coumarin and terephthalic acid as probes. From this, the slides were determined to be photocatalytically active, and the rate of formation of $\cdot OH$ using $TiO_2$ as a photocatalyst was determined. A built in-house fluorescence cell was also crafted, built to allow the catalyst-coated slide to be held in a chamber that could be filled with the gaseous reaction mixture and irradiated. A new technique and excitation source were also employed to form and react the radicals in order to overcome difficulties experienced using the previous techniques. A residual gas analyser (RGA) was used to detect mass fragments from gas-phase reactions, and a spectrofluorophotometer was used as the excitation source since it provided control over the wavelength applied. Mixtures of water and argon or of water, ethylene, and argon were held in the cell and irradiated at $\lambda = 360$ nm. Unfortunately, equipment malfunctions meant that a multichannel scaler had to be used to count the incoming fragments. The low pressures required for this experimental setup meant that any reaction products or intermediates would be formed in very small amounts that were potentially not detectable. The experiments were inconclusive in providing evidence of any reaction occurring.

In Chapter 5, an indicative zero-dimensional model was established to investigate the effects of adding $TiO_2$ to the atmosphere. The model was crafted using an iterative method to solve for concentration. A total of 27 atmospheric variables were included, with around 18 remaining fixed for most of the simulations, and 79 equations used to construct the total production and loss rates for each variable. Additionally, a separate modelling program SMARTS was used to calculate the photolysis rates for the equations used, so that the conditions being simulated were specific to New Zealand data. The model was found to be able to replicate atmospheric concentrations of some of the variables calculated for, experiencing some instabilities in some variables (namely $NO\cdot$), but when using atmospheric steady-state concentrations as inputs the simulation did not vary largely from them, indicating stability. A perturbation term, for the formation of $\cdot OH$ using $TiO_2$ as a photocatalyst, was then introduced to the $\cdot OH$ production equation to investigate the effects on the concentrations of the other atmospheric molecules. This added $\cdot OH$ production resulted in a decreased $\cdot OH$ concentration, with large decreases in

$O_3$ and $CH_4$ concentrations, indicating that the solution could be viable as a short term or small scale $CH_4$ removal option, potentially suitable for applications like $CH_4$ leaks in landfills.

The goal of the fluorescence cell used in Chapter 4 was to replicate atmospheric conditions in terms of $CH_4$ concentration and relative humidity, to find the rate of degradation via ·OH oxidation when using $TiO_2$ as a photocatalyst. If the work were to continue, reactions using $CH_4$ instead of ethylene should be run, using an experimental setup that allows for higher pressures or for tracking of pressures over time. Fixing the RGA software so that multiple pressures can be tracked over time would be preferable to continuing experiments with the MCS. Optimal conditions of relative humidity and $TiO_2$ concentration for degradation of $CH_4$ could then be determined.

As discussed in Chapter 5, future work on the model would improve upon the construction of the production and loss rates for each molecule, such that all variables calculated for would reach literature steady-state values. This would improve the accuracy of the model. Additionally, the relationship between the amount of $TiO_2$ used and amount of $CH_4$ removed could be established by creating a “calibration curve” of simulation results using rates calculated from different $TiO_2$ particle densities. This would allow for optimal $TiO_2$ particle densities to be chosen for target $CH_4$ removal amounts.

# Appendix

# Contents

A. Chapter 2: Assigned Calculated And Experimental Data ........ 171
A.1 2-methyl-2-butene ........ 173
A.2 Acetylene ........ 177
A.3 α-Pinene ........ 178
A.4 α-Pinene Oxide ........ 181
A.5 Benzene ........ 187
A.6 β-Pinene ........ 191
A.7 Cyclopropylacetylene ........ 196
A.8 Ethylene ........ 200
A.9 Geraniol ........ 204
A.10 Isoprene ........ 207
A.11 Limonene ........ 211
A.12 Methacrolein ........ 216
A.13 Myrcene ........ 222
A.14 Natural Gas (Methane, Ethane, Propane) ........ 228
A.15 Propyne ........ 233
A.16 Toluene ........ 236
A.17 Tert-butyl Hydroperoxide ........ 240
B. Chapter 2: Correction Factor Additional Data ........ 243
C. Chapter 4: Additional Data ........ 249
D. Chapter 5: Photolysis Rate (J) Data ........ 255
D.1 Ozone ($O_3$) ........ 255
D.2 Formaldehyde ($H_2CO$) ........ 256
D.3 Methyl Hydroperoxide ($CH_3OOH$) ........ 257
D.4 Hydrogen Peroxide ($H_2O_2$) ........ 258
D.5 Nitrogen Dioxide ($NO_2\cdot$) ........ 259
D.6 Nitrate Radical ($NO_3\cdot$) ........ 260
D.7 Nitrous Acid ($HNO_2$) ........ 261
D.8 Nitric Acid ($HNO_3$) ........ 262
D.9 Peroxynitric Acid ($HNO_4$) ........ 263
D.10 Nitrogen Pentoxide ($N_2O_5$) ........ 264
E. References ........ 265

# A. Chapter 2: Assigned Calculated And Experimental Data

For each molecule in the reference library, the following data is presented:

1. A table of experimentally recorded wavenumbers and the corresponding calculated wavenumbers for both B3LYP and MP2 levels of theory and the corresponding literature wavenumbers (where available). All calculations are run with anharmonic corrections, and the basis set used is stated, where DZ, TZ, and QZ means cc-pVDZ, cc-pVTZ, or cc-pVQZ respectively.
2. Sections of the annotated spectrum for each molecule.
3. Graphs plotting the experimental wavenumber and corresponding assigned calculated wavenumber for both B3LYP and MP2 levels of theory. A linear trendline is fitted for each and displayed on the graph, along with the $R^2$ value.
4. A table of linear regression analysis values for each graph, of slope, intercept, standard error of both.

Not all molecules collected in the reference library were used to create the correction and scaling factors. These molecules were instead collected as references to be used to compare reaction spectra to, in order to find product or intermediate peaks.

Table A.1 Table of matrix isolation experiments run to collect reference library data. Some molecules have had multiple spectra collected, usually to gain a clearer, sharper spectrum or because the initial spectrum had contamination.

| **Date** | **Sample Molecule** | **Deposition Time of Sample** |
|---|---|---|
| 03/05/2019 | 2-methyl-2-butene | 1hr |
| 06/03/2020 | 2-methyl-2-butene | 1hr |
| 30/03/2022 | 2-methyl-2-butene | 2hrs |
| 18/03/2019 | α-pinene | 75mins |
| 01/04/2021 | α-pinene | 1hr |
| 05/04/2019 | α-pinene oxide | 1hr30mins |
| 02/12/2019 | β-pinene | 2hr30mins |
| 20/03/2020 | β-pinene | 1hr30mins |
| 22/03/2019 | Benzene | 1hr10mins |
| 05/04/2022 | Benzene | 1hr |
| 12/04/2019 | Cyclopropylacetylene | 1hr40mins |
| 08/03/2019 | Isoprene | - |
| 22/04/2021 | Isoprene | 1hr |
| 22/03/2022 | Isoprene | 1hr |
| 15/04/2019 | Limonene | 1hr |
| 25/03/2021 | Limonene | 1hr |
| 13/04/2021 | Geraniol | 1hr30mins |
| 10/05/2019 | Methacrolein | 20mins |
| 13/03/2020 | Myrcene | 2hrs |
| 29/03/2019 | Propyne | 30mins |
| 01/04/2019 | Propyne | 80mins |
| 18/03/2021 | Toluene | 1hr |
| 26/06/2019 | Acetylene | 2hrs |
| 21/06/2019 | Ethylene | 1hr30mins |
| 19/06/2019 | Natural Gas | 3hrs20mins |
| 01/07/2019 | Tert-butyl hydroperoxide | 2hrs15mins |
| 02/07/2019 | Tert-butyl hydroperoxide | 2hrs |

## A.1 2-methyl-2-butene

Table A.2 Table of assigned calculated wavenumbers to experimental data for 2-methyl-2-butene. Calculations are anharmonic and at TZ level. Not all calculated or experimental peaks are assigned.

| **Literature Wavenumber (cm$^{-1}$)[1]** | **B3LYP TZ Wavenumber (cm$^{-1}$)** | **MP2 TZ Wavenumber (cm$^{-1}$)** | **Experimental** | |
|---|---|---|---|---|
| | | | **Wavenumber (cm$^{-1}$)** | **Shape** |
| 3024 | | 3003.7 | 3002.1 | Medium |
| | | 2984.1 | 2985.3 | Medium, shoulder |
| | | 2976.9 | 2976.5 | Medium, shoulder |
| 2972 | | 2973.9 | 2972.2 | Sharp |
| | 2958.2 | | 2952.7 | Broad, shoulder |
| 2931 | 2943.6 | 2955.5 | 2944.9 | Broad |
| 2908 | 2928.4 | | 2926.1 | Broad |
| | 2892.4 | | 2871.9 | Broad, shoulder |
| | 2844.0 | | 2864.9 | Broad |
| 1681 | 1690.7 | 1688.9 | 1624.2 | Medium |
| | 1384.9 | 1386.0 | 1384.7 | Sharp |
| | 1379.3 | 1378.5 | 1378.3 | Sharp |
| | 1201.6 | 1220.2 | 1215.6 | Broad |
| | 1101.1 | 1116.2 | 1114.2 | Sharp, shoulder |
| | 1077.0 | 1077.7 | 1082.1 | Medium |
| | 1046.3 | 1052.6 | 1052.7 | Sharp |
| | 1042.3 | 1040.7 | 1036.5 | Sharp |
| | 992.6 | 993.7 | 989.1 | Medium, shoulder |

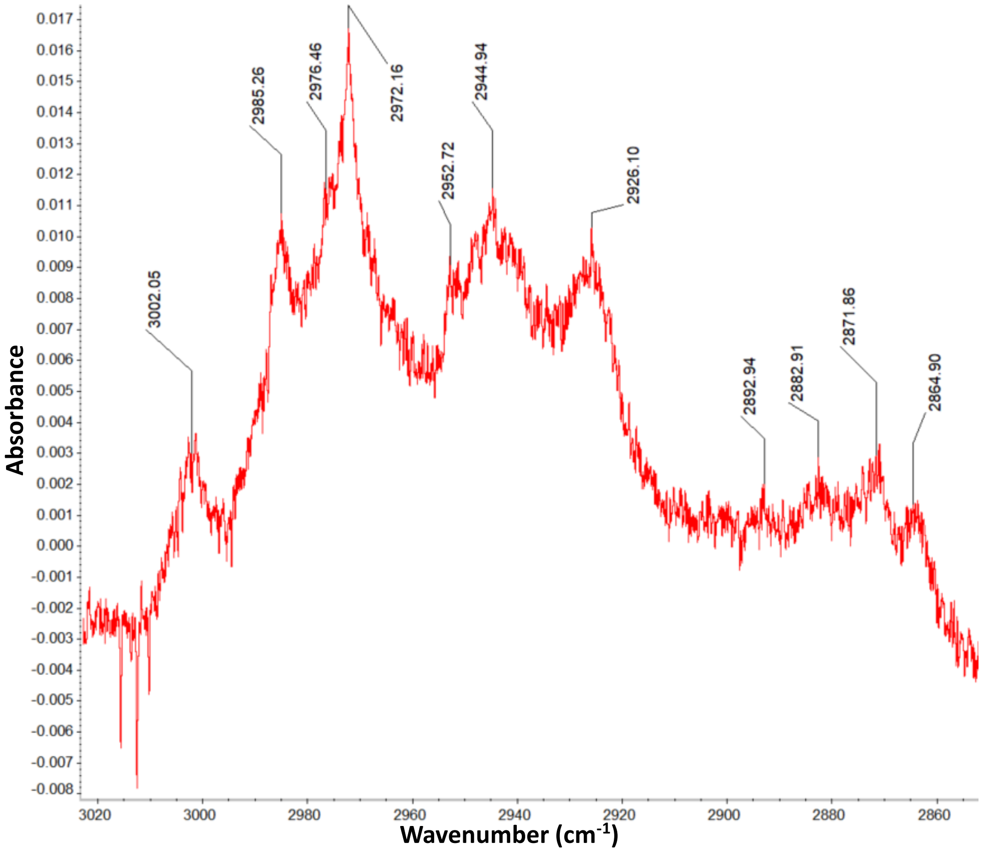

Figure A.1 Section from ~ 3020 – 2850 cm$^{-1}$ of annotated 2-methyl-2-butene spectrum.

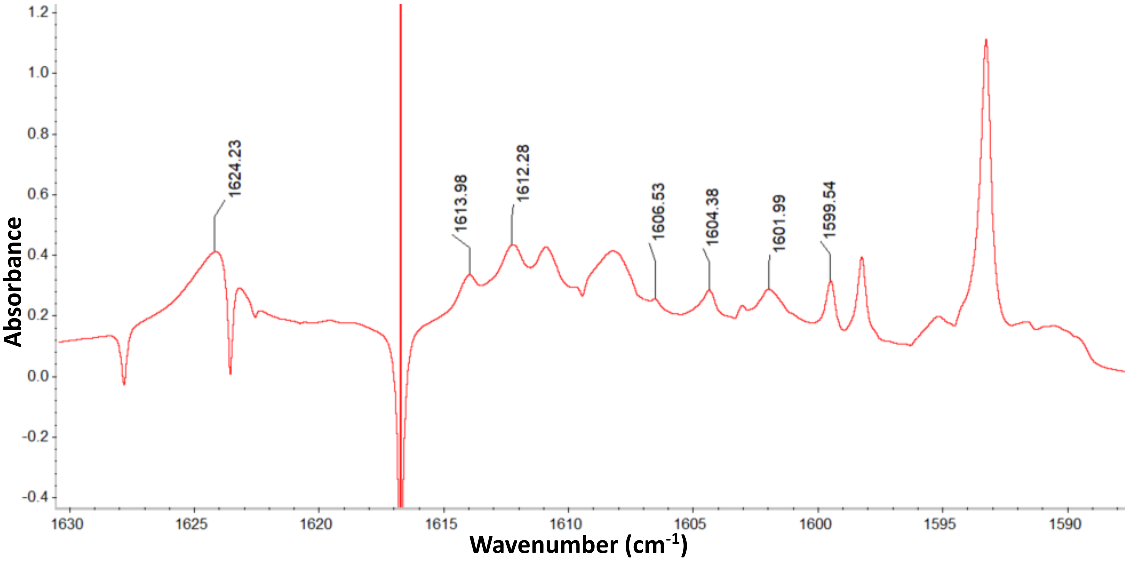

Figure A.2 Section from ~ 1630 – 1580 cm$^{-1}$ of annotated 2-methyl-2-butene spectrum.

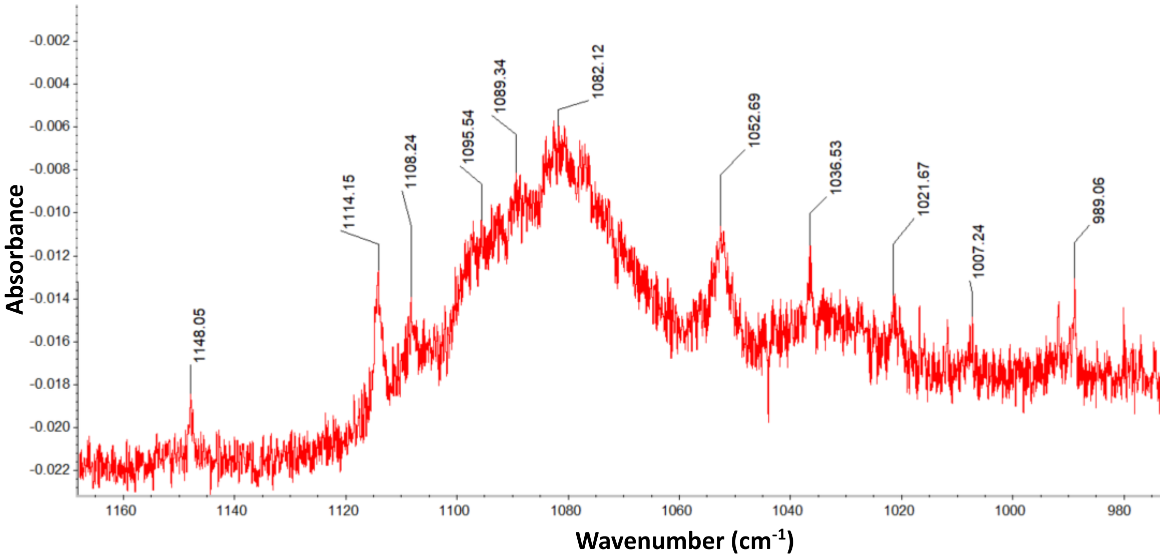

Figure A.3 Section from ~ 1160 – 980 cm$^{-1}$ of annotated 2-methyl-2-butene spectrum.

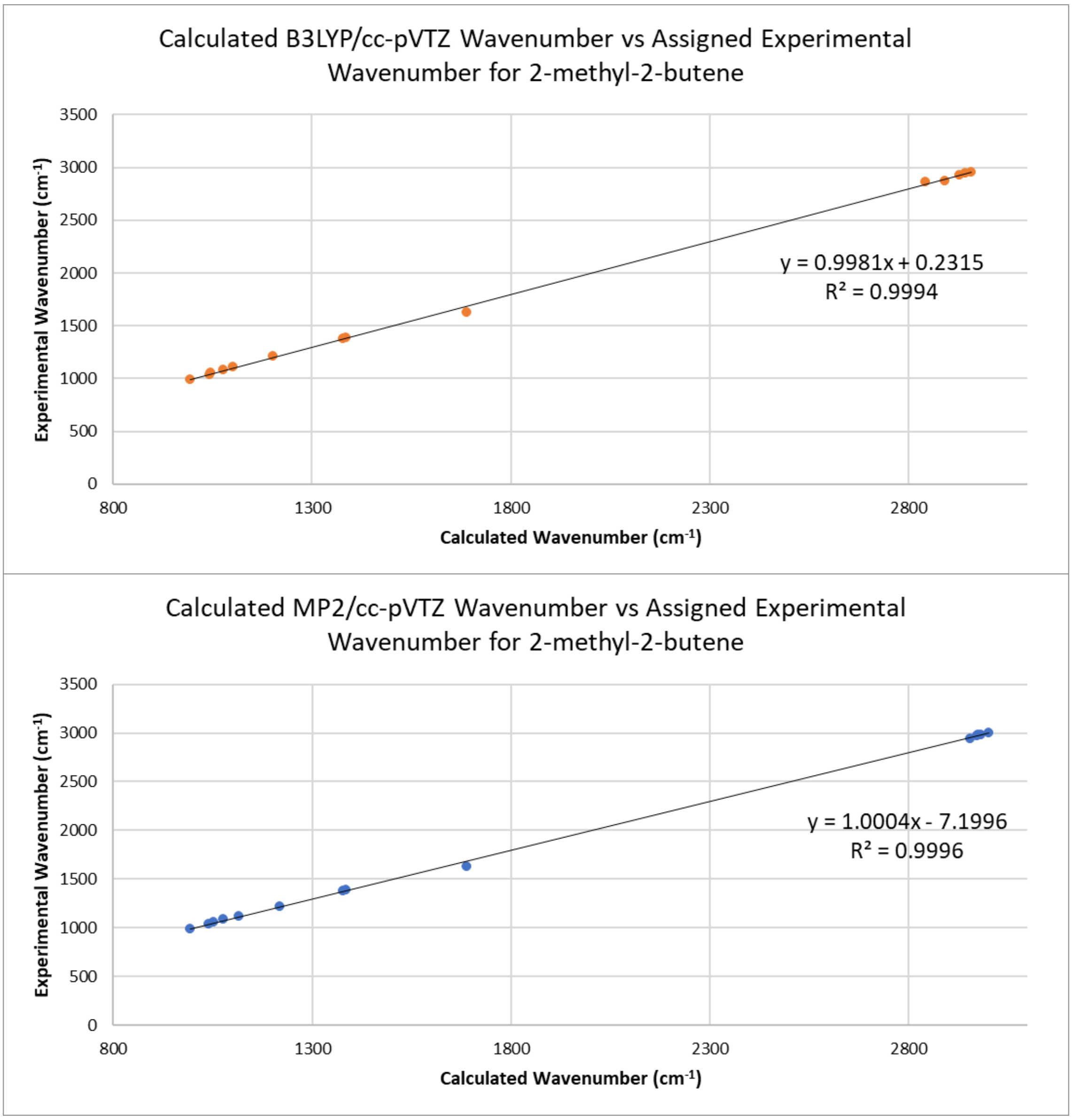

Figure A.4 Comparison graphs for experimental wavenumber versus calculated wavenumber.

Table A.3 Slope, intercept, and standard errors of each for the comparison graphs for 2-methyl-2-butene.

| **Value** | **B3LYP** | **MP2** |
|---|---|---|
| m | 0.9981 | 1.0004 |
| c | 0.2315 | -7.1996 |
| Standard error for m | 0.0069 | 0.0055 |
| Standard error for c | 13.8919 | 11.2546 |

## A.2 Acetylene

Table A.4 Table of assigned calculated wavenumbers to experimental data for acetylene. Calculations are anharmonic and at QZ level. Not all calculated or experimental peaks are assigned.

| Literature Wavenumber (cm$^{-1}$)[2] | B3LYP QZ Wavenumber (cm$^{-1}$) | MP2 QZ Wavenumber (cm$^{-1}$) | Experimental | |
|---|---|---|---|---|
| | | | Wavenumber (cm$^{-1}$) | Shape |
| 3289 | 3291.0 | | 3288.6 | Sharp |
| | | 3245.6 | 3240.7 | Sharp |

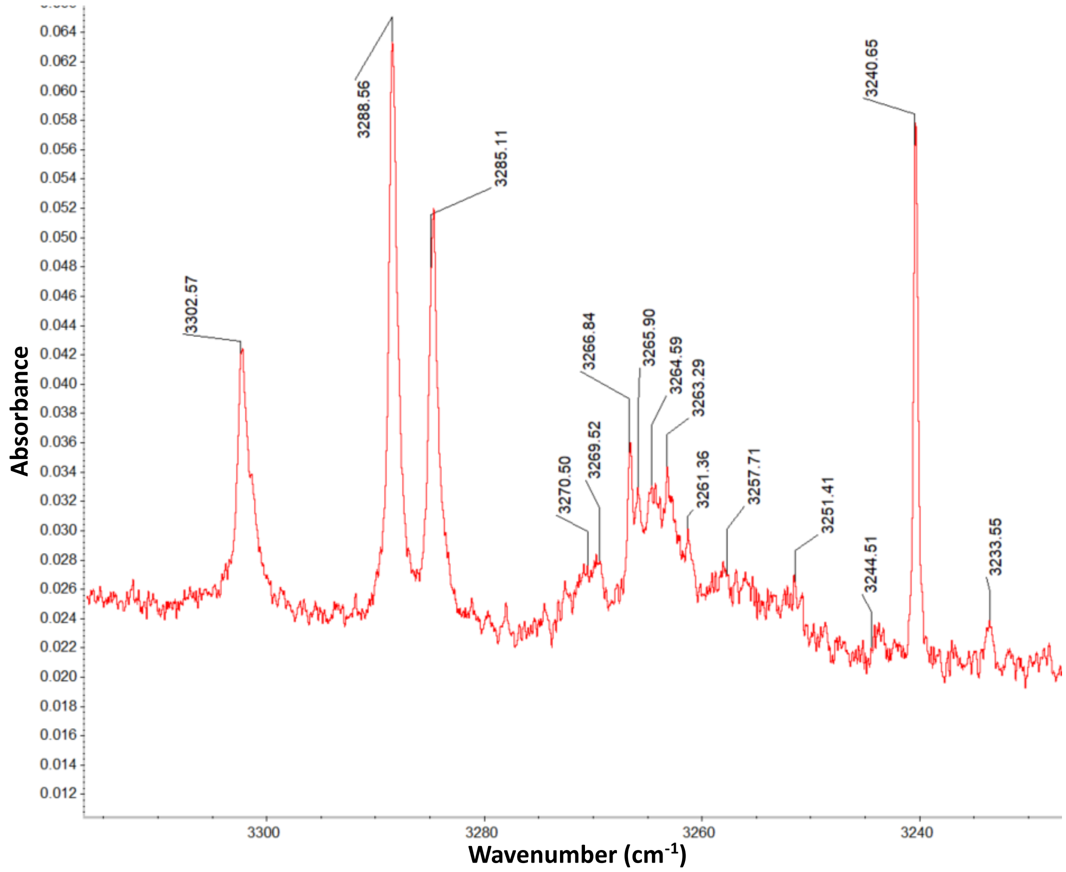

Figure A.5 Section from ~ 3350 – 3200 cm$^{-1}$ of annotated acetylene spectrum.

## A.3 α-Pinene

Table A.5 Table of assigned calculated wavenumbers to experimental data for α-pinene. Calculations are anharmonic and at DZ level. Not all calculated or experimental peaks are assigned.

| B3LYP DZ Wavenumber ($cm^{-1}$) | MP2 DZ Wavenumber ($cm^{-1}$) | Experimental | |
|---|---|---|---|
| | | Wavenumber ($cm^{-1}$) | Shape |
| | 3047.6 | 3054.4 | Broad |
| 3022.3 | 3030.3 | 3030.2 | Very broad |
| 3015.7 | 3000.5 | 3000.0 | Sharp |
| 2980.6 | 2995.5 | 2984.8 | Sharp |
| 2955.5 | 2960.0 | 2960.6 | Medium |
| 2950.9 | 2946.1 | 2945.5 | Sharp |
| 2933.9 | | 2933.6 | Sharp |
| 2931.3 | | 2930.3 | Broad |
| 2925.9 | 2929.2 | 2925.8 | Sharp |
| 2913.7 | | 2919.3 | Sharp |
| 2903.7 | | 2900.5 | Broad |
| 2893.5 | | 2894.5 | Broad |
| 2889.1 | | 2890.8 | Broad |
| 2885.8 | | 2884.0 | Broad |
| 2875.2 | | 2874.1 | Medium |
| 1397.0 | 1371.5 | 1382.5 | Broad |
| 1367.8 | 1368.2 | 1379.4 | Broad |
| 1366.8 | 1355.7 | 1366.3 | Broad |
| 1327.1 | 1332.9 | 1333.8 | Very broad |
| 1293.9 | 1271.1 | 1272.4 | Broad, shoulder |
| 1235.8 | 1228.4 | 1223.7 | Medium |
| 1211.3 | 1218.9 | 1218.9 | Medium, shoulder |
| 1195.8 | 1205.5 | 1207.8 | Sharp |
| 1191.3 | 1173.1 | 1183.2 | Broad |
| 1169.2 | 1168.7 | 1169.4 | Broad |
| 1114.3 | 1127.3 | 1127.8 | Medium |
| | 1097.4 | 1104.5 | Broad, shoulder |
| 1087.8 | 1086.3 | 1086.2 | Broad, split peak |
| 1078.4 | 1065.5 | 1064.6 | Medium, shoulder |
| 1050.4 | 1047.0 | 1053.3 | Broad |
| 1030.9 | 1029.1 | 1044.8 | Broad |
| 1009.5 | 1014.8 | 1016.4 | Sharp, split peak |
| 985.8 | 994.4 | 998.9 | Broad |
| 952.1 | 964.2 | 960.8 | Medium |
| 939.0 | 950.0 | 954.1 | Medium |
| 924.8 | 938.0 | 930.1 | Broad |
| 897.0 | 889.8 | 887.6 | Medium |
| 878.1 | | 878.6 | Medium |

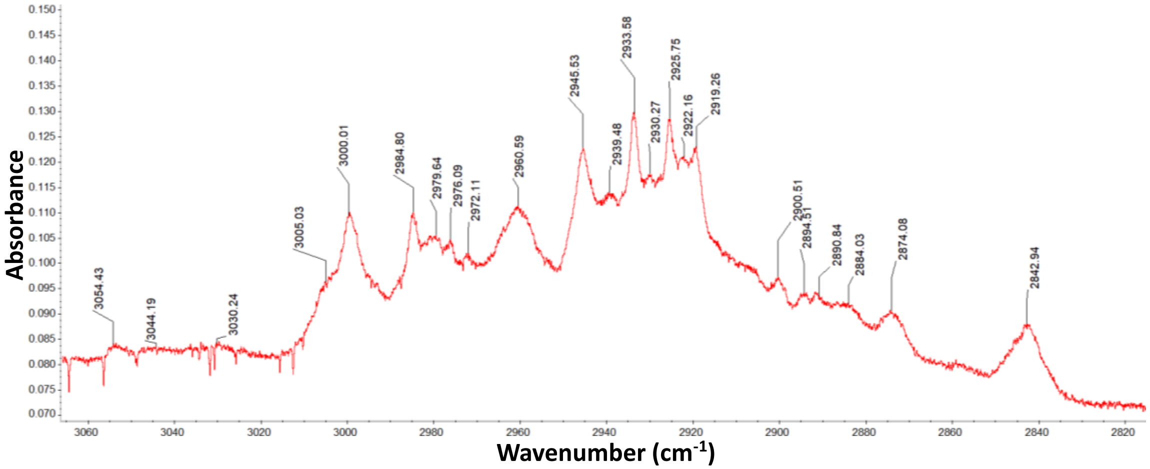

Figure A.6 Section from ~ 3060 – 2820 cm$^{-1}$ of annotated α-pinene spectrum.

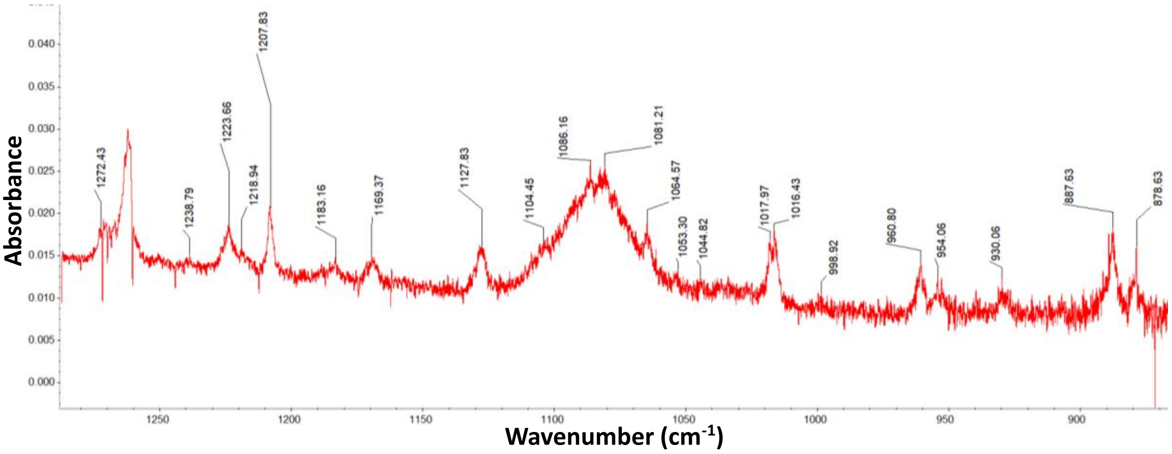

Figure A.7 Section from ~ 1250 – 850 cm$^{-1}$ of annotated α-pinene spectrum.

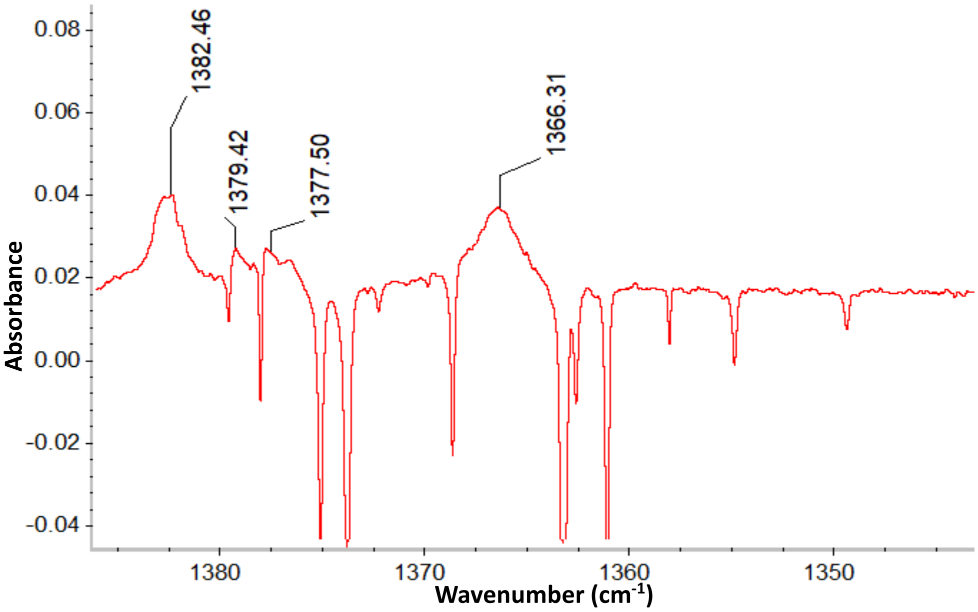

Figure A.8 Section from ~ 1390 – 1350 cm$^{-1}$ of annotated α-pinene spectrum.

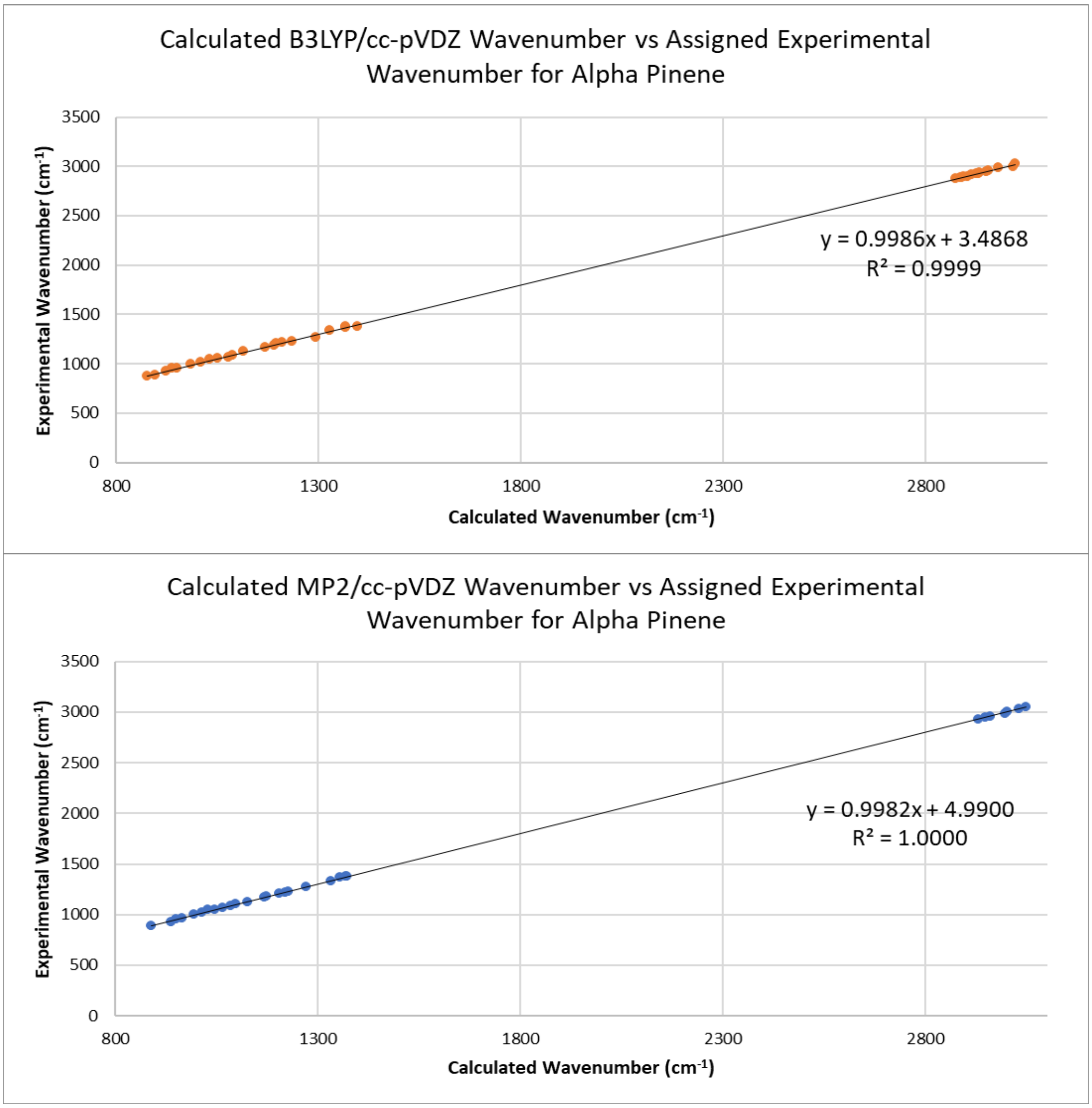

Figure A.9 Comparison graphs for experimental wavenumber versus calculated wavenumber.

Table A.6 Slope, intercept, and standard errors of each for the comparison graphs for α-pinene.

| **Value** | **B3LYP** | **MP2** |
|---|---:|---:|
| m | 0.9986 | 0.9982 |
| c | 3.4868 | 4.9900 |
| Standard error for m | 0.0017 | 0.0014 |
| Standard error for c | 3.4659 | 2.4043 |

## A.4 α-Pinene Oxide

Table A.7 Table of assigned calculated wavenumbers to experimental data for α-pinene oxide. Calculations are anharmonic and at DZ level. Not all calculated or experimental peaks are assigned.

| B3LYP DZ Wavenumber ($cm^{-1}$) | MP2 DZ Wavenumber ($cm^{-1}$) | Experimental | |
|---|---|---|---|
| | | Wavenumber ($cm^{-1}$) | Shape |
| | 3074.2 | 3079.4 | Sharp |
| | 3050.7 | 3063.3 | Sharp |
| | 3046.0 | 3046.7 | Sharp |
| | 3035.3 | 3040.0 | Broad |
| | 3032.6 | 3037.9 | Broad |
| | 3011.9 | 3012.4 | Sharp |
| 3006.6 | | 2994.1 | Sharp |
| 2992.4 | | 2992.5 | Sharp |
| 2982.0 | 2983.6 | 2983.6 | Sharp |
| 2974.8 | | 2974.7 | Sharp |
| | 2968.0 | 2965.3 | Sharp |
| 2963.0 | 2959.4 | 2962.0 | Broad |
| | 2959.4 | | |
| | 2956.4 | 2956.9 | Broad |
| | 2956.7 | | |
| 2949.6 | | 2948.9 | Broad |
| 2936.0 | 2939.9 | 2939.2 | Broad |
| 2935.8 | | 2935.2 | Sharp |
| 2930.5 | | 2927.4 | Sharp |
| 2916.1 | | 2916.6 | Broad |
| 2914.0 | | 2914.2 | Sharp |
| 2889.3 | | 2867.9 | Sharp |
| | 1374.5 | 1379.4 | Sharp |
| 1371.3 | 1369.2 | 1369.6 | Sharp |
| 1359.6 | | 1361.4 | Sharp |
| 1354.7 | 1358.4 | 1354.1 | Sharp |
| | 1336.2 | 1343.1 | Broad |
| 1330.9 | 1319.4 | 1323.4 | Sharp |
| 1306.6 | 1307.7 | 1307.1 | Broad |
| 1287.3 | 1274.6 | 1277.3 | Sharp |
| | 1266.9 | 1268.3 | Sharp |
| 1259.2 | | 1262.2 | Broad |
| 1256.3 | | 1246.9 | Sharp |
| | 1233.6 | 1235.2 | Sharp |
| 1223.0 | | 1225.0 | Sharp |
| | 1218.4 | 1216.6 | Sharp |
| | 1219.2 | | |

| B3LYP DZ Wavenumber (cm$^{-1}$) | MP2 DZ Wavenumber (cm$^{-1}$) | Experimental | |
|---|---|---|---|
| | | Wavenumber (cm$^{-1}$) | Shape |
| 1207.4 | | 1201.0 | Broad |
| 1199.7 | 1195.2 | 1197.0 | Broad |
| 1181.3 | 1178.0 | 1180.2 | Sharp |
| 1144.9 | 1152.2 | 1156.7 | Sharp |
| | 1122.9 | 1123.8 | Sharp |
| 1111.2 | 1103.5 | 1101.0 | Sharp |
| 1089.3 | 1082.1 | 1086.1 | Sharp |
| 1071.6 | 1062.8 | 1068.7 | Sharp |
| 1051.6 | 1060.1 | 1059.6 | Broad |
| 1046.0 | | 1047.9 | Sharp |
| | 1044.7 | 1040.7 | Sharp |
| 1039.1 | | 1039.2 | Sharp |
| | 1003.2 | 1008.6 | Sharp |
| 994.9 | | 995.8 | Sharp |
| | 990.4 | 993.8 | Sharp |
| | 967.5 | 967.3 | Sharp |
| 958.2 | | 946.1 | Sharp |
| | 947.8 | 943.1 | Sharp |
| 935.5 | 939.2 | 936.2 | Sharp |
| | 939.7 | 934.3 | Sharp |
| 929.4 | | 928.3 | Sharp |
| | 895.8 | 898.7 | Sharp |
| 888.9 | | 896.9 | Broad |
| 881.4 | | 882.6 | Sharp |
| | 867.0 | 862.6 | Sharp |
| 852.5 | | 859.7 | Broad |
| | 849.4 | 842.2 | Sharp |
| 832.6 | | 835.7 | Broad |
| | 824.5 | 818.5 | Sharp |
| 807.0 | | 817.2 | Sharp |

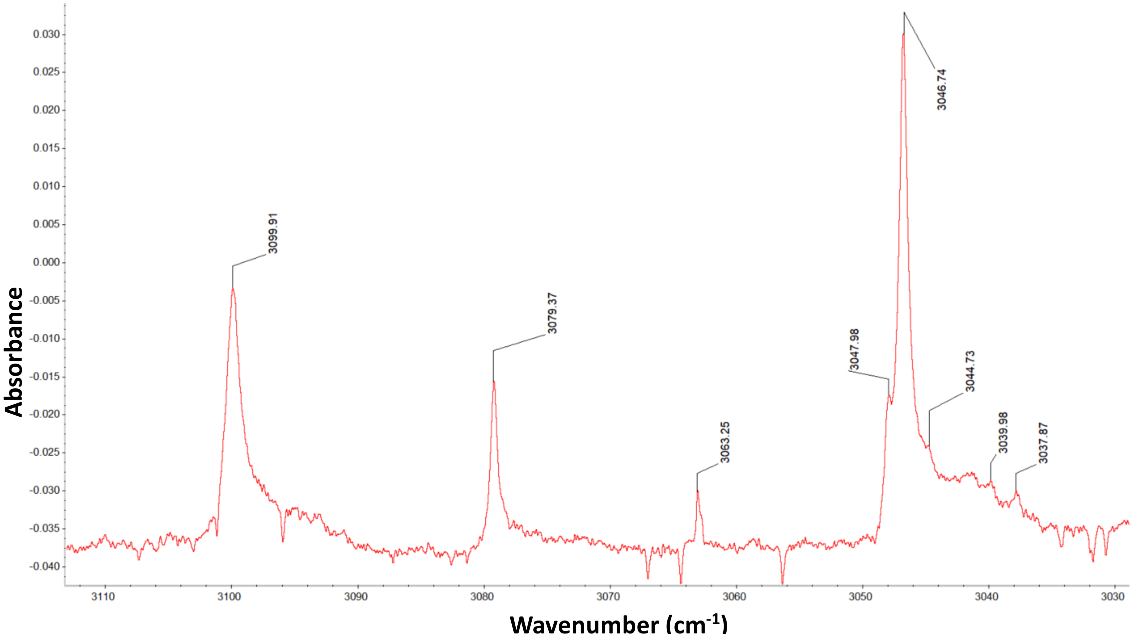

Figure A.10 Section from ~ 3110 – 3030 cm$^{-1}$ of annotated α-pinene oxide spectrum.

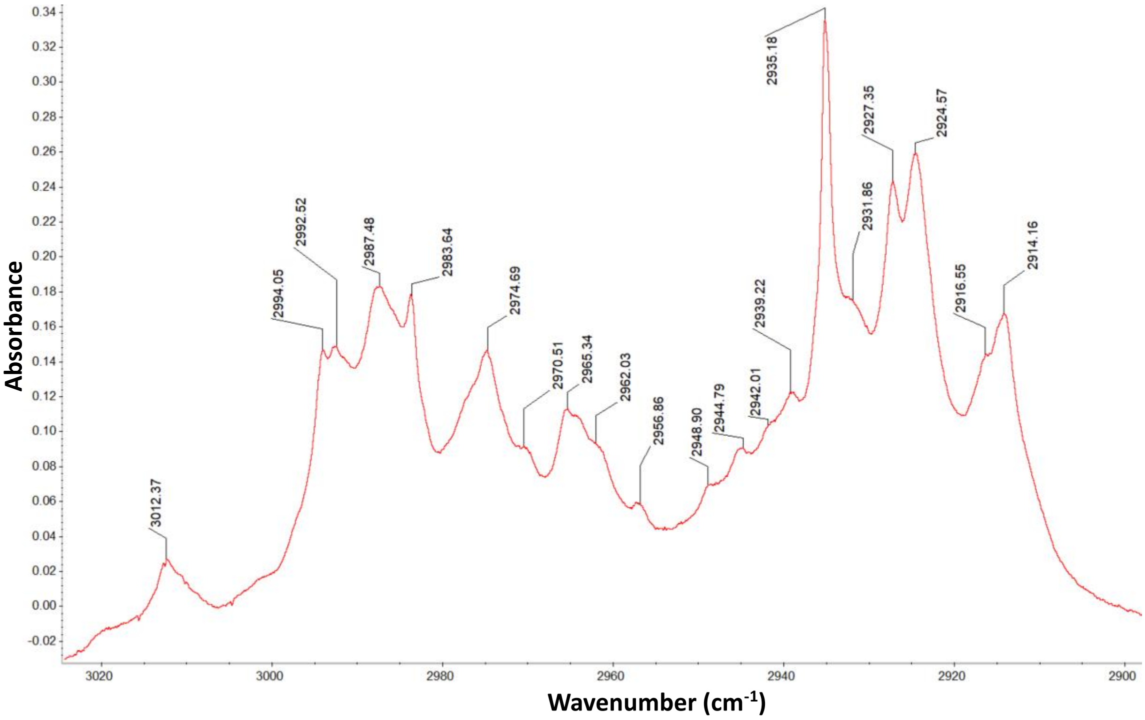

Figure A.11 Section from ~ 3000 – 2900 cm$^{-1}$ of annotated α-pinene oxide spectrum.

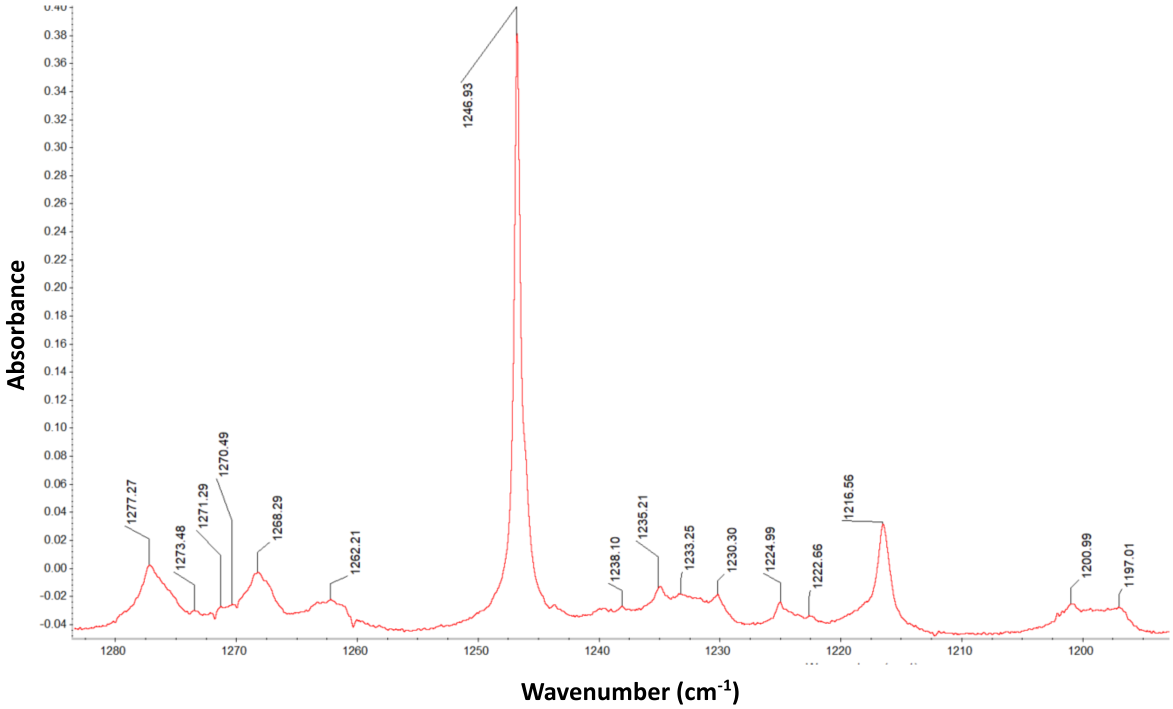

Figure A.12 Section from ~ 1280 – 1200 cm$^{-1}$ of annotated α-pinene oxide spectrum.

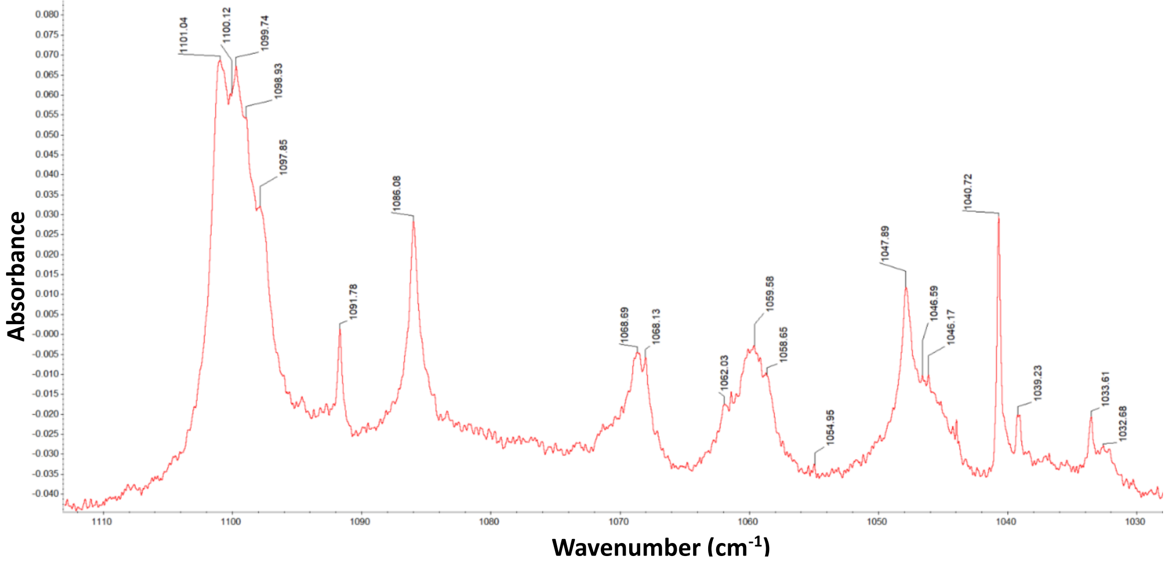

Figure A.13 Section from ~ 1100 – 1030 cm$^{-1}$ of annotated α-pinene oxide spectrum.

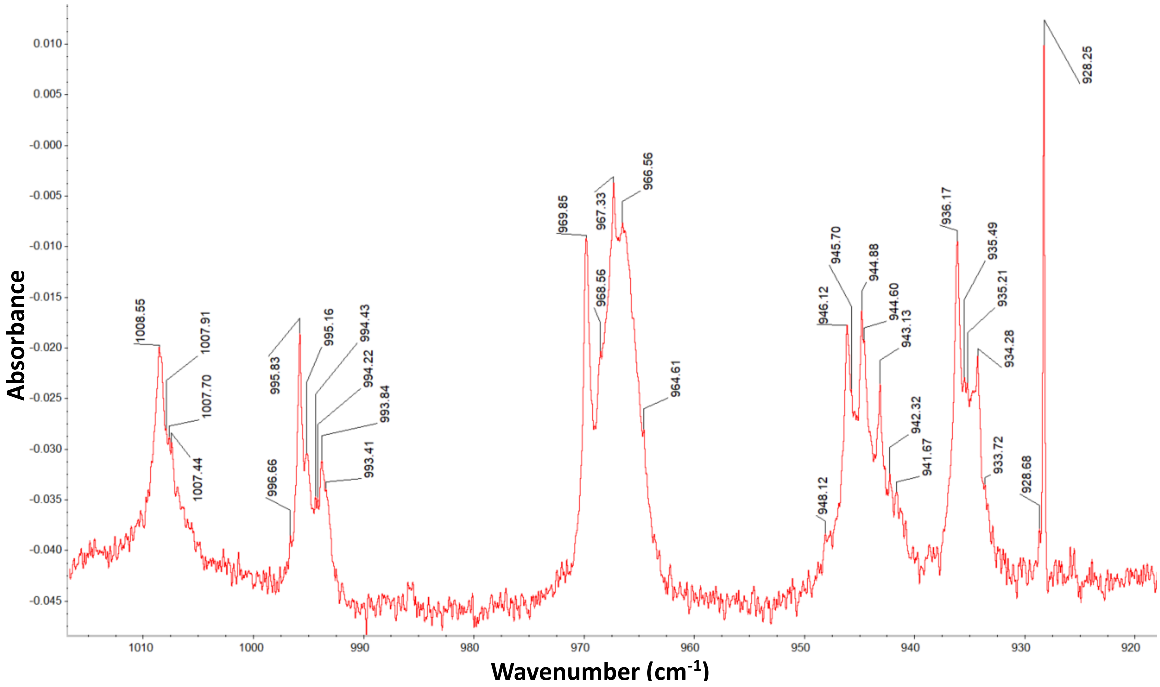

Figure A.14 Section from ~ 1010 – 900 cm$^{-1}$ of annotated α-pinene oxide spectrum.

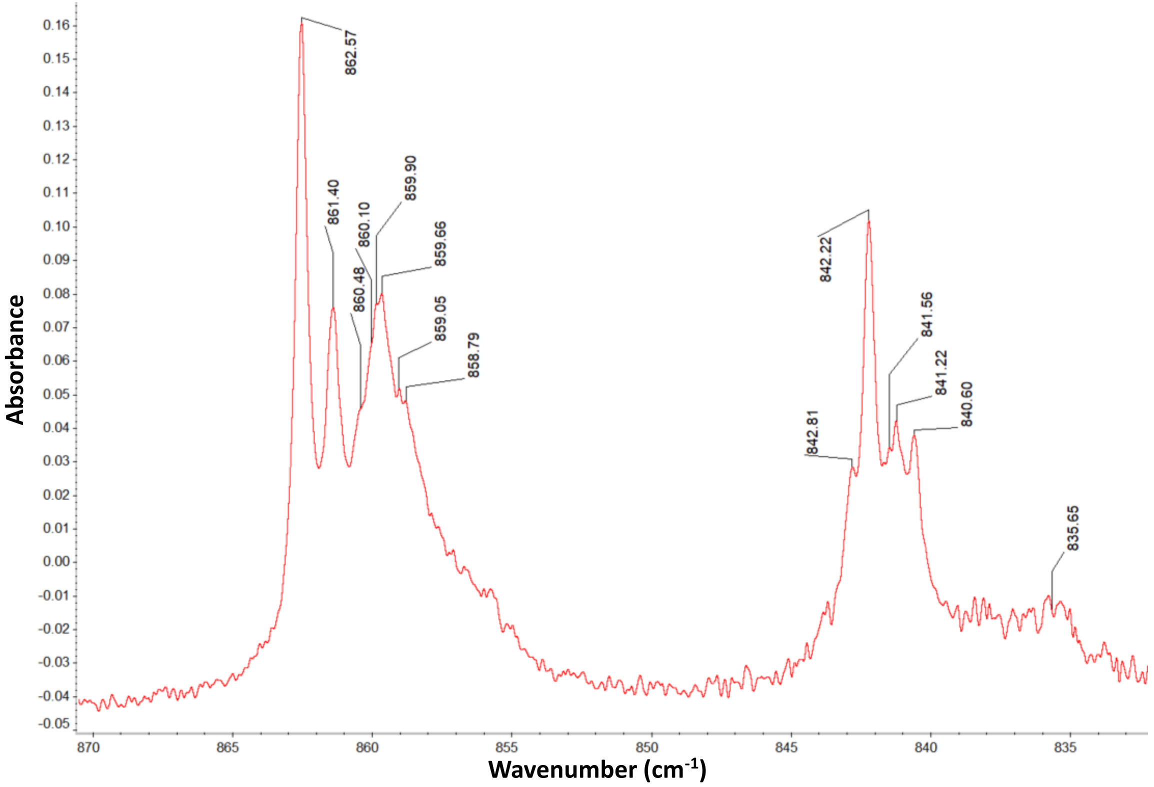

Figure A.15 Section from ~ 870 – 830 cm$^{-1}$ of annotated α-pinene oxide spectrum.

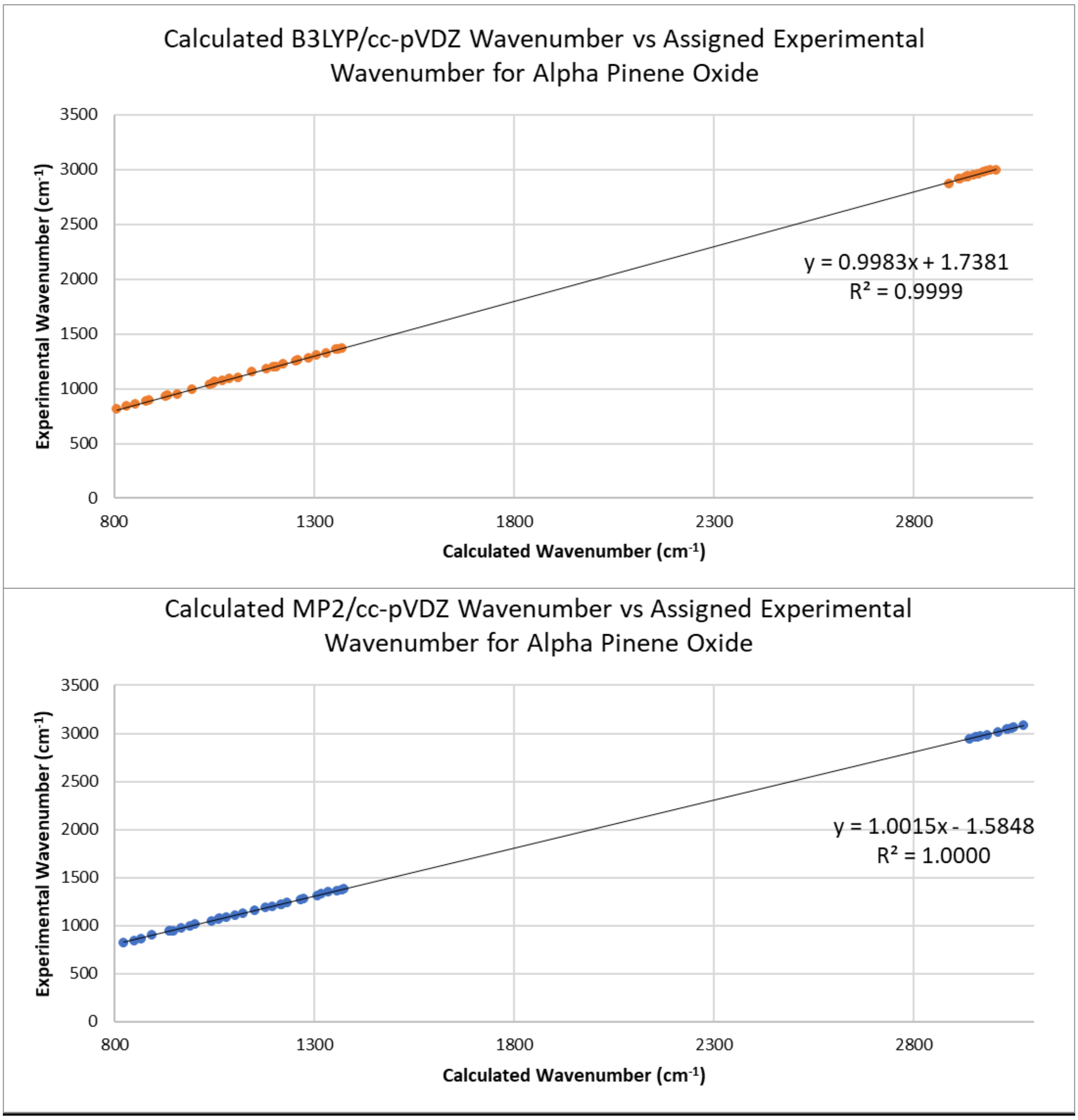

Calculated B3LYP/cc-pVDZ Wavenumber vs Assigned Experimental Wavenumber for Alpha Pinene Oxide

Calculated MP2/cc-pVDZ Wavenumber vs Assigned Experimental Wavenumber for Alpha Pinene Oxide

Figure A.16 Comparison graphs for experimental wavenumber versus calculated wavenumber.

Table A.8 Slope, intercept, and standard errors of each for the comparison graphs for α-pinene oxide.

| Value | B3LYP | MP2 |
|---|---|---|
| m | 0.9983 | 1.0015 |
| c | 1.7381 | -1.5848 |
| Standard error for m | 0.0012 | 0.0007 |
| Standard error for c | 2.1875 | 1.3381 |

## A.5 Benzene

Table A.9 Table of assigned literature and calculated wavenumbers to experimental data for benzene. Calculations are anharmonic and at QZ level. Not all calculated or experimental peaks are assigned.

| Literature Wavenumber ($cm^{-1}$)[16] | B3LYP QZ Wavenumber ($cm^{-1}$) | MP2 QZ Wavenumber ($cm^{-1}$) | Experimental | |
|---|---|---|---|---|
| | | | Wavenumber ($cm^{-1}$) | Shape |
| 3103 | | 3086.1 | 3099.7 | Sharp |
| 3080 | | 3079.2 | 3079.4 | Sharp |
| | | 3079.2 | 3077.2 | Sharp, shoulder |
| | | 3079.2 | 3075.8 | Sharp, shoulder |
| 3048 | | | 3047.7 | Sharp, shoulder |
| 3044 | 3030.3 | 3030.9 | 3037.6 | Medium |
| 1481 | 1487.2 | 1481.1 | 1483.3 | Sharp |
| 1481 | 1487.6 | 1481.2 | 1483.0 | Broad, shoulder |
| | 1186.3 | 1182.0 | 1180.2 | Sharp |
| | | 1182.0 | | |
| 1178 | 1182.4 | 1156.1 | 1179.5 | Sharp |
| 1038 | | 1042.3 | 1040.7 | Sharp |
| 1038 | | 1042.3 | | |
| 1010 | | 1030.2 | 1039.1 | Sharp |

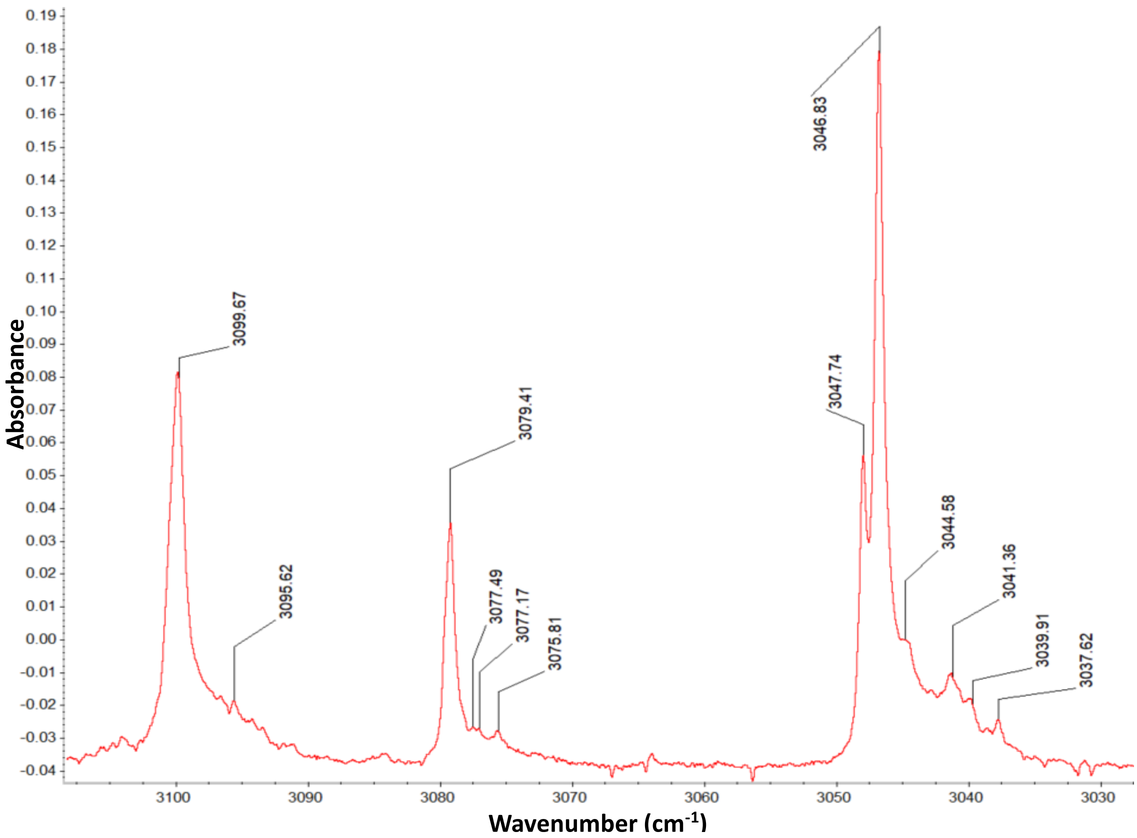

Figure A.17 Section from ~ 3150 – 3030 cm$^{-1}$ of annotated benzene spectrum.

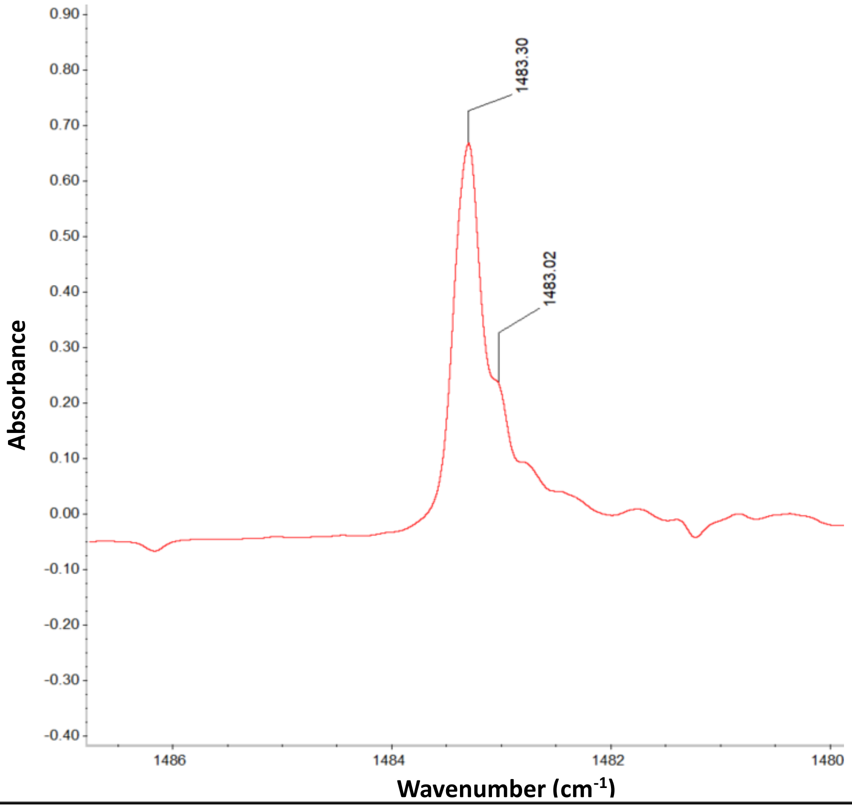

Figure A.18 Section from ~ 1490 – 1480 cm$^{-1}$ of annotated benzene spectrum.

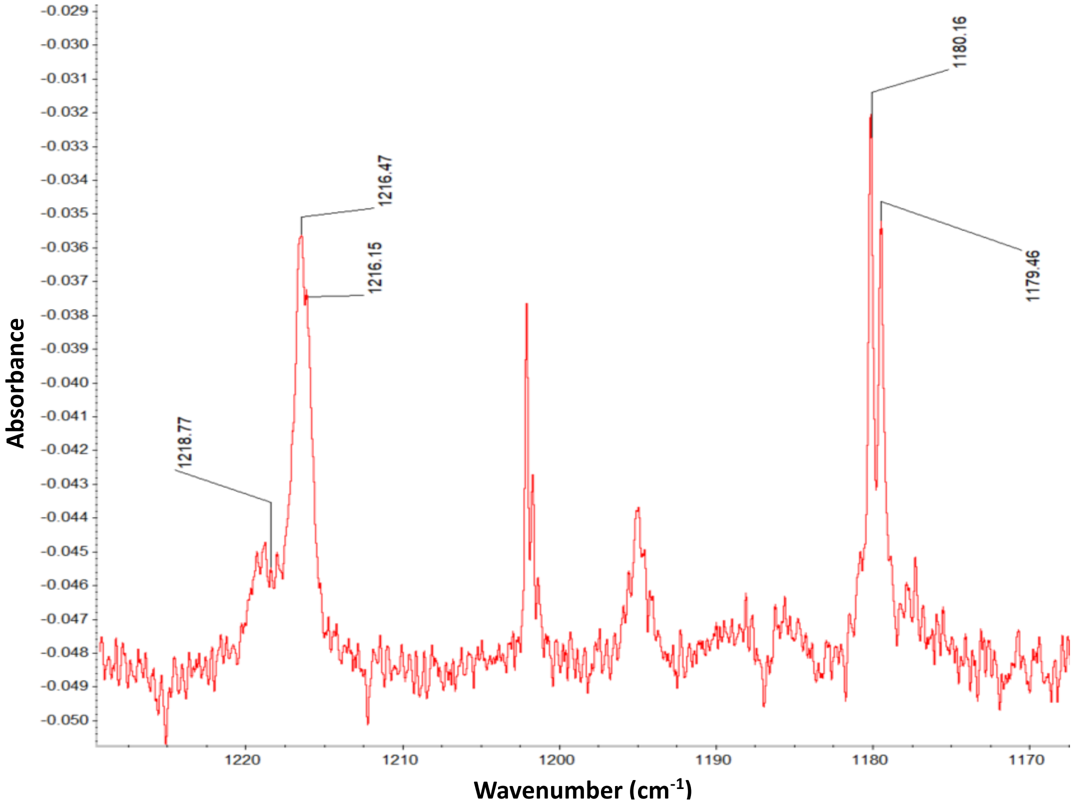

Figure A.20 Section from ~ 12300 - 1170 cm$^{-1}$ of annotated benzene spectrum.

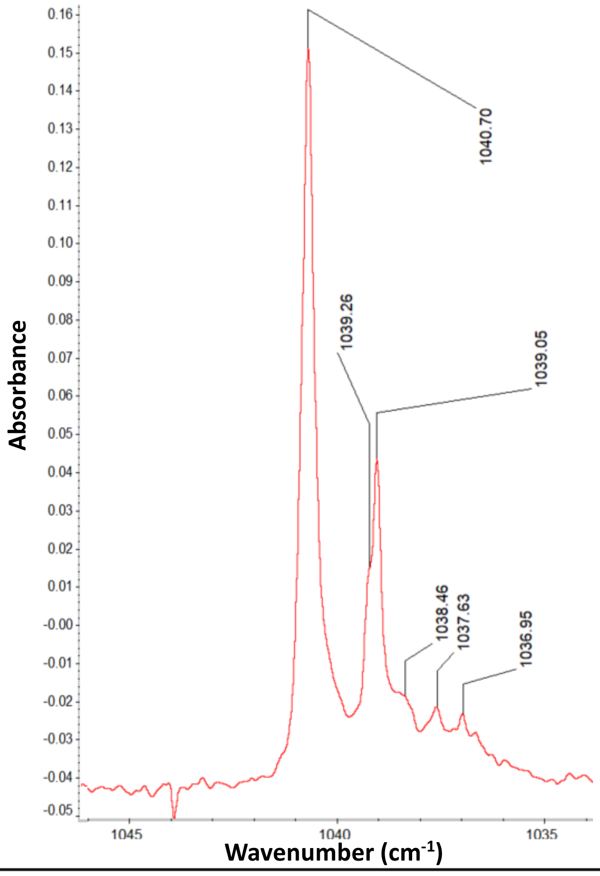

Figure A.19 Section from ~ 1050 - 1030 cm$^{-1}$ of annotated benzene spectrum.

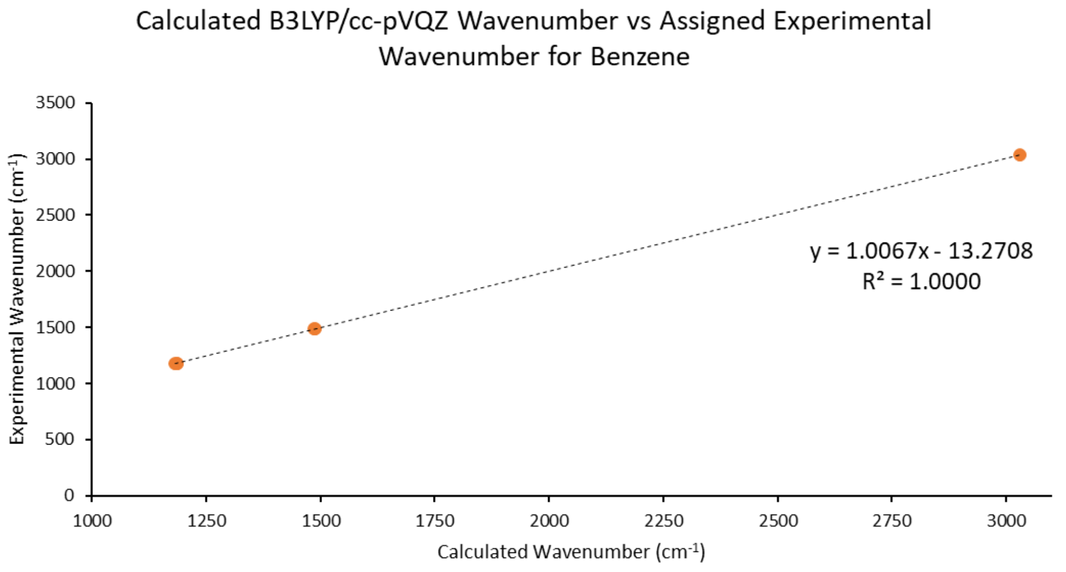

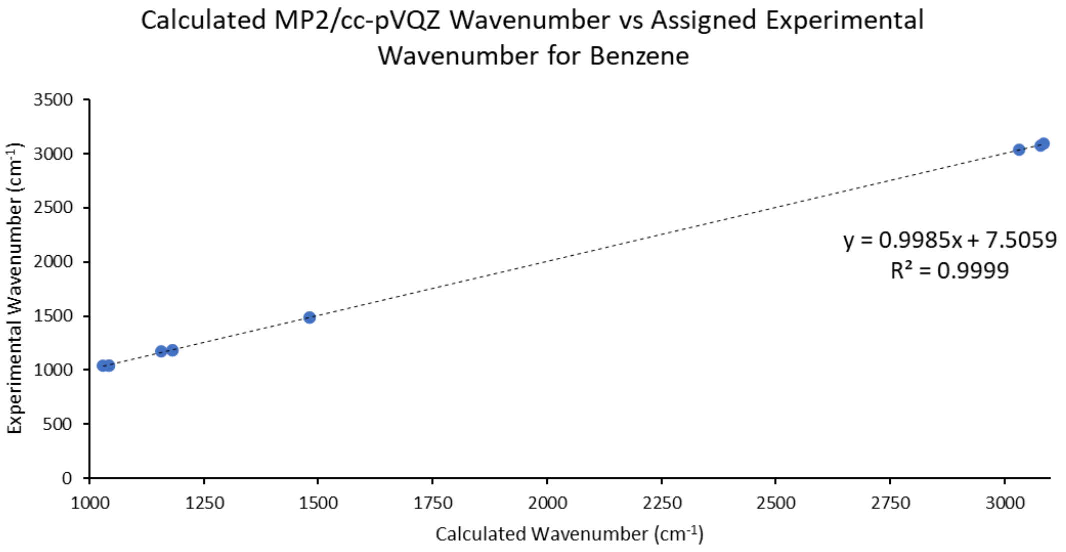

Figure A.21 Comparison graphs for experimental wavenumber versus calculated wavenumber.

Table A.10 Slope, intercept, and standard errors of each for the comparison graphs for benzene.

| Value | B3LYP | MP2 |
|---|---|---|
| m | 1.0067 | 0.9985 |
| c | -13.2708 | 7.5059 |
| Standard error for m | 0.0011 | 0.0028 |
| Standard for c | 1.9707 | 6.2632 |

## A.6 β-Pinene

Table A.11 Table of assigned literature and calculated wavenumbers to experimental data for β-pinene. Calculations are anharmonic and at DZ level. Not all calculated or experimental peaks are assigned.

| **B3LYP DZ Wavenumber (cm$^{-1}$)** | **MP2 DZ Wavenumber (cm$^{-1}$)** | **Experimental** | |
|---|---|---|---|
| | | **Wavenumber (cm$^{-1}$)** | **Shape** |
| | 3138.2 | 3161.8 | Sharp |
| 3069.5 | 3083.7 | 3075.8 | Sharp |
| 3021.7 | 3012.1 | 3014.6 | Broad, shoulder |
| | 3002.1 | 3004.0 | Medium, shoulder |
| | 2997.4 | 2994.8 | Sharp |
| | 2993.6 | 2985.0 | Broad, shoulder |
| 2980.7 | 2975.9 | 2975.9 | Sharp |
| 2963.9 | 2958.1 | 2962.6 | Medium |
| 2954.0 | 2955.5 | 2958.5 | Medium, shoulder |
| 2945.8 | 2946.1 | 2945.8 | Medium |
| 2936.2 | 2930.9 | 2932.5 | Sharp |
| 2914.2 | | 2919.3 | Sharp |
| 2907.4 | | 2909.4 | Medium, shoulder |
| 2905.0 | | 2901.7 | Medium, shoulder |
| 2885.6 | | 2886.9 | Medium |
| 2864.5 | | 2875.4 | Sharp |
| 2898.2 | | 2826.2 | Broad |
| 1452.3 | 1465.3 | 1460.1 | Medium |
| 1445.3 | 1450.9 | 1446.8 | Broad |
| 1389.3 | 1373.1 | 1384.2 | Sharp |
| 1372.0 | 1358.0 | 1369.0 | Sharp |
| 1324.9 | 1318.1 | 1319.6 | Broad |
| | 1292.3 | 1296.4 | Medium |
| 1278.2 | 1261.6 | 1262.9 | Sharp |
| 1274.4 | | 1258.4 | Medium, shoulder |
| 1248.9 | | 1234.3 | Sharp, shoulder |
| 1242.3 | 1249.8 | 1231.9 | Sharp |
| | 1226.2 | 1220.7 | Broad |
| 1220.6 | 1223.7 | 1216.6 | Sharp, shoulder |
| 1201.4 | 1205.7 | 1203.8 | Sharp |
| 1191.1 | 1192.0 | 1195.5 | Sharp |
| 1183.5 | 1176.0 | 1187.1 | Sharp |
| 1131.8 | 1140.5 | 1144.0 | Sharp |
| | 1100.9 | 1104.2 | Sharp |
| 1087.8 | 1083.3 | 1081.6 | Broad |
| 1072.9 | | 1076.4 | Broad, shoulder |
| 1047.3 | 1057.1 | 1056.3 | Sharp |
| 1033.6 | 1045.4 | 1049.4 | Medium |
| 1002.2 | 1015.9 | 1012.9 | Medium |
| 977.9 | 969.5 | 974.2 | Medium |
| 964.1 | 958.0 | 955.2 | Sharp |
| 942.4 | 942.9 | 941.1 | Sharp |
| 929.1 | 934.9 | 927.5 | Sharp |

| B3LYP DZ Wavenumber ($cm^{-1}$) | MP2 DZ Wavenumber ($cm^{-1}$) | Experimental | |
|---|---|---|---|
| | | Wavenumber ($cm^{-1}$) | Shape |
| 882.3 | 888.5 | 878.5 | Sharp |
| 914.5 | 905.0 | 903.5 | Sharp |
| 898.3 | | 884.9 | Medium, shoulder |
| 869.1 | 880.1 | 877.2 | Sharp |
| 841.4 | 852.9 | 853.1 | Broad |

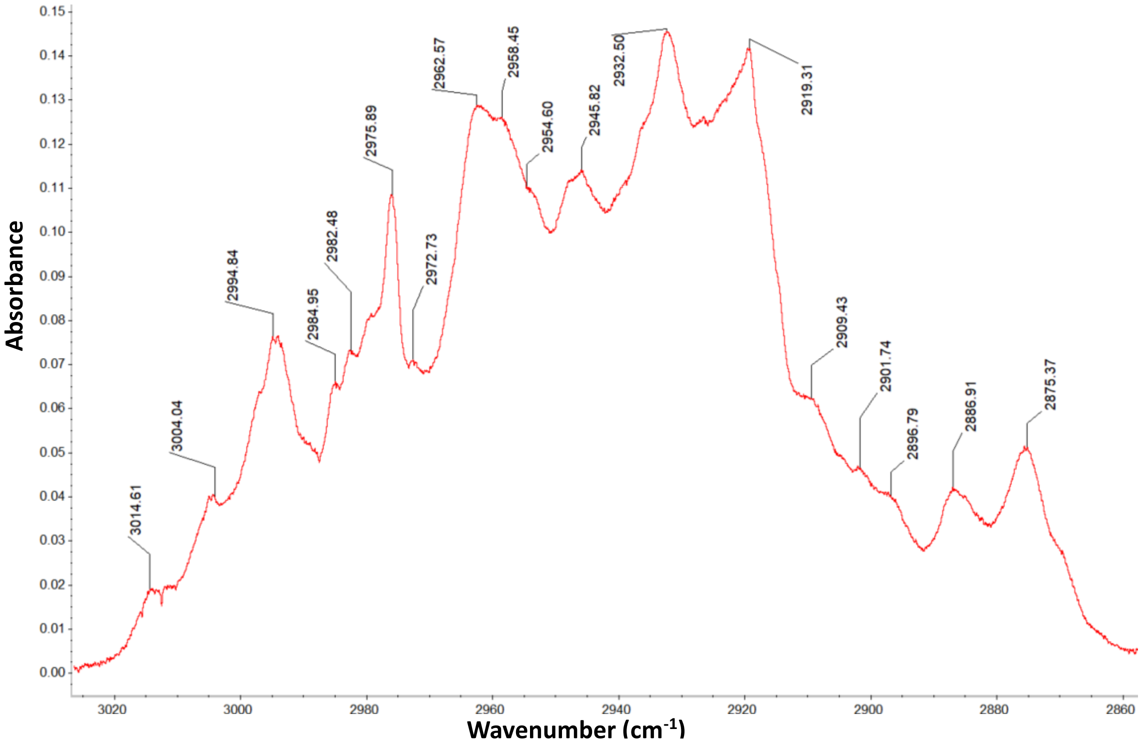

Figure A.22 Section from ~ 3020 – 3860 cm$^{-1}$ of annotated β-pinene spectrum.

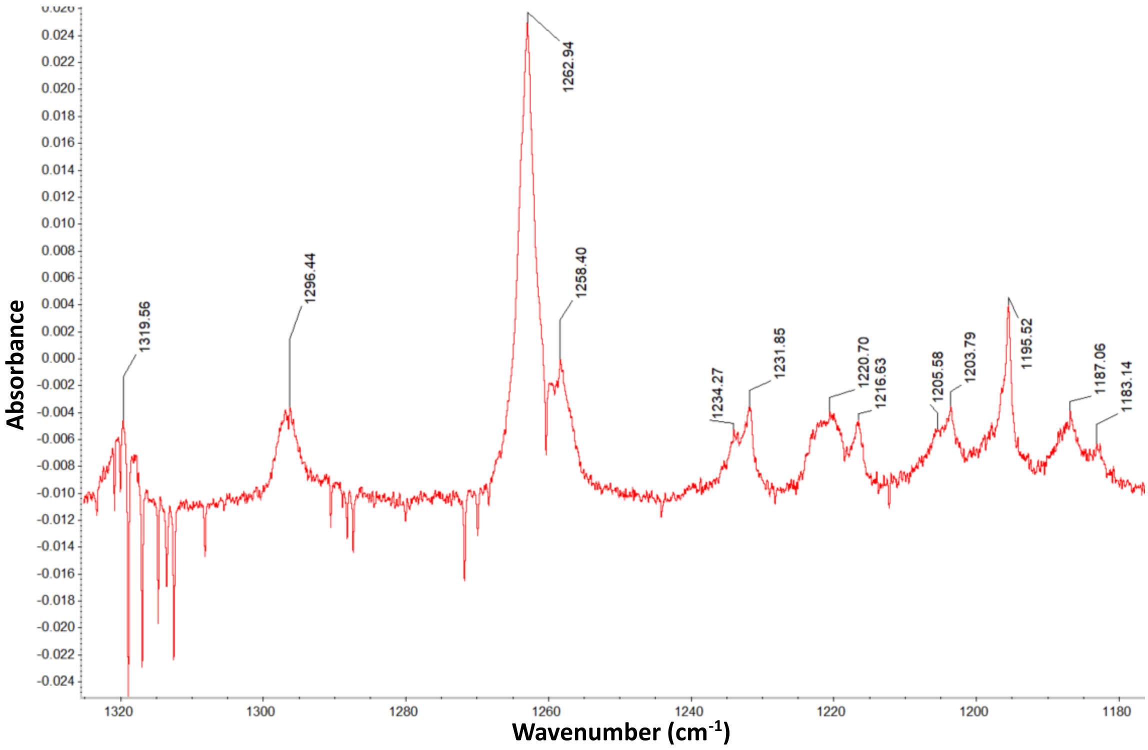

Figure A.23 Section from ~ 1320 – 1180 cm$^{-1}$ of annotated β-pinene spectrum.

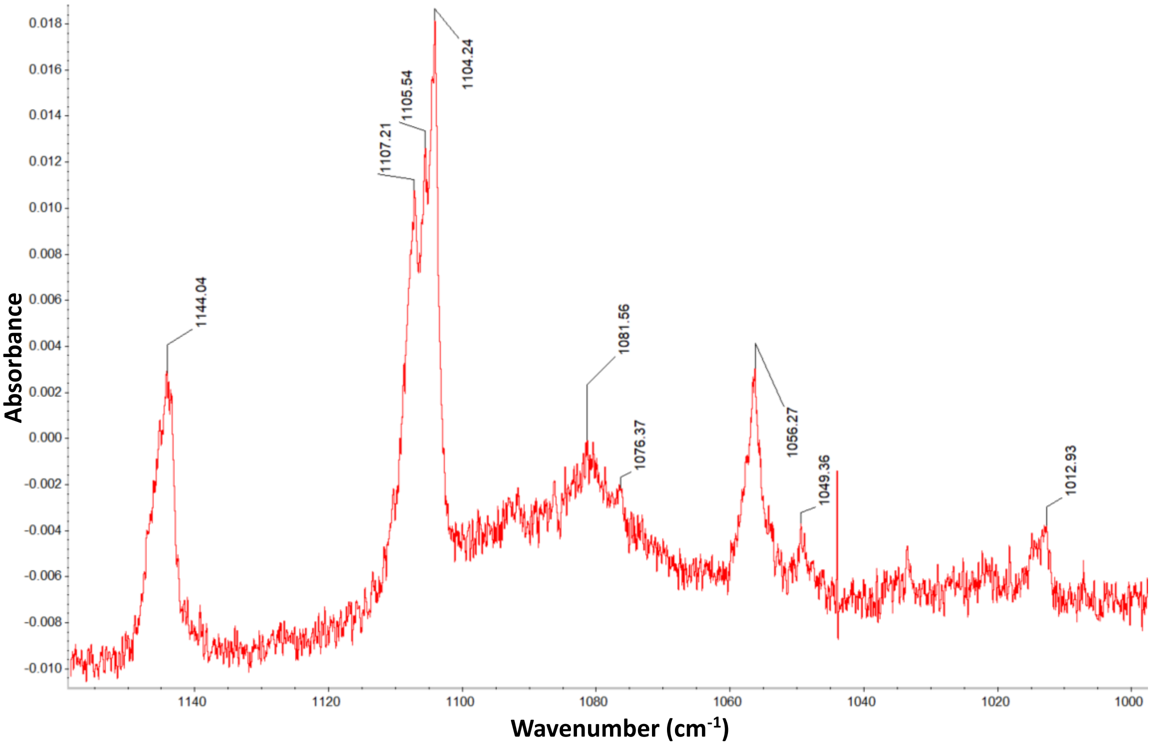

Figure A.24 Section from ~ 1150 – 1000 cm$^{-1}$ of annotated β-pinene spectrum.

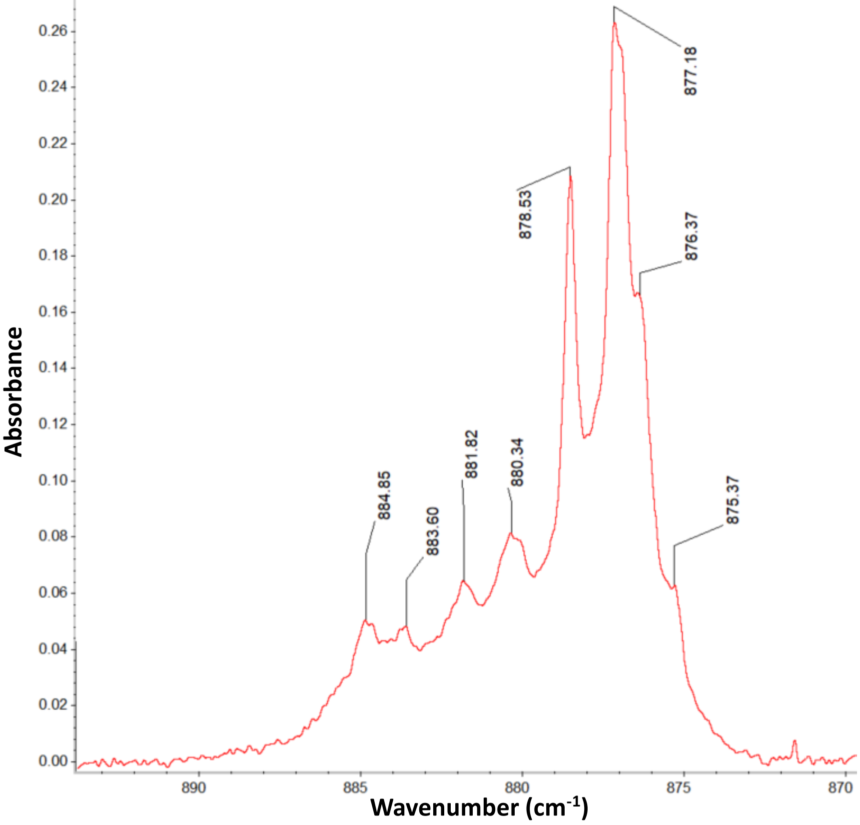

Figure A.25 Section from ~ 890 – 870 cm$^{-1}$ of annotated β-pinene spectrum.

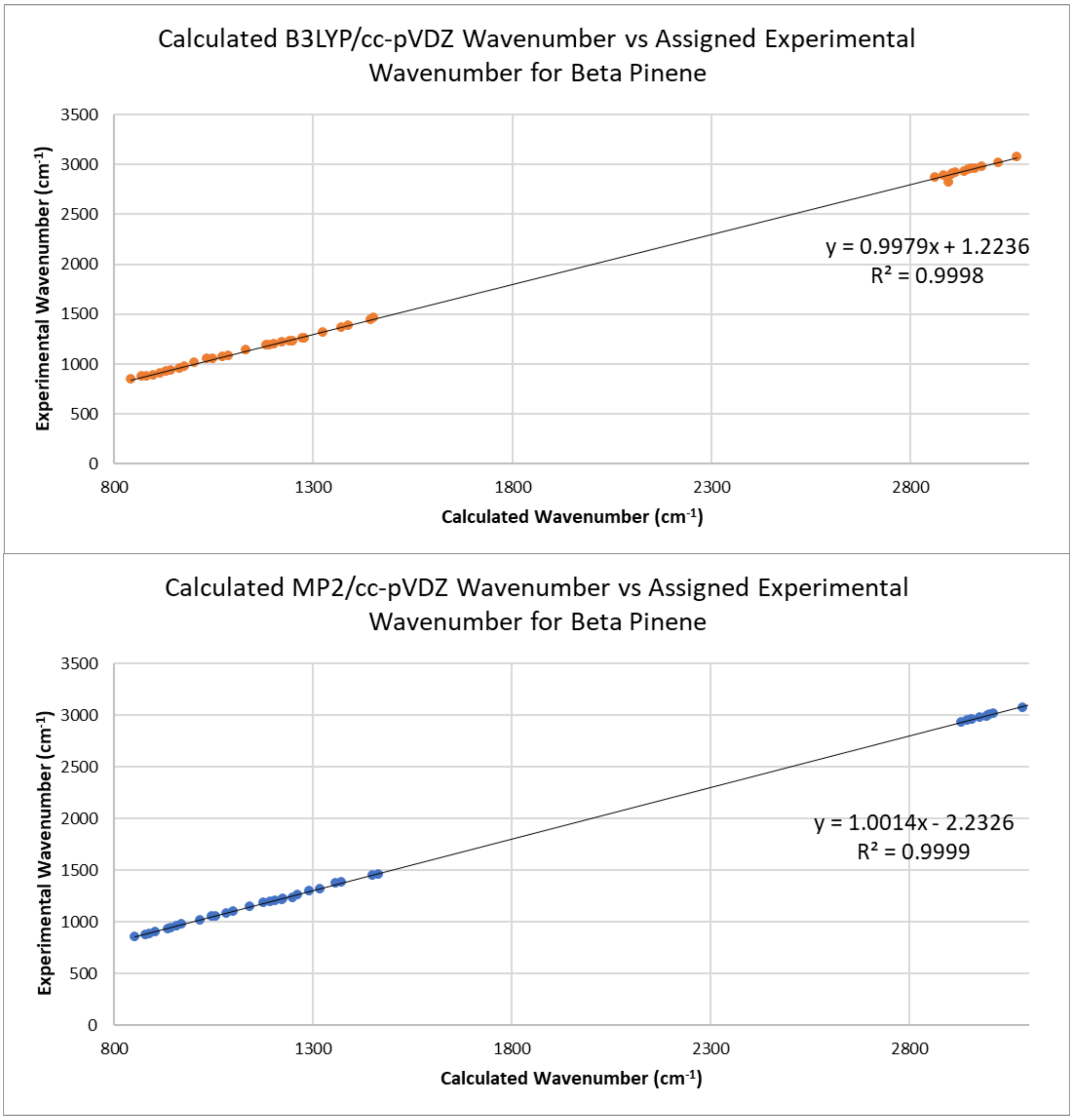

Figure A.26 Comparison graphs for experimental wavenumber versus calculated wavenumber.

Table A.12 Slope, intercept, and standard errors of each for the comparison graphs for β-pinene.

| Value | B3LYP | MP2 |
|---|---|---|
| m | 0.9979 | 1.0014 |
| c | 1.2236 | -2.2326 |
| Standard error for m | 0.0025 | 0.0013 |
| Standard error for c | 4.7584 | 2.4968 |

## A.7 Cyclopropylacetylene

Table A.13 Table of assigned literature and calculated wavenumbers to experimental data for cyclopropylacetylene. Calculations are anharmonic and at QZ level. Not all calculated or experimental peaks are assigned.

| Literature Wavenumber ($cm^{-1}$)[3] | B3LYP QZ Wavenumber ($cm^{-1}$) | MP2 QZ Wavenumber ($cm^{-1}$) | Experimental | |
|---|---|---|---|---|
| | | | Wavenumber ($cm^{-1}$) | Shape |
| 3340 | 3343.7 | 3365.1 | 3339.9 | Sharp |
| 3112 | 3083.1 | 3155.2 | 3101.8 | Sharp |
| 3105 | 3066.1 | 3142.7 | 3100.6 | Sharp |
| 3044 | 3038.0 | 3085.0 | 3026.5 | Sharp |
| 3042 | 3018.2 | 3066.7 | 3024.4 | Sharp |
| 3036 | 2990.9 | 3067.0 | 3021.5 | Sharp |
| 2144 | 2185.7 | 2095.2 | 2137.1 | Sharp |
| 1355 | 1362.8 | 1352.9 | 1356.3 | Broad |
| 1204 | 1190.0 | 1202.5 | 1200.1 | Sharp |
| 1199 | 1174.8 | 1179.3 | 1174.9 | Sharp |
| 1123 | 1123.4 | 1121.0 | 1122.5 | Sharp |
| 1094 | 1090.4 | 1089.3 | 1089.5 | Sharp |
| 1060 | 1062.1 | 1048.7 | 1053.2 | Sharp |
| 1038 | 1036.5 | 1026.2 | 1031.7 | Sharp |
| 942 | 940.2 | 950.9 | 940.6 | Sharp |

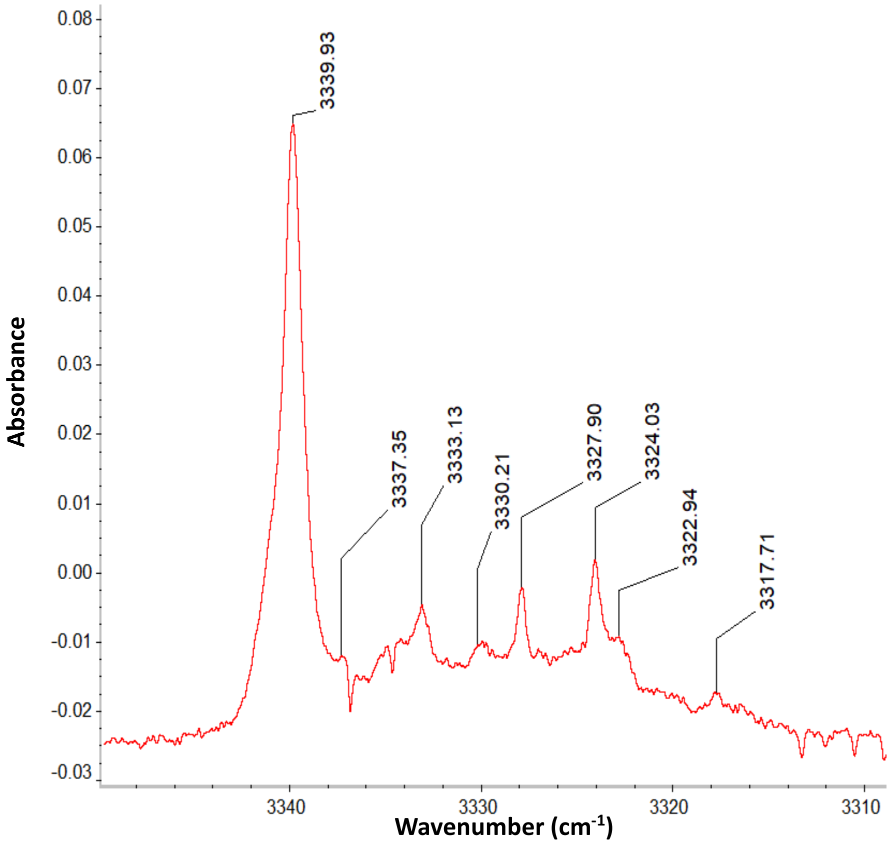

Figure A.27 Section from ~ 3350 – 3310 cm$^{-1}$ of annotated cyclopropylacetylene spectrum.

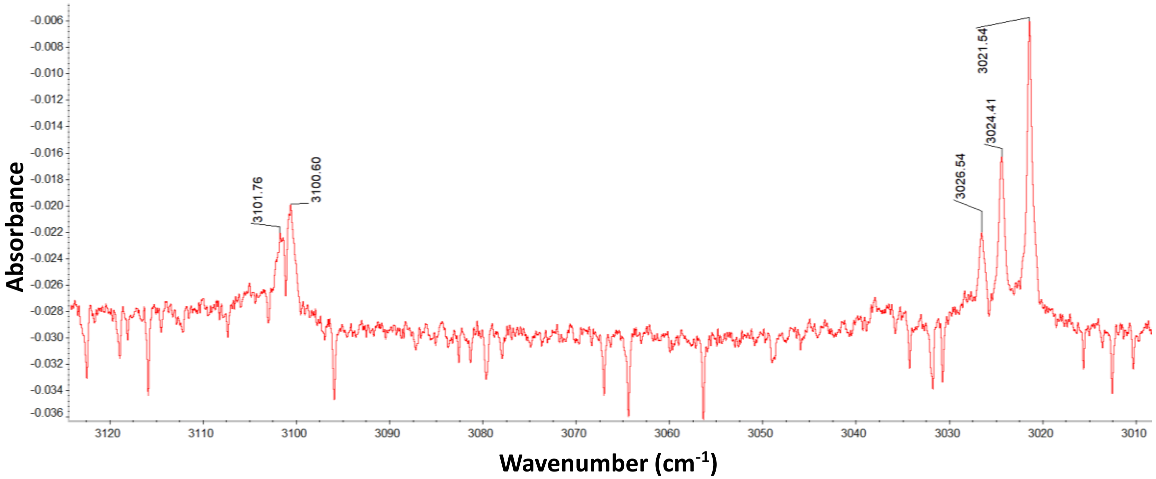

Figure A.28 Section from ~ 3130 – 3000 cm$^{-1}$ of annotated cyclopropylacetylene spectrum.

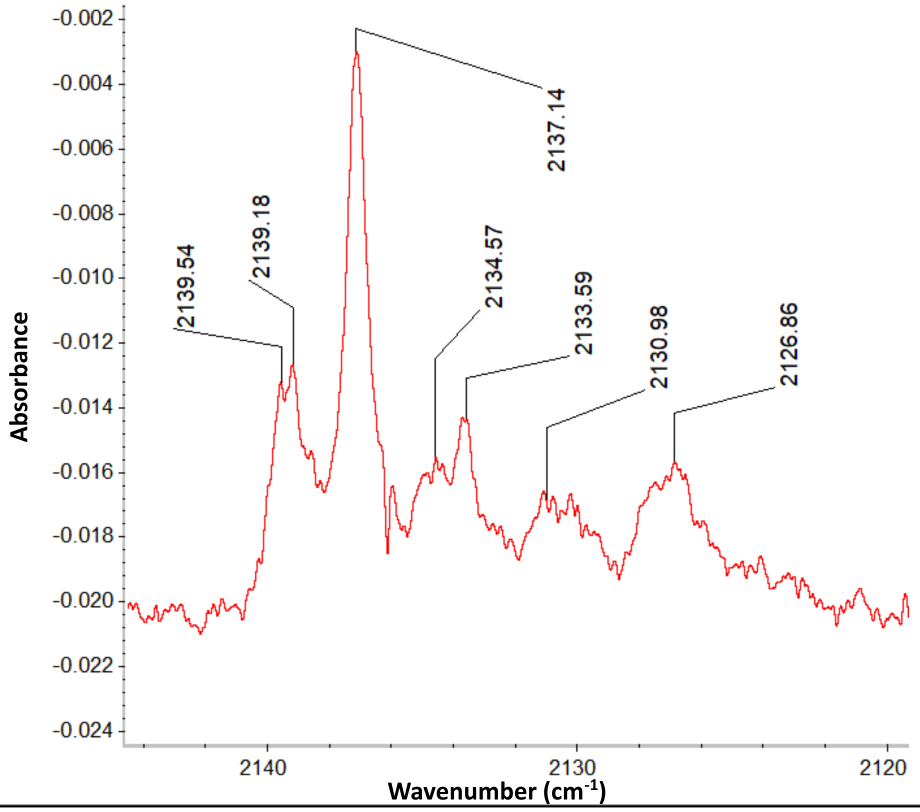

Figure A.29 Section from ~ 2150 – 2120 cm$^{-1}$ of annotated cyclopropylacetylene spectrum.

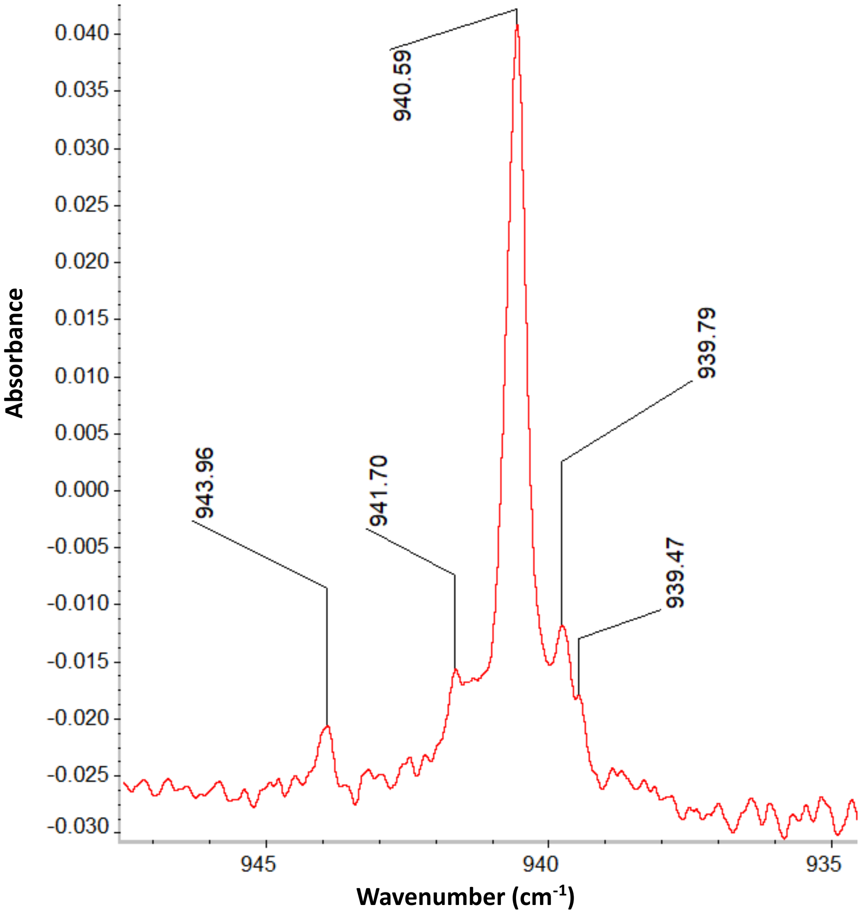

Figure A.30 Section from ~ 950 – 935 cm$^{-1}$ of annotated cyclopropylacetylene spectrum.

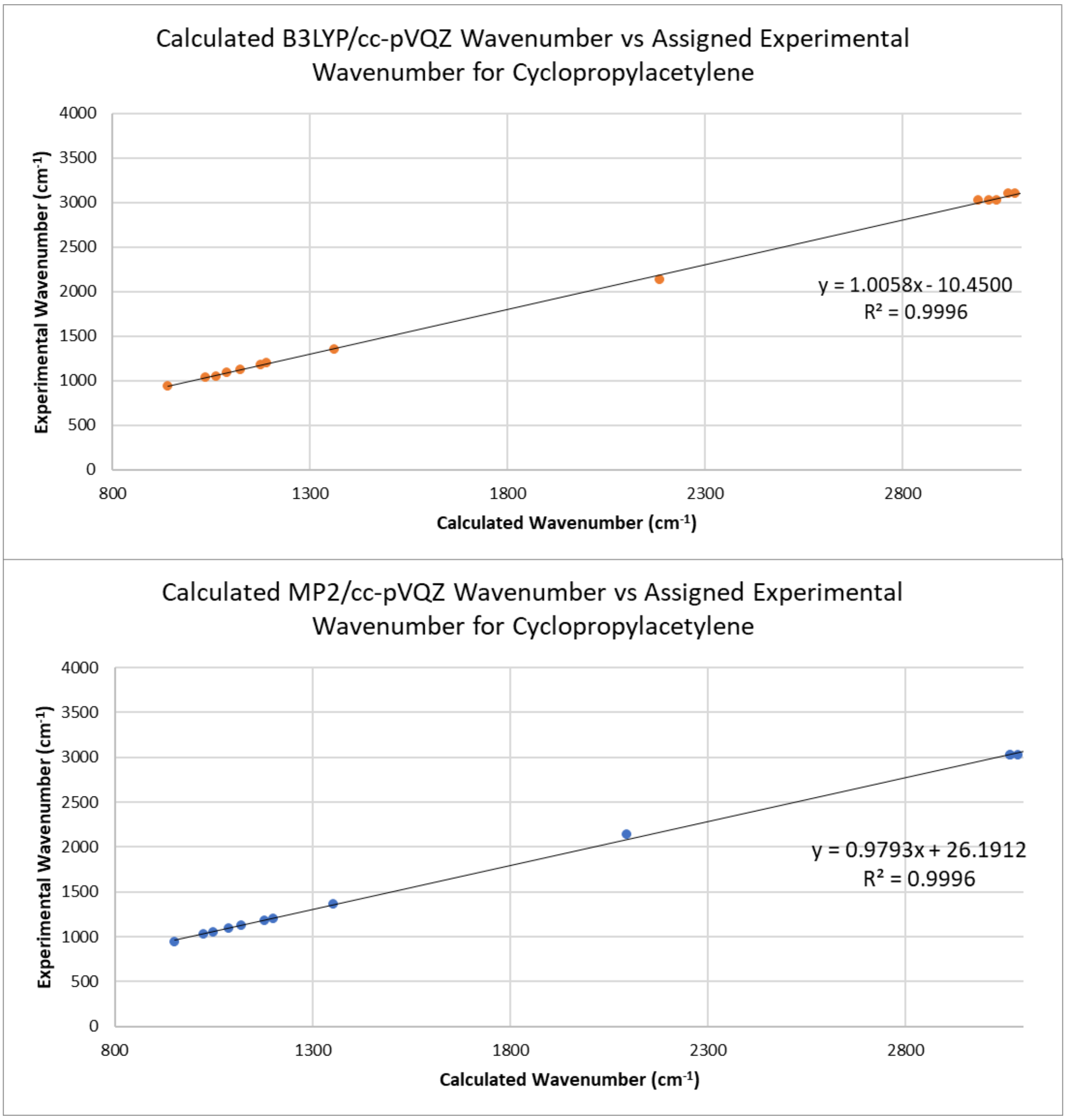

Figure A.31 Comparison graphs for experimental wavenumber versus calculated wavenumber.

Table A.14 Slope, intercept, and standard errors of each for the comparison graphs for cyclopropylacetylene.

| **Value** | **B3LYP** | **MP2** |
|---|---|---|
| m | 1.0058 | 0.9793 |
| c | -10.4500 | 26.1912 |
| Standard error for m | 0.0052 | 0.0052 |
| Standard error for c | 11.4804 | 11.4777 |

## A.8 Ethylene

Table A.15 Table of assigned literature and calculated wavenumbers to experimental data for ethylene. Calculations are anharmonic and at QZ level. Not all calculated or experimental peaks are assigned.

| Literature Wavenumber (cm$^{-1}$)[4] | B3LYP QZ Wavenumber (cm$^{-1}$) | MP2 QZ Wavenumber (cm$^{-1}$) | Experimental | |
|---|---|---|---|---|
| | | | Wavenumber (cm$^{-1}$) | Shape |
| | | 3157.1 | 3163.4 | Sharp |
| 3105.0 | | | 3112.3 | Medium |
| 3086.0 | 3079.6 | 3019.9 | 3083.7 | Very sharp |
| 2988.7 | 2976.8 | | 2996.2 | Very sharp |
| 1622.9 | | | 1624.0 | Medium, split peak |
| 1443.5 | 1444.6 | 1446.2 | 1440.6 | Sharp |
| 1342.2 | | | 1360.9 | Broad, shoulder |
| 1217.0 | | | 1261.7 | Broad |
| | | | 959.4 | Medium |
| 949.3 | 963.5 | 965.2 | 947.1 | Medium |
| 939.6 | | | 945.8 | Medium, shoulder |

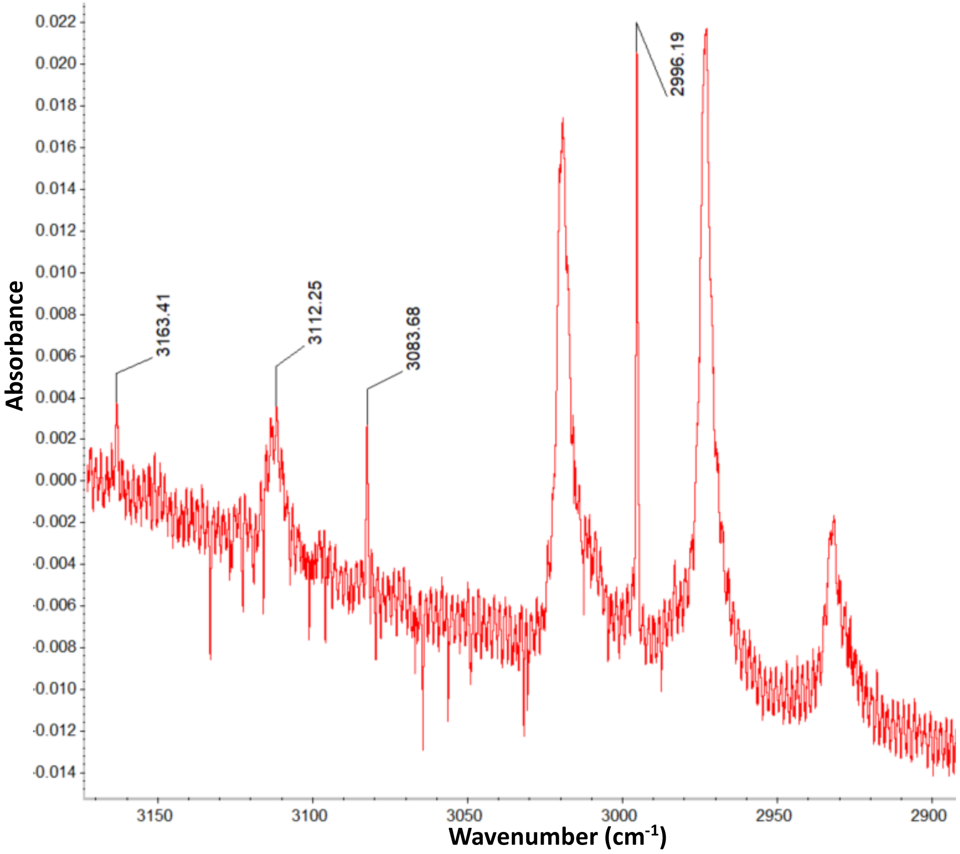

Figure A.32 Section from ~ 3160 – 2900 cm$^{-1}$ of annotated ethylene spectrum.

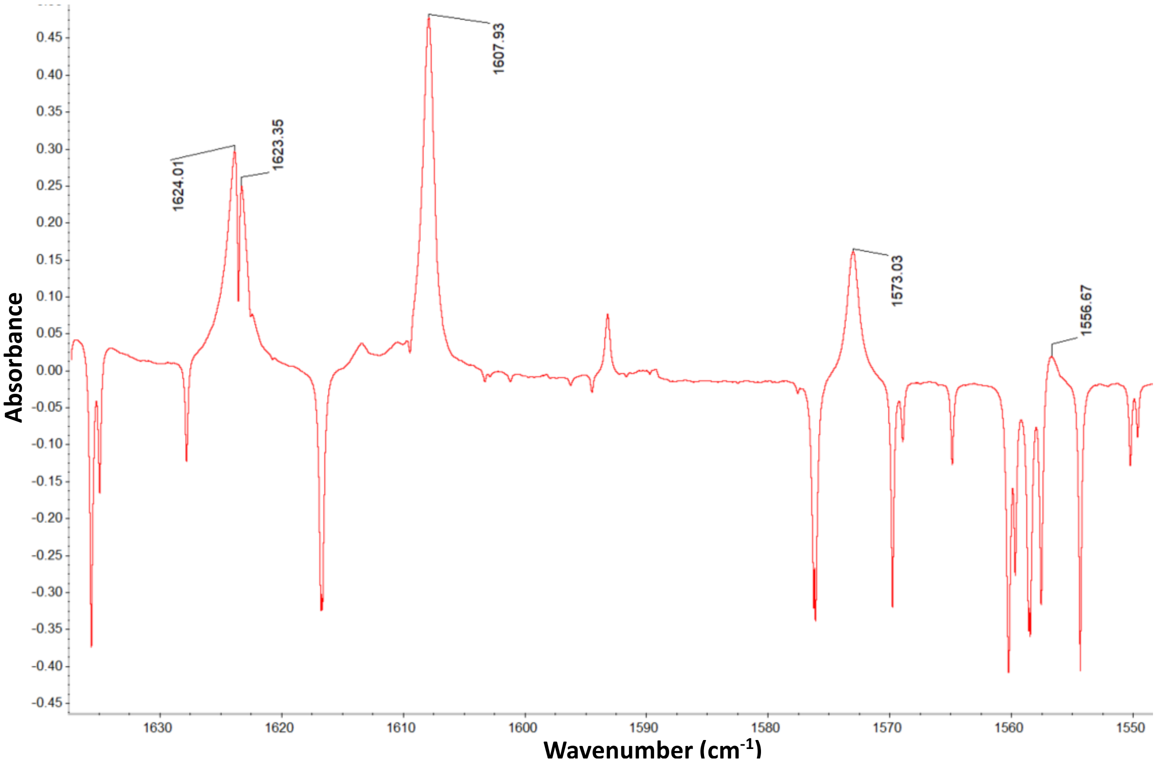

Figure A.33 Section from ~ 1640 – 1540 cm$^{-1}$ of annotated ethylene spectrum.

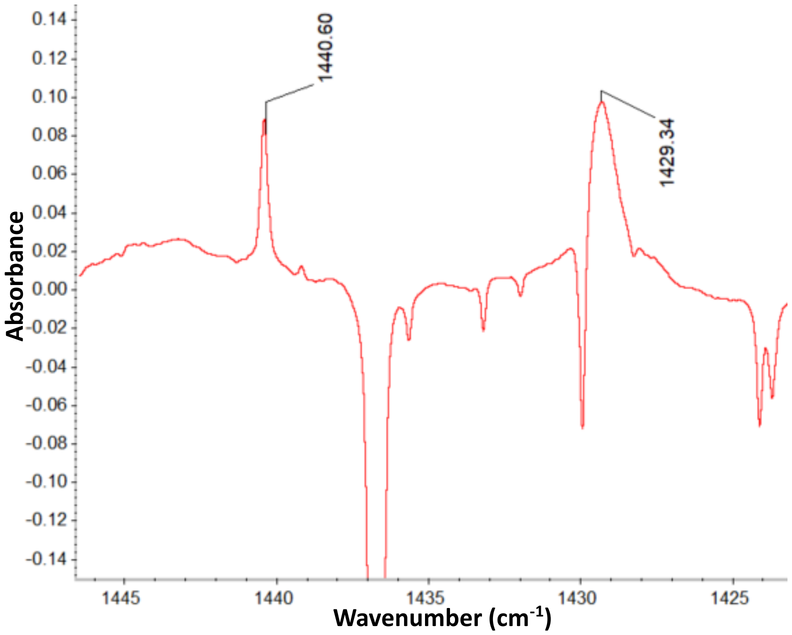

Figure A.34 Section from ~ 1450 – 1420 cm$^{-1}$ of annotated ethylene spectrum.

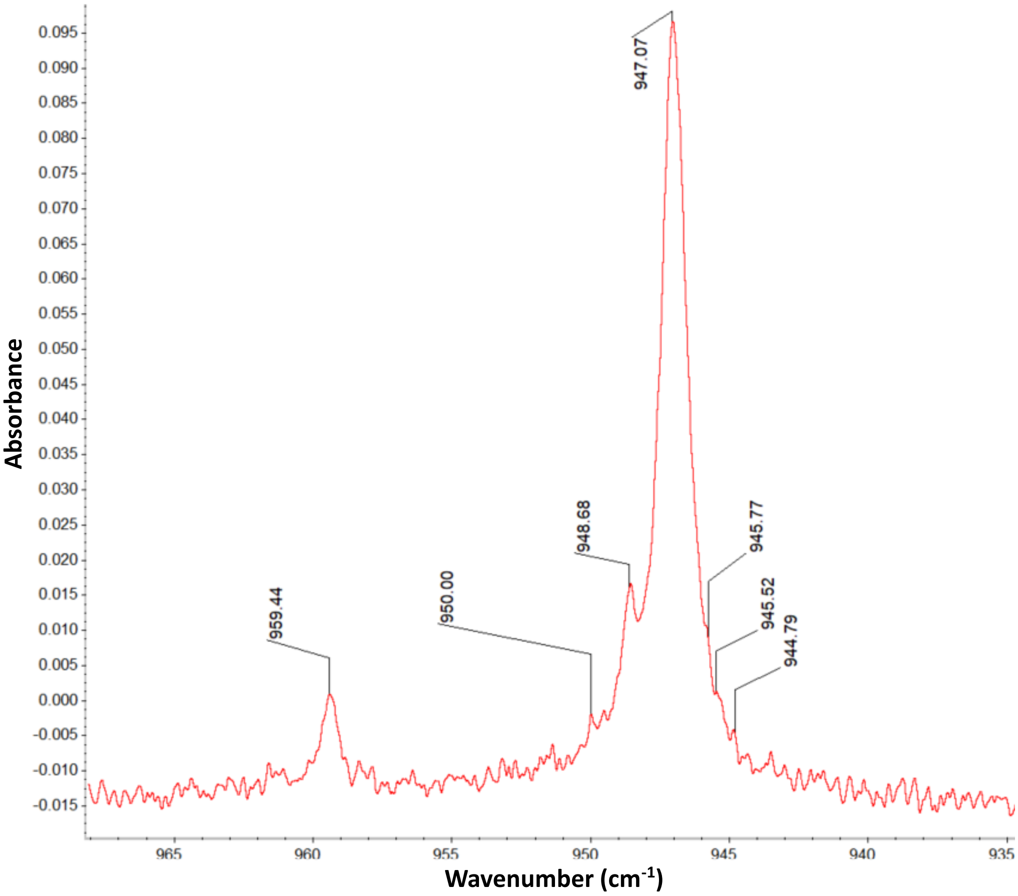

Figure A.35 Section from ~ 970 – 930 cm$^{-1}$ of annotated ethylene spectrum.

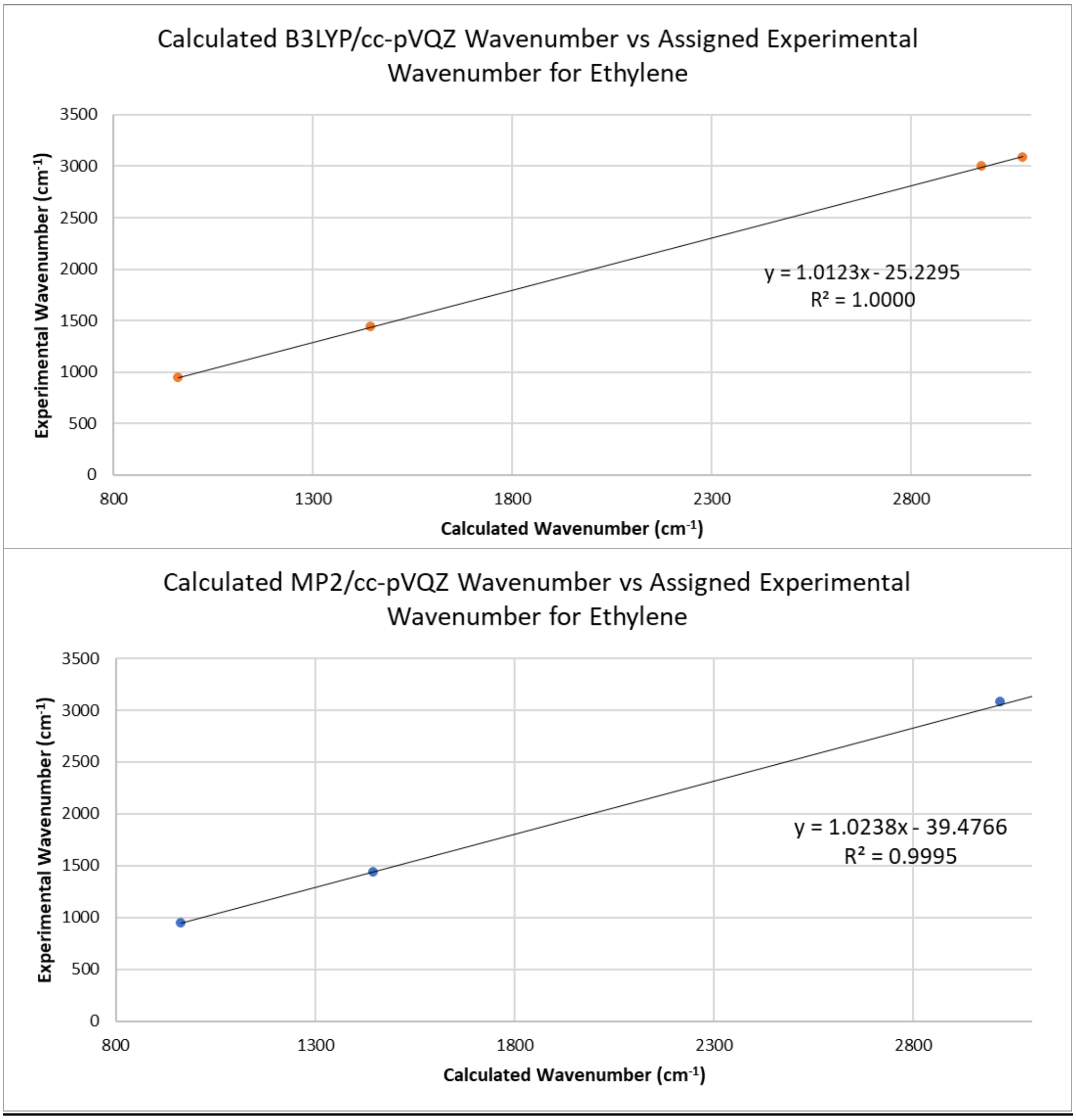
Calculated B3LYP/cc-pVQZ Wavenumber vs Assigned Experimental Wavenumber for Ethylene

Calculated MP2/cc-pVQZ Wavenumber vs Assigned Experimental Wavenumber for Ethylene

Figure A.36 Comparison graphs for experimental wavenumber versus calculated wavenumber.

Table A.16 Slope, intercept, and standard errors of each for the comparison graphs for ethylene.

| Value | B3LYP | MP2 |
|---|---:|---:|
| m | 1.0123 | 1.0238 |
| c | -25.2295 | -39.4766 |
| Standard error for m | 0.0048 | 0.0159 |
| Standard error for c | 11.0800 | 37.3328 |

## A.9 Geraniol

Table A.17 Table of assigned literature and calculated wavenumbers to experimental data for geraniol. Calculations are anharmonic and at DZ level. Not all calculated or experimental peaks are assigned.

| Literature Wavenumber ($cm^{-1}$)[5] | B3LYP DZ Wavenumber ($cm^{-1}$) | MP2 DZ Wavenumber ($cm^{-1}$) | Experimental | |
|---|---|---|---|---|
| | | | Wavenumber ($cm^{-1}$) | Shape |
| | 2974.2 | 2976.9 | 2977.9 | Medium |
| | 2960.5 | 2944.6 | 2942.6 | Medium |
| 2922.16 | 2924.3 | 2924.2 | 2925.2 | Medium |
| | 2891.9 | 2890.6 | 2894.2 | Broad, shoulder |
| | 2862.0 | | 2863.7 | Medium |
| | 2847.3 | | 2846.8 | Broad, shoulder |
| | 2761.1 | | 2736.9 | Broad |
| 1234.44 | 1250.9 | 1276.1 | 1267.1 | Medium, shoulder |
| | 1192.3 | 1187.2 | 1181.1 | Very broad |
| | 1167.1 | | 1168.9 | Very broad |
| | 1161.7 | 1152.2 | 1160.1 | Very broad |
| | | 1126.2 | 1128.2 | Broad |
| | 1101.9 | | 1109.6 | Broad |
| 1099.43 | | 1097.1 | 1096.4 | Broad |
| | 1074.9 | | 1084.3 | Broad |
| | 1052.6 | 1052.2 | 1049.2 | Broad |
| | 1041.9 | 1044.4 | 1032.7 | Broad, shoulder |
| 1004.93 | 1017.8 | 1016.1 | 1010.2 | Broad |
| | 980.7 | 988.7 | 989.4 | Medium |
| | 978.5 | 984.4 | 974.5 | Broad, shoulder |
| | 934.7 | 954.5 | 951.0 | Broad |
| | 877.7 | | 893.9 | Medium |

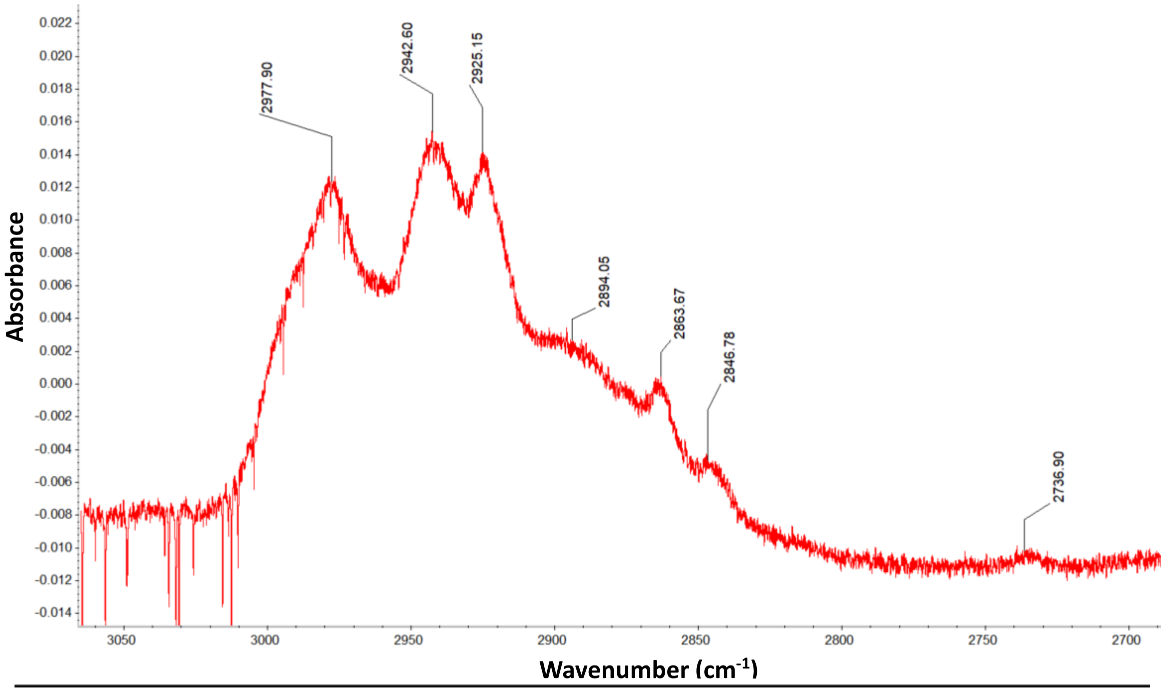

Figure A.38 Section from ~ 3050 – 2700 cm$^{-1}$ of annotated geraniol spectrum.

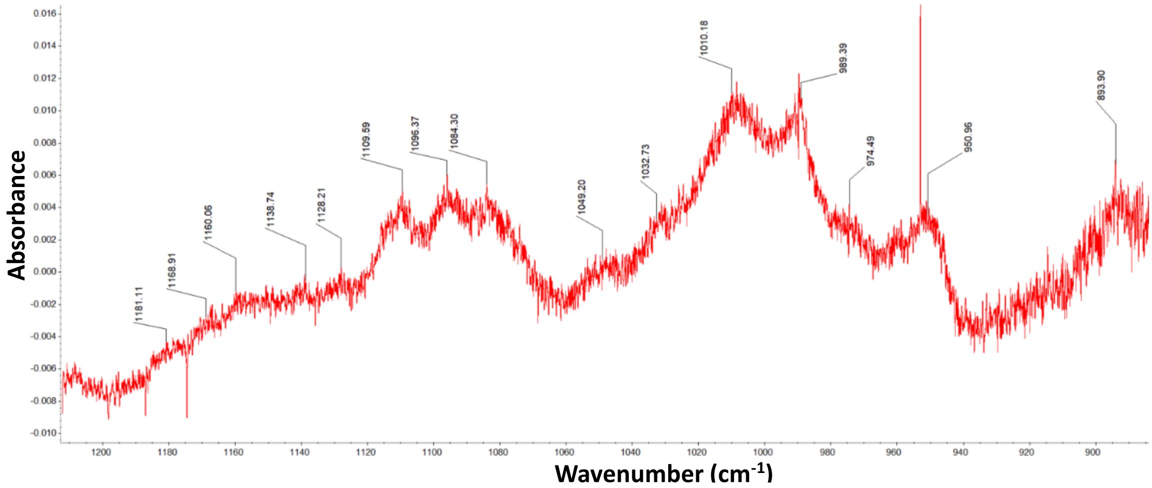

Figure A.37 Section from ~ 1200 – 900 cm$^{-1}$ of annotated geraniol spectrum.

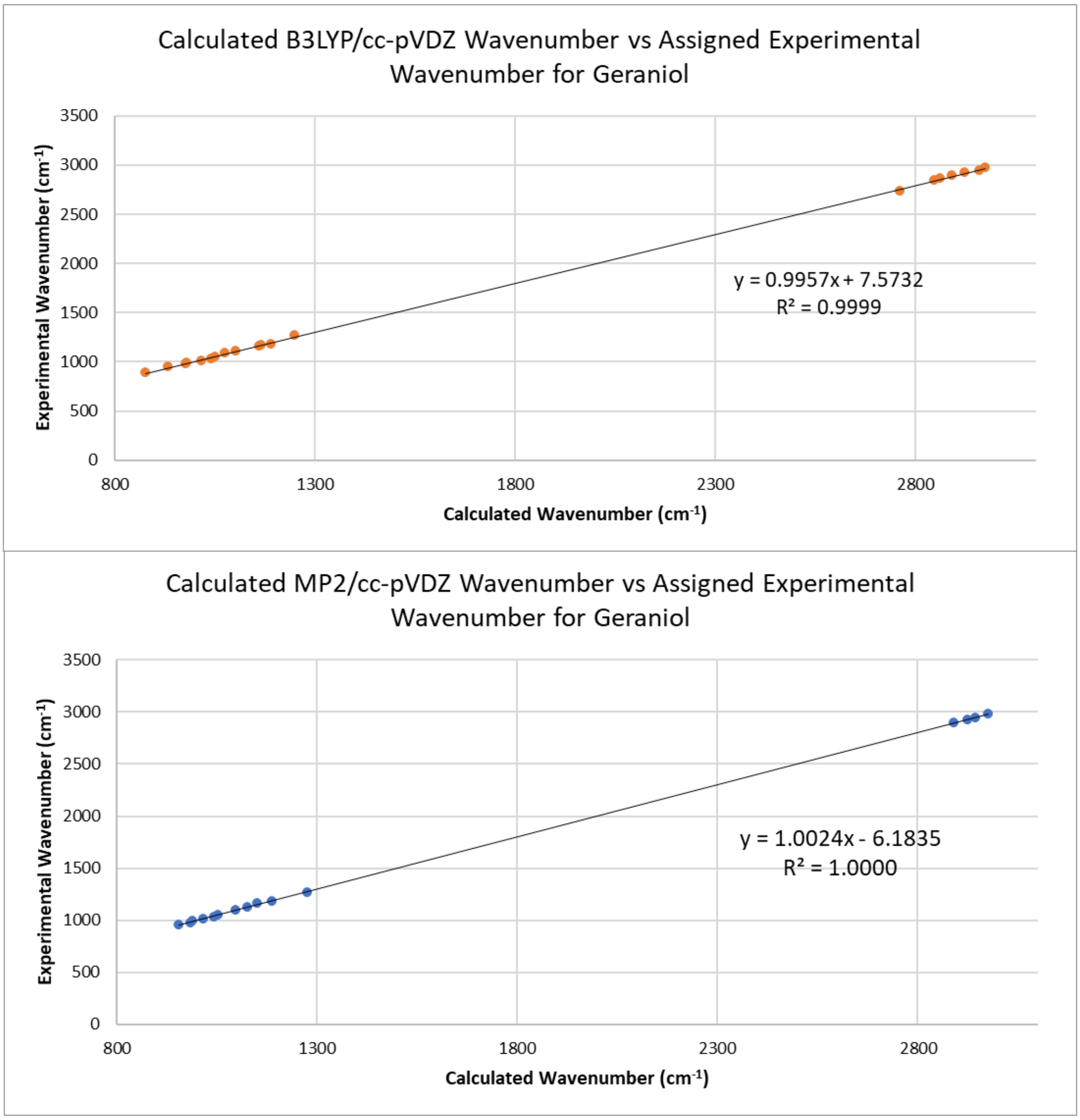

Figure A.39 Comparison graphs for experimental wavenumber versus calculated wavenumber.

Table A.18 Slope, intercept, and standard errors of each for the comparison graphs for geraniol.

| Value | B3LYP | MP2 |
|---|---|---|
| m | 0.9957 | 1.0024 |
| c | 7.5732 | -6.1835 |
| Standard error for m | 0.0027 | 0.0016 |
| Standard error for c | 5.1129 | 2.8833 |

## A.10 Isoprene

Table A.19 Table of assigned literature and calculated wavenumbers to experimental data for isoprene. Calculations are anharmonic and at QZ level. Not all calculated or experimental peaks are assigned.

| Literature Wavenumber (cm$^{-1}$)[1] | B3LYP QZ Wavenumber (cm$^{-1}$) | MP2 QZ Wavenumber (cm$^{-1}$) | Experimental | |
|---|---|---|---|---|
| | | | **Wavenumber (cm$^{-1}$)** | **Shape** |
| 3095 | | 3099.3 | 3109.2 | Medium |
| 3095 | 3089.8 | 3090.8 | 3096.7 | Broad |
| | 3079.6 | | 3072.1 | Broad |
| | | 3041.8 | 3034.8 | Broad |
| 3000 | 3003.9 | 3007.1 | 3028.6 | Sharp |
| 3000 | 2991.8 | 3001.9 | 2991.0 | Sharp |
| 3000 | 2974.8 | 2972.5 | 2983.6 | Sharp |
| | 2968.9 | | 2954.4 | Sharp |
| | 2932.2 | | 2935.2 | Sharp |
| | 2906.9 | | 2913.2 | Sharp |
| 1607 | 1654.2 | 1608.3 | 1605.0 | Sharp |
| | 1612.7 | | 1599.5 | Sharp |
| 1464 | | 1471.0 | 1463.3 | Medium |
| 1451 | 1465.7 | 1447.4 | 1440.4 | Medium |
| 1420 | 1433.1 | 1425.8 | 1426.3 | Broad |
| | 1424.6 | | 1424.5 | Broad |
| 1389 | | 1398.6 | 1407.6 | Sharp |
| | 1385.7 | | 1384.9 | Broad |
| | 1376.8 | | 1374.9 | Broad |
| | | 1371.9 | 1374.1 | Broad |
| 1313 | | | 1315.3 | Sharp |
| 1303 | | 1309.0 | 1312.0 | Sharp |
| | 1299.3 | | 1296.6 | Sharp |
| | 1290.0 | 1293.3 | 1292.8 | Sharp |
| 1072 | 1070.6 | 1066.9 | 1067.7 | Medium |
| | 1045.3 | 1010.8 | 1000.6 | Broad, shoulder |
| 991 | 1000.2 | 996.5 | 999.2 | Sharp |
| | 1000.8 | | 994.6 | Broad, shoulder |
| | | 956.7 | 988.9 | Sharp |
| | 941.1 | | 949.6 | Broad |
| | | 917.0 | 916.1 | Broad |
| | 921.4 | | 909.2 | Broad, shoulder |
| | 921.3 | | 908.5 | Sharp |
| 907 | | 907.8 | 903.3 | Sharp |

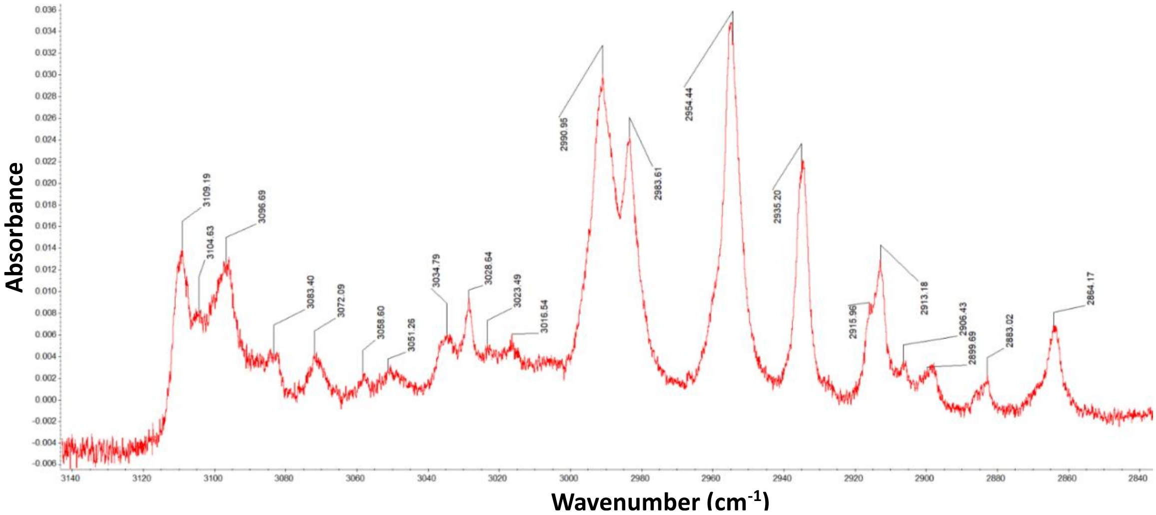

Figure A.40 Section from ~ 3140 – 2840 cm$^{-1}$ of annotated isoprene spectrum.

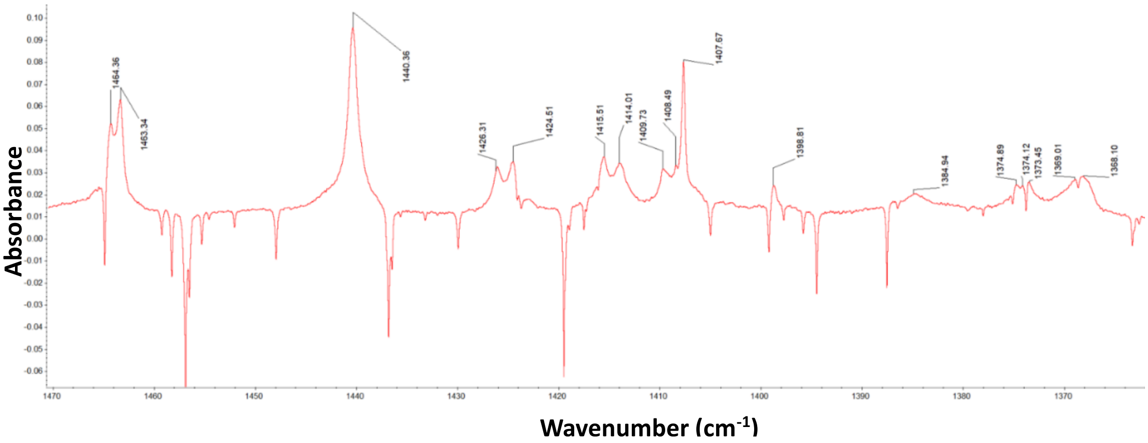

Figure A.41 Section from ~ 1470 – 1360 cm$^{-1}$ of annotated isoprene spectrum.

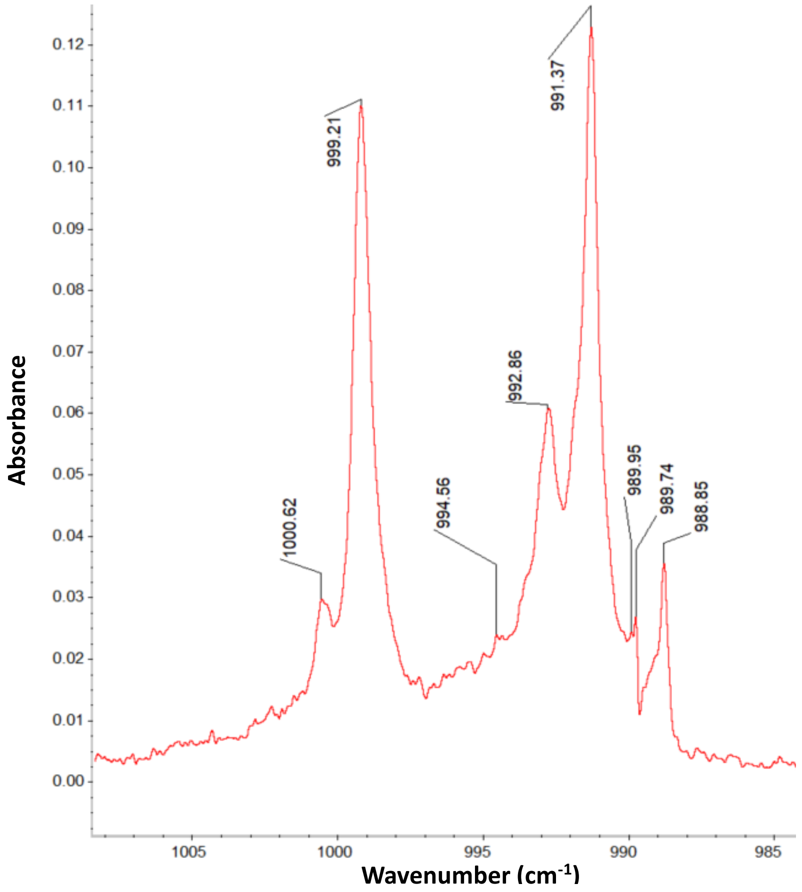

Figure A.42 Section from ~ 1005 - 985 cm$^{-1}$ of annotated isoprene spectrum.

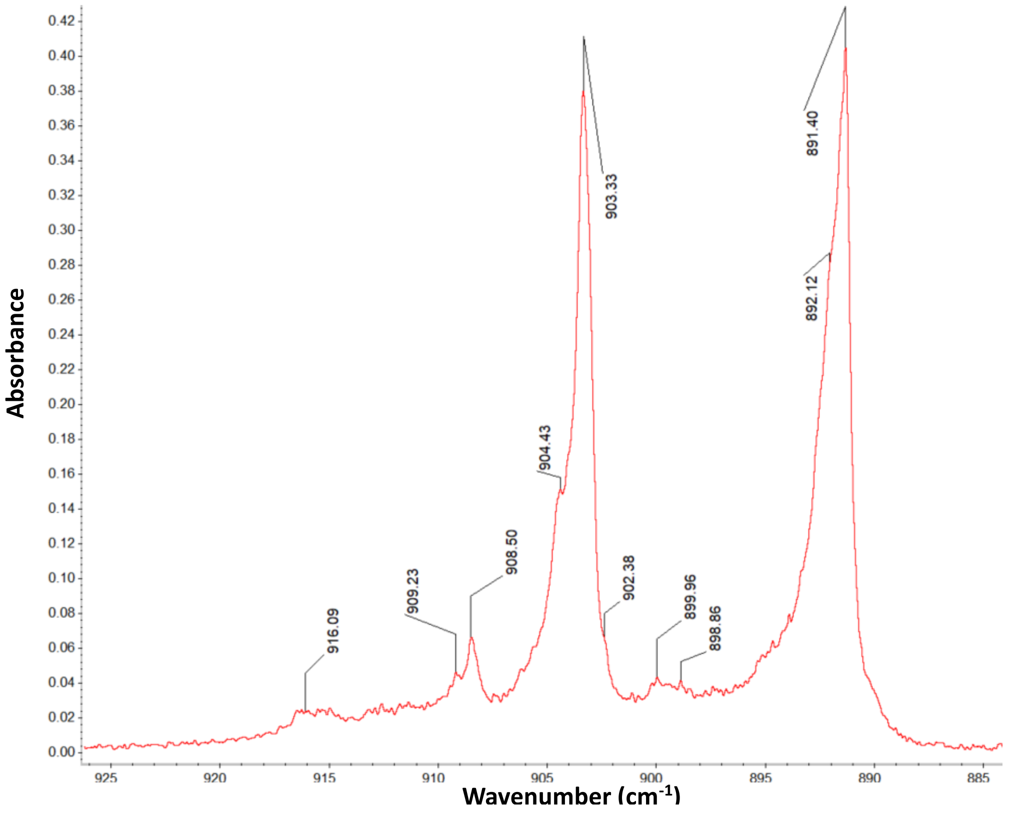

Figure A.43 Section from ~ 925 - 885 cm$^{-1}$ of annotated isoprene spectrum.

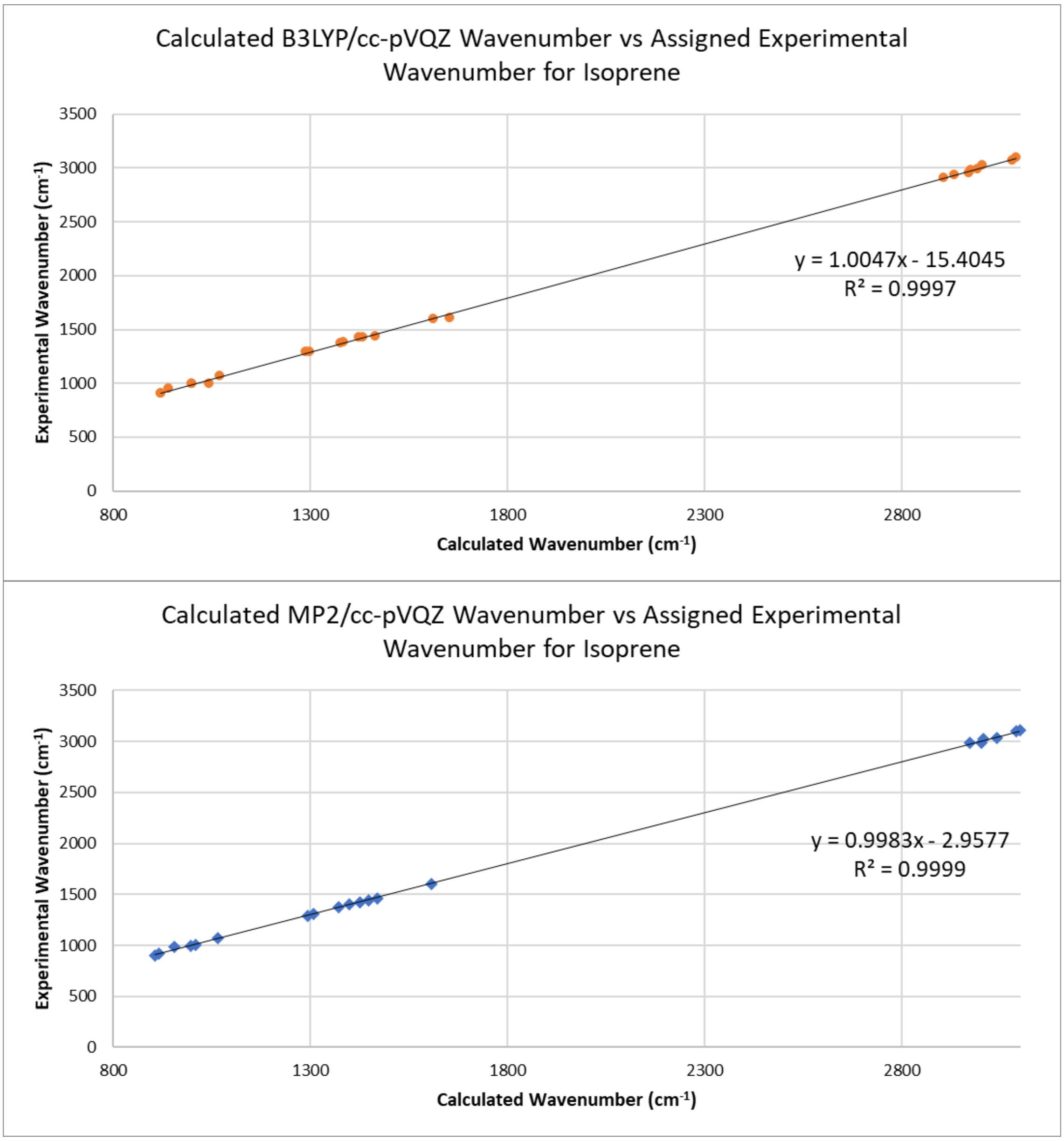

Figure A.44 Comparison graphs for experimental wavenumber versus calculated wavenumber.

Table A.20 Slope, intercept, and standard errors of each for the comparison graphs for isoprene.

| Value | B3LYP | MP2 |
|---|---|---|
| m | 1.0047 | 0.9983 |
| c | -15.4045 | 2.9577 |
| Standard error for m | 0.0035 | 0.0026 |
| Standard error for c | 7.0989 | 5.0174 |

## A.11 Limonene

Table A.21 Table of assigned literature and calculated wavenumbers to experimental data for limonene. Calculations are anharmonic and at TZ level. Not all calculated or experimental peaks are assigned.

| B3LYP TZ Wavenumber (cm$^{-1}$) | MP2 TZ Wavenumber (cm$^{-1}$) | Experimental Wavenumber (cm$^{-1}$) | Shape |
|---|---|---|---|
| 3084.9 | 3141.7 | 3100.6 | Sharp, split peak |
|  | 3054.5 | 3046.6 | Sharp |
|  | 3034.8 | 3036.6 | Sharp |
|  | 3024.2 | 3024.2 | Sharp |
|  | 3024.8 |  |  |
| 3001.0 | 3015.9 | 3021.2 | Sharp |
| 2972.1 | 2963.1 | 2975.9 | Broad |
| 2946.6 | 2950.8 | 2944.3 | Broad |
| 2926.7 | 2922.4 | 2926.1 | Broad |
| 2907.9 |  | 2907.5 | Broad |
| 2844.7 | 2895.7 | 2848.3 | Broad |
| 1428.3 | 1437.8 | 1431.0 | Sharp |
| 1288.4 | 1284.3 | 1287.7 | Sharp, split peak |
| 1235.6 | 1239.9 | 1216.6 | Sharp |
| 1198.3 | 1197.1 | 1192.2 | Sharp |
|  | 1162.5 | 1174.7 | Sharp |
| 1146.4 | 1123.2 | 1122.5 | Sharp |
| 1094.5 |  | 1094.3 | Sharp |
| 1083.0 | 1086.1 | 1089.4 | Sharp |
| 1056.1 | 1058.9 | 1053.2 | Sharp |
| 1035.4 | 1038.6 | 1034.4 | Broad |
|  | 1029.4 | 1032.5 | Sharp |
|  | 1022.9 | 1031.7 | Sharp |
| 998.4 | 986.3 | 951.9 | Broad |
| 955.4 | 962.9 | 940.5 | Sharp |
| 925.5 | 923.5 | 939.8 | Sharp, shoulder |
| 895.7 | 891.4 | 891.2 | Broad |
| 878.8 |  | 880.3 | Sharp |
| 816.5 | 817.8 | 815.2 | Sharp |

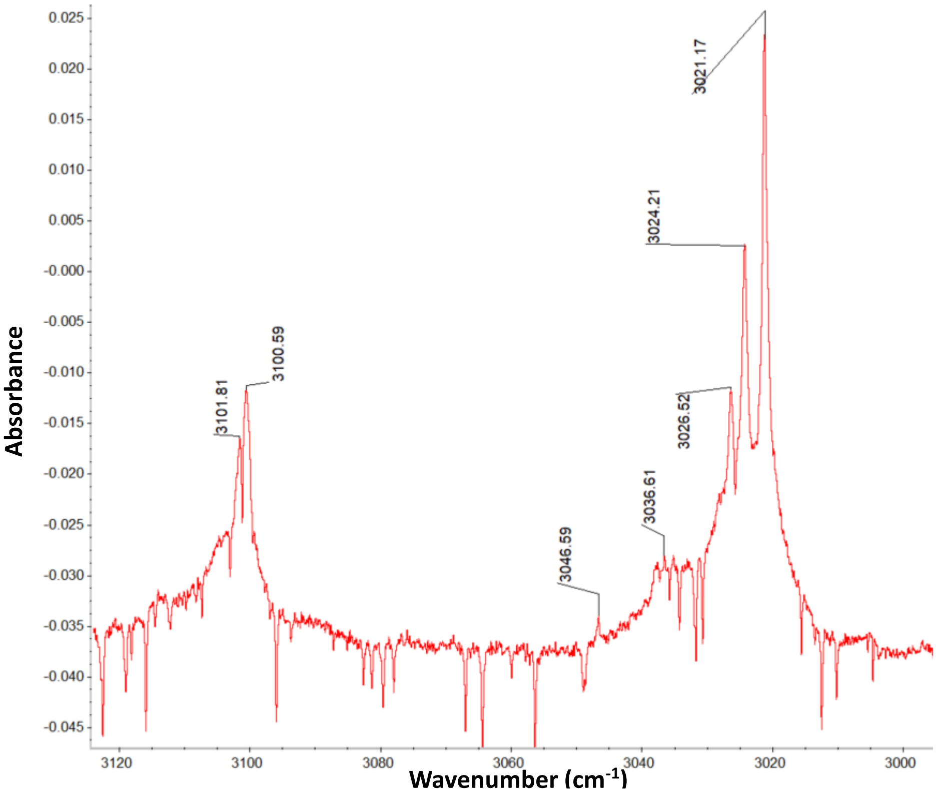

Figure A.45 Section from ~ 3120 - 3000 cm$^{-1}$ of annotated limonene spectrum.

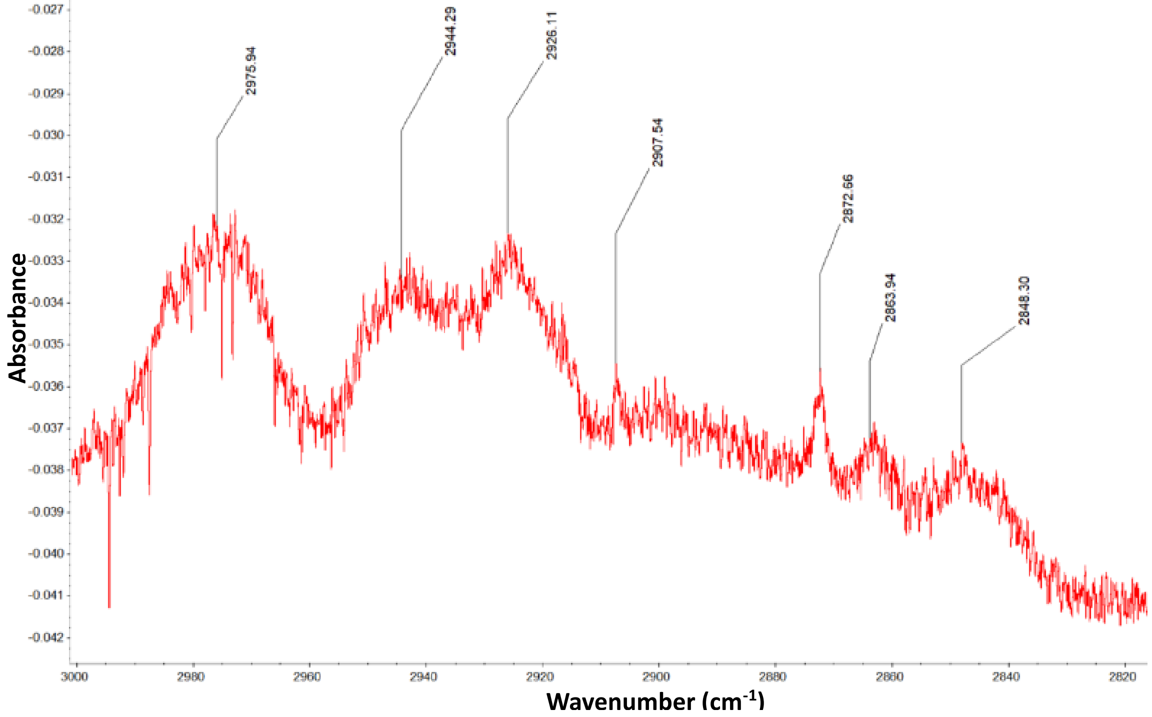

Figure A.46 Section from ~ 3000 - 2800 cm$^{-1}$ of annotated limonene spectrum.

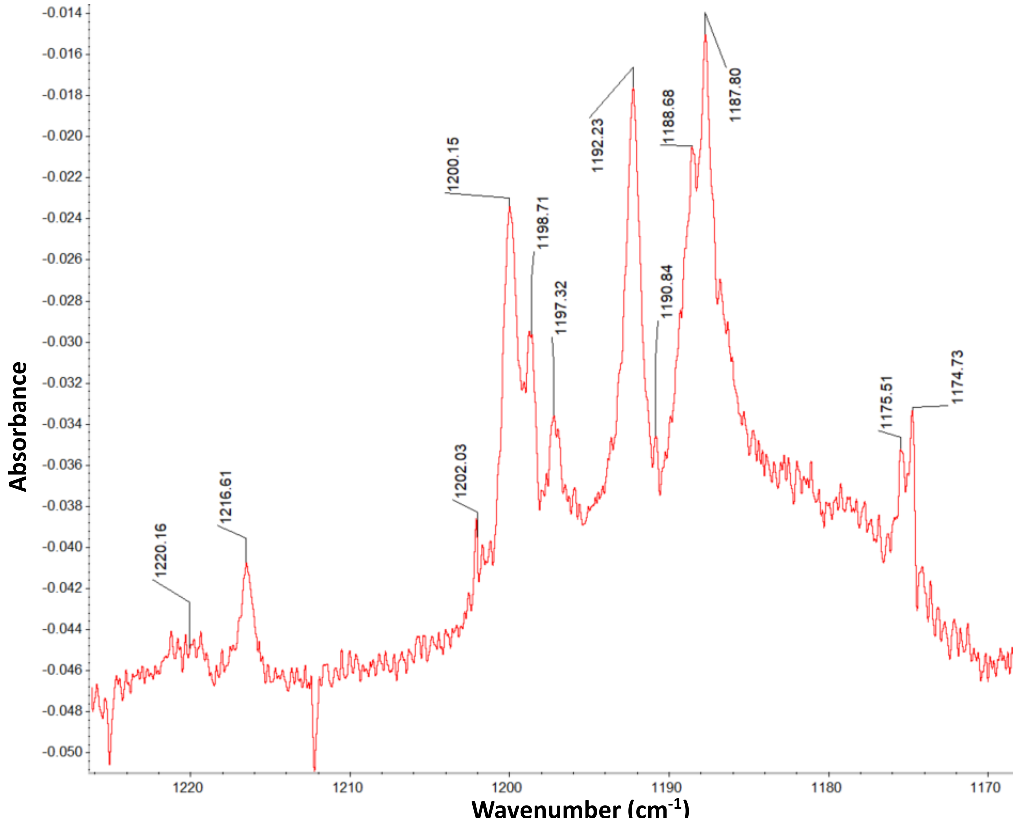

Figure A.47 Section from ~ 1230 - 1170 cm$^{-1}$ of annotated limonene spectrum.

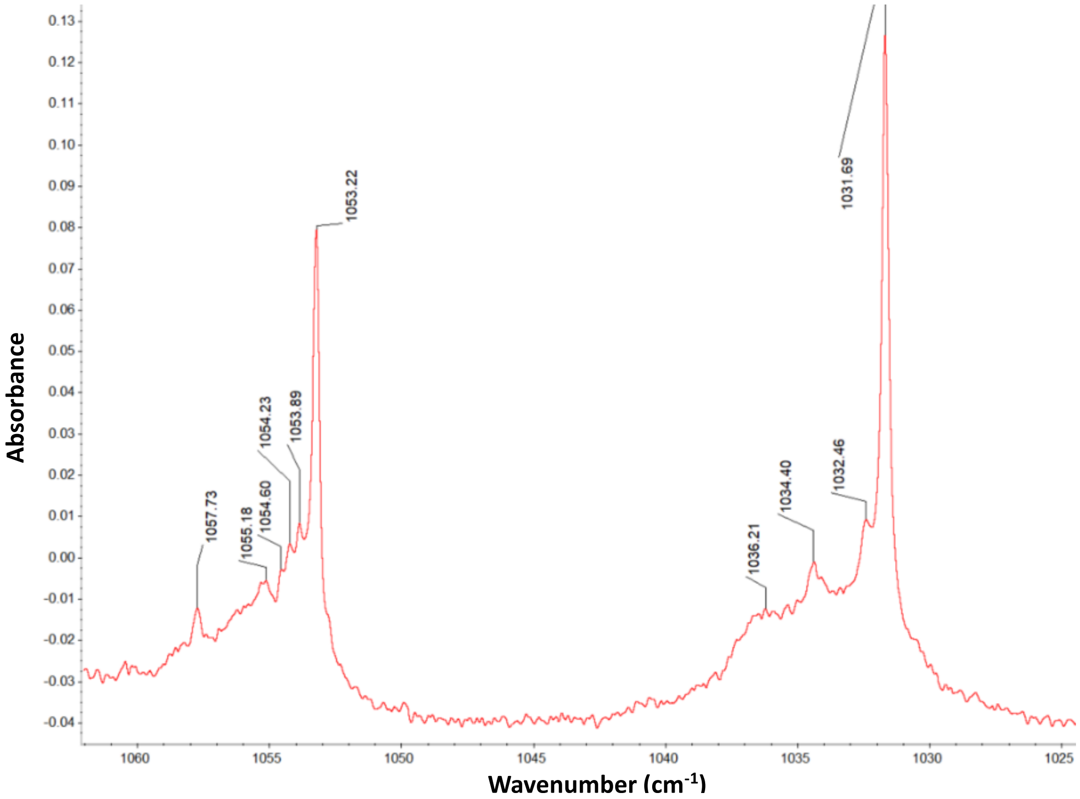

Figure A.48 Section of ~ 1060 - 1025 cm$^{-1}$ of annotated limonene spectrum.

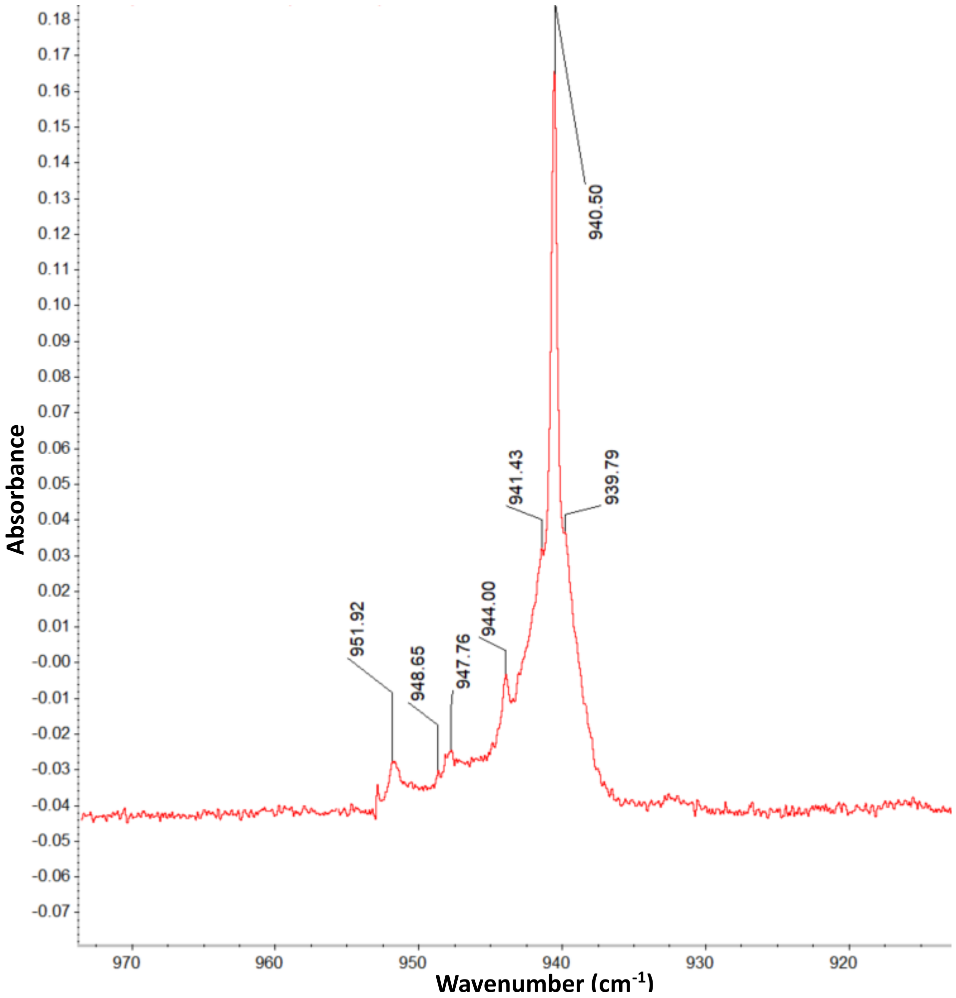

Figure A.49 Section from ~ 970 - 920 cm$^{-1}$ of annotated limonene spectrum.

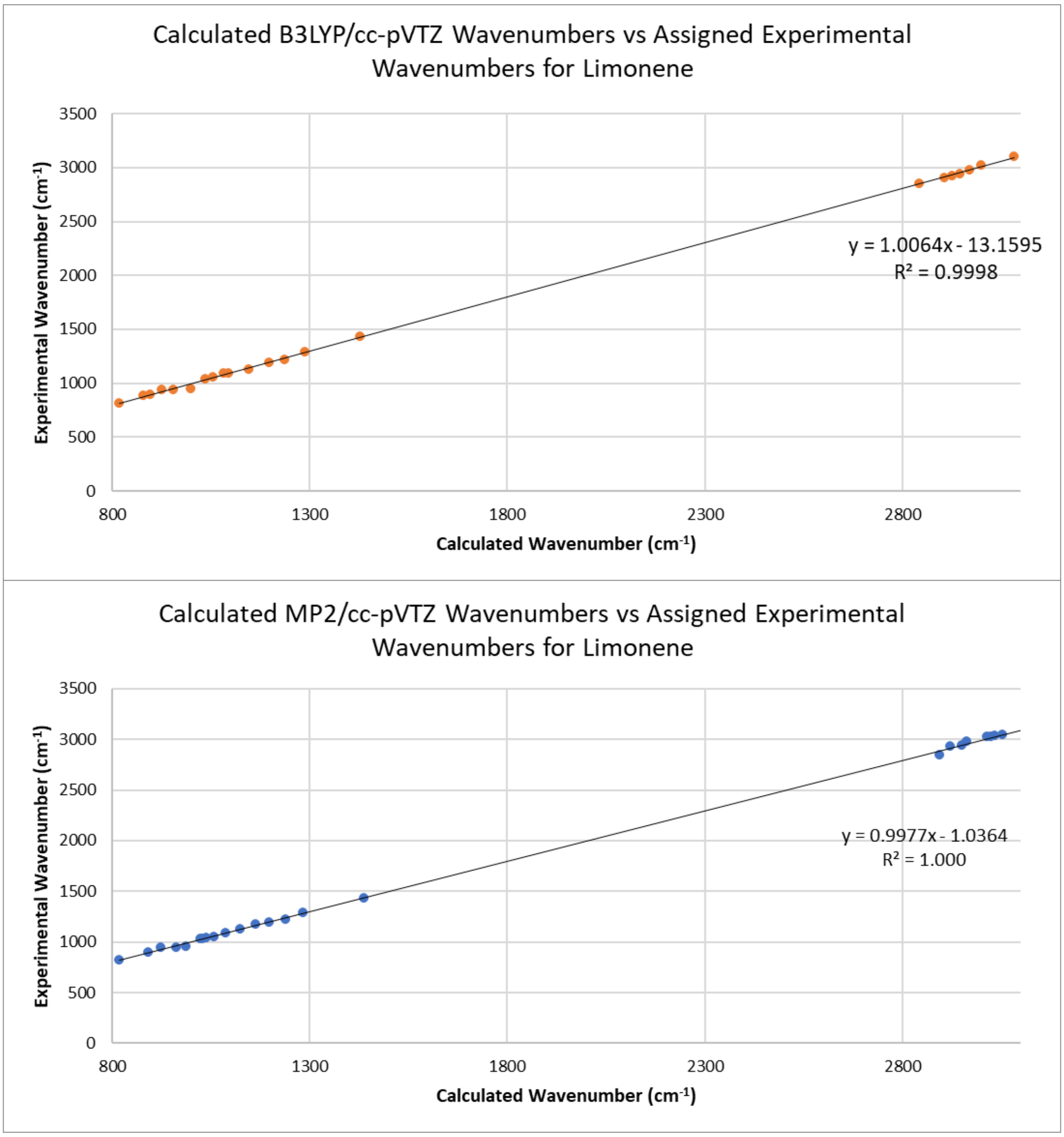

Figure A.50 Comparison of experimental versus calculated wavenumber for limonene.

Table A.22 Slope, intercept, and standard errors of each for the comparison graphs for limonene.

| Value | B3LYP | MP2 |
|---|---|---|
| m | 1.0064 | 0.9977 |
| c | -13.1595 | -1.0364 |
| Standard error for m | 0.0032 | 0.0034 |
| Standard error for c | 5.9767 | 6.8776 |

## A.12 Methacrolein

Wang et al. (1993) noted that methacrolein has two conformers, AP and SP as shown in Figure A.51, which have some differing vibrational peaks.[6] Both conformers have been calculated and data for both is given below.

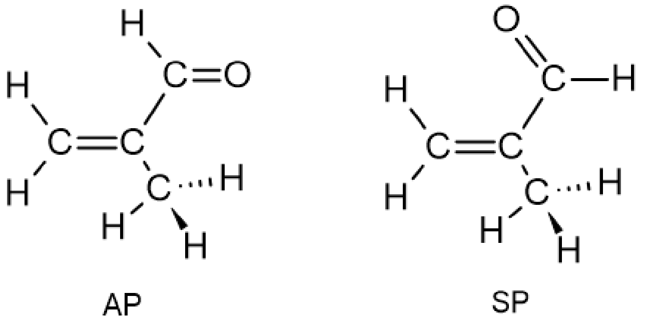

Figure A.51 Conformers of methacrolein. Reproduced from Wang et al. (1993).[6]

Table A.23 Table of assigned literature and calculated wavenumbers to experimental data for the AP conformer of methacrolein. Calculations are anharmonic and at QZ level. Not all calculated or experimental peaks are assigned.

| Literature AP Wavenumber ($cm^{-1}$)[6] | B3LYP QZ Wavenumber ($cm^{-1}$) | MP2 QZ Wavenumber ($cm^{-1}$) | Experimental | |
|---|---|---|---|---|
| | | | Wavenumber ($cm^{-1}$) | Shape |
| 3092 | 3076.7 | | 3092.4 | Sharp |
| | | 3046.5 | 3037.4 | Broad |
| 2993 | 2992.8 | | 2985.3 | Sharp |
| 2971 | 2978.0 | 2973.9 | 2969.2 | Sharp |
| 2941 | 2934.4 | | 2937.8 | Sharp |
| 2820 | | 2813.0 | 2822.1 | Sharp |
| 1718 | 1739.7 | | 1711.4 | Sharp |
| | | 1708.6 | 1707.8 | Sharp |
| 1640 | 1657.8 | 1644.1 | 1640.0 | Broad |
| | | 1461.9 | 1460.4 | Sharp |
| 1455 | 1455.2 | 1456.9 | 1450.7 | Sharp |
| 1427 | 1427.9 | 1436.5 | 1426.6 | Broad |
| 1387 | 1386.1 | 1382.8 | 1382.1 | Sharp |
| 1364 | 1357.4 | 1357.0 | 1356.5 | Broad |
| 1310 | | 1315.9 | 1310.3 | Sharp |
| 1054 | 1060.6 | 1055.5 | 1050.6 | Broad |
| 1018 | 1019.6 | 1020.6 | 1015.0 | Sharp |
| 995 | 995.6 | 996.0 | 990.4 | Broad |
| 963 | 959.5 | 966.4 | 961.4 | Sharp, shoulder |
| 957 | 958.5 | 945.8 | 952.6 | Broad, shoulder |
| | 809.9 | 821.6 | 816.5 | Sharp |

Table A.24 Table of assigned literature and calculated wavenumbers to experimental data for the SP conformer of methacrolein. Calculations are anharmonic and at QZ level. Not all calculated or experimental peaks are assigned.

| Literature SP Wavenumber ($cm^{-1}$)[6] | B3LYP QZ Wavenumber ($cm^{-1}$) | MP2 QZ Wavenumber ($cm^{-1}$) | Experimental | |
|---|---|---|---|---|
| | | | Wavenumber ($cm^{-1}$) | Shape |
| 3092 | 3088.1 | 3074.0 | 3092.4 | Sharp |
| | | 3044.1 | 3037.4 | Broad |
| | 2999.2 | 3005.8 | 2985.3 | Sharp |
| 2971 | 2975.0 | 2973.3 | 2969.2 | Sharp |
| 2971 | | | | |
| 2903 | | | 2902.3 | Broad |
| 2820 | | | 2822.1 | Sharp |
| | 2674.9 | 2742.9 | 2749.6 | Broad |
| 1717 | 1754.8 | 1717.6 | 1711.4 | Sharp |
| 1640 | 1639.0 | 1641.4 | 1640.0 | Broad |
| 1478 | 1454.2 | 1467.9 | 1460.4 | Sharp |
| | 1448.4 | 1458.6 | 1450.7 | Sharp |
| 1427 | 1434.0 | 1422.2 | 1426.6 | Broad |
| 1387 | 1386.5 | 1383.1 | 1382.1 | Sharp |
| 1375 | 1379.4 | | 1378.2 | Sharp |
| | 1245.9 | 1263.7 | 1235.7 | Broad |
| 1054 | 1062.5 | 1057.9 | 1050.6 | Broad |
| 1025 | 1008.2 | | 1015.0 | Sharp |
| 995 | 995.5 | 996.1 | 990.4 | Broad |
| 967 | 971.5 | | 969.8 | Broad |
| | | 960.7 | 960.1 | Sharp |
| 950 | 940.2 | 955.5 | 935.5 | Sharp |
| 850 | 864.9 | 873.4 | 889.2 | Broad |

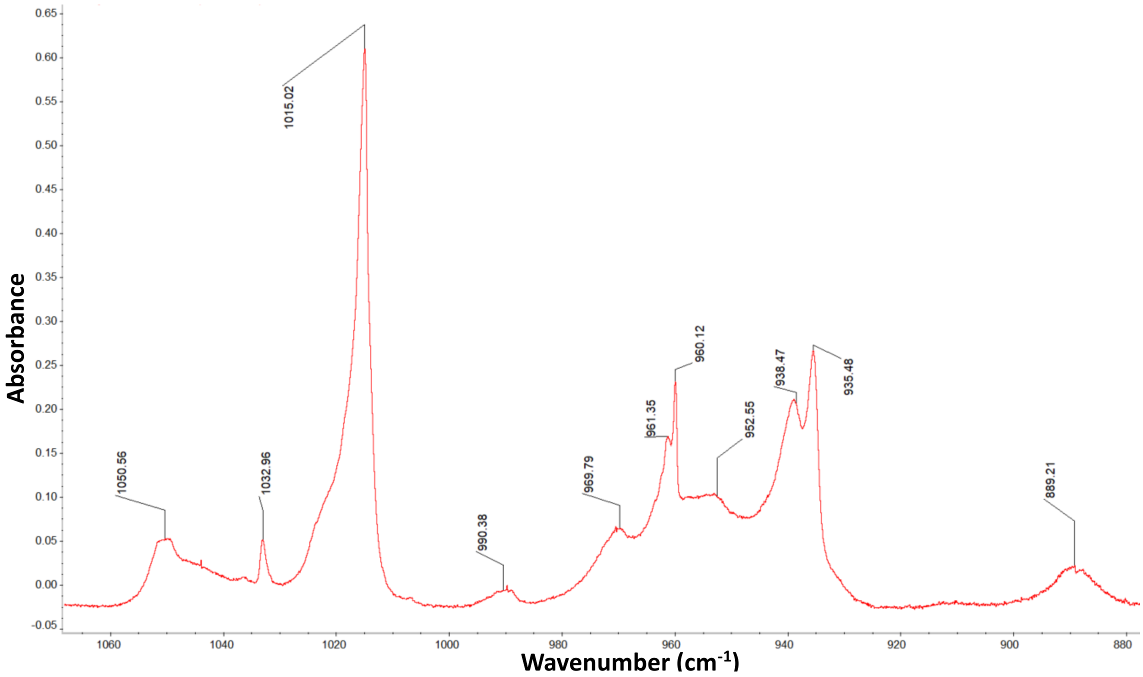

Figure A.52 Section from ~ 1100 - 850 cm$^{-1}$ of annotated methacrolein spectrum.

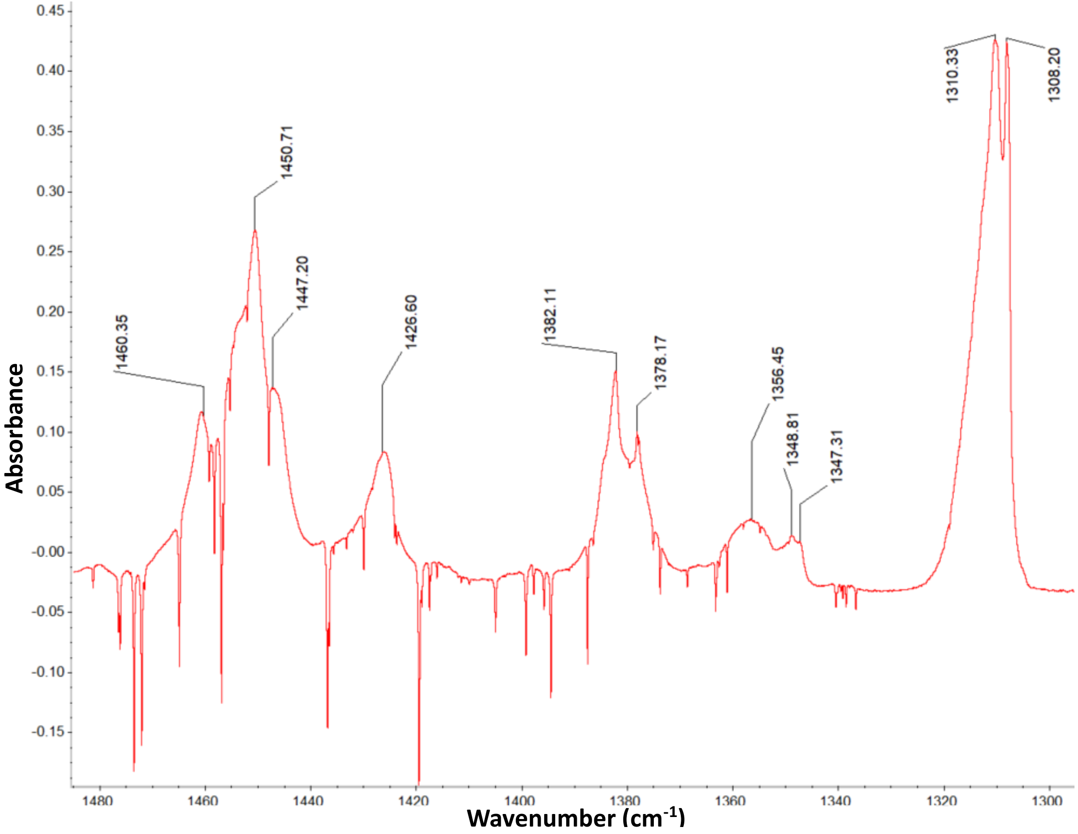

Figure A.53 Section from ~ 1500 - 1300 cm$^{-1}$ of annotated methacrolein spectrum.

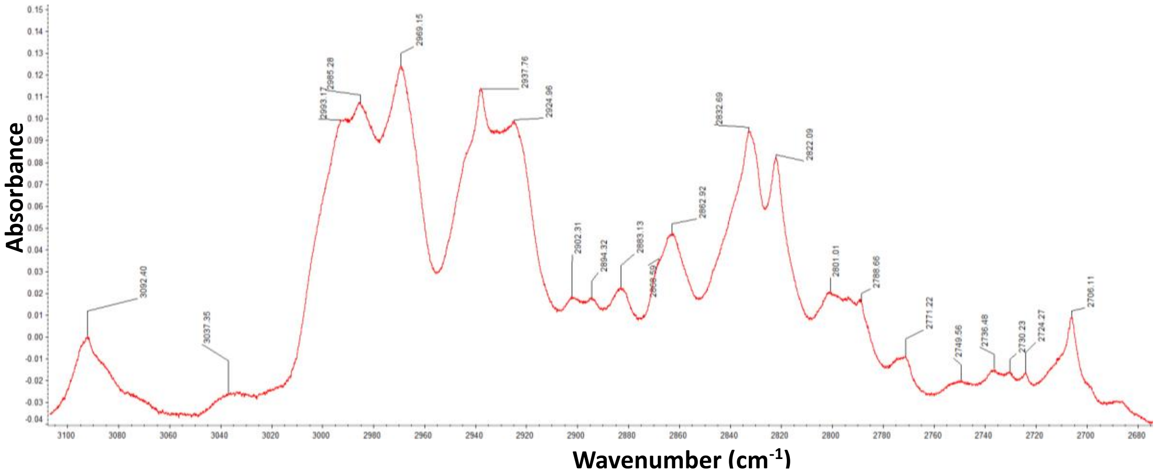

Figure A.54 Section from ~ 3100 - 2700 cm$^{-1}$ of annotated methacrolein spectrum.

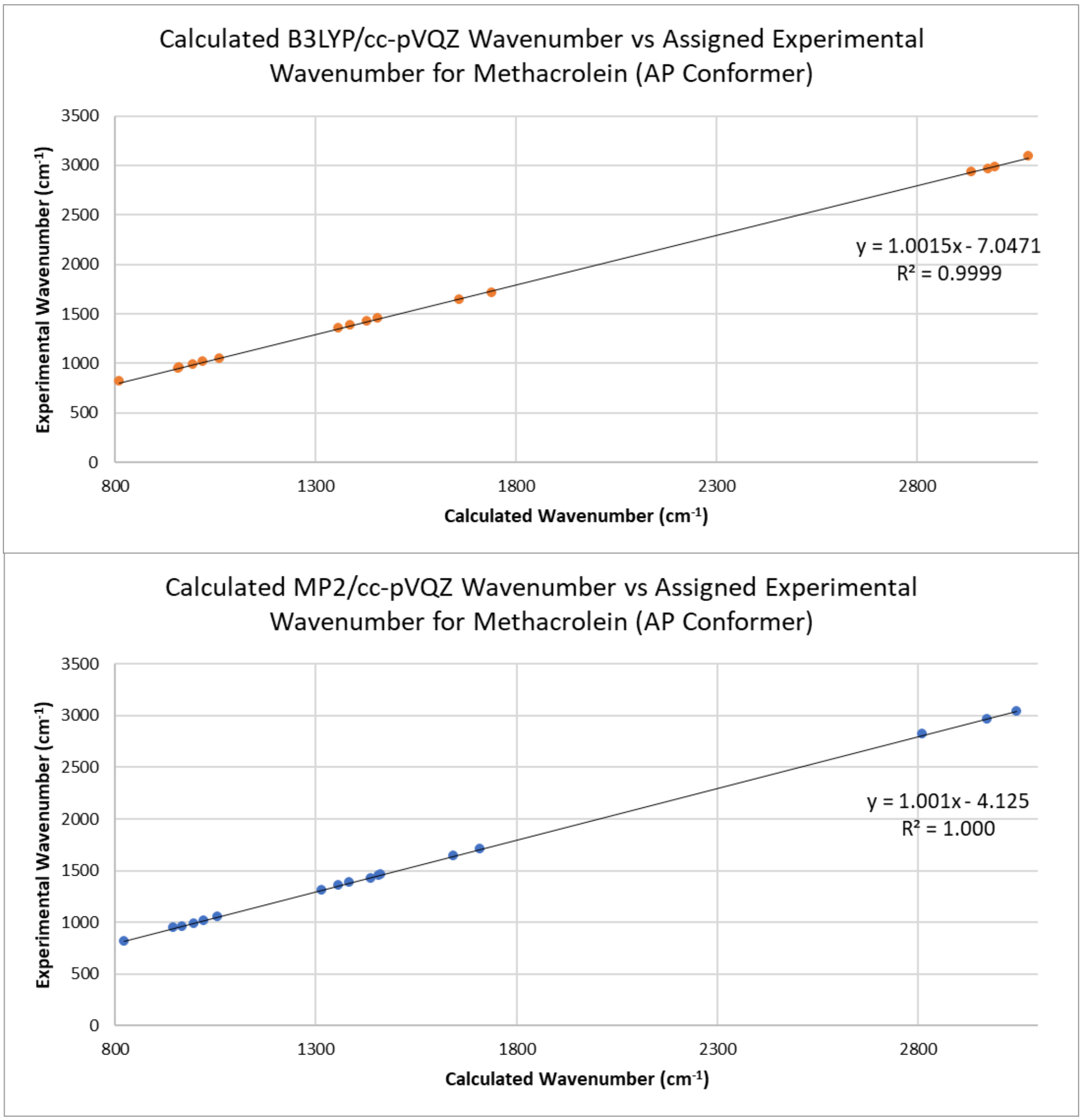

Figure A.55 Comparison graph of calculated versus experimental wavenumber for methacrolein (AP conformer).

Table A.25 Slope, intercept, and standard errors of each for the comparison graphs for methacrolein (AP conformer).

| Value | B3LYP | MP2 |
|---|---:|---:|
| m | 1.0015 | 1.0006 |
| c | -7.0471 | -4.1250 |
| Standard error for m | 0.0032 | 0.0018 |
| Standard error for c | 5.8586 | 3.0290 |

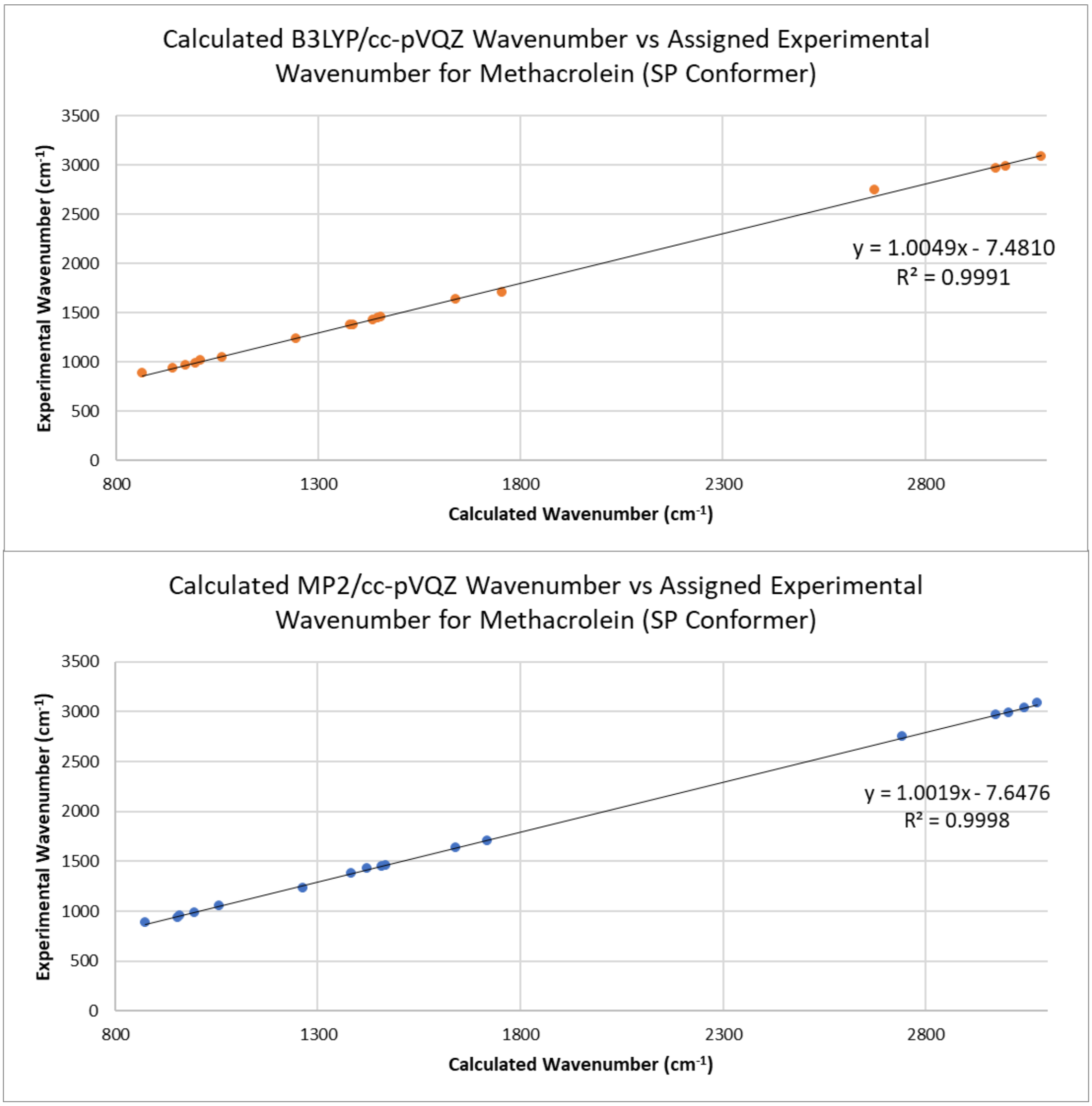

Figure A.56 Comparison graph of calculated versus experimental wavenumber for methacrolein (SP conformer).

Table A.26 Slope, intercept, and standard errors of each for the comparison graphs for methacrolein (SP conformer).

| Value | B3LYP | MP2 |
|---|---|---|
| m | 1.0049 | 1.0019 |
| c | -7.4810 | -7.6476 |
| Standard error for m | 0.0073 | 0.0036 |
| Standard error for c | 13.1270 | 7.0631 |

## A.13 Myrcene

Table A.27 Table of assigned literature and calculated wavenumbers to experimental data for myrcene. Calculations are anharmonic and at QZ level. Not all calculated or experimental peaks are assigned.

| B3LYP TZ Wavenumber ($cm^{-1}$) | MP2 TZ Wavenumber ($cm^{-1}$) | Experimental Wavenumber ($cm^{-1}$) | Shape |
|---|---|---|---|
| | 3146.6 | 3162.2 | Sharp |
| 3097.3 | | 3099.2 | Sharp |
| 3081.7 | 3087.0 | 3093.3 | Broad, shoulder |
| | 3073.0 | 3069.4 | Broad |
| 3050.0 | | 3052.9 | Broad |
| | 3040.6 | 3042.0 | Broad |
| | 3017.7 | 3022.5 | Broad |
| 2995.7 | 2989.9 | 2988.9 | Medium, shoulder |
| | 2989.2 | | |
| 2983.7 | | 2984.7 | Medium, shoulder |
| | 2973.3 | 2977.3 | Sharp |
| 2964.2 | 2970.6 | 2971.4 | Broad, shoulder |
| 2936.7 | 2951.6 | 2943.2 | Medium |
| 2924.2 | | 2924.9 | Medium |
| 2923.0 | | | |
| 2897.1 | | 2896.7 | Broad |
| 2878.9 | | 2880.1 | Broad |
| 2854.0 | | 2864.0 | Medium |
| 2838.5 | | 2838.5 | Broad, shoulder |
| 1460.5 | 1450.1 | 1460.0 | Broad |
| 1438.5 | 1444.6 | 1443.0 | Broad |
| | 1442.6 | | |
| 1397.5 | 1395.1 | 1393.4 | Broad |
| 1388.6 | 1381.7 | 1385.1 | Medium |
| 1377.6 | 1376.5 | 1379.9 | Medium |
| 1341.7 | 1333.9 | 1334.7 | Broad |
| 1293.8 | 1297.3 | 1296.0 | Broad |
| | 1236.1 | 1235.9 | Broad |
| 1229.4 | | 1227.0 | Broad |
| 1155.3 | 1156.8 | 1156.2 | Broad |
| 1103.8 | 1104.6 | 1110.7 | Sharp |
| 1080.0 | | 1081.1 | Medium |
| | 1071.7 | 1073.6 | Broad |
| 1064.1 | | 1064.5 | Broad |
| | 1052.1 | 1059.4 | Sharp |
| 1024.9 | | 1033.6 | Sharp |

| B3LYP TZ Wavenumber ($cm^{-1}$) | MP2 TZ Wavenumber ($cm^{-1}$) | Experimental | |
|---|---|---|---|
| | | Wavenumber ($cm^{-1}$) | Shape |
| 994.5 | | 995.6 | Sharp |
| | 989.2 | 993.2 | Medium, shoulder |
| 987.3 | 988.6 | 992.5 | Sharp, shoulder |
| 976.9 | 973.4 | 975.9 | Broad |
| 947.6 | 950.6 | 949.2 | Broad |
| 923.0 | 920.3 | 914.4 | Broad |
| 908.3 | | 906.8 | Broad, shoulder |
| | 904.2 | 904.7 | Sharp |
| | 896.4 | 896.7 | Sharp, shoulder |
| 874.0 | 876.8 | 894.0 | Sharp |

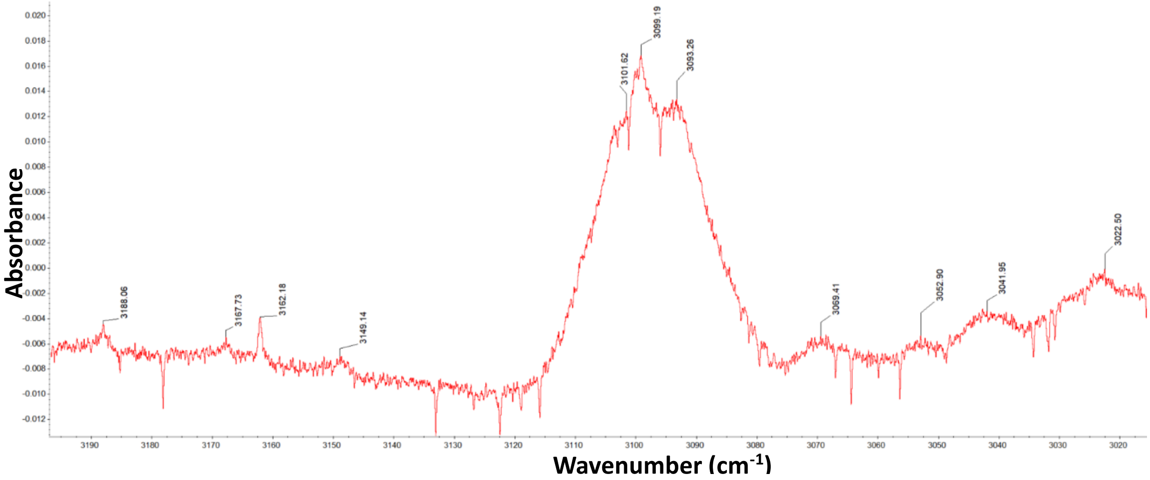

Figure A.57 Section from ~ 3200 – 3000 cm$^{-1}$ of annotated myrcene spectrum.

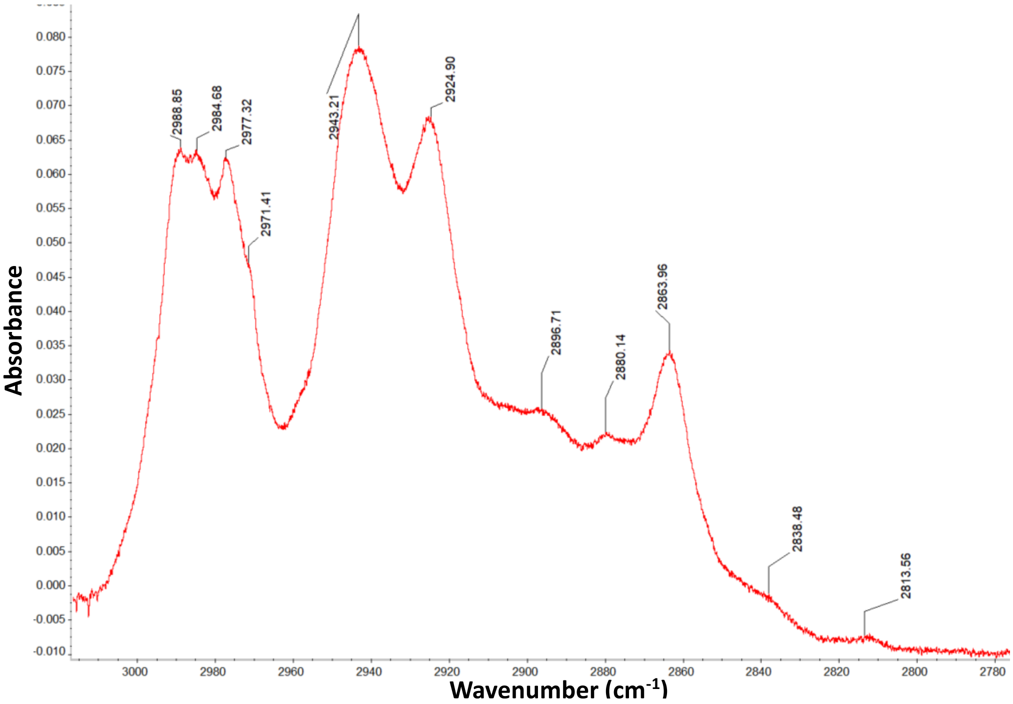

Figure A.58 Section from ~ 3000 – 2700 cm$^{-1}$ of annotated myrcene spectrum.

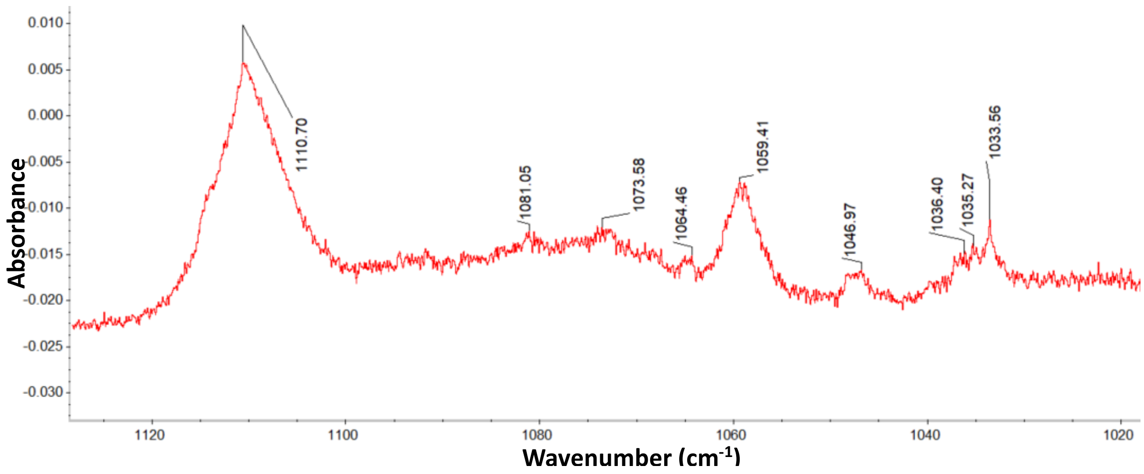

Figure A.59 Section from ~ 1150 – 1000 cm$^{-1}$ of annotated myrcene spectrum.

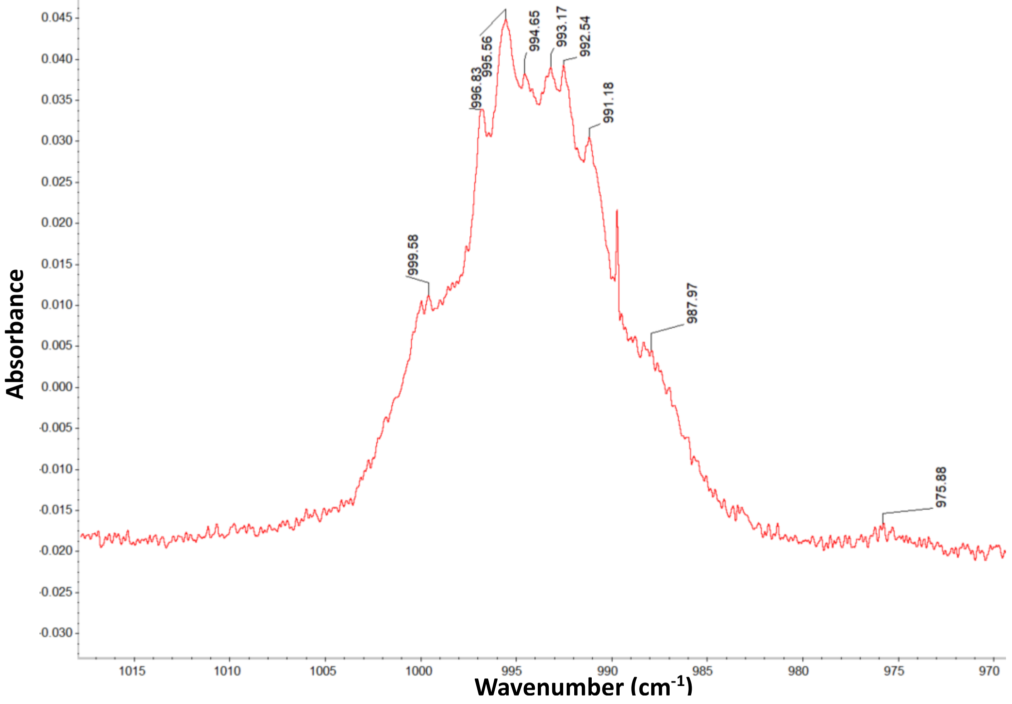

Figure A.60 Section from ~ 1000 – 950 cm$^{-1}$ of annotated myrcene spectrum.

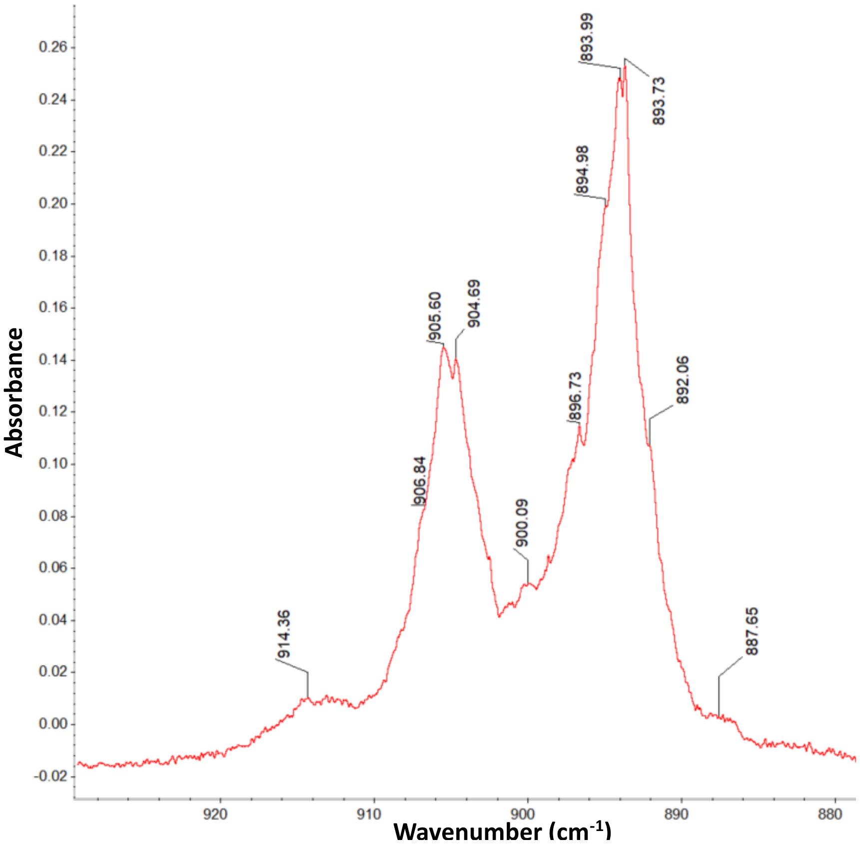

Figure A.61 Section from ~ 950 – 850 cm$^{-1}$ of annotated myrcene spectrum.

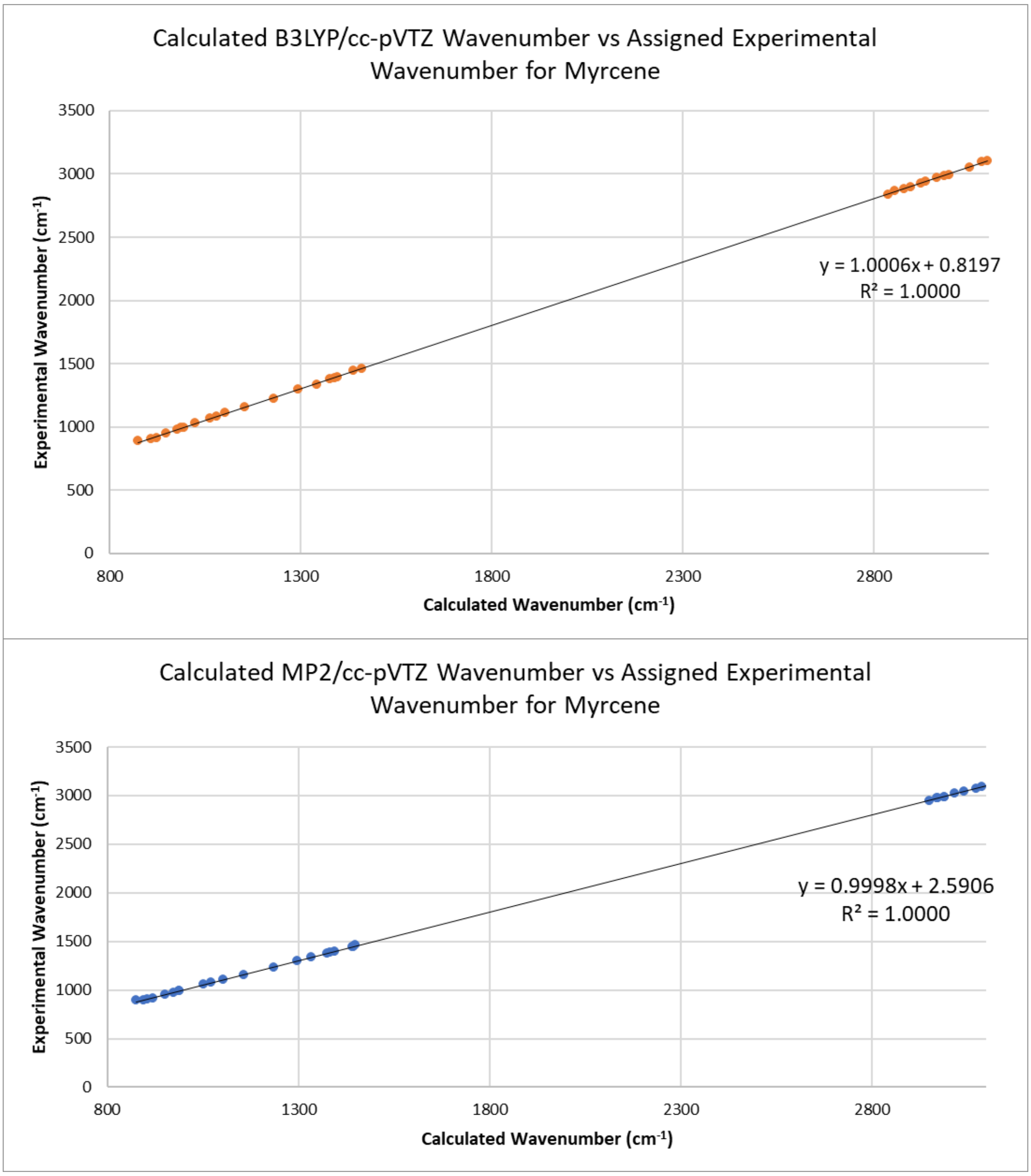

Figure A.62 Comparison graph of calculated versus experimental wavenumber for myrcene.

Table A.28 Slope, intercept, and standard errors of each for the comparison graphs for myrcene.

| Value | B3LYP | MP2 |
|---|---|---|
| m | 1.0006 | 0.9998 |
| c | 0.8197 | 2.5906 |
| Standard error for m | 0.0011 | 0.0011 |
| Standard error for c | 2.2832 | 2.1526 |

## A.14 Natural Gas (Methane, Ethane, Propane)

The natural gas sample was deposited at 20 K for 5 minutes, then the matrix was allowed to slowly warm up as the sample was deposited. This allowed the trapped molecules to move within the matrix, so peaks for the smaller molecules will appear first as they are the first molecules to move, with peaks for larger molecules appearing later. This is seen in the assigned Tables A.16 - 18 below, as peaks for methane are seen within the first 15 minutes. After this, more peaks associated with ethane appear, and at the final scan (approx. 3 hours after the initial deposit) more peaks associated with propane are present. Analysis was performed by assigning peaks that grew over time (as background peaks were present but did not increase in intensity as deposition continued).

Table A.29 Table of assigned literature wavenumbers to experimental data for methane, ethane, and propane in natural gas after 15 minutes of depositing and slowly warming the matrix. All literature peaks for methane can be assigned at this point due to methane being the smallest hydrocarbon in natural gas and therefore the first molecule to shift within the warming matrix.

| Methane Wavenumber ($cm^{-1}$)$^2$ | Ethane Wavenumber ($cm^{-1}$)$^2$ | Propane Wavenumber ($cm^{-1}$)$^2$ | Experimental (15 minutes of deposition) | |
|---|---|---|---|---|
| | | | Wavenumber ($cm^{-1}$) | Shape |
| 3018.9 | | | 3019.2 | Medium |
| | 2985.4 | 2977 | 2973.6 | Sharp |
| 1533.0 | | | 1572.9 | Medium |
| | 1379.2 | 1378 | 1368.1 | Sharp |
| | | 1338 | 1354.0 | Sharp |
| 1306.2 | | | 1307.8 | Medium |

Table A.30 Table of assigned literature wavenumbers to experimental data for methane, ethane, and propane in natural gas after 35 minutes of depositing and slowly warming the matrix. At this point more peaks associated with hydrocarbons larger than methane are appearing.

| Ethane Wavenumber ($cm^{-1}$)$^2$ | Propane Wavenumber ($cm^{-1}$)$^2$ | Experimental (35 minutes of deposition) | |
|---|---|---|---|
| | | Wavenumber ($cm^{-1}$) | Shape |
| | 2973 | 2979.7 | Medium, shoulder |
| 2895.8 | 2887 | 2891.7 | Sharp |
| | 869 | 882.5 | Sharp |

Table A.31 Table of assigned literature wavenumbers to experimental data for methane, ethane, and propane in natural gas after 3 hours of depositing and slowly warming the matrix.

| Ethane Wavenumber (cm$^{-1}$)[2] | Propane Wavenumber (cm$^{-1}$)[2] | Experimental (3 hours of deposition) | |
|---|---|---|---|
| | | Wavenumber (cm$^{-1}$) | Shape |
| | 2962 | 2951.5 | Medium |
| | 2887 | 2883.1 | Sharp |
| | 1472 | 1467.1 | Broad, shoulder |
| 1469 | 1464 | 1466.2 | Sharp |
| | 1392 | 1392.4 | Broad |

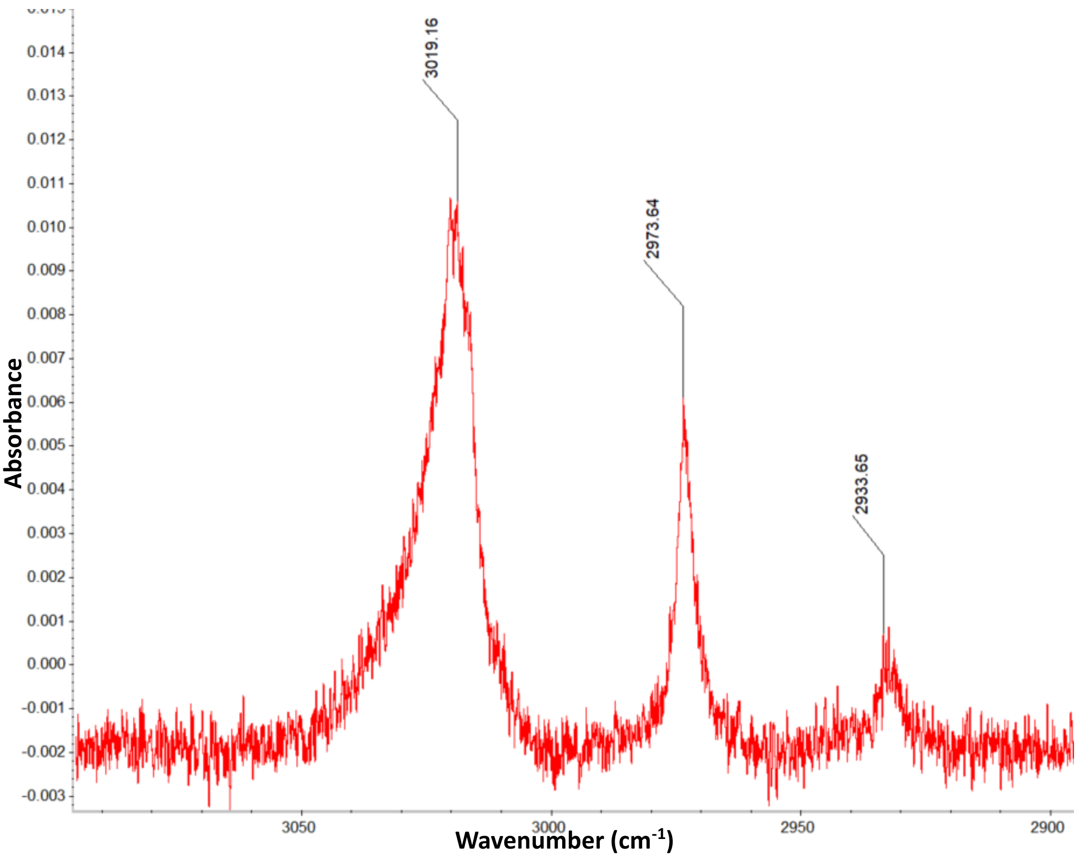

Figure A.63 Section from ~ 3100 – 2900 cm$^{-1}$ of annotated natural gas spectrum after depositing for 15 minutes. The peaks are assigned to methane (3019.16 cm$^{-1}$) and ethane and propane (2973.64 cm$^{-1}$).

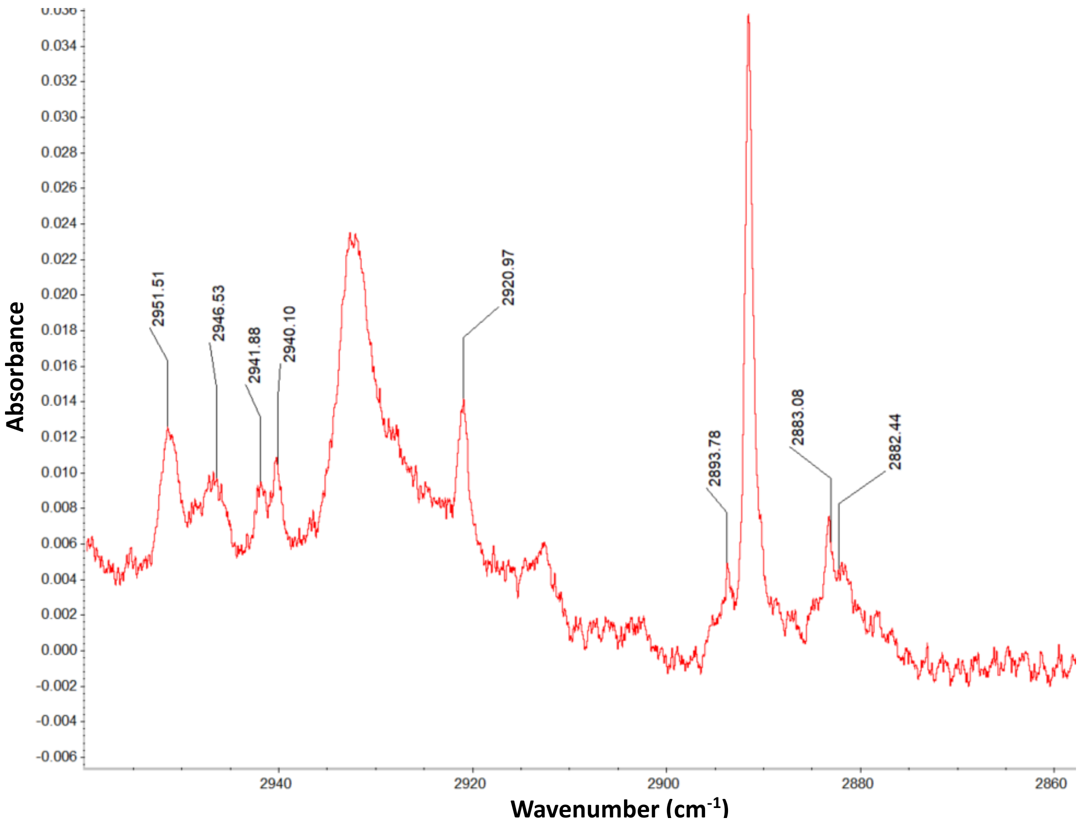

Figure A.65 Section from ~ 2950 – 2860 cm$^{-1}$ of annotated natural gas spectrum after 3 hours of depositing. The annotated peaks here resolved out of peaks previously noted in the spectra, indicating they are related to the larger hydrocarbons in natural gas (nominally propane).

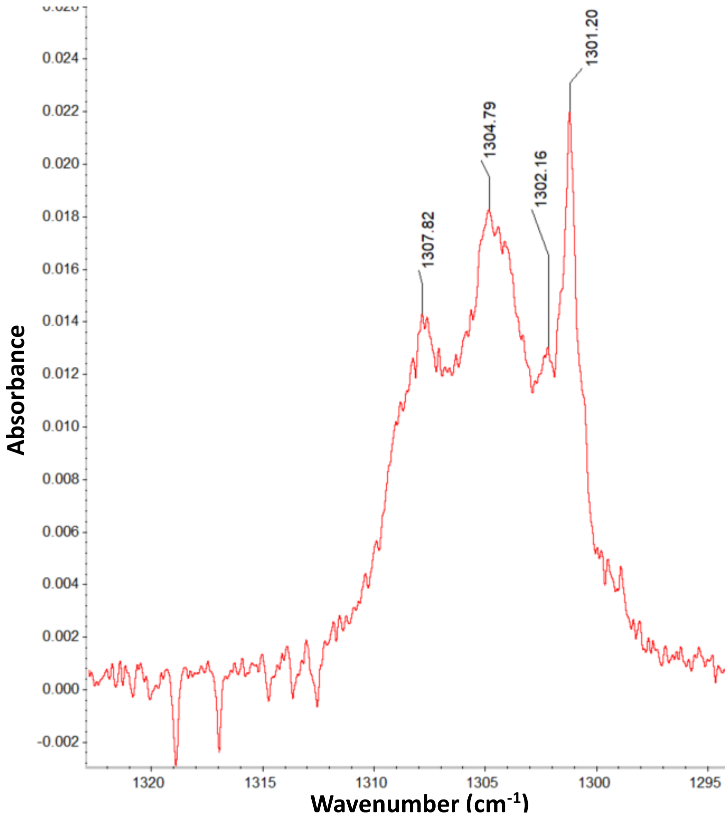

Figure A.64 Section from ~ 1320 – 1290 cm$^{-1}$ of annotated natural gas spectrum after 15 minutes of depositing.

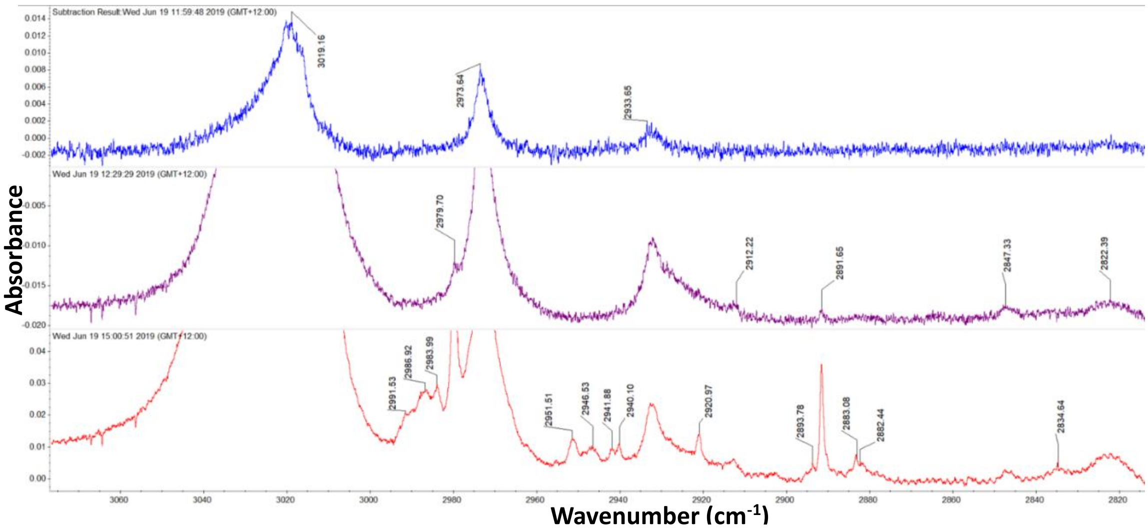

Figure A.66 Section from ~ 3000 – 2800 cm$^{-1}$ of annotated natural gas spectrum. The top scan (blue) is after 15 minutes of depositing the middle scan (purple) is after 45 minutes of depositing, and the bottom scan (red) is after 3 hours of depositing. The emergence and resolution of new peaks is seen after an extended deposition time, as well as the continued growth of peaks seen in initial scans.

Table A.32 Slope, intercept, and standard errors of each for the comparison graph for methane, ethane, and propane.

| Value | Methane | Ethane | Propane |
|---|---:|---:|---:|
| m | 0.9899 | 0.9993 | 0.9966 |
| c | 33.6874 | -6.0287 | 8.0075 |
| Standard error for m | 0.0220 | 0.0037 | 0.0032 |
| Standard error for c | 46.0355 | 8.5278 | 7.0029 |

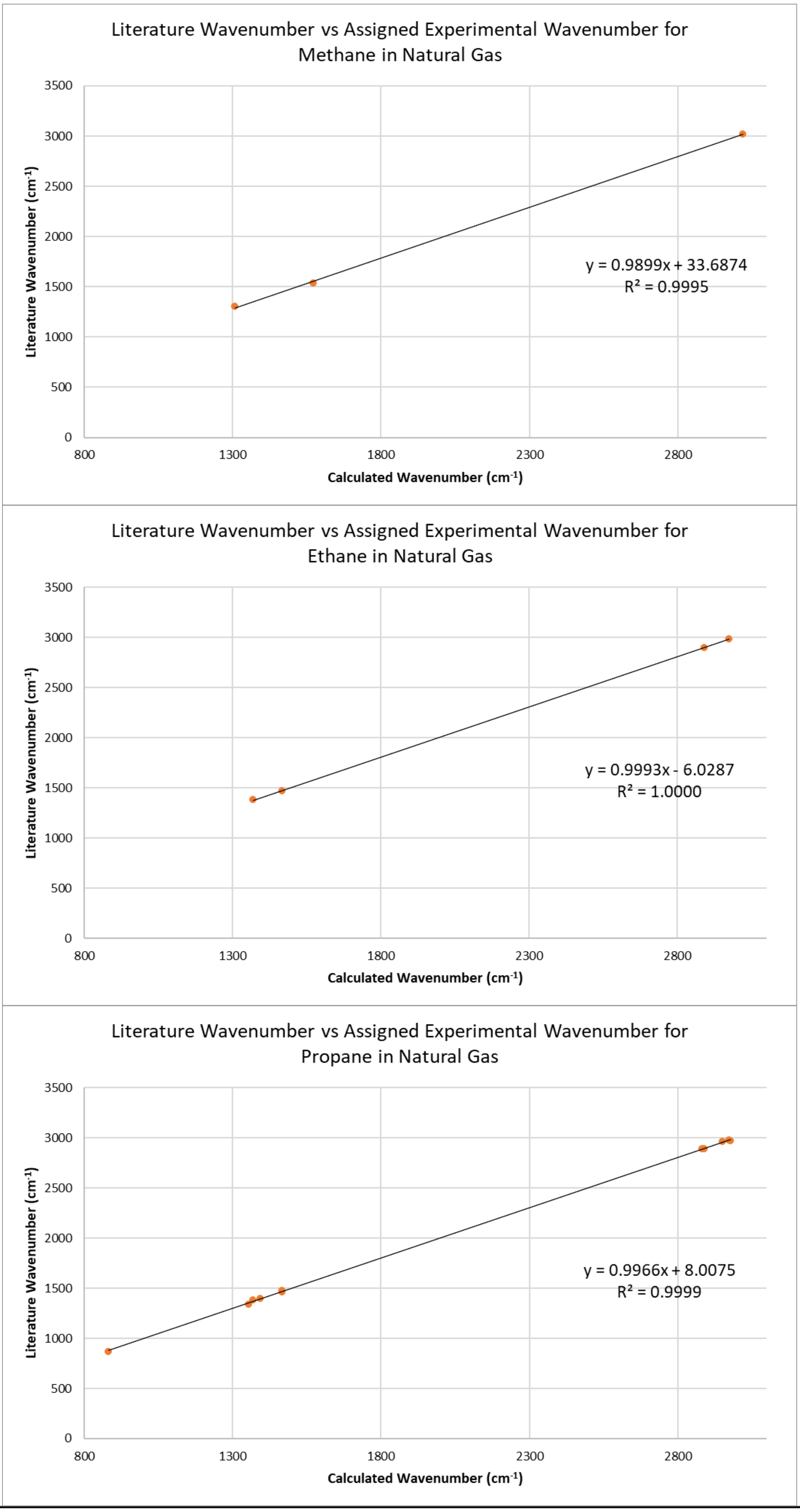

Figure A.67 Comparison graph of assigned literature versus experimental wavenumber for methane, ethane, and propane in natural gas.

## A.15 Propyne

Table A.33 Table of assigned literature and calculated wavenumbers to experimental data for propyne. Calculations are anharmonic and at QZ level. Not all calculated or experimental peaks are assigned.

| Literature Wavenumber (cm$^{-1}$)[2] | B3LYP QZ Wavenumber (cm$^{-1}$) | MP2 QZ Wavenumber (cm$^{-1}$) | Experimental | |
|---|---|---|---|---|
| | | | Wavenumber (cm$^{-1}$) | Shape |
| 3334 | 3344.9 | 3368.4 | 3323.0 | Sharp |
| 3008 | 2960.4 | 2972.7 | 2978.3 | Broad, coming to a point |
| 2918 | 2940.7 | | 2935.4 | Sharp |
| 2142 | | 2110.1 | 2136.8 | Sharp |
| 1452 | 1443.0 | 1460.9 | 1413.8 | Broad |
| | 1442.9 | 1460.9 | | |
| | 1387.5 | 1386.5 | 1383.1 | Broad |
| 1053 | 1036.9 | 1039.6 | 1246.8 | Sharp |
| | 1036.7 | 1039.6 | | |
| 931 | 933.6 | 940.2 | 928.3 | Sharp |

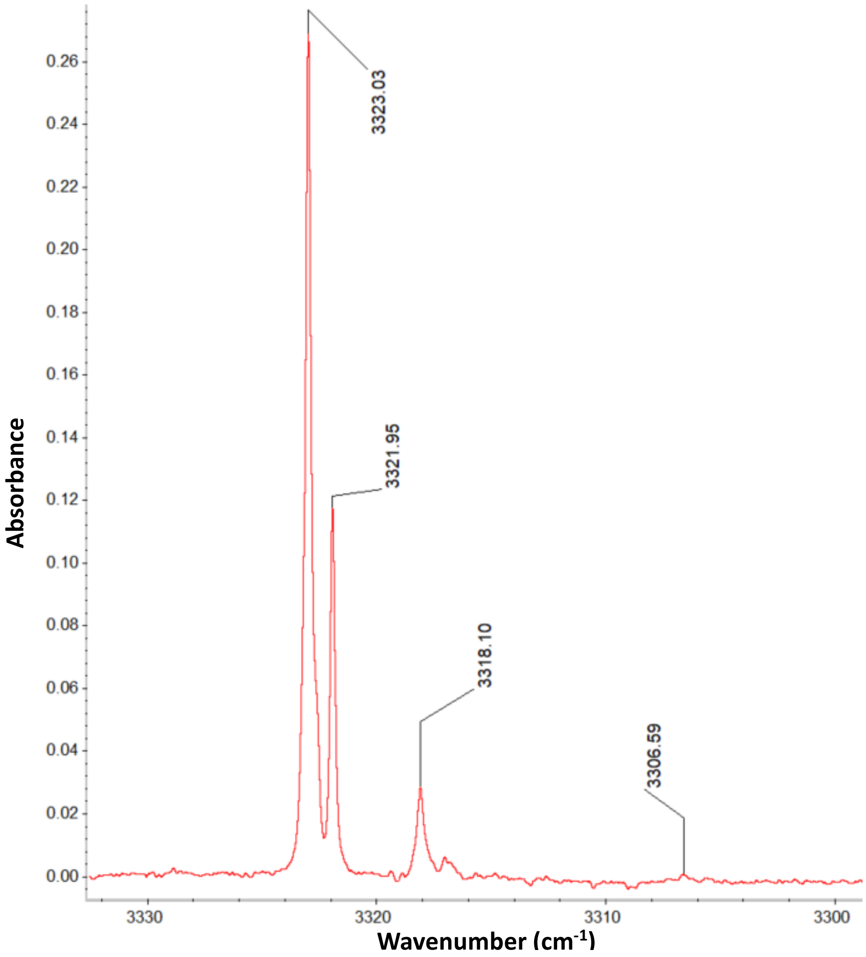

Figure A.68 Section from ~ 3330 – 3300 cm$^{-1}$ of annotated propyne spectrum.

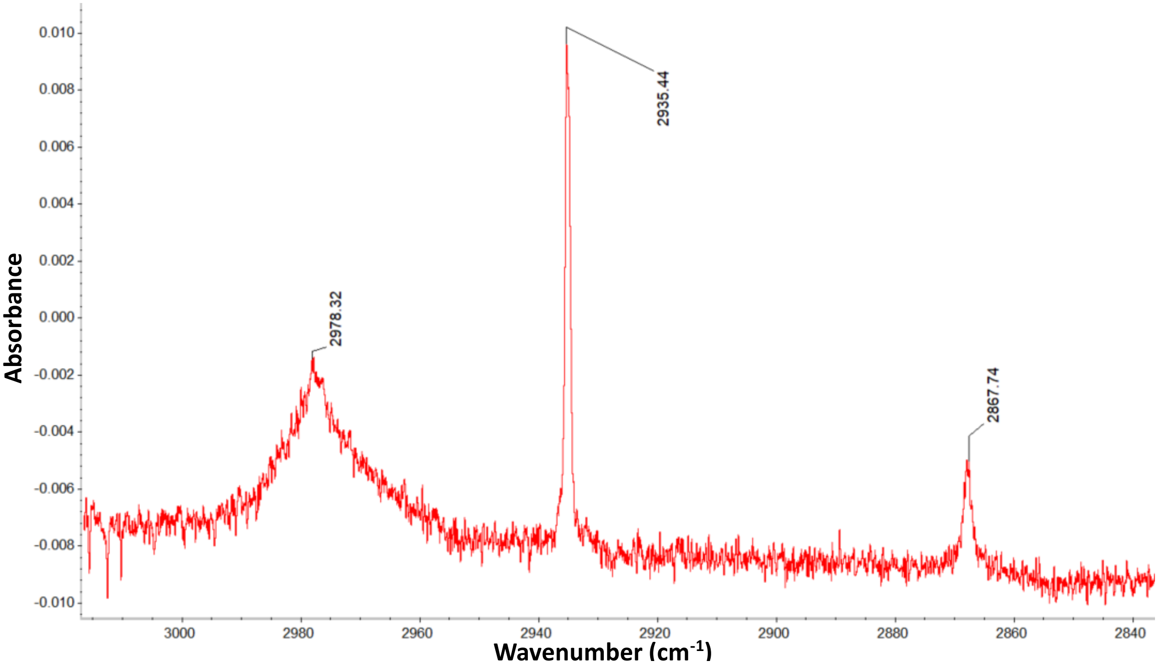

Figure A.69 Section from ~ 3000 – 2840 cm$^{-1}$ of annotated propyne spectrum.

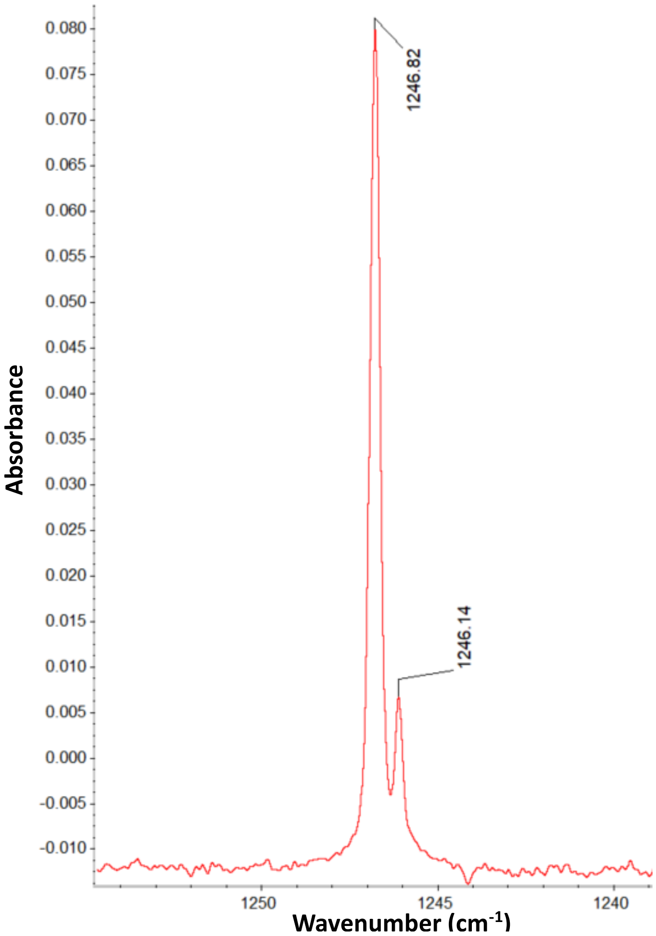

Figure A.70 Section from ~ 1260 – 1240 cm$^{-1}$ of annotated propyne spectrum.

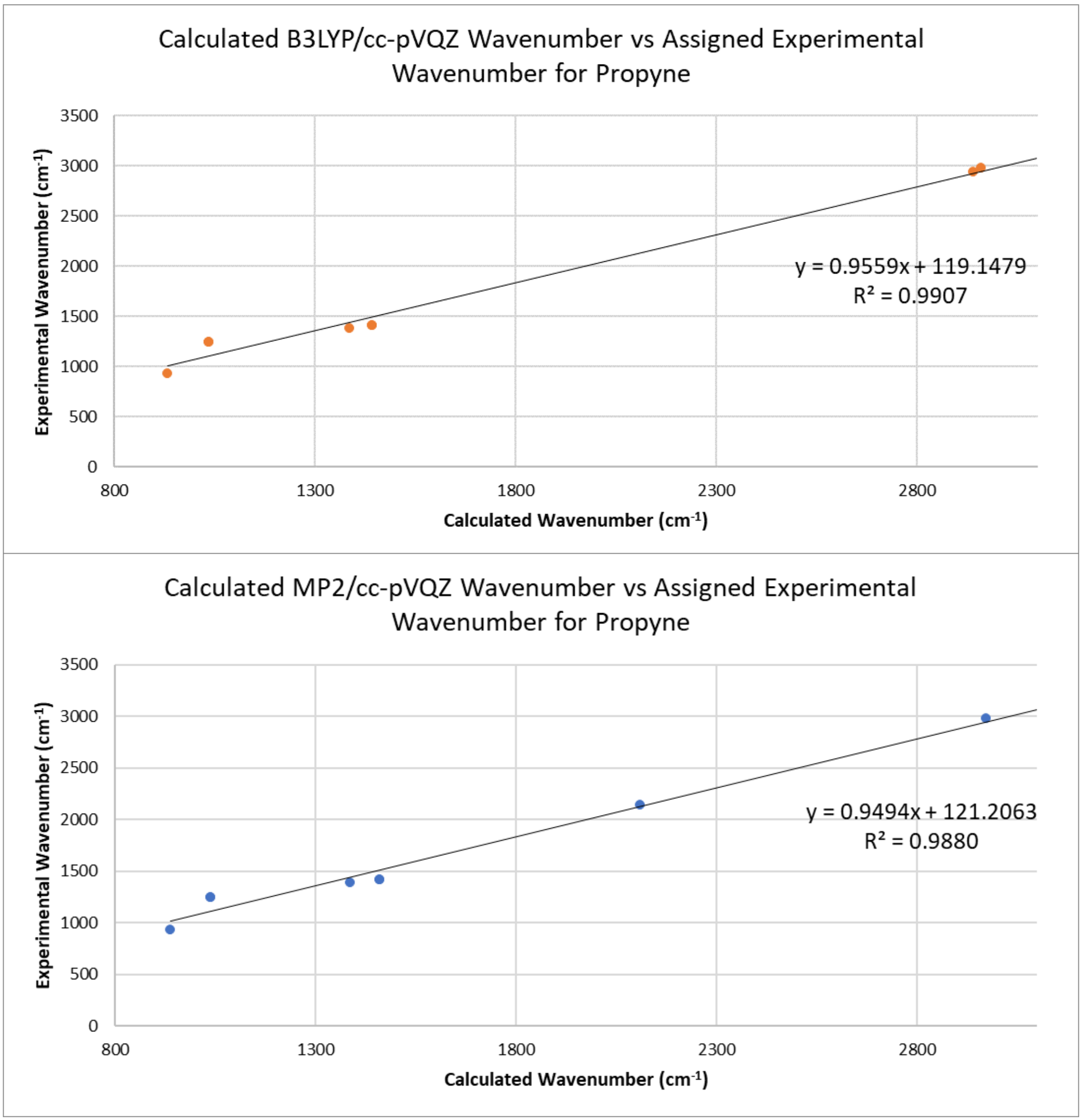

Figure A.71 Comparison graph of assigned calculated versus experimental wavenumber for propyne.

Table A.34 Slope, intercept, and standard errors of each for the comparison graphs for propyne.

| Value | B3LYP | MP2 |
|---|---|---|
| m | 1.0050 | 1.0013 |
| c | -21.2882 | -20.0611 |
| Standard error for m | 0.0074 | 0.0146 |
| Standard error for c | 16.7396 | 31.1128 |

## A.16 Toluene

Table A.35 Table of assigned literature and calculated wavenumbers to experimental data for toluene. Calculations are anharmonic and at TZ level. Not all calculated or experimental peaks are assigned.

| **Literature Wavenumber (cm$^{-1}$)[7]** | **B3LYP TZ Wavenumber (cm$^{-1}$)** | **MP2 TZ Wavenumber (cm$^{-1}$)** | **Experimental** | |
|---|---|---|---|---|
| | | | **Wavenumber (cm$^{-1}$)** | **Shape** |
| | | 3136.5 | 3151.1 | Sharp |
| | | 3107.7 | 3109.7 | Broad |
| 3087 | | 3083.3 | 3098.1 | Sharp |
| 3063 | 3078.8 | 3064.0 | 3067.9 | Medium |
| | | 3051.9 | 3064.9 | Medium |
| 3055 | 3048.5 | 3039.5 | 3044.1 | Sharp |
| 3039 | 3039.9 | | 3038.3 | Medium |
| | 3031.5 | | 3035.2 | Medium |
| 3029 | 3029.7 | 3017.8 | 3028.5 | Sharp |
| 2979 | 2991.9 | | 2989.3 | Medium |
| 2952 | | | 2965.6 | Sharp |
| 2921 | 2931.4 | 2937.4 | 2924.4 | Sharp |
| | 2835.2 | | 2860.9 | Broad |
| 1605 | 1605.3 | 1611.9 | 1601.9 | Broad |
| 1586 | 1587.3 | 1590.0 | 1573.1 | Very broad |
| 1494 | 1499.9 | 1494.4 | 1497.8 | Sharp |
| 1463 | 1460.9 | 1459.4 | 1468.8 | Broad |
| | 1387.8 | | 1391.8 | Sharp |
| 1379 | 1380.9 | 1380.0 | 1380.2 | Sharp |
| 1330 | 1341.8 | 1323.8 | 1354.0 | Sharp |
| 1280 | 1283.7 | | 1272.9 | Sharp |
| 1210 | 1202.3 | 1217.4 | 1216.6 | Sharp |
| 1175 | 1188.1 | 1183.5 | 1180.4 | Sharp |
| 1155 | 1168.7 | 1164.3 | 1141.0 | Sharp |
| 1080 | 1089.7 | 1093.1 | 1082.4 | Sharp |
| | 1080.5 | | 1081.3 | Sharp, shoulder |
| | | 1056.2 | 1044.2 | Sharp |
| 1040 | | | 1038.3 | Broad |
| | | 1035.5 | 1033.9 | Sharp |
| 1030 | 1029.7 | 1024.8 | 1030.9 | Sharp |
| 1003 | 1006.0 | 1006.0 | 1016.4 | Medium |

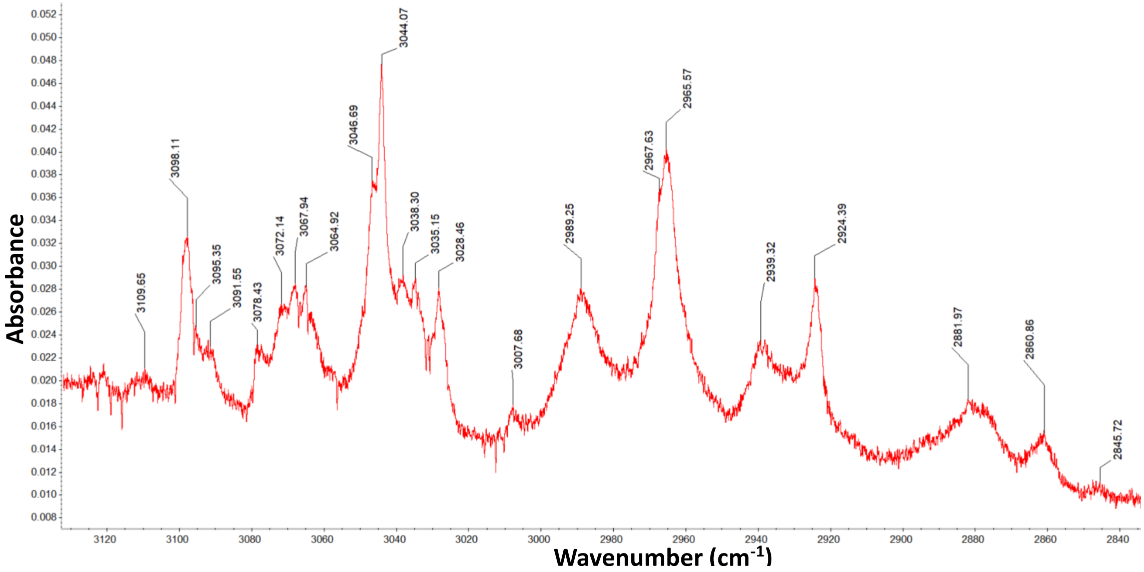

Figure A.72 Section from ~ 3120 – 2840 cm$^{-1}$ of annotated toluene spectrum.

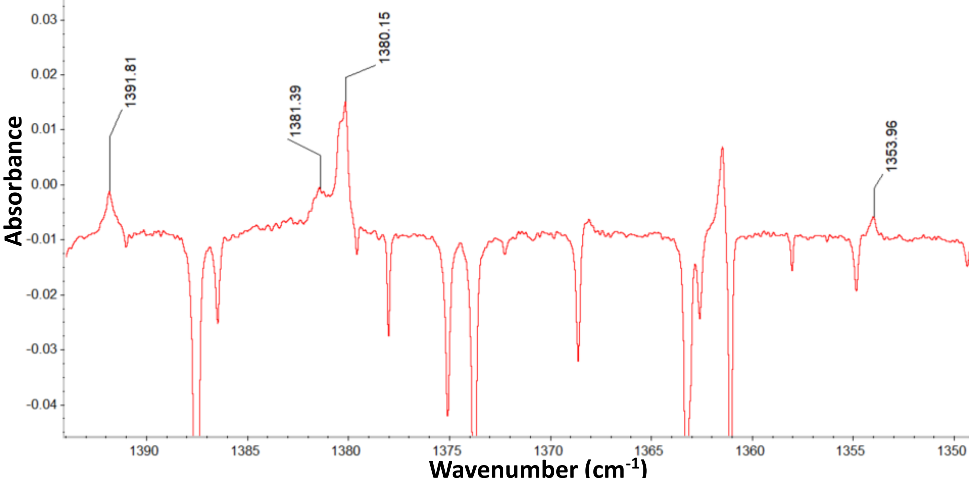

Figure A.73 Section from ~ 1400 – 1350 cm$^{-1}$ of annotated toluene spectrum.

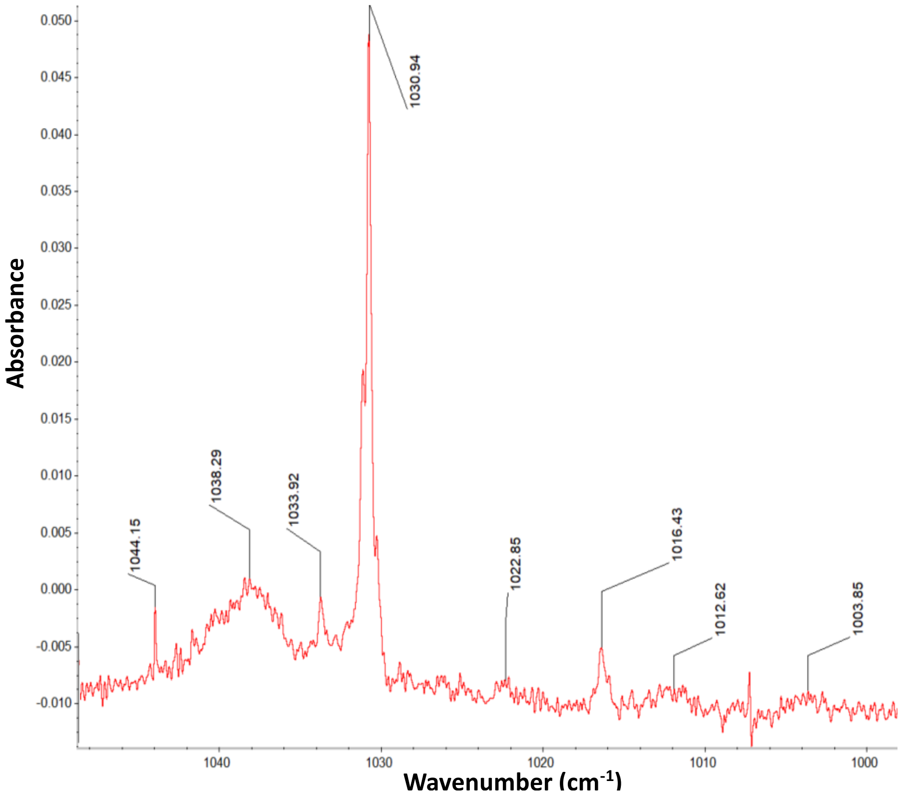

Figure A.74 Section from ~ 1050 – 1000 cm$^{-1}$ of annotated toluene spectrum.

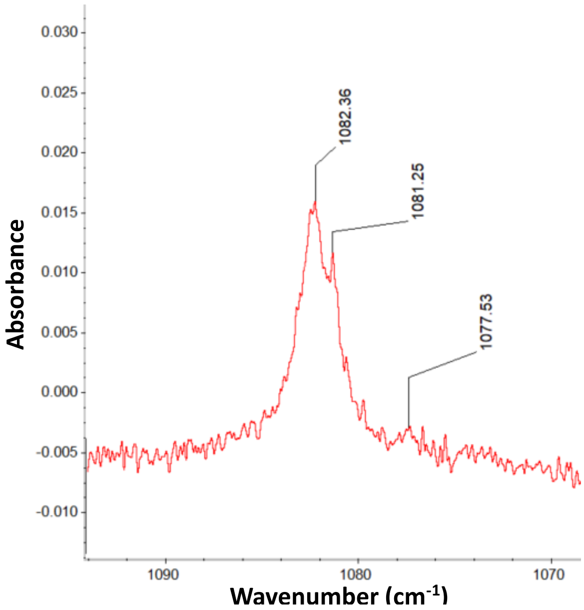

Figure A.75 Section from ~ 1100 – 1060 cm$^{-1}$ of annotated toluene spectrum.

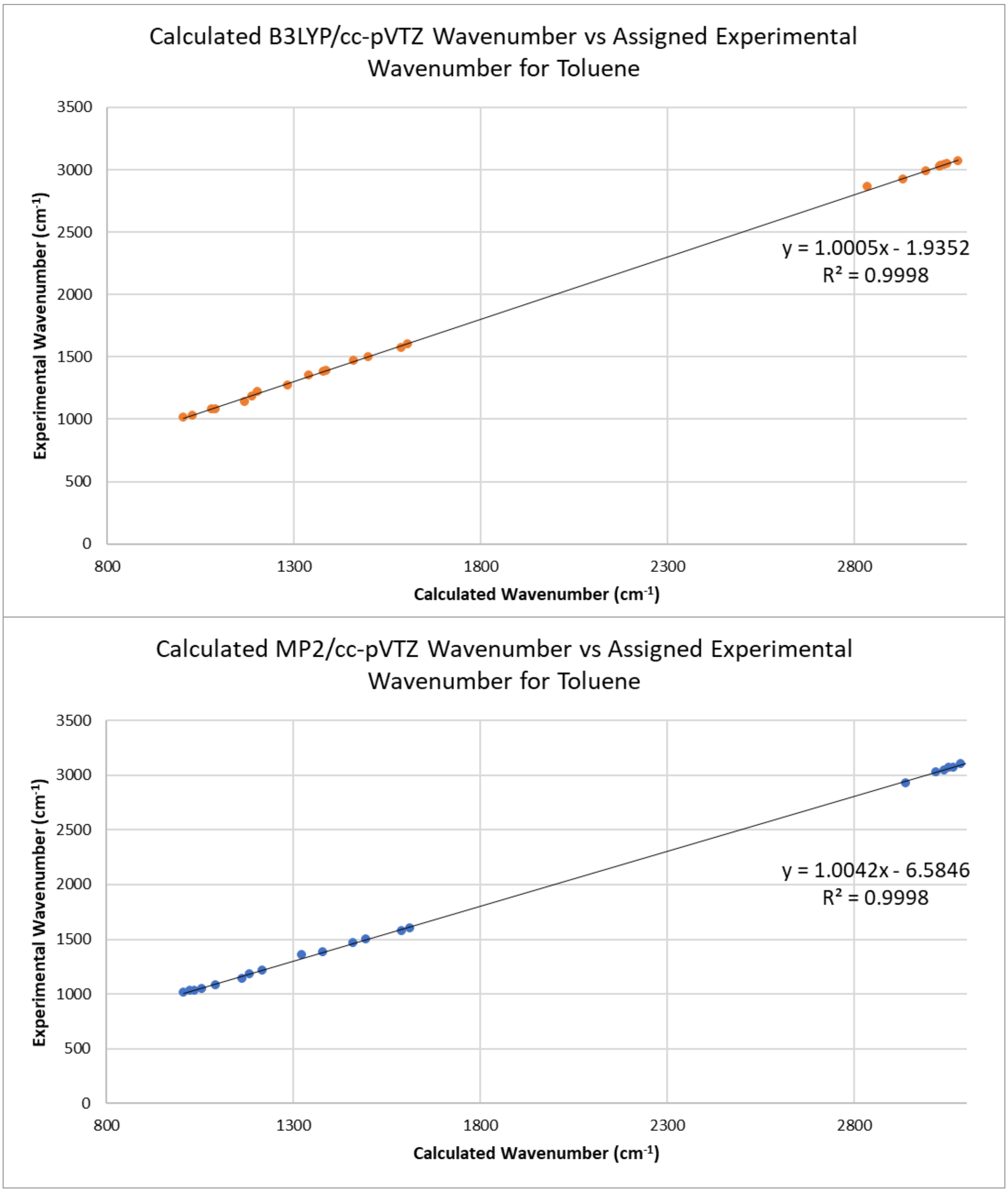

Figure A.76 Comparison graph of assigned calculated versus experimental wavenumber for toluene.

Table A.36 Slope, intercept, and standard errors of each for the comparison graphs for toluene.

| Value | B3LYP | MP2 |
|---|---|---|
| m | 1.0005 | 1.0042 |
| c | -1.9352 | -6.5846 |
| Standard error for m | 0.0028 | 0.0029 |
| Standard error for c | 5.7484 | 6.1845 |

## A.17 Tert-butyl Hydroperoxide

Table A.37 Table of assigned literature and calculated wavenumbers to experimental data for tert-butyl hydroperoxide. Calculations are anharmonic and at TZ level. Not all calculated or experimental peaks are assigned.

| Literature Wavenumber ($cm^{-1}$)[8] | B3LYP TZ Wavenumber ($cm^{-1}$) | MP2 TZ Wavenumber ($cm^{-1}$) | Experimental | |
|---|---|---|---|---|
| | | | Wavenumber ($cm^{-1}$) | Shape |
| 3436.4 | | | 3436.8 | Medium |
| | 2987.4 | 2988.4 | 2988.6 | Sharp |
| | 2978.5 | 2976.8 | 2982.8 | Sharp, shoulder |
| 1481.4 | 1485.1 | 1473.7 | 1478.7 | Broad |
| 1470.5 | 1460.6 | 1464.0 | 1465.6 | Broad, split peak |
| 1385.0 | 1391.9 | 1384.8 | 1388.5 | Medium, split peak |
| 1371.7 | | | 1370.0 | Medium, shoulder |
| | 1367.3 | | 1367.2 | Medium, shoulder |
| | 1364.4 | 1363.7 | 1365.0 | Sharp, shoulder |
| | 1328.6 | 1324.5 | 1317.2 | Sharp |
| | | 1255.3 | 1254.6 | Medium |
| | 1235.5 | 1249.3 | 1246.8 | Medium |
| 1204.8 | | 1209.3 | 1201.1 | Sharp |
| | 1190.1 | | 1196.8 | Sharp, shoulder |
| 1033.0 | | | 1033.6 | Sharp, shoulder |
| | 1025.9 | 1031.3 | 1032.0 | Sharp |
| | 1015.5 | 1022.2 | 1021.5 | Medium |
| 888.8 | 897.3 | 864.2 | 883.4 | Medium |

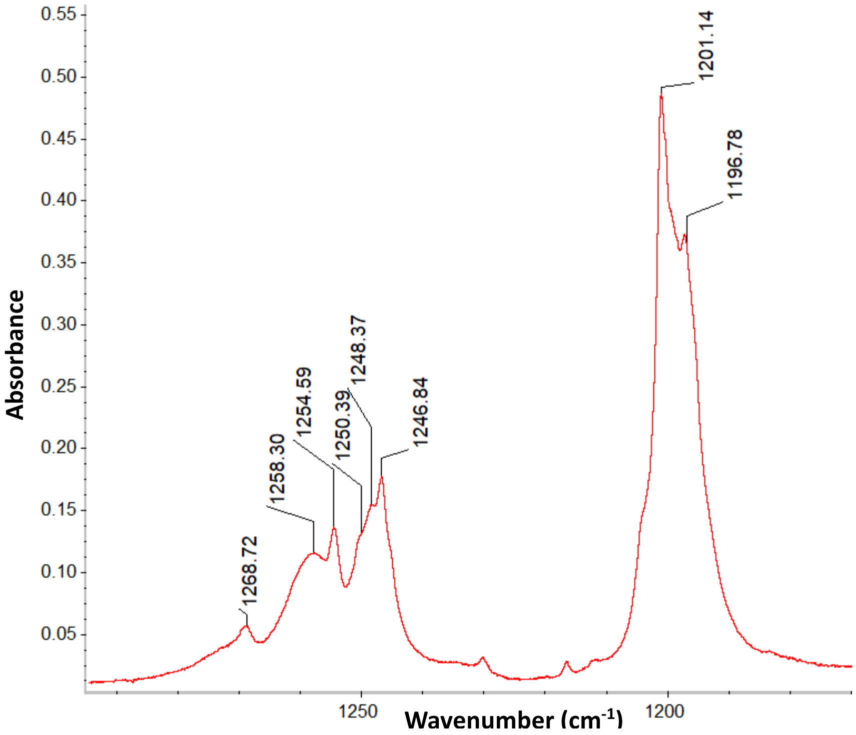

Figure A.77 Section from ~ 1260 – 1190 cm$^{-1}$ of annotated tert-butyl hydroperoxide spectrum.

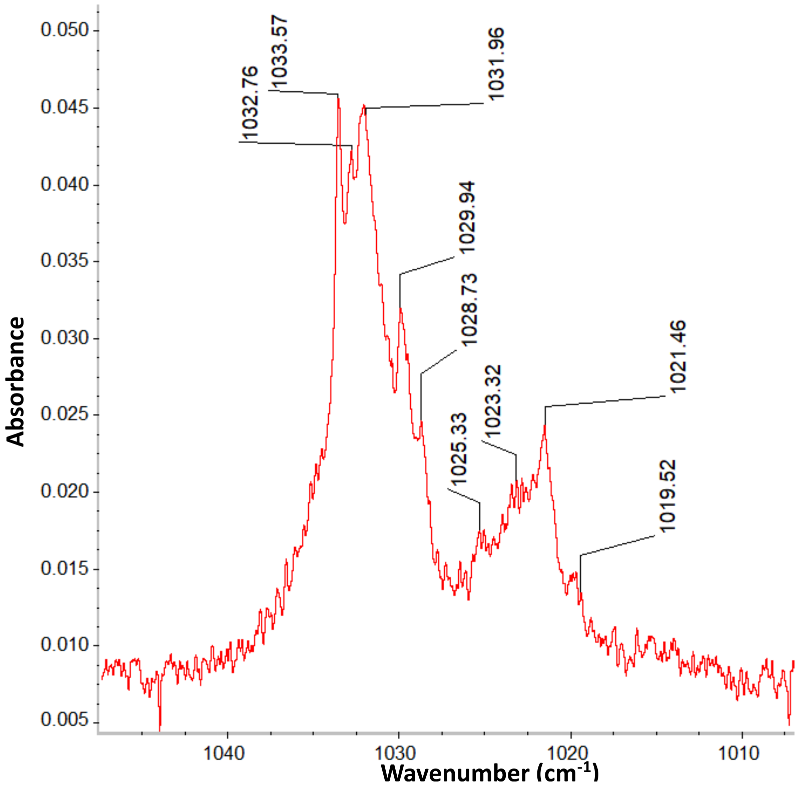

Figure A.78 Section from ~ 1050 – 1000 cm$^{-1}$ of annotated tert-butyl hydroperoxide spectrum.

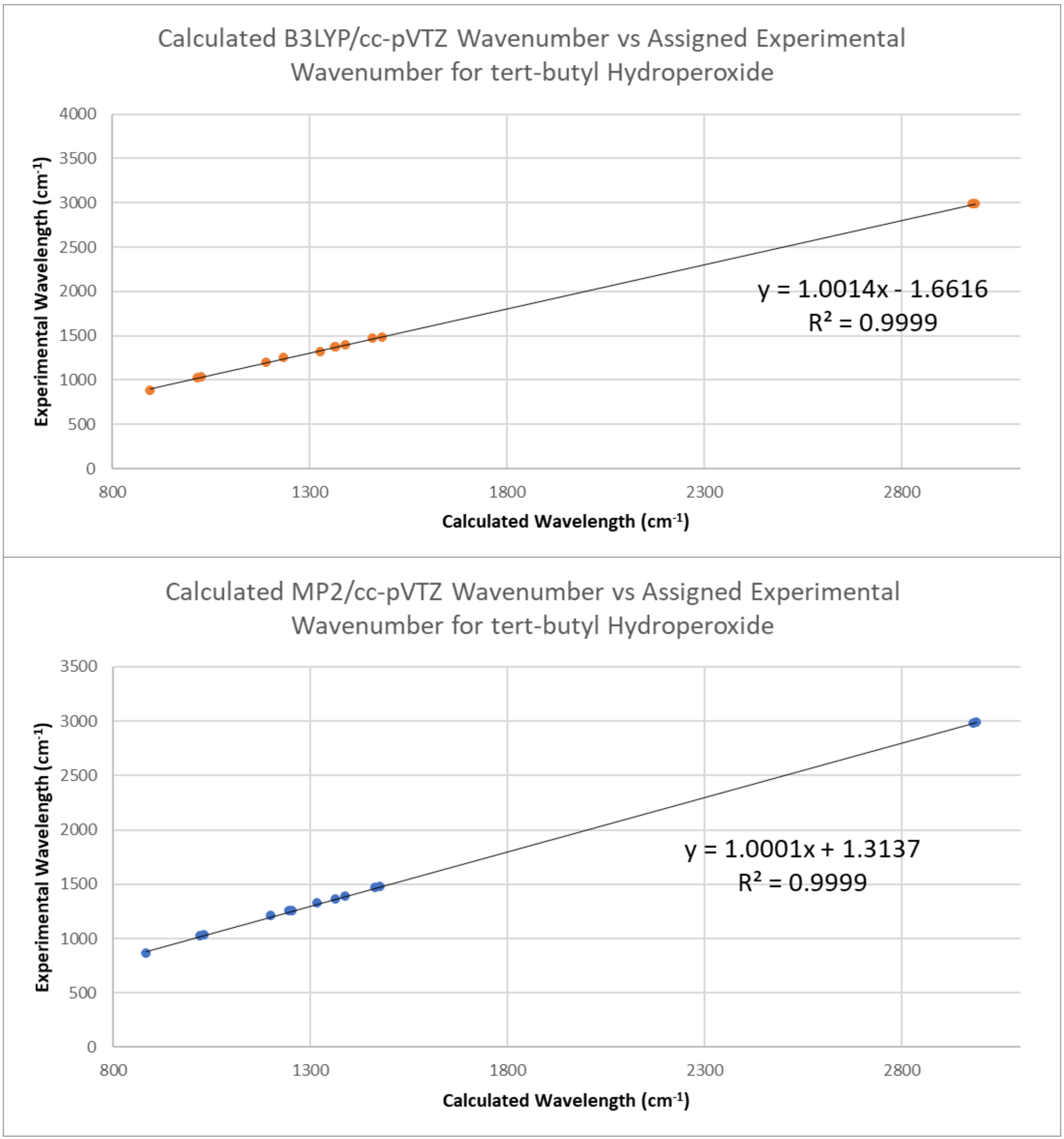

Figure A.79 Comparison graph of assigned calculated versus experimental wavenumber for tert-butyl hydroperoxide.

Table A.38 Slope, intercept, and standard errors of each for the comparison graphs for tert-butyl hydroperoxide.

| Value | B3LYP | MP2 |
|---|---|---|
| m | 1.0014 | 1.0001 |
| c | -1.6616 | 1.3137 |
| Standard error for m | 0.0033 | 0.0030 |
| Standard error for c | 5.4286 | 4.9428 |

# B. Chapter 2: Correction Factor Additional Data

This chapter contains the graphs used to construct the correction factor, separated into categories of basis set and spectral range (high, mid, and low).

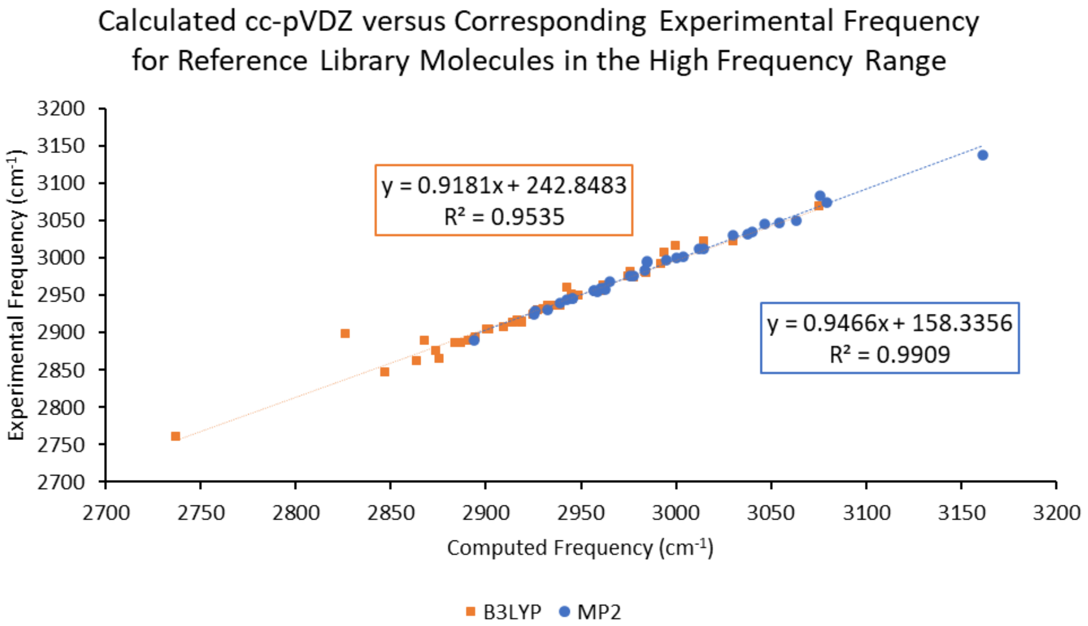

Figure B.1 Graph of computed versus corresponding assigned experimental frequency for reference library molecules, calculated at the cc-pVDZ level in the high-frequency range.

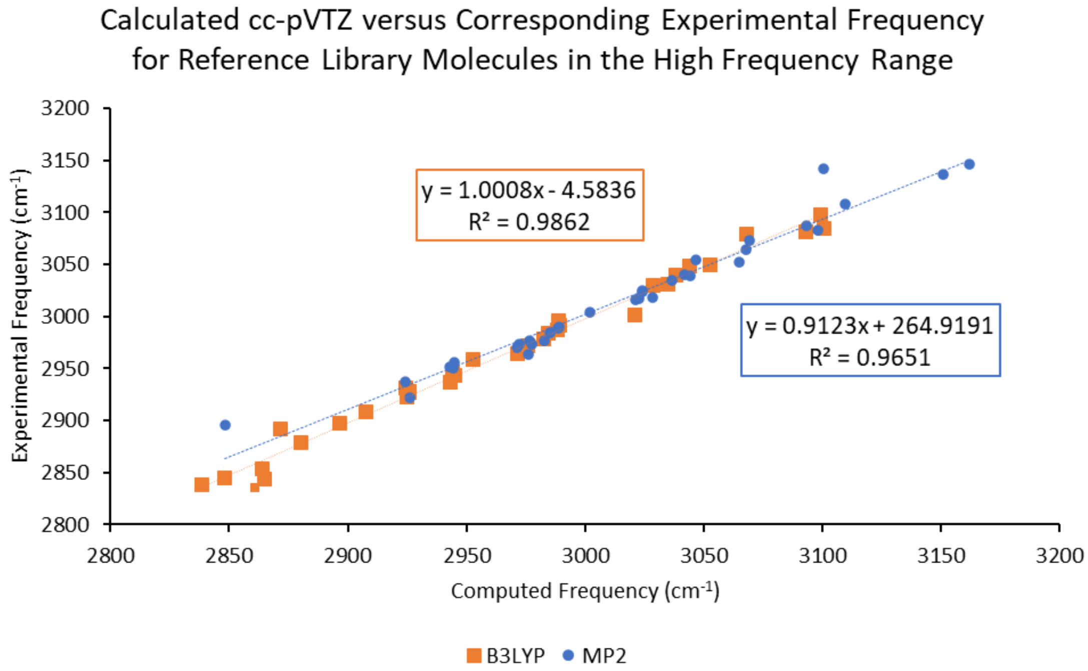

Figure B.2 Graph of computed versus corresponding assigned experimental frequency for reference library molecules, calculated at the cc-pVTZ level in the high-frequency range.

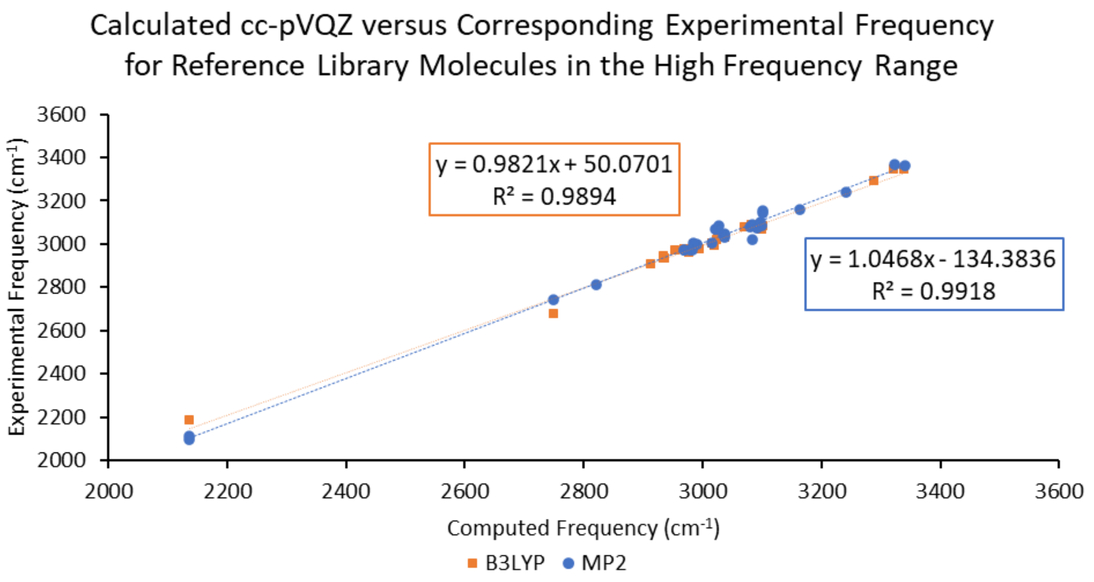

Figure B.3 Graph of computed versus corresponding assigned experimental frequency for reference library molecules, calculated at the cc-pVQZ level in the high-frequency range.

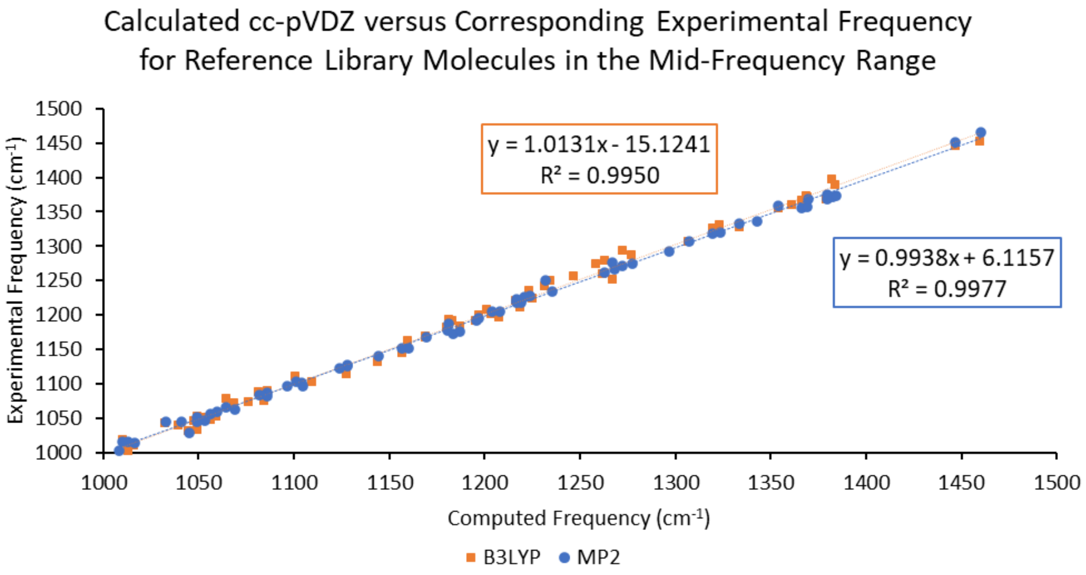

Figure B.4 Graph of computed versus corresponding assigned experimental frequency for reference library molecules, calculated at the cc-pVDZ level in the mid-frequency range.

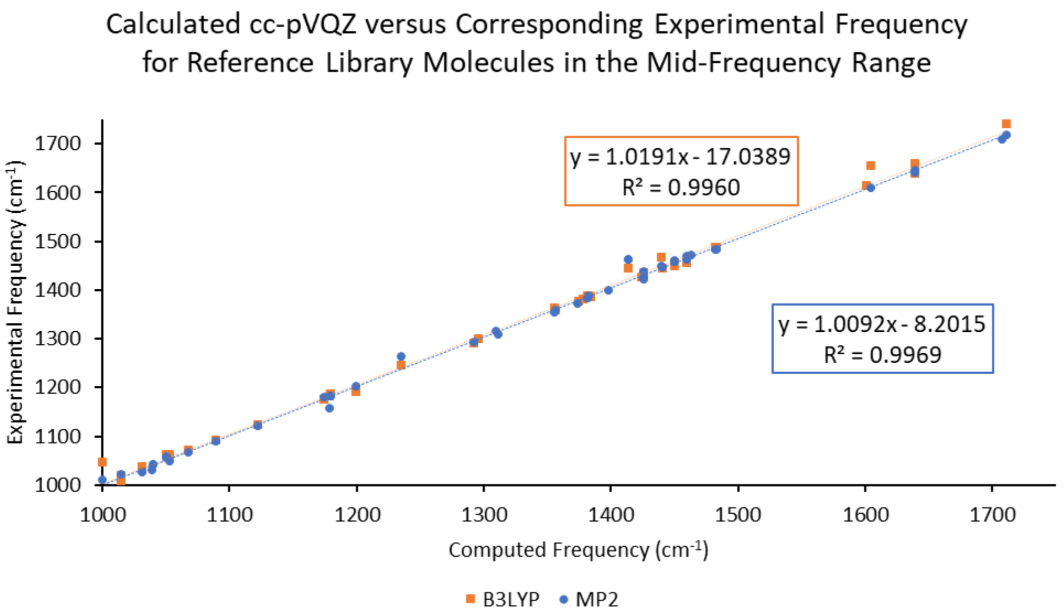

Figure B.5 Graph of computed versus corresponding assigned experimental frequency for reference library molecules, calculated at the cc-pVTZ level in the mid-frequency range.

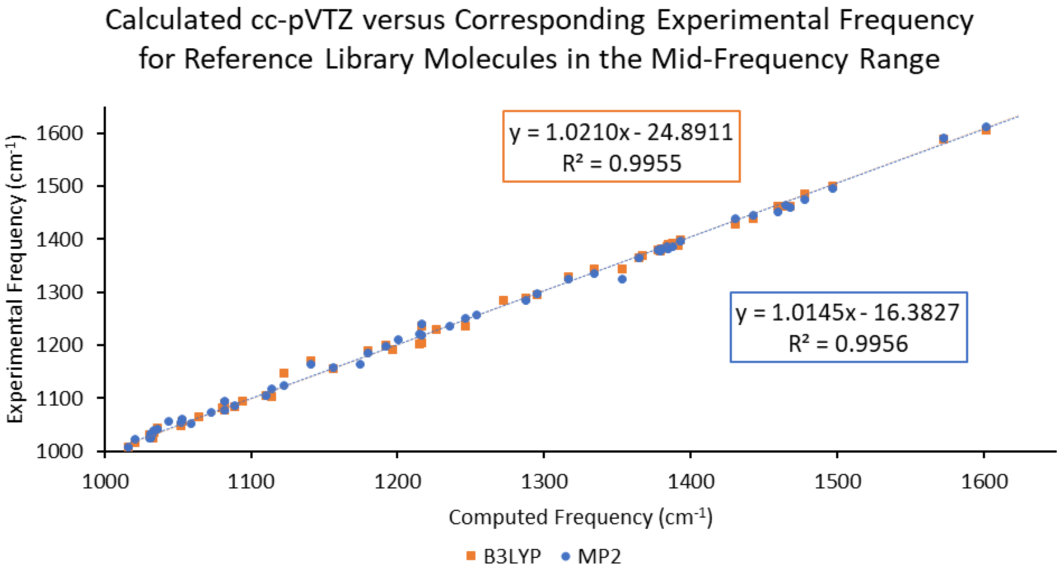

Figure B.6 Graph of computed versus corresponding assigned experimental frequency for reference library molecules, calculated at the cc-pVQZ level in the mid-frequency range.

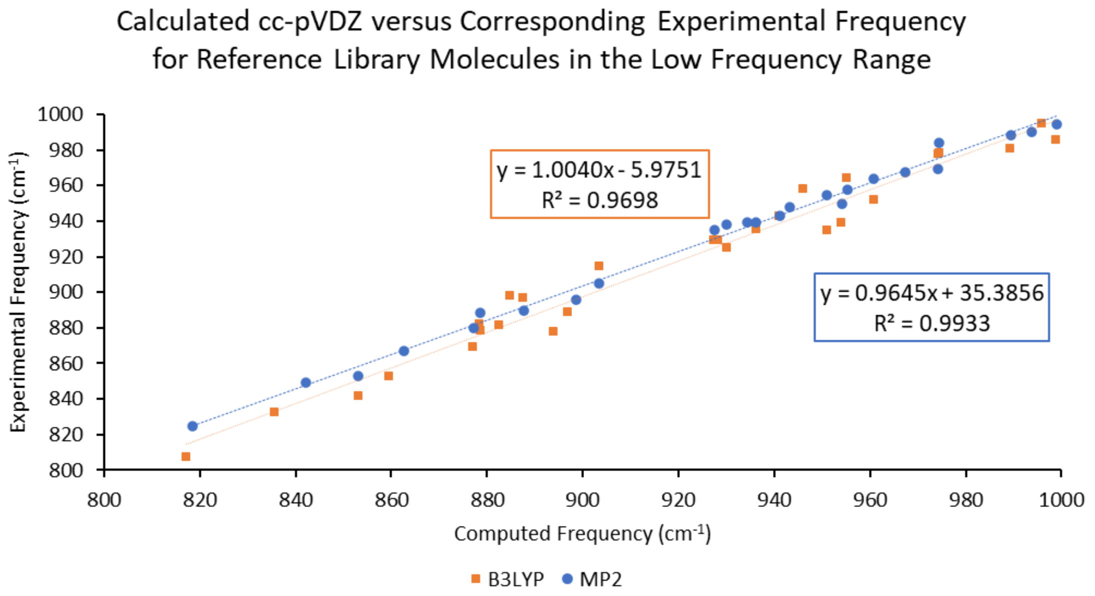

Figure B.7 Graph of computed versus corresponding assigned experimental frequency for reference library molecules, calculated at the cc-pVDZ level in the low-frequency range.

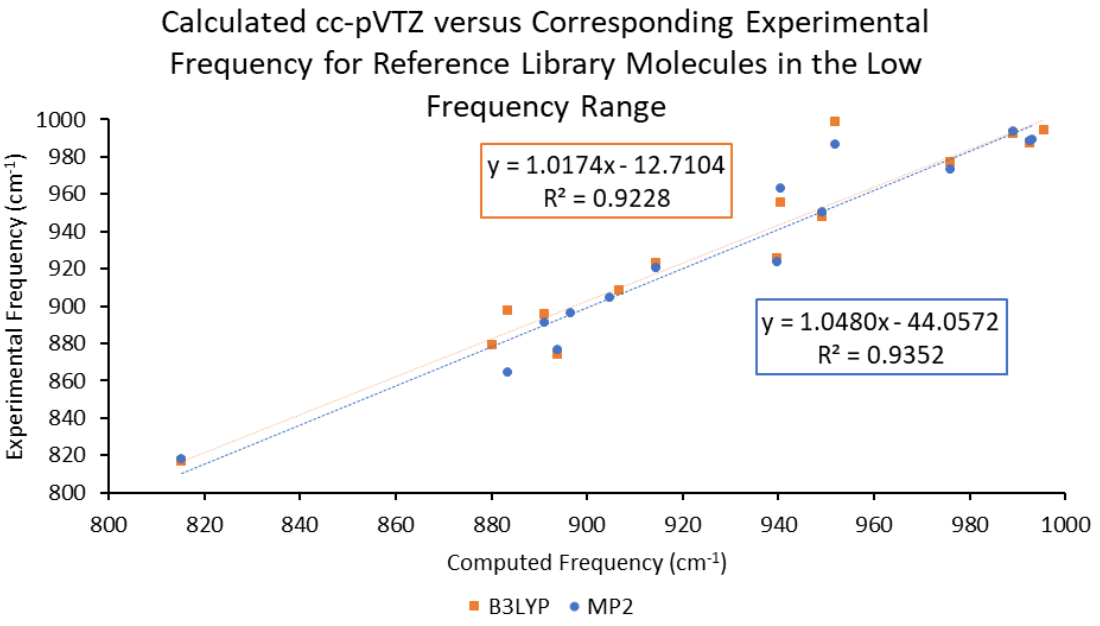

Figure B.8 Graph of computed versus corresponding assigned experimental frequency for reference library molecules, calculated at the cc-pVTZ level in the low-frequency range.

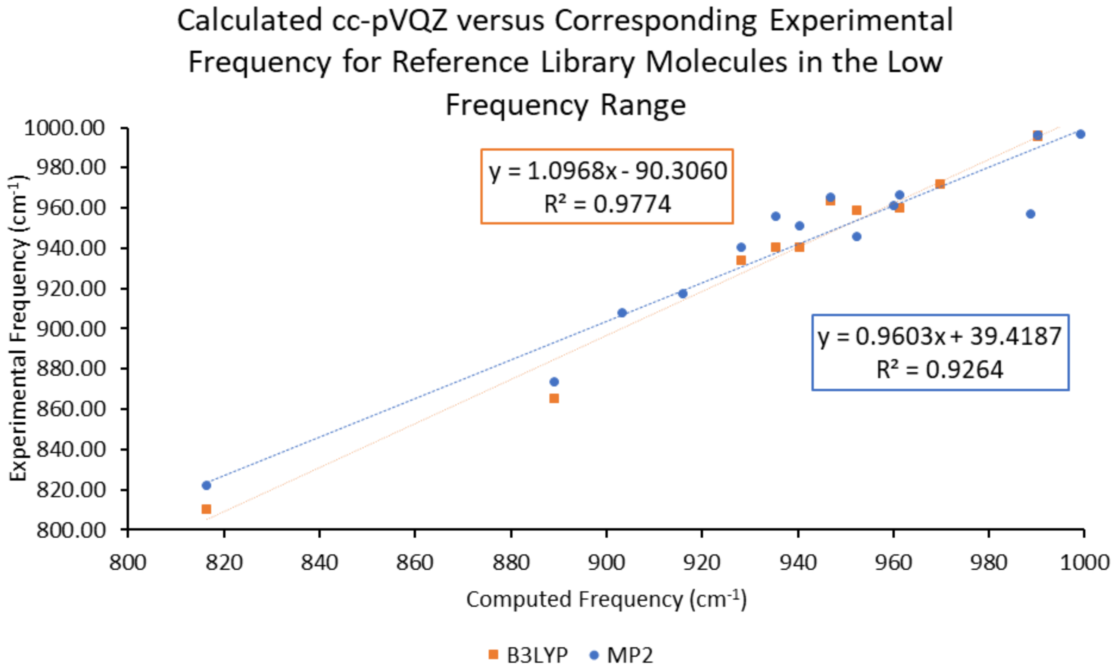

Figure B.9 Graph of computed versus corresponding assigned experimental frequency for reference library molecules, calculated at the cc-pVQZ level in the low-frequency range.

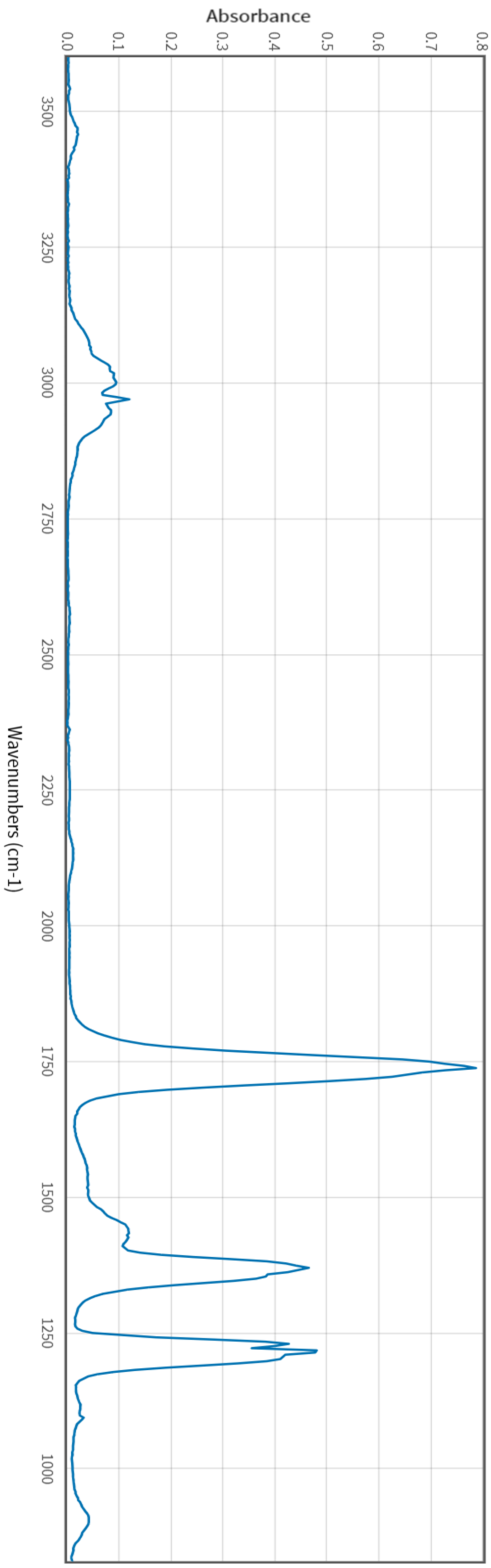

Figure B.10 Reference acetone spectrum. Source: NIST Standard Reference Data Program Collection[17]

# C. Chapter 4: Additional Data

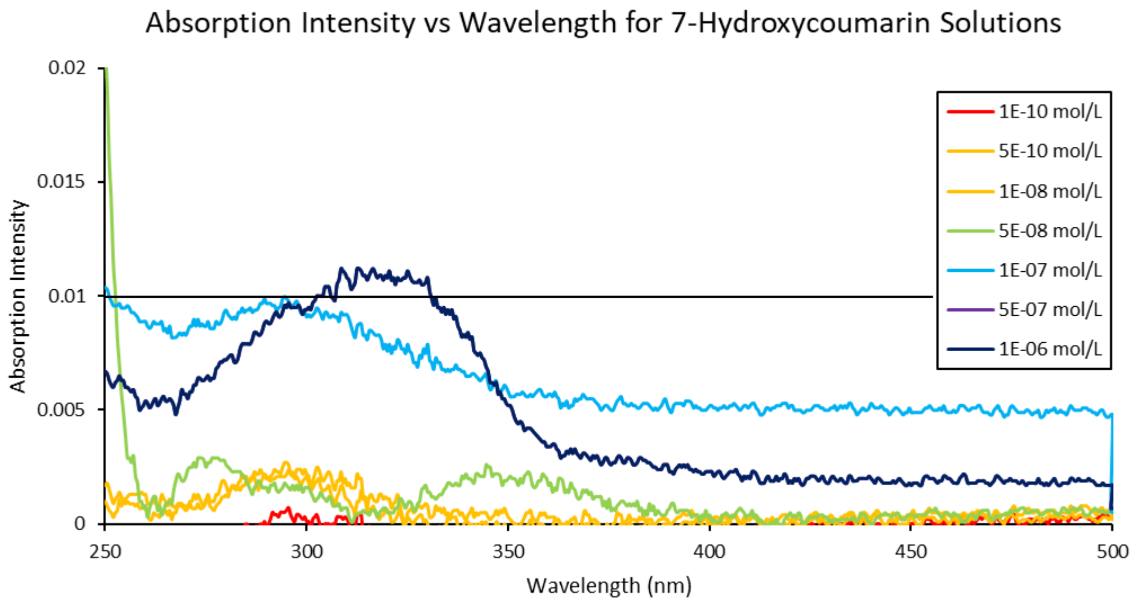

Figure C.1 UV-Vis absorption intensity for 7-hydroxycoumarin solutions used to form the calibration curve, proving absorbance for all solutions at λ = 460 nm is < 0.01 (below black line), avoiding inner-filter effect.

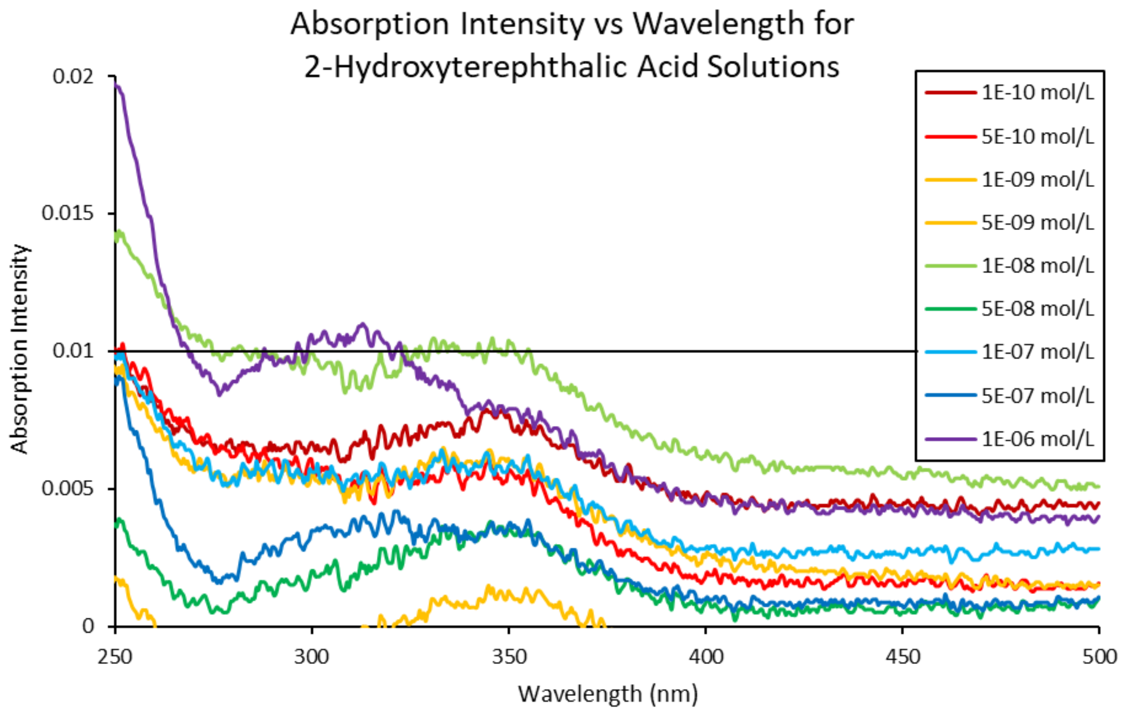

Figure C.2 UV-Vis absorption intensity for the 2-hydroxyterephthalic acid solutions used to form the calibration curve, proving absorbance for all solutions at λ = 425 nm is < 0.01 (below black line), avoiding inner-filter effect.

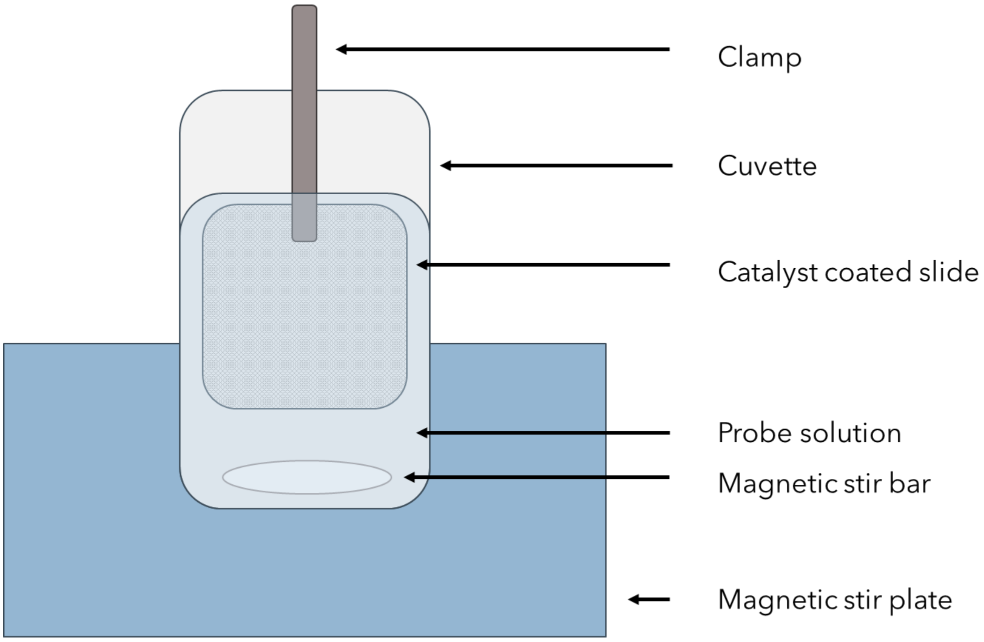

Figure C.3 Diagram of the experimental setup used in section 4.3.2 during the fluorescent probe experiments, in the same plane as the light from the fluorometer.

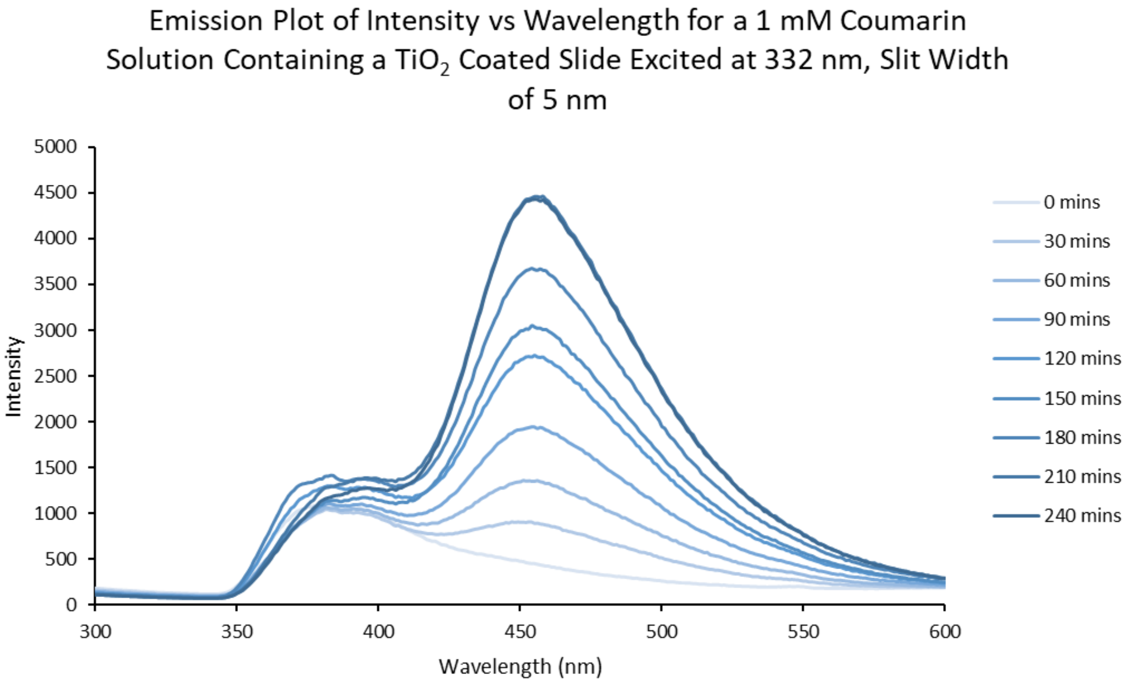

Figure C.4 Emission plot for the 1 mM coumarin solution containing a $TiO_2$-coated slide undergoing continuous UV irradiation ($\lambda_{ex}$ = 332 nm), using raw intensity data. Data were recorded every 10 minutes but for simplicity scans taken every 30 minutes are shown. Slit widths were 5 nm, and a 360 nm filter was used. Normalised data given in Figure 4.4.

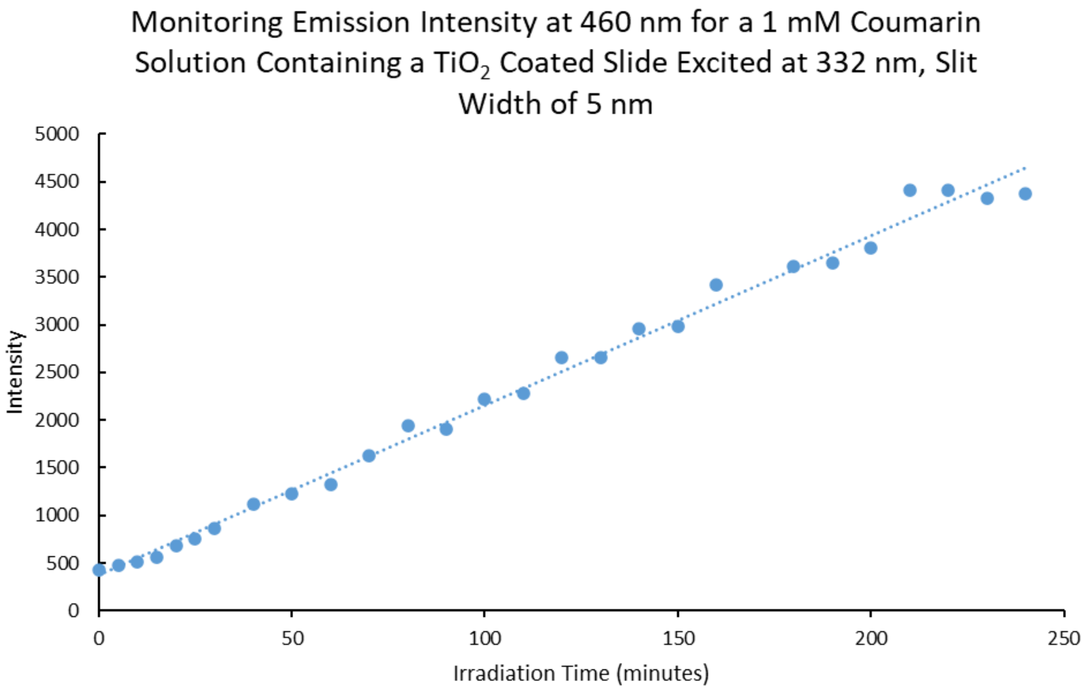

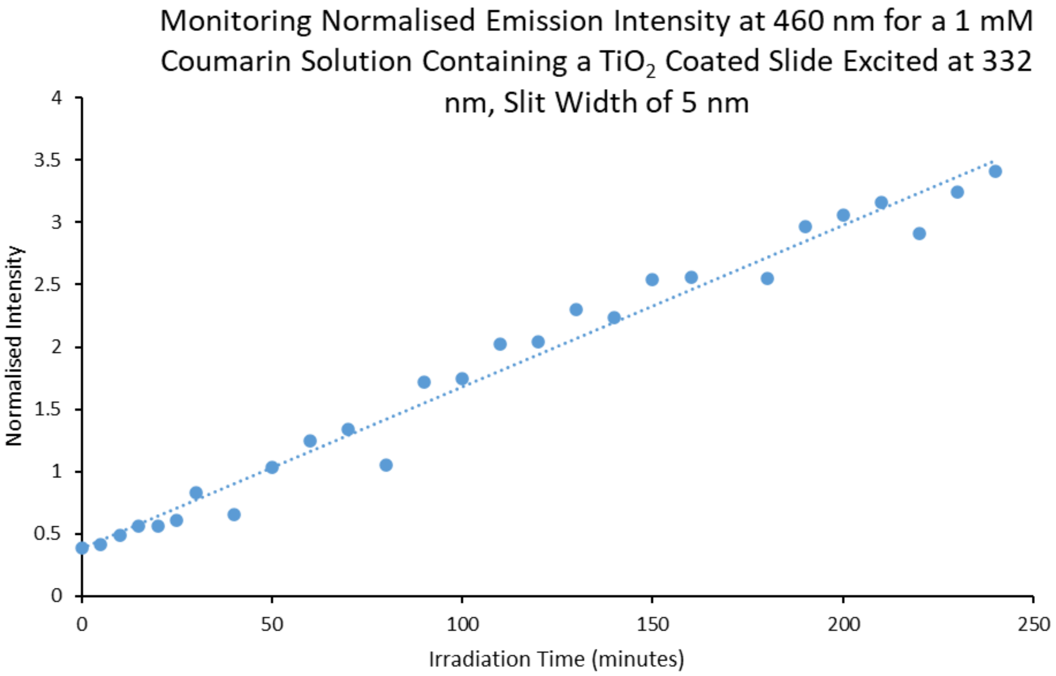

Figure C.5 Raw and normalised intensity plots monitoring 460 nm for a 1 mM coumarin solution containing a $TiO_2$-coated slide undergoing continuous UV irradiation ($\lambda_{ex}$ = 332 nm), Figure 4.4.

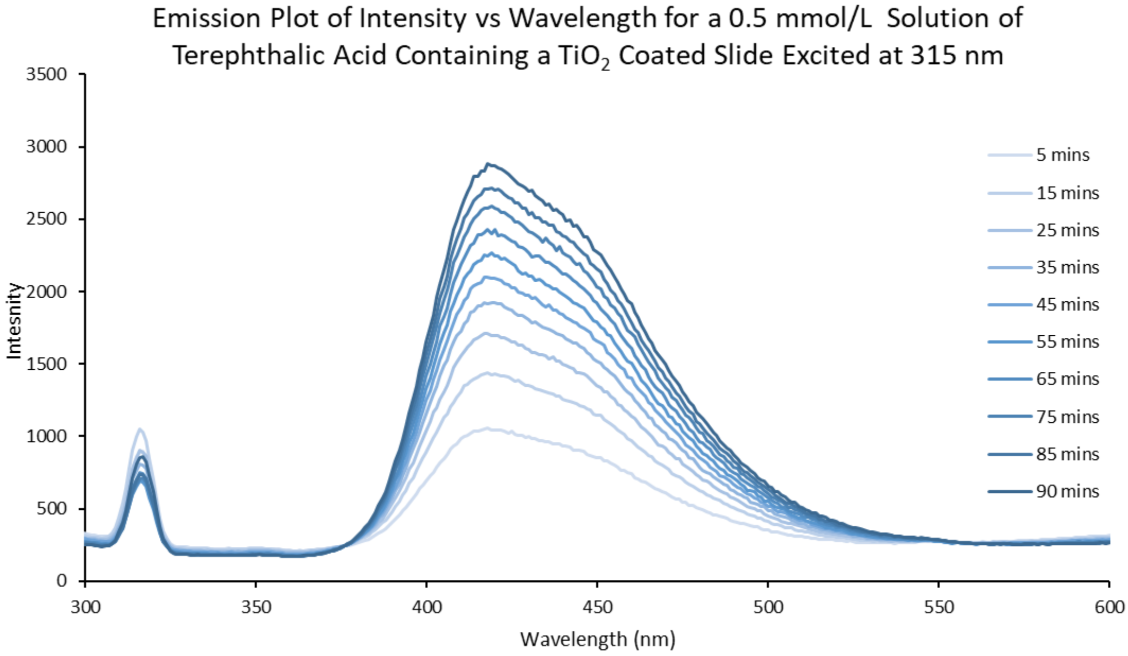

Figure C.6 Emission plot for the 0.5 mM terephthalic acid solution containing a $TiO_2$-coated slide undergoing continuous UV irradiation ($\lambda_{ex}$ = 315 nm), using raw intensity data. Data were recorded every 10 minutes but for simplicity scans taken every 30 minutes are shown. Slit widths were 5 nm, and a 340 nm filter was used. Normalised data given in Figure 4.5.

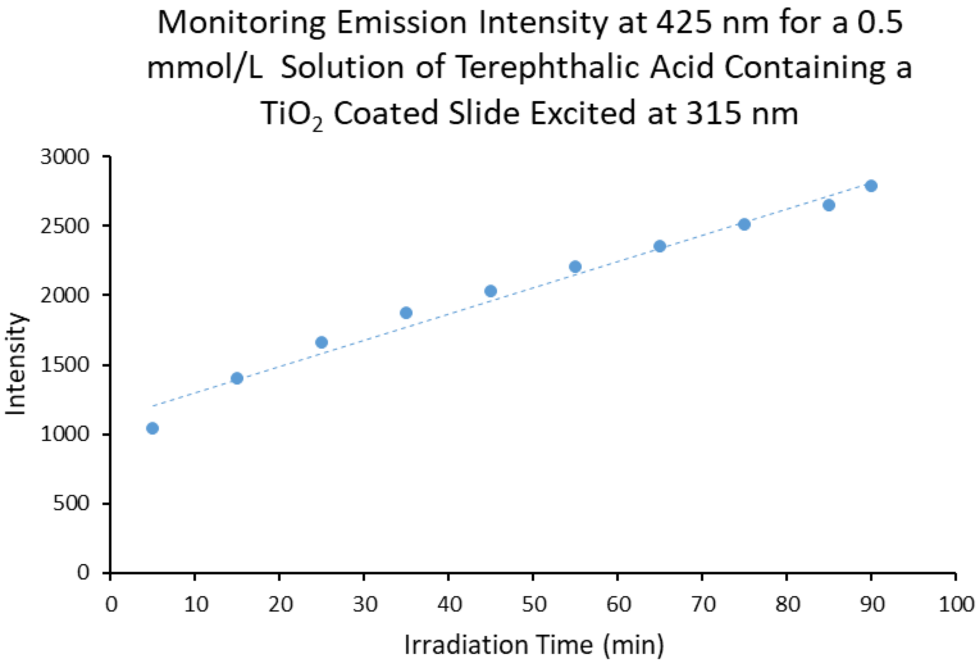

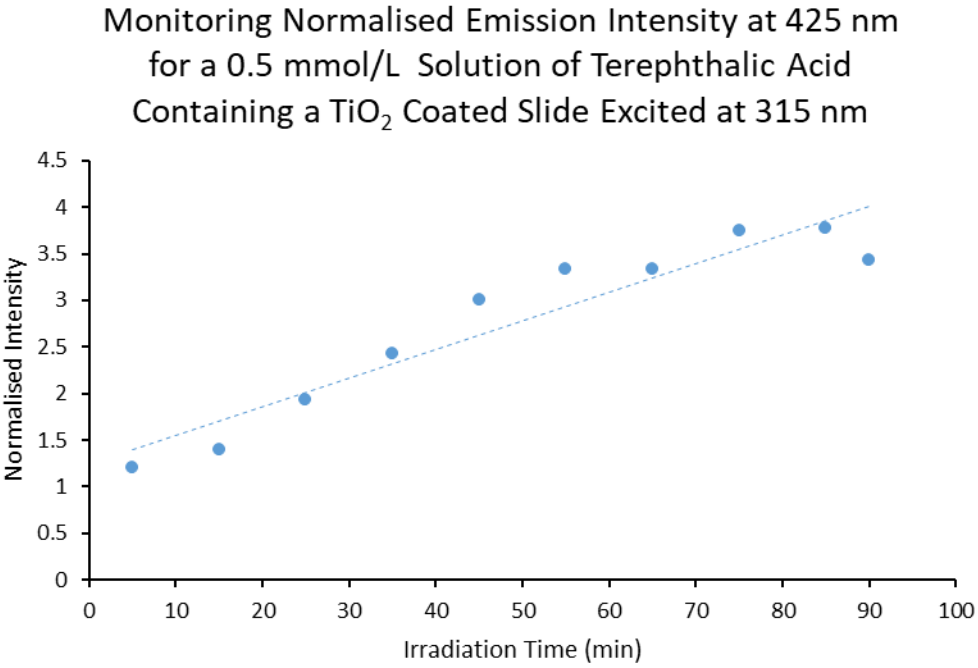

Figure C.7 Raw and normalised intensity plots monitoring 425 nm for a 0.5 mM terephthalic acid solution containing a TiO$_2$-coated slide undergoing continuous UV irradiation ($\lambda_{ex}$ = 315 nm), Figure 4.5.

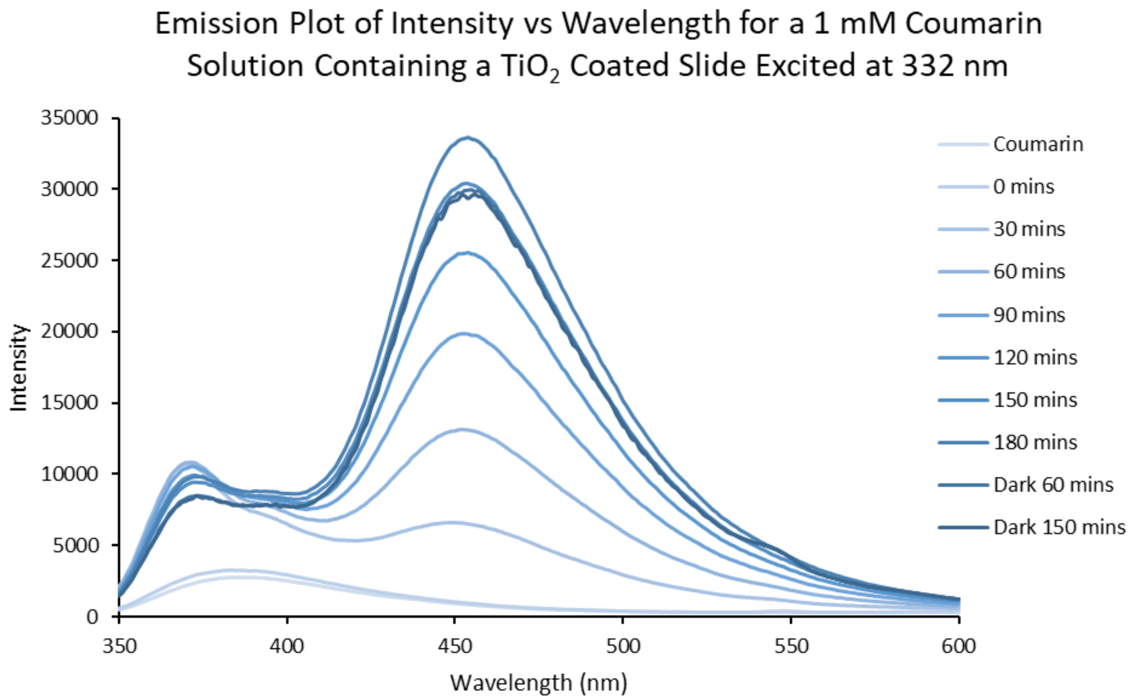

Figure C.8 Emission plot for the 1 mM coumarin solution containing a $TiO_2$-coated slide undergoing continuous UV irradiation (λex = 332 nm), using raw intensity data. Slit widths were 10 nm, and a 360 nm filter was used. Normalised data given in Figure 4.6.

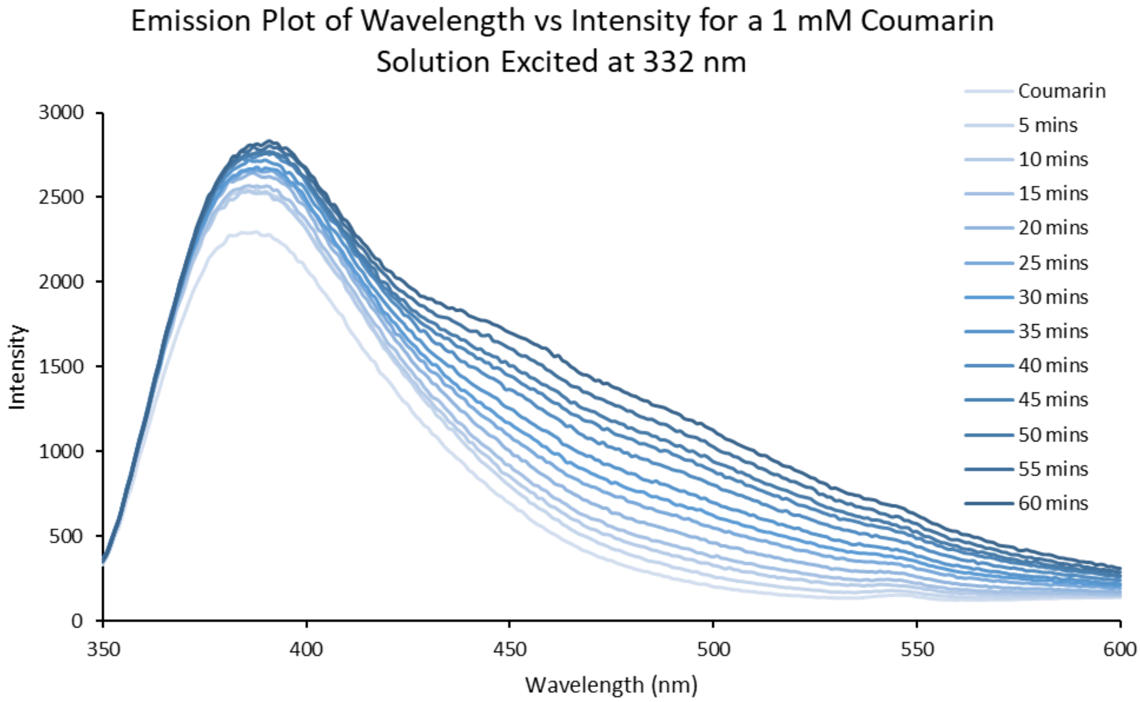

Figure C.9 "Blank" run of the 1 mM coumarin probe solution, run without a $TiO_2$ slide, plotted with raw intensity data. Slit width 10 nm, λex = 332 nm. Normalised data given in Figure 4.7.

# D. Chapter 5: Photolysis Rate (J) Data

Each photolysis rate was calculated as detailed in section 5.3.1.

## D.1 Ozone ($O_3$)

The J value for photolysis of ozone for equations D1 and D2 are listed in Table D.1 below.

$$O_3 + hv \rightarrow O^1D + O_2 \tag{D1}$$

$$O_3 + hv \rightarrow O^3P + O_2 \tag{D2}$$

Table D.1 Values used to calculate the J value for photolysis reactions (D1, D2) of ozone to form products $O^1D$ and $O^3P$.

| **λ (nm)** | **F (cm$^2$ s$^{-1}$ nm$^{-1}$)** | **σ (cm$^{-2}$ molecule$^{-1}$)[10]** | **ϕ (O$^1$D)[9]** | **J (O$^1$D) (s$^{-1}$ nm$^{-1}$)** | **ϕ (O$^3$D) [9]** | **J (O$^3$P) (s$^{-1}$ nm$^{-1}$)** |
|---:|---:|---:|---:|---:|---:|---:|
| 300 | 4.53E+11 | 4.09E-19 | 0.9 | 1.67E-07 | 0.1 | 1.85E-08 |
| 305 | 8.02E+12 | 2.11E-19 | 0.9 | 1.52E-06 | 0.1 | 1.69E-07 |
| 310 | 1.90E+13 | 9.92E-20 | 0.523 | 9.83E-07 | 0.477 | 8.97E-07 |
| 315 | 5.67E+13 | 5.24E-20 | 0.239 | 7.09E-07 | 0.761 | 2.26E-06 |
| 320 | 8.13E+13 | 2.59E-20 | 0.166 | 3.50E-07 | 0.834 | 1.76E-06 |
| 325 | 9.45E+13 | 1.84E-20 | 0.092 | 1.60E-07 | 0.908 | 1.58E-06 |
| 330 | 1.74E+14 | 6.68E-21 | 0.08 | 9.31E-08 | 0.92 | 1.07E-06 |
| 335 | 1.55E+14 | 2.53E-21 | 0.08 | 3.13E-08 | 0.92 | 3.6E-07 |
| 340 | 1.92E+14 | 2.04E-21 | 0.08 | 3.14E-08 | 0.92 | 3.61E-07 |
| **Total J (s$^{-1}$)** | | | | 4.05E-06 | | 8.47E-06 |

## D.2 Formaldehyde ($H_2CO$)

The J value for photolysis of formaldehyde for equations D3 and D4 are listed in Table D.2 below.

$$H_2CO + hv \rightarrow CO + H_2 \tag{D3}$$

$$H_2CO + hv \rightarrow H\cdot + HCO\cdot \tag{D4}$$

Table D.2 Values used to calculate the J value for photolysis reactions (D3, D4) of formaldehyde.

| **λ (nm)** | **F (cm$^2$ s$^{-1}$ nm$^{-1}$)** | **σ (cm$^{-2}$ molecule$^{-1}$)[9]** | **ϕ(D3)[9]** | **J(D3) (s$^{-1}$ nm$^{-1}$)** | **ϕ(D4)[9]** | **J(D4) (s$^{-1}$ nm$^{-1}$)** |
|---:|---:|---:|---:|---:|---:|---:|
| 280 | 1.61E-05 | 2.34E-20 | 0.3 | 1.13E-25 | 0.58 | 2.18E-25 |
| 285 | 9.90E+00 | 4.05E-20 | 0.31 | 1.24E-19 | 0.67 | 2.69E-19 |
| 290 | 3.35E+06 | 1.17E-20 | 0.28 | 1.10E-14 | 0.72 | 2.83E-14 |
| 295 | 5.22E+09 | 4.05E-20 | 0.21 | 4.45E-11 | 0.79 | 1.67E-10 |
| 300 | 4.53E+11 | 9.64E-21 | 0.3 | 1.31E-09 | 0.7 | 3.06E-09 |
| 305 | 8.02E+12 | 4.75E-20 | 0.29 | 1.11E-07 | 0.71 | 2.71E-07 |
| 310 | 1.90E+13 | 1.74E-20 | 0.3 | 9.88E-08 | 0.7 | 2.30E-07 |
| 315 | 5.67E+13 | 5.57E-20 | 0.22 | 6.94E-07 | 0.78 | 2.46E-06 |
| 320 | 8.13E+13 | 1.19E-20 | 0.4 | 3.88E-07 | 0.6 | 5.83E-07 |
| 325 | 9.45E+13 | 1.58E-20 | 0.54 | 8.06E-07 | 0.46 | 6.86E-07 |
| 330 | 1.74E+14 | 3.87E-20 | 0.62 | 4.17E-06 | 0.38 | 2.56E-06 |
| 335 | 1.55E+14 | 9.70E-22 | 0.56 | 8.41E-08 | 0.07 | 1.05E-08 |
| 340 | 1.92E+14 | 3.15E-20 | 0.64 | 3.88E-06 | 0.01 | 6.06E-08 |
| 345 | 1.80E+14 | 4.37E-21 | 0.5 | 3.94E-07 | 0.007 | 5.51E-09 |
| 350 | 2.03E+14 | 3.60E-22 | 0.36 | 2.63E-08 | 0.006 | 4.38E-10 |
| 355 | 2.23E+14 | 6.69E-21 | 0.12 | 1.79E-07 | 0.005 | 7.47E-09 |
| 360 | 2.39E+14 | 9.00E-23 | 0 | 0.00E+00 | 0 | 0.00E+00 |
| **Total J (s$^{-1}$)** | | | | 1.08E-05 | | 6.88E-06 |

## D.3 Methyl Hydroperoxide ($CH_3OOH$)

The J value for photolysis of methyl hydroperoxide for equation D5 is listed in Table D.3 below.

$$CH_3OOH + hv \rightarrow CH_3O\cdot + \cdot OH \qquad \text{(D5)}$$

Table D.3 Values used to calculate the J value for the photolysis reaction (D5) of methyl hydroperoxide.

| **λ (nm)** | **F ($cm^2$ $s^{-1}$ $nm^{-1}$)** | **σ ($cm^{-2}$ $molecule^{-1}$)[11]** | **ϕ(D5)[11]** | **J(D5) ($s^{-1}$ $nm^{-1}$)** |
|---:|---:|---:|---:|---:|
| 280 | 1.61E-05 | 1.09E-20 | 1 | 1.75E-25 |
| 285 | 9.90E+00 | 8.63E-21 | 1 | 8.54E-20 |
| 290 | 3.35E+06 | 6.91E-21 | 1 | 2.32E-14 |
| 295 | 5.22E+09 | 5.51E-21 | 1 | 2.88E-11 |
| 300 | 4.53E+11 | 4.13E-21 | 1 | 1.87E-09 |
| 305 | 8.02E+12 | 3.13E-21 | 1 | 2.51E-08 |
| 310 | 1.90E+13 | 2.39E-21 | 1 | 4.53E-08 |
| 315 | 5.67E+13 | 1.82E-21 | 1 | 1.03E-07 |
| 320 | 8.13E+13 | 1.37E-21 | 1 | 1.11E-07 |
| 325 | 9.45E+13 | 1.05E-21 | 1 | 9.93E-08 |
| 330 | 1.74E+14 | 7.90E-22 | 1 | 1.38E-07 |
| 335 | 1.55E+14 | 6.10E-22 | 1 | 9.44E-08 |
| 340 | 1.92E+14 | 4.70E-22 | 1 | 9.03E-08 |
| 345 | 1.80E+14 | 3.50E-22 | 1 | 6.31E-08 |
| 350 | 2.03E+14 | 2.70E-22 | 1 | 5.48E-08 |
| 355 | 2.23E+14 | 2.10E-22 | 1 | 4.69E-08 |
| 360 | 2.39E+14 | 1.60E-22 | 1 | 3.82E-08 |
| 365 | 2.14E+14 | 1.20E-22 | 1 | 2.57E-08 |
| **Total J ($s^{-1}$)** | | | | 9.37E-07 |

## D.4 Hydrogen Peroxide ($H_2O_2$)

The J value for photolysis of hydrogen peroxide for equation D6 is listed in Table D.4 below.

$$H_2O_2 + hv \rightarrow 2HO\cdot \tag{D6}$$

Table D.4 Values used to calculate the J value for the photolysis reaction (D6) of hydrogen peroxide.

| λ (nm) | F ($cm^2$ $s^{-1}$ $nm^{-1}$) | σ ($cm^{-2}$ $molecule^{-1}$)[9] | ϕ(D6)[9] | J(D6) ($s^{-1}$ $nm^{-1}$) |
|---|---|---|---|---|
| 280 | 1.61E-05 | 2.00E-20 | 1.00 | 3.22E-25 |
| 285 | 9.90E+00 | 1.50E-20 | 1.00 | 1.48E-19 |
| 290 | 3.35E+06 | 1.20E-20 | 1.00 | 4.02E-14 |
| 295 | 5.22E+09 | 9.00E-21 | 1.00 | 4.70E-11 |
| 300 | 4.53E+11 | 6.80E-21 | 1.00 | 3.08E-09 |
| 305 | 8.02E+12 | 5.10E-21 | 1.00 | 4.08E-08 |
| 310 | 1.90E+13 | 3.90E-21 | 1.00 | 7.39E-08 |
| 315 | 5.67E+13 | 2.90E-21 | 1.00 | 1.64E-07 |
| 320 | 8.13E+13 | 2.20E-21 | 1.00 | 1.79E-07 |
| 325 | 9.45E+13 | 1.60E-21 | 1.00 | 1.51E-07 |
| 330 | 1.74E+14 | 1.30E-21 | 1.00 | 2.26E-07 |
| 335 | 1.55E+14 | 1.00E-21 | 1.00 | 1.55E-07 |
| 340 | 1.92E+14 | 7.00E-22 | 1.00 | 1.35E-07 |
| 345 | 1.80E+14 | 5.00E-22 | 1.00 | 9.01E-08 |
| 350 | 2.03E+14 | 4.00E-22 | 1.00 | 8.11E-08 |
| **Total J ($s^{-1}$)** | | | | 1.30E-06 |

## D.5 Nitrogen Dioxide ($NO_2\cdot$)

The J value for photolysis of nitrogen dioxide for equation D7 is listed in Table D.5 below.

$$NO_2 \cdot + hv \rightarrow NO \cdot + O^3P \tag{D7}$$

Table D.5 Values used to calculate the J value for the photolysis reaction (D7) of nitrogen dioxide.

| **λ (nm)** | **F (cm$^2$ s$^{-1}$ nm$^{-1}$)** | **σ (cm$^{-2}$ molecule$^{-1}$)[12]** | **ϕ(D7)[13]** | **J(D7) (s$^{-1}$ nm$^{-1}$)** |
|---:|---:|---:|---:|---:|
| 280 | 1.61E-05 | 2.00E-20 | 1.00 | 3.22E-25 |
| 285 | 9.899066 | 6.99E-20 | 1.00E+00 | 6.92E-19 |
| 290 | 3350696 | 8.18E-20 | 9.99E-01 | 2.74E-13 |
| 295 | 5.22E+09 | 9.67E-20 | 9.98E-01 | 5.04E-10 |
| 300 | 4.53E+11 | 1.17E-19 | 9.97E-01 | 5.29E-08 |
| 305 | 8.02E+12 | 1.66E-19 | 9.96E-01 | 1.33E-06 |
| 310 | 1.9E+13 | 1.76E-19 | 9.95E-01 | 3.32E-06 |
| 315 | 5.67E+13 | 2.25E-19 | 9.94E-01 | 1.27E-05 |
| 320 | 8.13E+13 | 2.54E-19 | 9.93E-01 | 2.05E-05 |
| 325 | 9.45E+13 | 2.79E-19 | 9.92E-01 | 2.62E-05 |
| 330 | 1.74E+14 | 2.99E-19 | 9.91E-01 | 5.16E-05 |
| 335 | 1.55E+14 | 3.45E-19 | 9.90E-01 | 5.29E-05 |
| 340 | 1.92E+14 | 3.88E-19 | 9.89E-01 | 7.38E-05 |
| 345 | 1.8E+14 | 4.07E-19 | 9.88E-01 | 7.24E-05 |
| 350 | 2.03E+14 | 4.1E-19 | 9.87E-01 | 8.21E-05 |
| 355 | 2.23E+14 | 5.13E-19 | 9.86E-01 | 1.13E-04 |
| 360 | 2.39E+14 | 4.51E-19 | 9.84E-01 | 1.06E-04 |
| 365 | 2.14E+14 | 5.78E-19 | 9.83E-01 | 1.22E-04 |
| 370 | 2.98E+14 | 5.42E-19 | 9.81E-01 | 1.59E-04 |
| 375 | 1.94E+14 | 5.35E-19 | 9.79E-01 | 1.02E-04 |
| 380 | 2.52E+14 | 5.99E-19 | 9.75E-01 | 1.47E-04 |
| 385 | 2.68E+14 | 5.94E-19 | 9.69E-01 | 1.54E-04 |
| 390 | 3.2E+14 | 6E-19 | 9.60E-01 | 1.84E-04 |
| 395 | 3.47E+14 | 5.89E-19 | 9.42E-01 | 1.93E-04 |
| 400 | 4.49E+14 | 6.76E-19 | 6.95E-01 | 2.11E-04 |
| 405 | 4.62E+14 | 6.32E-19 | 3.50E-01 | 1.02E-04 |
| 410 | 4.42E+14 | 5.77E-19 | 1.30E-01 | 3.31E-05 |
| **Total J (s$^{-1}$)** | | | | 2.02E-03 |

## D.6 Nitrate Radical ($NO_3\cdot$)

The J value for photolysis of the nitrate radical for equations D8 and D9 are listed in Table D.6 below.

$$NO_3\cdot + hv \rightarrow NO\cdot + O_2 \qquad \text{(D8)}$$

$$NO_3\cdot + hv \rightarrow NO_2\cdot + O^3P \qquad \text{(D9)}$$

---

Table D.6 Values used to calculate the J value for the photolysis reactions (D8 and D9) of the nitrate radical.

| **λ (nm)** | **F ($cm^2$ $s^{-1}$ $nm^{-1}$)** | **σ ($cm^{-2}$ $molecule^{-1}$)[14]** | **ϕ(D8)[15]** | **J(D8) ($s^{-1}$ $nm^{-1}$)** | **ϕ(D9)[15]** | **J(D9) ($s^{-1}$ $nm^{-1}$)** |
|---|---|---|---|---|---|---|
| 585 | 8.35E+14 | 2.46E-18 | | | 0.983 | 2.02E-03 |
| 590 | 7.22E+14 | 5.67E-18 | 0.19 | 7.78E-04 | 0.793 | 3.25E-03 |
| 595 | 7.56E+14 | 3.91E-18 | 0.359 | 1.06E-03 | 0.608 | 1.80E-03 |
| 600 | 8.15E+14 | 2.45E-18 | 0.291 | 5.81E-04 | 0.472 | 9.42E-04 |
| 605 | 8.41E+14 | 4.18E-18 | 0.264 | 9.28E-04 | 0.323 | 1.13E-03 |
| 610 | 8.40E+14 | 1.35E-18 | 0.236 | 2.67E-04 | 0.226 | 2.56E-04 |
| 615 | 8.44E+14 | 1.99E-18 | 0.166 | 2.79E-04 | 0.147 | 2.47E-04 |
| 620 | 8.48E+14 | 2.47E-18 | 0.131 | 2.74E-04 | 0.0897 | 1.88E-04 |
| 625 | 8.12E+14 | 8.65E-18 | 0.0985 | 6.92E-04 | 0.0487 | 3.42E-04 |
| 630 | 8.08E+14 | 6.41E-18 | 0.0649 | 3.36E-04 | 0.0264 | 1.37E-04 |
| 635 | 8.49E+14 | 1.06E-18 | 0.0373 | 3.36E-05 | 0.0146 | 1.31E-05 |
| 640 | 8.48E+14 | 9.8E-19 | 0.0203 | 1.69E-05 | 0.00715 | 5.94E-06 |
| **Total J ($s^{-1}$)** | | | | 5.25E-03 | | 1.03E-02 |

## D.7 Nitrous Acid ($HNO_2$)

The J value for photolysis of nitrous acid ($HNO_2$) for equation D10 is listed in Table D.7 below.

$$HNO_2 + hv \rightarrow NO\cdot + \cdot OH \qquad \text{(D10)}$$

Table D.7 Values used to calculate the J value for the photolysis reaction (D10) of nitrous acid.

| **λ (nm)** | **F (cm$^2$ s$^{-1}$ nm$^{-1}$)** | **σ (cm$^{-2}$ molecule$^{-1}$)**[9] | **ϕ(D10)**[9] | **J(D10) (s$^{-1}$ nm$^{-1}$)** |
|---:|---:|---:|---:|---:|
| 300 | 4.53E+11 | 0.00E+00 | 1 | 0.00E+00 |
| 305 | 8.02E+12 | 7.00E-21 | 1 | 5.62E-08 |
| 310 | 1.90E+13 | 1.60E-20 | 1 | 3.03E-07 |
| 315 | 5.67E+13 | 2.50E-20 | 1 | 1.42E-06 |
| 320 | 8.13E+13 | 4.40E-20 | 1 | 3.58E-06 |
| 325 | 9.45E+13 | 5.00E-20 | 1 | 4.73E-06 |
| 330 | 1.74E+14 | 9.30E-20 | 1 | 1.62E-05 |
| 335 | 1.55E+14 | 6.50E-20 | 1 | 1.01E-05 |
| 340 | 1.92E+14 | 1.68E-19 | 1 | 3.23E-05 |
| 345 | 1.80E+14 | 9.60E-20 | 1 | 1.73E-05 |
| 350 | 2.03E+14 | 1.15E-19 | 1 | 2.33E-05 |
| 355 | 2.23E+14 | 2.36E-19 | 1 | 5.27E-05 |
| 360 | 2.39E+14 | 8.00E-20 | 1 | 1.91E-05 |
| 365 | 2.14E+14 | 1.61E-19 | 1 | 3.45E-05 |
| 370 | 2.98E+14 | 2.05E-19 | 1 | 6.12E-05 |
| 375 | 1.94E+14 | 4.90E-20 | 1 | 9.53E-06 |
| 380 | 2.52E+14 | 9.20E-20 | 1 | 2.32E-05 |
| 385 | 2.68E+14 | 1.45E-19 | 1 | 3.89E-05 |
| 390 | 3.20E+14 | 2.40E-20 | 1 | 7.69E-06 |
| 395 | 3.47E+14 | 6.00E-21 | 1 | 2.08E-06 |
| **Total J (s$^{-1}$)** | | | | 3.58E-04 |

## D.8 Nitric Acid ($HNO_3$)

The J value for photolysis of nitric acid ($HNO_3$) for equation D11 is listed in Table D.8 below.

$$HNO_3 + hv \rightarrow NO_2 \cdot + \cdot OH \quad \text{(D11)}$$

Table D.8 Values used to calculate the J value for the photolysis reaction (D11) of nitric acid.

| λ (nm) | F ($cm^2$ $s^{-1}$ $nm^{-1}$) | σ ($cm^{-2}$ $molecule^{-1}$)[9] | ϕ(D11)[9] | J(D11) ($s^{-1}$ $nm^{-1}$) |
|---|---|---|---|---|
| 300 | 4.53E+11 | 2.60E-21 | 0.97 | 1.14E-09 |
| 305 | 8.02E+12 | 1.50E-21 | 0.97 | 1.17E-08 |
| 310 | 1.90E+13 | 8.10E-22 | 0.97 | 1.49E-08 |
| 315 | 5.67E+13 | 4.10E-22 | 0.97 | 2.25E-08 |
| 320 | 8.13E+13 | 2.00E-22 | 0.97 | 1.58E-08 |
| 325 | 9.45E+13 | 9.50E-23 | 0.97 | 8.71E-09 |
| 330 | 1.74E+14 | 4.30E-23 | 0.97 | 7.27E-09 |
| 335 | 1.55E+14 | 2.20E-23 | 0.97 | 3.30E-09 |
| 340 | 1.92E+14 | 1.00E-23 | 0.97 | 1.86E-09 |
| 345 | 1.80E+14 | 6.00E-24 | 0.97 | 1.05E-09 |
| 350 | 2.03E+14 | 4.00E-24 | 0.97 | 7.87E-10 |
| **Total J ($s^{-1}$)** | | | | 8.90E-08 |

## D.9 Peroxynitric Acid ($HNO_4$)

The J value for photolysis of peroxynitric acid ($HNO_4$) for equations D12 and D13 are listed in Table D.9 below.

$$HNO_4 + hv \rightarrow NO_2\cdot + HOO\cdot \tag{D12}$$

$$HNO_4 + hv \rightarrow NO_3\cdot + \cdot OH \tag{D13}$$

Table D.9 Values used to calculate the J value for the photolysis reactions (D12 and D13) of peroxynitric acid.

| λ (nm) | F (cm$^2$ s$^{-1}$ nm$^{-1}$) | σ (cm$^{-2}$ molecule$^{-1}$)[9] | ϕ(D12)[9] | J(D12) (s$^{-1}$ nm$^{-1}$) | ϕ(D13)[9] | J(D13) (s$^{-1}$ nm$^{-1}$) |
|---|---|---|---|---|---|---|
| 285 | 9.90E+00 | 6.20E-20 | 0.59 | 3.62E-19 | 0.41 | 2.52E-19 |
| 290 | 3.35E+06 | 3.90E-20 | 0.59 | 7.71E-14 | 0.41 | 5.36E-14 |
| 295 | 5.22E+09 | 2.40E-20 | 0.59 | 7.39E-11 | 0.41 | 5.14E-11 |
| 300 | 4.53E+11 | 1.40E-20 | 0.59 | 3.74E-09 | 0.41 | 2.60E-09 |
| 305 | 8.02E+12 | 8.50E-21 | 0.59 | 4.02E-08 | 0.41 | 2.80E-08 |
| 310 | 1.90E+13 | 5.30E-21 | 0.59 | 5.93E-08 | 0.41 | 4.12E-08 |
| 315 | 5.67E+13 | 3.90E-21 | 0.59 | 1.30E-07 | 0.41 | 9.06E-08 |
| 320 | 8.13E+13 | 2.40E-21 | 0.59 | 1.15E-07 | 0.41 | 8.00E-08 |
| 325 | 9.45E+13 | 1.50E-21 | 0.59 | 8.37E-08 | 0.41 | 5.81E-08 |
| 330 | 1.74E+14 | 9.00E-22 | 0.59 | 9.25E-08 | 0.41 | 6.43E-08 |
| **Total J (s$^{-1}$)** | | | | 5.25E-07 | | 3.65E-07 |

## D.10 Nitrogen Pentoxide ($N_2O_5$)

The J value for photolysis of nitrogen pentoxide ($N_2O_5$) for equation D14 is listed in Table D.10 below.

$$N_2O_5 + hv \rightarrow NO_3\cdot + NO_2\cdot \tag{D14}$$

Table D.10 Values used to calculate the J value for the photolysis reaction (D14) of nitrogen pentoxide.

| λ (nm) | F (cm$^2$ s$^{-1}$ nm$^{-1}$) | σ (cm$^{-2}$ molecule$^{-1}$)[9] | ϕ(D14)[9] | J(D14) (s$^{-1}$ nm$^{-1}$) |
|---:|---:|---:|---:|---:|
| 285 | 9.90E+00 | 8.59E-20 | 0.8 | 6.80E-19 |
| 290 | 3.35E+06 | 6.71E-20 | 0.8 | 1.80E-13 |
| 295 | 5.22E+09 | 5.11E-20 | 0.8 | 2.13E-10 |
| 300 | 4.53E+11 | 3.87E-20 | 0.8 | 1.40E-08 |
| 305 | 8.02E+12 | 2.91E-20 | 1 | 2.34E-07 |
| 310 | 1.90E+13 | 2.17E-20 | 1 | 4.11E-07 |
| 315 | 5.67E+13 | 1.62E-20 | 1 | 9.18E-07 |
| 320 | 8.13E+13 | 1.21E-20 | 1 | 9.84E-07 |
| 325 | 9.45E+13 | 8.90E-21 | 1 | 8.41E-07 |
| 330 | 1.74E+14 | 6.70E-21 | 1 | 1.17E-06 |
| 335 | 1.55E+14 | 5.00E-21 | 1 | 7.74E-07 |
| 340 | 1.92E+14 | 3.80E-21 | 1 | 7.30E-07 |
| 345 | 1.80E+14 | 2.79E-21 | 1 | 5.03E-07 |
| 350 | 2.03E+14 | 2.15E-21 | 1 | 4.36E-07 |
| 355 | 2.23E+14 | 1.64E-21 | 1 | 3.66E-07 |
| 360 | 2.39E+14 | 1.24E-21 | 1 | 2.96E-07 |
| 365 | 2.14E+14 | 9.10E-22 | 1 | 1.95E-07 |
| 370 | 2.98E+14 | 7.20E-22 | 1 | 2.15E-07 |
| 375 | 1.94E+14 | 5.30E-22 | 1 | 1.03E-07 |
| 380 | 2.52E+14 | 4.10E-22 | 1 | 1.03E-07 |
| 385 | 2.68E+14 | 3.20E-22 | 1 | 8.59E-08 |
| 390 | 3.20E+14 | 2.28E-22 | 1 | 7.30E-08 |
| 395 | 3.47E+14 | 1.71E-22 | 1 | 5.93E-08 |
| 400 | 4.49E+14 | 1.38E-22 | 1 | 6.20E-08 |
| 405 | 4.62E+14 | 1.03E-22 | 1 | 4.76E-08 |
| 410 | 4.42E+14 | 8.00E-23 | 1 | 3.53E-08 |
| **Total J (s$^{-1}$)** | | | | 8.65E-06 |

# E. References

1. Sverdlov, L. M.; Krainov, E. P.; Kovner, M. A., *Vibrational Spectra of Polyatomic Molecules*. John Wiley & Sons: New York, NY, USA, 1975; p 644.
2. Shimanouchi, T., *Tables of Molecular Vibrational Frequencies Consolidated Volume I*. National Bureau of Standards: 1972.
3. Schrumpf, G.; Klein, A. W., The Vibrational-Spectra of Cyclopropylacetylene and Cyclopropylacetylene-D1. *Spectrochim. Acta A* **1985,** *41* (10), 1251-1257.
4. van Lerberghe, D.; Wright, I. J.; Duncan, J. L., High-resolution infrared spectrum and rotational constants of ethylene-H4. *J. Mol. Spectrosc.* **1972,** *42*, 251-273.
5. Wany, A.; Kumar, A.; Nallapeta, S., et al., Extraction and characterization of essential oil components based on geraniol and citronellol from Java citronella (Cymbopogon winterianus Jowitt). *J. Plant Growth Regul.* **2014,** *73* (2), 133-145.
6. Wang, Y.; Desmedt, J.; Coucke, I., et al., Methacrolein in the Gas-Phase, Investigated by Electron-Diffraction, Microwave and Vibrational Spectroscopy, Supplemented with Ab-Initio Calculations of Geometries and Force-Fields. *J. Mol. Struct.* **1993,** *299*, 43-59.
7. Gardner, A. M.; Green, A. M.; Tamé-Reyes, V. M., et al., Vibrations of the low energy states of toluene (1A1 and 1B2) and the toluene cation (2B1). *J. Chem. Phys.* **2013,** *138* (13).
8. Williams, H. R.; Mosher, H. S., Infrared Spectra of Alkyl Hydroperoxides. *Anal. Chem.* **1955,** *27* (4), 517-521.
9. Atkinson, R.; Baulch, D. L.; Cox, R. A., et al., Evaluated kinetic and photochemical data for atmospheric chemistry: Volume I - gas phase reactions of $O_x$, $HO_x$, $NO_x$ and $SO_x$ species. *Atmos. Chem. Phys.* **2004,** *4* (6), 1461-1738.
10. Davenport, J. E. *Parameters for Ozone Photolysis as a Function of Temperature at 280-330 nm. Revision.*; FAA-EE-80-44; National Technical Information Service: 1982; p 43.
11. Atkinson, R.; Baulch, D. L.; Cox, R. A., et al., Evaluated kinetic and photochemical data for atmospheric chemistry: Volume II; gas phase reactions of organic species. *Atmos. Chem. Phys.* **2006,** *6* (11), 3625-4055.
12. Bass, A. M.; Ledford, A. E., Jr.; Laufer, A. H., Extinction Coefficients of $NO_2$ and $N_2O_4$. *J Res Natl Bur Stand A Phys Chem* **1976,** *80a* (2), 143-166.
13. Gardner, E. P.; Sperry, P. D.; Calvert, J. G., Primary quantum yields of $NO_2$ photodissociation. *J. Geophys. Res. Atmos.* **1987,** *92* (D6), 6642-6652.
14. Graham, R. A.; Johnston, H. S., The photochemistry of the nitrate radical and the kinetics of the nitrogen pentoxide-ozone system. *J. Phys. Chem.* **1978,** *82* (3), 254-268.
15. Johnston, H. S.; Davis, H. F.; Lee, Y. T., NO3 Photolysis Product Channels: Quantum Yields from Observed Energy Thresholds. *J. Phys. Chem.* **1996,** *100* (12), 4713-4723.
16. Brown, K. G.; Person, W. B., Infrared spectrum of benzene isolated in argon and krypton matrices. *Spectrochimica Acta Part A: Molecular Spectroscopy* **1978,** *34* (2), 117-122.
17. NIST Standard Reference Data Program Collection, Acetone Infrared Spectrum. In *NIST Chemistry WebBook, NIST Standard Reference Database Number 69*, NIST Mass Spectrometry Center; W. E. Wallace, Eds. Gaithersburg MD, 2018.